Monitoring of biotherapeutic purification by vibrational spectroscopy

Imperial College London

James William Beattie

2023

Supervised by Professor Bernadette Byrne, Professor Sergei Kazarian, Dr Ruth Roland-Jones, Dr Monika Farys, Hamish Bettany

Submitted to Imperial College London for the degree of Doctor of Philosophy

Declaration

The work and results in this thesis were carried out at Imperial colleges Department of Life Sciences, Department of Chemical Engineering as well as GSK Biopharm Process Research. Except where acknowledged the material is the original work of the author and no part of it has been submitted for a degree at any other university.

Copyright

Abstract

Monoclonal antibodies (mAbs) are used extensively as biotherapeutics (BTs) for a range of chronic and acute conditions. mAb treatments cost on average ~$100 000 per year per patient, limiting their use. Protein A chromatography (PrAc) accounts for a substantial portion of downstream processing costs, primarily due to expensive resin and its degradation, resulting in reduced binding capacity. This research utilised vibrational spectroscopy to investigate these issues.

ATR-FTIR and Raman spectroscopy successfully assessed static binding capacity (SBC) of Protein A resin. Spatial location within the column affected resin performance, with the inlet showing greater binding capacity reduction compared to the outlet. Vibrational spectroscopic methods provided valuable chemical insights into protein conformation that traditional analysis methods lack.

In-situ ATR-FTIR spectroscopy revealed that changes in ligand density did not align with the reduction in binding capacity. Irreversibly bound contaminants were suggested as the primary cause of reduction in binding capacity. Confocal Raman spectroscopy demonstrated heterogeneous binding of BTs within resin beads, indicating reduced ligand accessibility in used resins. Spectral analysis of used resin samples without BTs loaded indicated the presence of Phenylalanine-rich co-eluting host cell protein species. This suggests irreversible binding of BTs and fouling mechanisms that reduce resin pore size.

Raman spectroscopy showed promise for monitoring dynamic binding capacity (DBC) of Protein A. High-throughput well plate Raman analysis proved as effective as industry-standard methods. By utilizing PLS analysis, Raman spectroscopy could quantify BTs not used in model training, reducing time and effort for each new BT. In-line Raman methodology successfully identified BTs in complex cell supernatant without separation or chemical labels, offering real-time monitoring potential.

in conclusion this thesis effectively used vibrational spectroscopy, specifically ATR-FTIR and Raman spectroscopy to characterise Protein A resin, elucidated binding capacity decay, and enabled DBC monitoring in BT downstream processing.

Acknowledgments

I would like to thank Professor Bernadette Byrne who has provided invaluable support and guidance throughout this PhD. Her mentorship has helped me not only academically and given me the confidence in my scientific abilities but has helped me in personal development. The time she dedicates to students' scientific development and personal development truly inspires me.

I would also like to thank Professor Sergei Kazarian for his invaluable guidance and support through my PhD especially the long conversations over cups of tea and coffee. His mentorship has truly helped guide me greatly and ignited a passion in vibrational spectroscopy. I hope one day to have the energy and overwhelming knowledge he has shown throughout mentoring me.

A special thanks to my industrial supervisors at GSK Dr Ruth Rowland jones, Dr Monica Farys and Hamish Bettany. I would like to thank Ruth for the support on guidance on multivariate analysis and modelling as well as being an extremely insightful and supportive supervisor. I would like to thank Monika for the support and extremely helpful discussions on downstream processing and for being an invaluable well of knowledge throughout the PhD. I would also like to thank Hamish for the support and mentorship particularly though the placement at GSK, His lab experience was invaluable and taught me a lot about working as an industry focused scientist.

A thank you for all the coffee/tea breaks, help in the lab and much needed time at the pub to the groups of Sergei and Bernadette: Dr Hannah Tiernan, Dr Cristina Cecchetti, Thomas Davis, Nicole Deacon Smith, Sara Cioccolo, Dr Euan Pyle, Dr Jack Houghton-Gisby, Celine Van Haaren, Guan-Lin, Menebere Woubshete and Dr Savvas Saouros.

A thank you to the team at GSK Biopharm development team who made me so welcome and supported my scientific endeavours during my placement to Rob Grinstead, Alena Istrate, Nathan Cumberbatch, David Hilton, Sophie Russel, Will Lewis and Gary Finka.

A thank you to my undergraduate supervisor Dr Bhaven Patel who first inspired me to study chemistry and ignited my initial passion for research.

Thank you to my family and friends who have been there to support me though the highs and lows and put up with all the terrible jokes along the way, specially to best friend Dr Corey Briffa and the rest of the gang who I have known since 2007: Tom Stone, Sarah McGillick, Natalie Polley, Darrel Hodges, Emily Tierney and Ross Freeman.

Finally, the biggest thank you to my wife Pei Li who has encouraged and believed in me!

Table of contents

Table of Figures

List of Tables

List of abbreviations

AEX	Anion exchange chromatography
ANOVA	Analysis of variance
ATR	Attenuated total reflection
ATR-FTIR	Attenuated total reflection Fourier transform Infrared
BBB	Blood brain barrier
BT	Biotherapeutic
CCD	Charge coupled detector
CCS	Cell culture supernatant
CEX	Cation exchange chromatography
CHO	Chinese hamster ovary
CIP	Cleaning in place
CLSM	Confocal laser scanning microscopy
CUB	Clarified unprocessed bulk
CV	Column volume
DBC	Dynamic binding capacity
DOE	Design of experiment
DR	Depth resolution
EMA	European medicines agency
Fab	Fragment antigen binding
FC	Fragment crystallisable
FDA	Food and drug administration
FPA	Focal plane array
FPLC	Fast protein liquid chromatography
FTIR	Fourier transform infrared
GS-CHO	Glutamine synthetase Chinese hamster ovary
GSK	GlaxoSmithKline
HCDNA	Host cell Deoxyribonucleic acid
HCP	Host cell protein
HIX	Hydrophobic interaction chromatography
HMWS	High molecular weight species
HPLC	High performance liquid chromatography
IgG	Immunoglobulin type gamma
IR	Infrared
IRE	Internal reflection element
LC-MS/MS	Liquid chromatography-mass spectrometry
LOOCV	Leave one out cross validation
mAb	Monoclonal antibodies
MCT	Mercury cadmium telluride
MMC	Multimodal chromatography
NA	Numerical aperture
NaCl	Sodium chloride
NaOH	Sodium hydroxide
OH	Hydroxyl group

pH	Potential hydrogen
PLS	Partial least squares
PQA	Product quality attribute
PrAc	Protein A affinity chromatography
RMSE	Root mean square error
RMSECV	Root mean square error cross validation
RMSEP	Root square error of prediction
RMSN	Root mean square noise
RSM	Response surface model
SARS-CoV-1	Severe acute respiratory syndrome coronavirus 1
SARS-CoV-2	Severe acute respiratory syndrome coronavirus 2
SBC	Static binding capacity
SEM	scanning electron microscopy
SIMPLS	Simple Partial least squares
SNV	Standard normal variate
SPA	Staphylococcus protein A
UB	Unprocessed bulk
Tris-Base	Tris(hydroxymethyl)aminomethane
Tris-HCL	Tris(hydroxymethyl)aminomethane hydrochloride
V_H3	Variable heavy chain type 3

List of symbols

d_e	effective thickness
%CV	coefficient of variation
$(\partial a/\partial Q)$	change in polarizability
Δ	attempted focus depth
μ'	induced dipole moment
μ_{eff}	effective mass
A	Absorbance
a	polarizability
$\bar{A}$	mean signal
a_0	polarizability at equilibrium
A_i	i^{th} data point
b	standard curve y intercept
c	speed of light in a vacuum
C	concentration
C_0	BT titre
C_0	initial concentration
C_{eq}	concentration of equilibrium
C_M	mass on column
C_s	oversaturation concertation
D	radius of confocal light
$DBC_{10\%}$	Dynamic binding capacity at 10% breakthrough
d_p	depth of penetration
E	electric field strength
E_G	ground state energy
E_1	higher energy state
f	distance to confocal point
h	Planck's constant
I	intensity of single channel measurement with sample
I_O	intensity of single channel without sample present
k	force constant
k_d	dissociation constant
l	pathlength
$\log_{10}$	logarithm base 10
m	standard curve gradient
m_1	mass of one atom in an atomic bond
m_2	mass of another atom in atomic bond
n	number of data points

n_1	refractive index of sample
n_2	Refractive index of second material
NA	numerical aperture
n_{IRE}	refractive index of IRE
n_I	refractive index of objective
Q	Binding capacity
Q_D	nuclear displacement
Qmax	maximum binding capacity
r	distance between two points
RMSE	root mean square error
RMSN	Root mean square noise
S_A	peak area
SD	standard deviation
T	transmittance
t	time
V_0	offset volume
$V_{10\%}$	volume at 10% breakthrough
V_c	column bed volume
V_I	injection volume
V_{resin}	Volume of resin
V_{sample}	Volume of sample
$\bar{y}$	average actual measurement
y_i	i^{th} iteration of predicted observation
$\hat{y}_i$	i^{th} iteration of predicted observation
α	molecular polarizability
ε	molar absorptivity
θ	angle of incidence
θ_1	max half angle of the confocal light
λ	wavelength
ν	frequency
ν_0	frequency of wave
ν_{vib}	frequency of vibration
π	ratio of the circumference of any circle to the diameter of that circle
$\tilde{\nu}$	wavenumber
σ	scattering intensity

Publications and conferences

Publications

- Byrne B, Beattie JW, Song CL, Kazarian SG. ATR-FTIR spectroscopy and spectroscopic imaging of proteins. In: Ozaki Y, Baranska M, Lednev IK, Wood BR, editors. Vibrational Spectroscopy in Protein Research: Academic Press; 2020. p. 1-22.
- Beattie JW, Rowland-Jones RC, Farys M, Tran R, Kazarian SG, Byrne B. Insight into purification of monoclonal antibodies in industrial columns via studies of Protein A binding capacity by in situ ATR-FTIR spectroscopy. Analyst. 2021.
- Beattie JW, Istrate A, Lu A, Marshall C, Rowland-Jones RC, Farys M, et al. Causes of Industrial Protein A Column Degradation, Explored Using Raman Spectroscopy. Analytical Chemistry. 2022;94(45):15703-10.

Conferences

- UK Japanese Engineering education league (UKJEEL), Queen Mary,05/09/2019-07/09/2019
- The International Society for Clinical Spectroscopy (CLIRSPEC) summer school, Lake Windermere, UK, oral presentation: On-Column Monitoring of Protein Purification by Spectroscopy Techniques, 02/07/2019-05/07/2019
- Tokyo Tech Academy for Convergence of Materials and Informatics (TAC-MI), Odawara, Japan, Oral presentation: On-Column Monitoring of Protein Purification by Spectroscopic Techniques, 02/12/2019-06/12/2019
- SCIX 2020, virtual conference, oral presentation: ATR-FTIR Spectroscopy to Assess Protein A Affinity Resin Performance as A Function of Spatial Location Within a Column, 15/10/20
- SCIX2021, Rhode Island, USA (virtual attendance), oral presentation: Vibrational spectroscopy to assess degradation of purification resins used in the downstream processing of monoclonal antibodies, 30/09/2021

Exhibitions

- The great exhibition road festival, chemical photography, 28/06/20 - 30/06/20
- The great exhibition road festival, chemical photography, 18/06/2022 - 19/06/2022

Chapter 1- Literature Review

1.1 Biotherapeutics

The biopharmaceutical industry is rapidly growing with 175 biotherapeutics (BTs) approved for market as of 2021 [1, 2]. BT is used in this thesis to collectively refer to antibody-based molecules such as Bispecific antibodies, monoclonal antibodies (mAbs) and antibody derivatives such as fusion proteins and single-chain variable fragments. By far the most common and successful BTs are monoclonal antibodies (mAbs) which are used to treat a wide range of diseases and account for 22% of the Food and Drug Administrations (FDA) newly approved drugs between 2016-2018 [3]. However other BTs are beginning to take a hold in the market. Bispecifics which can bind to two targets simultaneously account for 4 market approvals [1]. Fusion proteins which combine desirable aspects of two proteins to treat disease account for 12 market approvals [4]. The best selling therapeutics for 2019 were mAbs with the top 9 generating cumulative sales of $75 billion in 2019 [5].

Overall mAbs make up the majority of BT's available with 90 approved for market as of 2021 [2].A total of 510 and 810 mAbs were in Phase I or Phase II clinical trials in 2019 and 2021 respectively [2, 6]. In addition, a record 61 cancer and 54 non-cancer targeted mAbs totalling 115 mAbs were in FDA and European Medicines Agency (EMA) late-stage studies as of November 2021 [2]. The increase from 240 mAbs in phase I-III clinical trials in 2010 illustrates the ever-increasing development of mAb based treatments by the pharmaceutical industry over the last decade [7-9].

1.1.1 Monoclonal antibodies

Currently, therapeutic mAbs available on the market are primarily of the subclass of Immunoglobulin type gamma (IgG) [10], also the most common isoform of antibody present in the body [11]. mAbs are monovalent antibodies that all recognise and bind to the same epitope of an antigen and different from polyclonal antibodies which are a mixture of antibodies which recognise the same antigen but bind different epitopes. mAbs are produced by a single clone of a hybridoma cell line.

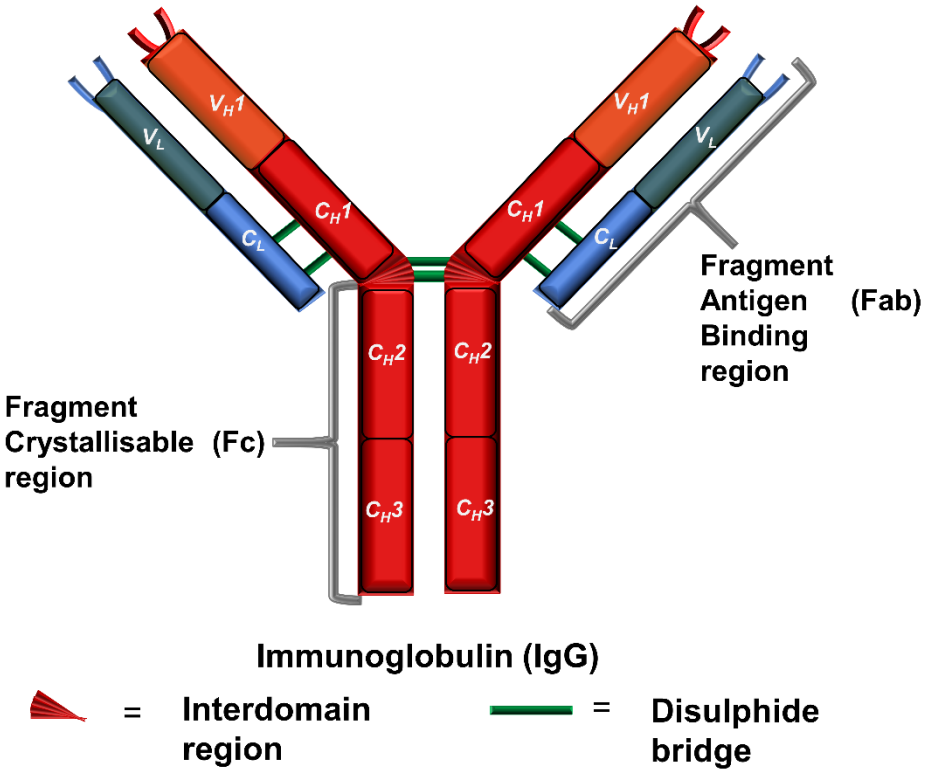

Figure 1.1 Structure of immunoglobulin type Gamma (IgG) with the Fc and Fab regions indicated. IgG consists of a Y shaped structure made up of 4 chains, 2 heavy and 2 light chains, with disulphide bonds (green) linking the interdomain regions of the heavy chains and the light and heavy chains. Red/orange denotes heavy chains and blue denotes light chains. V_H1= variable heavy chain, V_L=variable light chain, C_L=constant light chain, C_H1= constant heavy chain 1, C_H2=constant heavy chain 2 and C_H3=constant heavy chain 3.

Antibodies have a Y-shaped structure and consist of a fragment crystallisable (Fc) and a fragment antigen binding (Fab) region (Figure 1.1). The Fc region is comprised of the constant regions of the heavy chains which determine the antibody class and allow for interaction with cell surface receptors [12]. For example, IgG4 Is associated with the downregulation of immune responses, whereas IgG3 is associated with inflammatory responses [13]. The Fab region consists of the constant and variable regions of both the light and heavy chains. The variability of these Fab domains provides highly specific binding to individual antigens. It is this exquisite specificity which allows mAbs to be used to alleviate disease symptoms or to actively treat diseases [12].

1.1.2 Use of therapeutic mAbs

Therapeutic mAbs are versatile treatments that have been modified to bind to a range of disease targets. Ofatumumab is a recombinant humanised IgG1 developed by GlaxoSmithKline (GSK) that targets the B-lymphocyte antigen CD20 and is used to treat Chronic lymphoblastic leukaemia [7, 14]. The IgG1 Sotrovlmab, marketed by GSK and VIR biotechnology, was derived from a B cell of a COVID-19 survivor and given emergency

authorisation use by the FDA to prevent progression to severe COVID-19 in adults and paediatric patients [2]. Sotrovlmab targets an epitope found in both SARS-CoV-2 (Covid-19) and SARS-CoV-1 (SARS) and blocks the virus from entering healthy cells [15]. The humanised IgG4, Inotuzumab ozogamicin, targets the transmembrane protein CD22 and is used to treat acute lymphoblastic leukaemia [16].

mAbs are highly specific and effective treatments, with less off target effects than small molecule pharmaceuticals in part because mAbs normally cannot cross the blood brain barrier (BBB). This limits the application of mAbs in the treatment of brain diseases such as cancer [17]. However, the BBB can be manipulated using Fc receptor-induced reverse-transcytosis to allow access of therapeutic mAbs to the brain tissues [18]. This targeted and controlled access of mAbs through the BBB has opened up further disease targets.

Compared to most proteins, mAbs are stable over a relatively wide range of temperatures, buffer conditions and concentrations meaning that they can be isolated effectively and stored safely prior to administration to patients. However, they are prone to cold and hot thermal aggregation [19]. Reversible nucleation of mAbs can occur, so mAb that has aggregated can refold and retain its function [19]. Overall it is their high specificity, their stability during manufacture and their wide range of potential disease-relevant targets [20] that has made mAbs drug discovery molecules for industry. A key downside, is that mAbs are extremely expensive costing on average $100,000 per year, per patient reducing patient accessibility of these lifesaving drugs. The high cost is associated in part with the high cost of manufacture [21].

The manufacture of mAbs is a complex process which, due to the biological nature of these molecules is subject to both strict regulations for patient safety and defined processes for both upstream (section 1.1.3) and downstream processing (section 1.1.4).

1.1.3 Upstream processing

Therapeutic mAbs were originally produced by the hybridoma technique which was discovered in by Köhler and Milstein, who were awarded the Nobel prize for their pioneering work [22]. This technique involves inoculating a mouse with the target antigen in order to raise antibodies against the antigen. After several weeks the spleen lymphocytes of the animal are harvested and fused with myeloma cells to form immortal hybridoma cell clones, with each clone producing a mAb that recognises and binds to a single site on the antigen. The mAb secreting hybridomas are selected for further culturing and non mAb producing hybridomas are discarded (Figure 1.2).

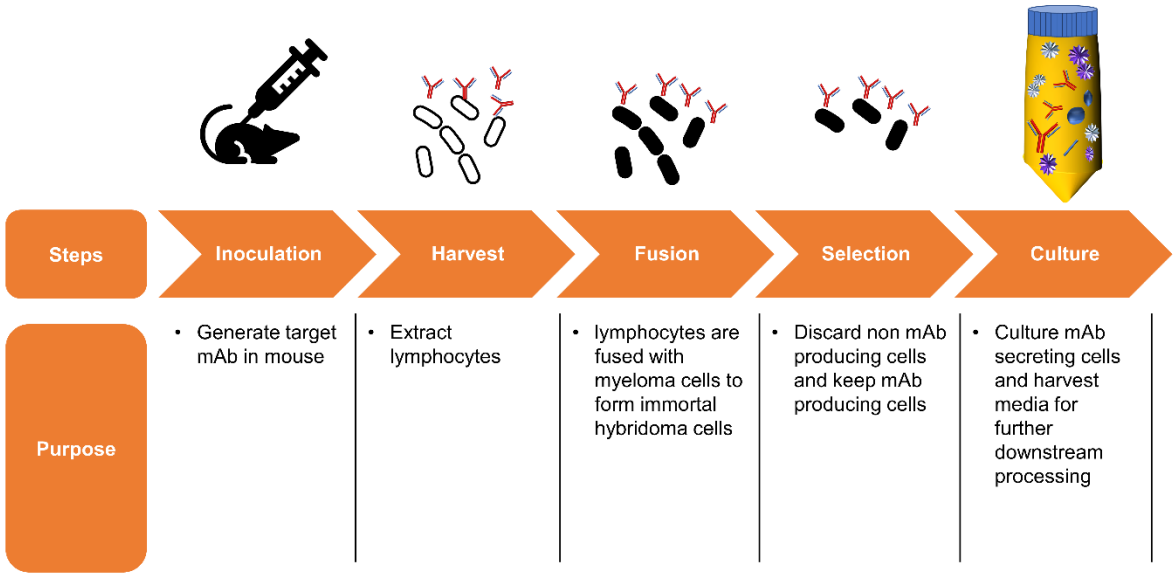

Figure 1.2 Schematic for the hybridoma technique in the production of mAbs

The mAbs produced in this way can then be cultured at scale in bio reactors to generate large volumes of mAb containing supernatant [23]. However, since the mAbs generated are murine in nature, they caused immunogenic reactions in human patients. To combat immunogenicity, recombinant DNA technologies have been utilised to generate human Fc region containing chimeric mAbs [24, 25] and fully human mAbs [25]. Hybridomas are still used but require transgenic mice that have had the murine immunoglobulin genes replaced with human genes [26].

Recombinant technology removes the need for the use of live animals as it utilises DNA libraries to select genes that express specific chimeric and human mAb products [25]. The engineered genes can then be cloned, expressed and selected for specific characteristics, i.e., ability to bind and have a desirable effect on a given protein or biological system (Figure 1.3). The majority of therapeutic mAbs are produced recombinantly in mammalian expression systems, with 60 % expressed in Chinese hamster ovary (CHO) cells [20]. In the 1980's productivity of cells was below 10 pg per cell per day, but this has been dramatically improved to ~ 90 pg per cell per day [26] thanks to the glutamine synthetase expression system which amplifies protein expression. The glutamine synthetase genes in recombinant cells ensures only transformed mAb producing cells survive in the absence of glutamine in media [27].

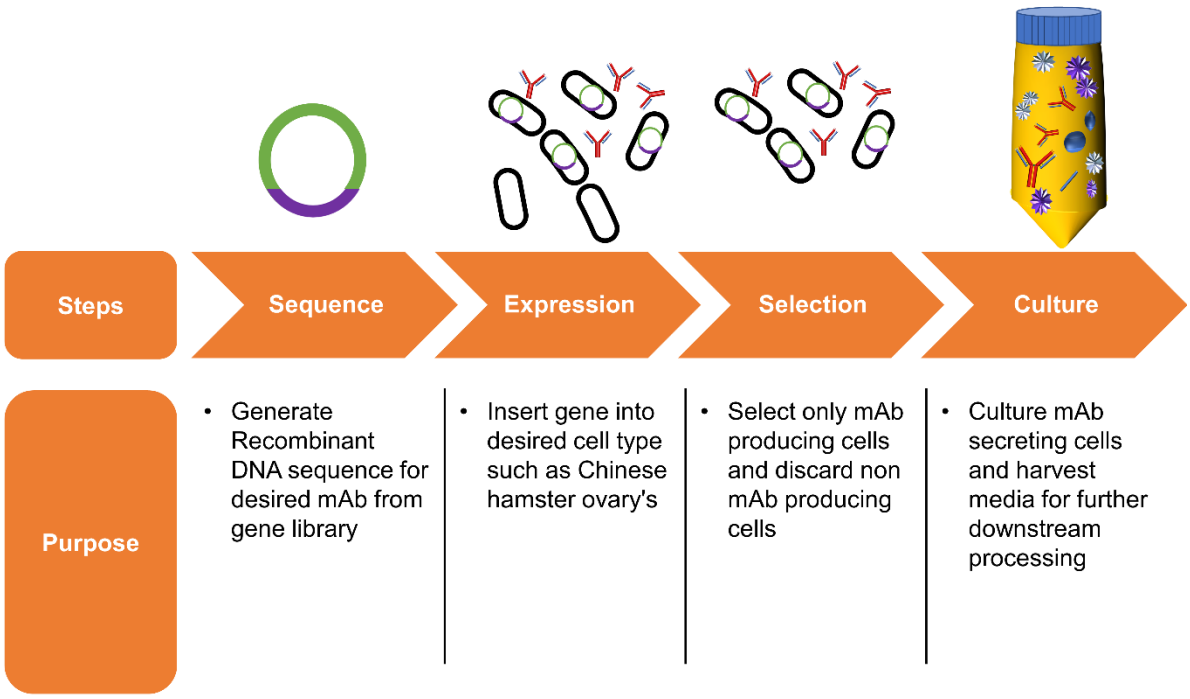

Figure 1.3 Schematic for recombinant production of mAbs

1.1.4 Downstream processing of monoclonal antibodies

Many therapeutic mAbs have been humanised, but there is still a risk of an immunogenic response in patients [10, 20], due to the presence of small amounts of host cell proteins (HCP) and host cell deoxyribonucleic acid (HCDNA) in isolated mAbs [28, 29]. Due to the high risk to patient safety caused by these contaminants, safe levels of HCP and HCDNA are recommended as below detectable limits by the FDA [30] but are typically in the 1ng mg^{-1} range [11]. Any contaminants present in final formulations must be studied for effects on patients and determined safe levels in product (Table 1.1) [30].

Table 1.1 FDA requirements for downstream processing of mAbs

Regulatory requirements	Defined by
Purification reuse limit for columns	Performance over time
Structural integrity of mAb	Physiochemical methods to assess aggregation
Product comparability	Batch to batch comparison
Removal of contaminants	Viral clearance, HCDNA and HCDNA characterisation studies

There are various steps employed in the downstream processing of mAbs from mammalian expression systems (Figure 1.4) in order to reach safe levels of HCP and HCDNA as well as to remove high molecular weight species (HMWS) and culture media components.

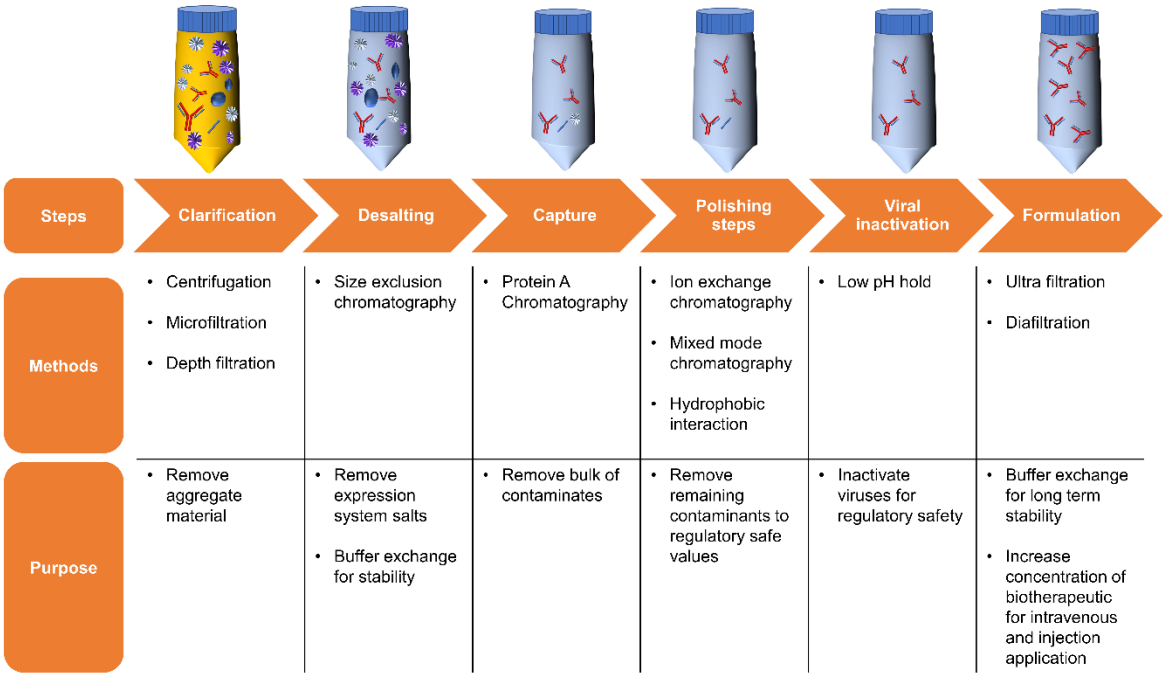

Figure 1.4 Downstream processing workflow for mAb purification. Centrifugation is the first step, followed by microfiltration, desalting in preparation for protein A chromatography to remove the bulk of contaminants. Polishing steps are then used to remove residue amounts of contaminants to meet regulations.

Typically the first step of downstream processing is clarification and involves centrifugation and microfiltration to remove cell debris and large particulate matter from the cell culture supernatant (CCS) [31]. The filtered media is desalted by size exclusion chromatography to remove culture media components and large amounts of salt and exchange into equilibration buffer suitable for the capture step binding. The bulk of contaminants are then removed via the utilisation of Protein A Affinity Chromatography (PrAc) in the capture step [29]. The solution is then refined by one or more chromatographic polishing steps such as Cation exchange chromatography (CEX), Anion exchange chromatography (AEX), hydrophobic interaction chromatography (HIC) and Multimodal chromatography (MMC) [32-34]. The polishing steps remove the majority of any remaining HCPs, viral DNA, protein aggregates or fragments, as well as any leached Protein A [35-37]. Any viruses present must be inactivated, typically by holding the mAb in low pH solution [36, 38]. Finally, the solution will be buffer exchanged into formulation buffer containing sugars and stabilisation agents such as PEG to ensure the long shelf life of mAbs [39]. The formulated solution is then concentrated for intravenous or subcutaneous injection applications [39]. Formulation is typically performed by ultra-filtration and diafiltration methods [36]. Overall, downstream processing is complex and will vary for each mAb producing cell line. PrAc, the major focus of the work outlined in this thesis, has been identified as the main bottleneck in the downstream processing of mAbs and will be further explored in section 1.1.5 [40].

1.1.5 Protein A affinity chromatography

Protein A is a 54 kDa linear polypeptide found in the cell wall of the bacterium *Staphylococcus aureus,* and consists of a cell wall associated region located at the C-terminus and five triple helix antibody binding domains (A, B, C, D and E) at the N terminus [41-43]. Each antibody binding domain of the *Staphylococcus* protein A (SPA) is 6.6 kDa and the five domains share 65-95% sequence identity [43]. The ~42 kDa truncated SPA lacking the cell wall associated region is used for biotechnological applications [41-43]. SPA is very stable as it can refold after denaturation and withstand a pH range of 2-11 [42]. SPA immobilised on chromatographic beads was first utilised to isolate IgG in 1972 by Hjelm et al, who achieved a 95% yield [44]. It is still used today as the gold standard method of isolation of a wide range of biotherapeutics including IgG1, IgG2, IgG4, Fc fusions and bispecific antibodies [42].

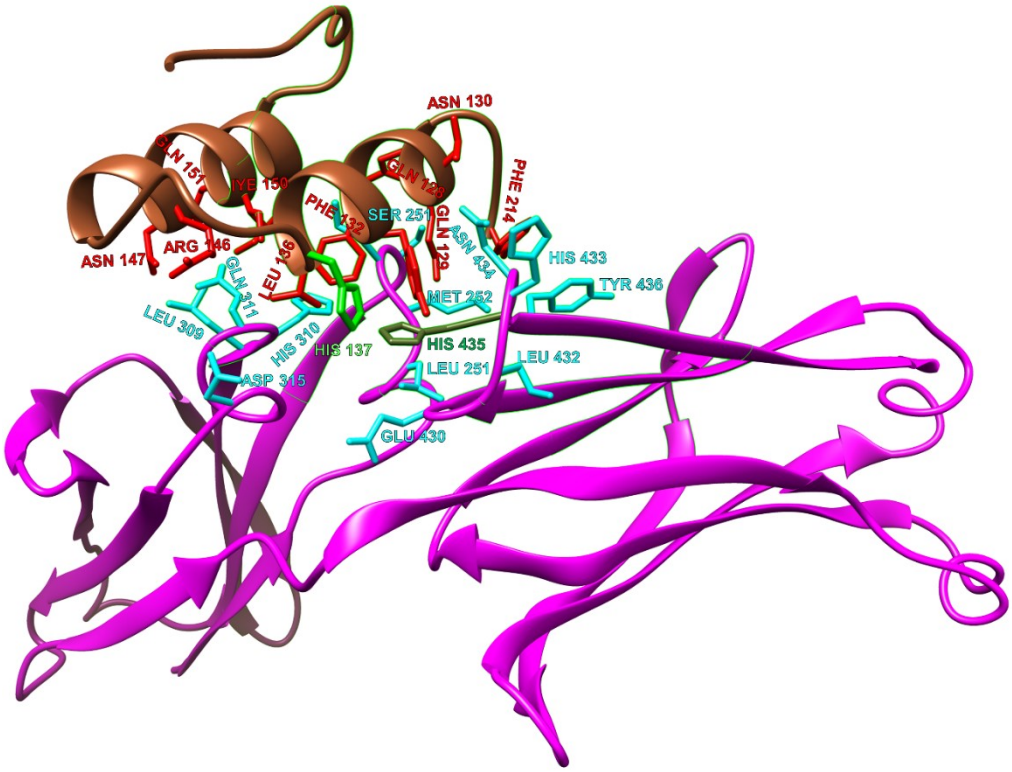

Figure 1.5 Structure of the Fc region of a mAb bound to the antibody binding domain B of SPA. Image generated in Chimera (PDB 1fc2 [45]. Key residues involved in the interaction between the two proteins are labelled. The Fc region is shown in magenta with the Fc residues involved in binding shown in cyan in stick representation. The antibody binding domain B of SPA in shown in brown with the key residues involved in the interaction shown in red in stick representation. In light (SPA) and dark green (mAb residue) are the two His residues which play a key role in both binding and elution.

PrAc is employed in a bind/elute mode. The mAb is bound to SPA immobilised onto chromatographic beads at a slightly alkaline pH allowing media components, HCP and DNA to flow through the column and for the IgG to bind to the SPA ligands chemically cross-linked

to the resin beads. X-ray crystallography has shown that the SPA binding domain helices bind to the IgG Fc region's constant heavy domains 2 and 3 [45], this reversible interaction consists of hydrophobic interactions, hydrogen bonding and two salt bridges (Figure 1.5) [42]. When binding occurs, only three out of five binding domains are occupied due to steric hindrance [41]. Although the Fc and SPA domain interaction is highly specific it was discovered that SPA domains D and E binds to the Fab region when variable heavy chain type 3 is present in IgG [42, 46].

Further alkaline pH buffer containing salt is washed though the column in order to remove weakly bound impurities. Elution is then performed by decreasing the pH of the column to ~3 resulting in protonation of histidine 137 of SPA and histidine 435 of IgG and subsequent release of the bound mAb due to electrostatic repulsion [47] (Figure 1.5). The protein is eluted into buffer at higher pH in order to bring the mAb closer to more neutral pH as quickly as possible.

This purification process is performed three times in each purification cycle, with each cycle followed with a strongly alkaline cleaning in place (CIP) step employing up to 0.5M NaOH [42, 48, 49], to remove contaminants strongly bound to the column after repeated use [29, 49-51]. Trace amounts of SPA binding domains can be observed in the CIP eluant [42, 49].

To minimize SPA leaching and extend column lifespan, agarose-based resins using engineered SPA ligands have been developed. MabSelect SuRe, for example, utilizes a SPA ligand with a modified binding domain B, engineered to be more alkaline resistant [42]. MabSelect Sure retains half its binding capacity even after 10 hours of exposure to 0.16 M NaOH [49]. Boulet-Audet et al have shown that the MabSelect SuRe modified SPA ligand undergoes denaturation at 1.60 M NaOH but that proteolysis only occurs in extremely harsh conditions, such as 6.46 M NaOH [49], a much higher concentration than used for column cleaning. The MabSelect SuRe modified SPA ligand is crosslinked to an agarose bead which is on average 60 μm in diameter but can be up to 120 μm in diameter. The agarose bead matrix is porous in nature allowing for increased surface area for capture of mAbs Further modifications to the SPA ligand and increased ligand density have been observed in the new MabSelect PrismA resin which is a further optimised version of MabSelect SuRe [52].

PrAc resins have been shown to possess unrivalled purification capabilities, able to remove 98% of contaminants [29] with a stepwise recovery yield of 99.4% [53]. Downstream processing has been shown to be responsible for up to 80% of overall mAb production costs [54]. PrAc accounts for the majority of those costs, due to the expense and lifetime degradation

of the resin [38, 54, 55] To make PrAc more economical and reduce production costs, increasing the reuse of resin is essential[55].

A potential source of lifetime degradation is the harsh alkaline CIP procedures (NaOH) causing proteolysis and cleaving the random coil linkages between individual binding domains of the SPA ligand [49, 56, 57]. Lifetime degradation of the resin is also attributed in part to irreversible binding of contaminants which may reduce SPA ligand accessibility. Although the precise nature of these contaminants is unclear, it has been shown that null-cell culture fluid causes less fouling than mAb containing culture fluid [58] and that HCPs accumulate on the Protein A resin after repeated cycles of purification [59].

1.1.6 Protein A performance monitoring

PrAc performance is mandated by the FDA and can be monitored by two different binding capacity analysis techniques (Table 1.1)[30]. Static binding capacity analysis assesses the maximum binding performance of a resin for a particular mAb. This method is a good indicator of resin performance and a way to choose which protein A resin or pH conditions will achieve the highest amount of mAb isolated. A chosen resin of known volume (V_{resin}) is loaded with a known volume of mAb (V_{Sample}) at a range of concentrations (C_0) ranging from no mAb to more than the resin should be able to bind. The liquid fraction is then separated from the resin and the equilibrium concentration is measured (C_{eq}) of the flow through to calculate binding capacity (Q) as shown by Equation 1.1.

$$Q = \frac{V_{Sample} \times (C_0 - C_{eq})}{V_{resin}} \quad 1.1$$

Where Q = binding capacity, V_{sample} = volume of mAb, C_0 = initial concentration, C_{eq} = equilibrium concentration and V_{resin} = volume of resin

The binding capacity is the maximum amount of mAb that can bind to a resin at a given pH, formulation and protein concentration. Once Q has been calculated the Langmuir isotherm can be used to explain binding behaviour as shown by Equation 1.2.

$$Q = \frac{Qmax \times C_{eq}}{K_d + C_{eq}} \quad 1.2$$

Where Q = binding capacity, Q_{max} = maximum binding capacity, C_{eq} = equilibrium concentration and K_d = disassociation constant

The Qmax is defined as the maximum capacity of mAb that the resin can hold. This method however assumes high protein loss and is not representative of industry processes where

protein loss is minimised to prevent product loss. To better represent purification conditions dynamic binding capacity (DBC) analysis is used. This approach assumes limited mAb loss, and indeed the amount of product loss can be chosen, with typically 10% utilised [52, 60-65]. DBC measurements identify the load of mAb where 10% of the initial concentration of mAb (C_0) flows through the column, unable to bind as every available Protein A ligand binding site is occupied. The chromatogram is offset as there is a delay between the sample pump and detector, and this delay is accounted for by subtracting the offset volume (V_0) from the chromatogram volume. The resultant volume is then multiplied by the concentration of mAb and then divided by the volume of the column to calculate the amount of mAb (mg) per ml of column (Equation 1.3).

$$DBC_{10\%} = \frac{(V_{10\%} - V_0) * C_0}{V_c} \quad 1.3$$

Where $DBC_{10\%}$ = Dynamic binding capacity at 10% breakthrough, $V_{10\%}$ = volume at 10% breakthrough, V_0 = offset volume, V_c = column bed volume, C_0= initial concentration

The mechanism of binding is driven by mass transport [65], thus in SBC the resin must be over saturated and in DBC the flow rate is varied; the lower the flow rate/ longer residence time of a mAb in a column then a higher chance of binding events occurring.

These methods have been used to reveal a reduction in Protein A column performance with repeated use but are unable to explain the chemical basis of this reduction. Suggested reasons for lifetime degradation include protein aggregation on the column [40, 51] and irreversible binding of contaminants [56]. A range of analytical techniques have been used to better understand the cause of lifetime degradation of protein A resin such as confocal laser scanning microscopy (CLSM) [57, 66], scanning electron microscopy (SEM) [57] and mass spectrometry [59]. CLSM showed an increase in both accumulation of foulant and bead pore blockages in protein A resin beads as a function of increased usage, a finding supported by SEM [66]. CLSM, although a powerful technique, requires fluorescent labelling which can change the absorption behaviour of proteins [67]. As a result, fluorescently labelled proteins can be displaced by non-fluorescent proteins with stronger binding affinity, affecting interpretation of CLSM results. An increase in irreversibly bound host cell protein (HCP) and mAb contaminant with an associated decrease in protein A resin binding capacity detected via liquid chromatography-mass spectrometry (LC-MS/MS) has also been reported. The analysis, carried out following an increasing number of purification cycles, revealed marked HCP accumulation after 80 bind/elution steps [59].

Vibrational spectroscopic methods like attenuated total reflection Fourier transform infrared (ATR-FTIR) and confocal Raman spectroscopy are alternative methods that can provide quantitative information as well as chemical and secondary structure information for a given sample. The fundamentals of these techniques are explained in section 1.2 and 1.3 respectively. ATR-FTIR spectroscopy has been used to assess SPA ligand stability after extended CIP exposure [49] as well as quantifying mAb bound to the surface layer of resin beads both on column and offline [56]. Confocal Raman spectroscopy represents a powerful alternative, as it is able to probe much deeper into samples, whilst, like ATR-FTIR spectroscopy, providing detailed chemical information and giving insights into protein secondary structure [68, 69]. Additional features are also detectable in Raman spectra, such as amino acid side chains and particularly aromatic amino acid side chains [70]. The ability to detect these additional features allows distinction between the desired protein analyte peaks and those obtained from the SPA ligand and the matrix. Both ATR-FTIR and Raman spectroscopy are label-free techniques, meaning native forms of the protein can be studied [71]. Importantly, they are also non-destructive meaning the sample is still suitable for further processing after analysis.

1.2 Infrared spectroscopy

Spectroscopy is the study of matter using electromagnetic radiation, which can be emitted, absorbed or scattered by matter. Infrared (IR) spectroscopy focuses on the use of electromagnetic radiation in the IR region of the electromagnetic spectrum to observe molecular vibrations in matter.

Table 1.2 Electromagnetic spectrum wavelengths and each classsificaions effect on matter

Energy	Radiation classification	Wavelength (nm)	Effect
Increasing ↓	Radio	>100000	Non ionising
	microwave	100000-25000	Non ionising
	infrared	100000-750	Non ionising
	visible	750-400	Non ionising
	ultraviolet	400-1	ionising
	x-rays	1-0.001	ionising
	gamma	<0.001	Ionising

Electromagnetic radiation with short wavelengths such as gamma rays and X-rays are high energy forms of radiation that can ionise and thus damage matter. In contrast, forms of radiation with long wavelengths like radio, micro-waves and IR are lower energy and are thus non-ionising and non-destructive. As shown by Planck's Equation energy is inversely proportional to wavelength (Equation 1.4).

$$E = \frac{hc}{\lambda} \qquad 1.4$$

Where E = energy, h = Planck's constant (6.62×10^{-34} J s), c =the speed of light (2.997×10^{8} m s $^{-1}$) and λ= wavelength.

The IR radiation can be divided into three types based on wavelength relative to visible light. In IR spectroscopy wavelength are referred to in μm. Near IR lies from 0.75 μm – 2.50 μm, mid IR from 2.50 μm – 25.00 μm and far IR at 25.00 μm -1000.00 μm. IR spectroscopy can analyse the chemical composition of matter in any state, liquid, solid or gas.

1.2.1 Fundamentals of Infrared spectroscopy

When IR radiation is absorbed by matter, the energy state of the matter changes. The matter will undergo a transition from its ground state energy (E_g) to a higher energy state (E_1). The energy of an absorbed photon has a fixed energy and therefore proportional frequency (ν) and is described by the Bohr frequency condition Equation 1.5 [72].

$$h\nu = E_G - E_1 \quad 1.5$$

Where h = Planck's constant, ν = frequency, E_g = the ground state energy and E_1 = the higher energy state

Equation 1.5 can be expressed in terms of ν (Equation 1.6).

$$\nu = c/\lambda \quad 1.6$$

Where ν = frequency c = speed of light and λ = wavelength

Since c is a constant, the frequency of a photon is directly proportional to the energy of a photon. In the case of IR radiation, the energy is reported in terms of wavenumber ($\tilde{\nu}$). Wavenumber is the number of complete wavelengths over one cm and is defined by Equation 1.7.

$$\tilde{\nu} = \frac{\nu}{c} = \frac{1}{\lambda} \quad 1.7$$

Where $\tilde{\nu}$= wavenumber, ν = frequency, c = speed of light and λ = wavelength

When the frequency of electromagnetic radiation matches the frequency at which molecular bonds are vibrating the radiation is absorbed. The number of vibrations for linear (Equation 1.8) and nonlinear (Equation 1.9) molecules are shown below.

$$n_{modes}=3N-5 \quad 1.8$$

$$n_{modes}=3N-6 \quad 1.9$$

Where N = number of atoms and n_{modes} = the number of normal vibrational modes

A heteronuclear diatomic molecule will contain different atoms bonded to one another. A heteronuclear bond in a diatomic molecule will be made up of different mass atoms for instance the case of C-H group i.e. Hydrogen (1 da) is smaller than Carbon (12 da). Because the mass of each atom is different the molecular vibrations for a diatomic molecule can be described by Hooke's law in Equations 1.10 and 1.11.

$$\mu_{eff} = \left(\frac{m_1 * m_2}{m_1 + m_2}\right) \quad 1.10$$

where μ_{eff} = effective mass, m_1 = mass of one atom in a chemical bond and m_2 = mass of the other atom in a chemical bond.

$$\tilde{\nu} = \frac{1}{2\pi c}\sqrt{\frac{k}{\mu_{eff}}} \quad 1.11$$

Where $\tilde{\nu}$= wavenumber, k =force constant, c= speed of light and μ_{eff}=effective mass

The wavenumber at which these vibrations occur overlaps with the frequency of the IR region of the electromagnetic spectrum. Absorption occurs when incoming IR radiation matches the frequency of the fundamental mode of vibration for the molecule. The IR spectrum, as previously described, is divided into three categories of far, mid and near. The Far IR region overlaps with rotational energy in molecules and the near IR region overlaps with the energy of overtone vibrations. The mid IR radiation used in this thesis overlaps with fundamental vibration transitions. The vibration of molecules acts like anharmonic oscillators; thus cannot be compressed beyond a certain point and will break at high enough energies where interatomic distance becomes too great for electron interaction.

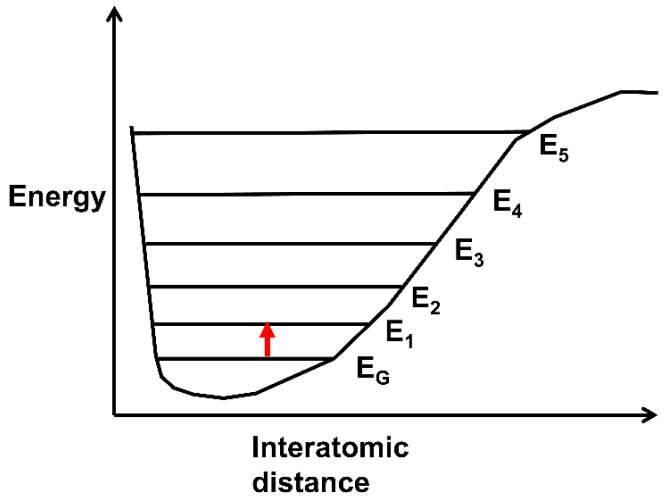

Figure 1.6 representation of the potential energy of a diatomic molecule showing fundimental vibrations.

As shown by the anharmonic oscillator for a diatomic molecule in Figure 1.6 when mid IR radiation is absorbed by molecular vibration the amplitude or interatomic distance two different atoms is increased. As this absorption occurs at discrete wavenumbers/energies we can determine the exact chemical species present within a sample.

As the electromagnetic radiation is an electric field, when the electric field matches the frequency of the chemical bond it causes a change in interatomic distance of the constituent atoms. An example is CO_2, which according to Equation 1.8 has 4 vibrational modes (Figure 1.7).

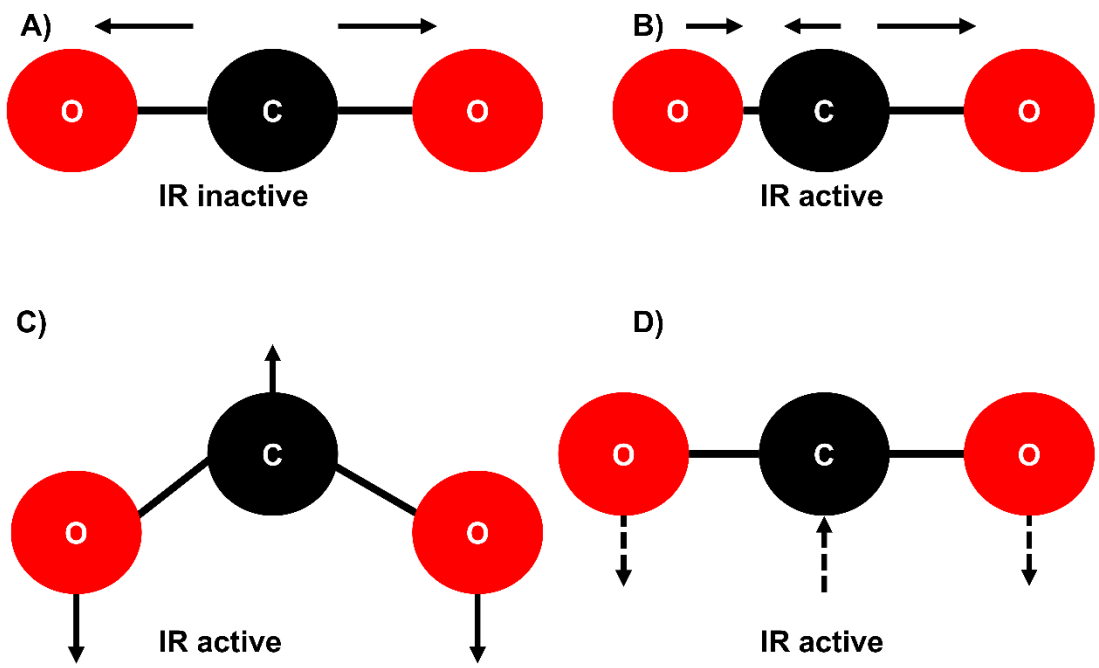

Figure 1.7 4 vibrational modes of CO_2 and their Infrared activity. A) IR inactive symmetric stretch B) IR active antisymmetric strecth C) IR active in-plane bending D) IR active out of plane bending.

Of these 4 modes of CO_2, only three are IR active modes. These modes are IR active due to the presence of an oscillating dipole which can interact with electromagnetic radiation. No net change in dipole occurs in the mode illustrated in the symmetric stretch in Figure 1.7 A. Other molecules can have other vibrational modes such as stretching, wagging, and bending in both antisymmetric and symmetric forms. As the wavenumber at which a molecule's vibrations can absorb IR radiation is unique, the resultant bands on an IR spectrum correlate to specific modes of vibration revealing a unique spectral fingerprint.

1.2.2 Fourier transform infrared spectroscopy

The first instrumentation allowing IR spectroscopy utilising a globar source was developed by Coblentz in the early 1900's [73]. Originally dispersive systems were utilised but were slow to allow generation of a full range spectrum, primarily due to the requirement for a monochromator to filter individual wavenumbers of IR radiation. This was be achieved by introduction of a moving prism or grating. Since this development, Fourier transform infrared (FTIR) spectrometers have been produced allowing for fast full spectrum analysis utilising the Michelson interferometer (Figure 1.8).

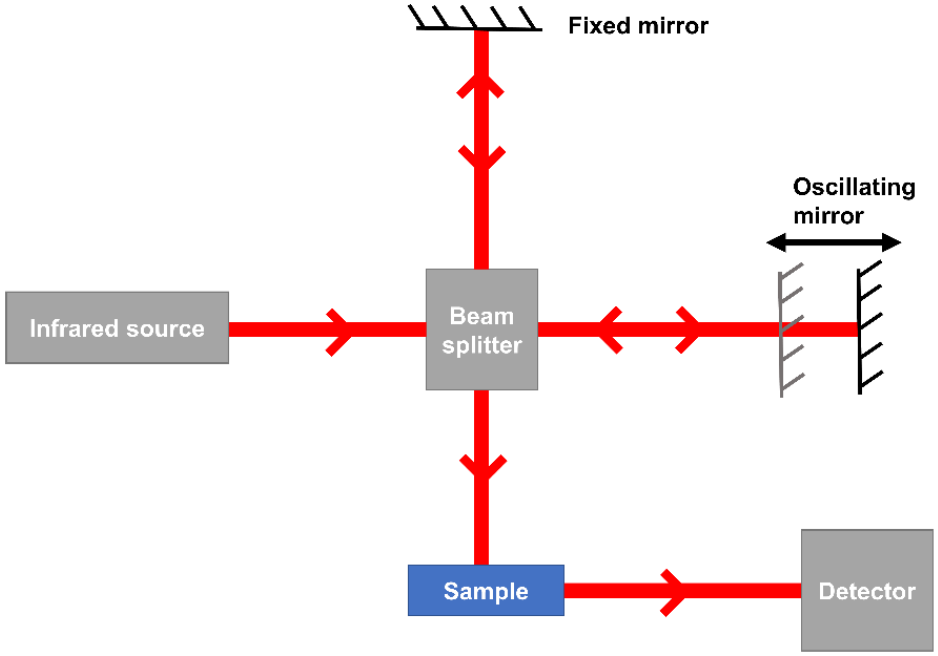

Figure 1.8 Schematic of the Michelson interferometer used in FTIR spectrometers. The IR beam path is shown in red with the specific elements of the interferometer shown in grey. The sample is shown in blue.

The Michelson interferometer is made up of a beam splitter and two mirrors, one fixed and one oscillating [74]. IR radiation is passed into the beam splitter where the radiation is split equally and directed to both the fixed and oscillating mirror. The beam splitter is made of KBr which is known to have little absorption in the mid IR region and is regarded as transparent in the mid IR region. The IR radiation directed to the fixed mirror is reflected straight back to the beam splitter with a fixed path length. The IR radiation directed to the oscillating mirror will have a varying path length. When the radiation from both perpendicular mirrors recombines at the beam splitter an interference pattern of both constructive and destructive interference is formed [74] (Figure 1.9). Typically, measurements are the average of multiple scans in order to minimise root mean square noise (RMSN, defined by Equation 1.12) and ensure clear observable peaks in a spectrum [75]. In the case of Figure 1.9 64 scans were used.

$$RMSN = \sqrt{\frac{\sum_i (A_i - \bar{A})^2}{n}} \qquad 1.12$$

Where RMSN= Root mean square noise A_i= i^{th} data point $\bar{A}$=mean signal and n= the number of data points

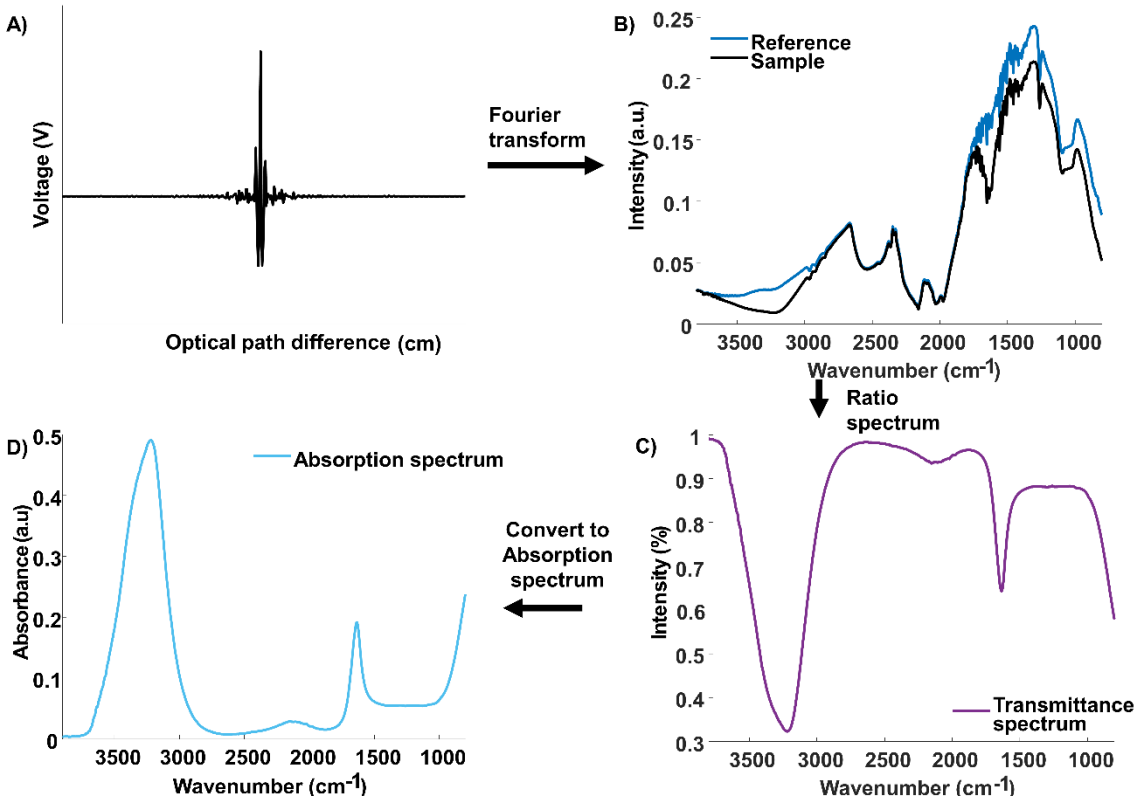

Figure 1.9 Measurement of liquid H_2O showing the interferogram obtained and the process to convert to the final absorption spectrum. A) interferogram of the sample measurement, B) reference (blue) and sample (black) single channel spectra, C) transmittance spectrum formed from the ratio of reference and sample single channel spectra, D) absorption spectrum of H_2O.

As shown in Figure 1.9 the interferogram is subjected to a Fourier transform algorithm, generating the single channel spectrum seen in Figure 1.9B. Since a single source of radiation is used, a ratio of the background and sample measurement is required to remove any spectral features other than the desired sample. This is needed to simplify the spectral system as this represents the difference between radiation in sample vs out. Bands from the atmosphere such as water vapour would be present if this step was not carried out. The ratio of the two single channels forms a transmittance (T) spectrum as defined by Equation 1.13. Transmittance spectrum is defined as the ratio of IR radiation to be transmitted by the sample.

$$T(\%) = \frac{I}{I_O} \qquad 1.13$$

Where T=transmittance I=intensity of single channel measurement with sample and I_O=intensity of single channel without sample present.

The transmittance spectrum can be converted to an absorption spectrum by Equation 1.14.

$$A = -\log_{10} T \qquad 1.14$$

Where A=absorbance and T=transmittance

An absorption spectrum is used in FTIR spectroscopy in preference to a transmission spectrum as absorbance is directly related to concentration as defined by the Beer-Lambert law (Equation 1.15) and all spectra in this work will herein be displayed as absorption.

$$A = \varepsilon C l \qquad 1.15$$

Where A=Absorbance, ε=molar absorptivity, C=concentration and l=pathlength

1.2.3 Transmission Fourier transform Infrared spectroscopy

Transmission mode FTIR spectroscopy is commonly used to measure matter in the physical states of liquid, solid and gas. In transmission mode some of the IR radiation is absorbed by the sample and the rest passes through the sample.

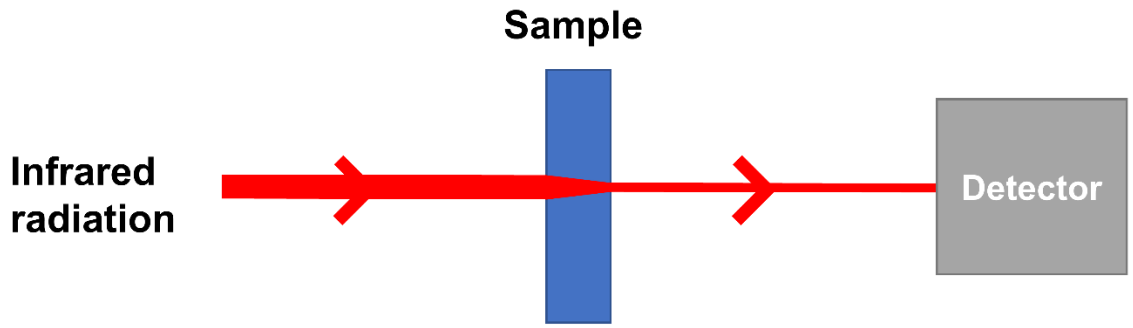

Figure 1.10 Schematic of transmission mode IR spectroscopy with IR radiation passing through sample to detector.

There are multiple ways in which to fix samples for measurement. Solid samples can be mixed with KBr to form a pellet that can be clamped into place [76]. Another method grinds the sample together to a paste with Nujol oil, which has a very simple IR spectrum, which can be placed on IR transparent windows [77]. Scattering effects can however occur in both the previously mentioned methods. Scattering occurs when sample size is comparable to that of the wavelength of IR radiation the scattering effects will cause distortions in the resultant spectrum [78]. A sample can be made into a thin film by melting or solvent evaporation on an IR inert glass, this however can cause samples to degrade [76].

For the analysis of liquids and gases transmission mode commonly utilises IR transparent glass such as CaF_2, which has absorption from 1000 cm^{-1} and below, and thus is at the extremities of the mid IR region. Therefore, the majority of fundamental vibrations in the mid IR are not absorbed by the CaF_2. The sample is wedged between two slides of CaF_2 to fix its position.

Protein samples are almost always analysed under aqueous conditions to ensure correct protein folding, however water is a very strong absorber of IR radiation. To ensure some IR

radiation that passes through the sample reaches the detector a very thin layer of sample of around 5-50 μm must be used [79, 80]. This adds a layer of preparation required for aqueous samples being measured in the mid-IR range. Transmission has been used to study protein containing agarose beads [80]. Agarose is the base matrix of protein A resins such as MabSelect SuRe. When performing measurements the H_2O bending mode will overlap with key protein regions such as the amide bands [81] as well as reducing IR radiation that reaches the detector. Transmission mode is not suitable for the study of mAb purification studies due to the up to 100 μm size of Protein A beads as well as high absorption of H_2O but can be used for the study of live cells [82] .

1.2.4 Attenuated transform Reflection Fourier transform Infrared spectroscopy

Another mode of measurement is Attenuated Total Reflection (ATR) FTIR spectroscopy which uses total internal reflection of IR radiation to generate an evanescent wave as illustrated in Figure 1.11. ATR allows for the probing of a sample layer of up to 6 μm thickness adjacent to the surface of the internal reflection element (IRE) crystal [83] overcoming the issue of strong water absorption in the mid-IR range beyond this depth.

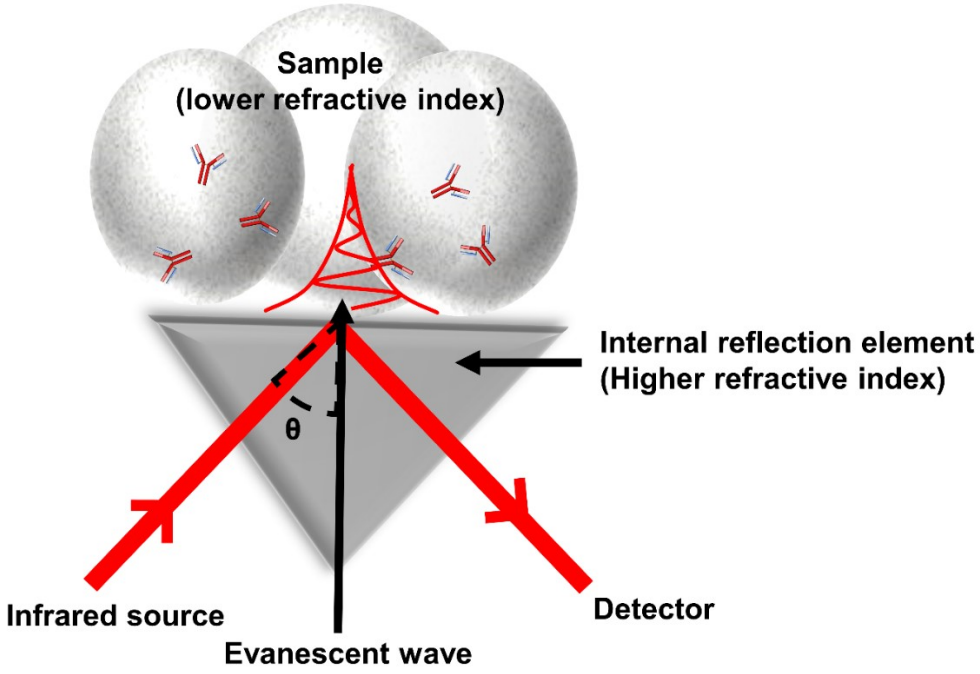

Figure 1.11 Schematic diagram of attenuated total reflection mode of FTIR spectroscopy. The red line represents IR radiation from the IR source. IR is passed through the IRE shown in grey at the critical angle where attenuated total reflection occurs. An evanescent wave probes the sample and remnant IR radiation is reflected to the detector.

One criterion that must be met for ATR-FTIR spectroscopy is that that the refractive index of the Sample (n_1) must be lower than that of the IRE (n_{IRE}). Typically materials such as diamond or germanium are used [77]. An additional criterion is that the IR radiation angle of incidence

(θ) must be greater than the critical angle. Typically the critical angle of commonly used systems will be 45° but this angle can be changed to adjust the depth of penetration by the evanescent wave in the z direction [84, 85]. The depth of penetration (d_p) of the evanescent wave is usually within the range of 0.2 - 6 μm and can be calculated according to the Harrick Equation (Equation 1.16) [86-88].

$$d_p = \frac{\lambda}{2\pi n_1 \left(\sin^2\theta - \left(\frac{n_{IRE}}{n_1}\right)^2\right)^{0.5}} \quad 1.16$$

Where d_p=depth of penetration, λ=wavelength, n_1=refractive index of sample, n_{IRE}=refractive index of IRE and θ=angle of incidence

The use of an evanescent wave prevents complete saturation by IR absorption in an aqueous sample [56]. This removes the need for preparation steps such as films, pellets or sandwiching windows ensuring minimal sample preparation.

ATR-FTIR spectroscopy has been applied to the quantification of BTs with measured spectra being shown in absorption format. According to Equation 1.14 the resultant spectra can be applied to the Beer Lambert law (Equation 1.15). Absorbance is commonly determined on an IR absorption spectrum by measuring the area under the curve (integration) or by the peak height.

Applying the Beer Lambert law in transmission mode is simple, as pathlength, l, is simply the distance the IR radiation travels through a sample and is the sample thickness. In ATR-FTIR spectroscopy the effective thickness is defined as the equivalent sample thickness required to give an equivalent absorption spectrum in transmission mode compared to ATR mode. As the IR radiation is non polarised, Equation 1.17 can be used [89]. This describes that each wavenumber of light will have a different effective thickness and is an important point to consider when using the Beer Lambert law to quantify ATR-FTIR spectra.

$$\frac{d_e}{\lambda} = \frac{\frac{n_{IRE}}{n_1} cos\theta \left[3sin^2\theta - 2(\frac{n_{IRE}}{n_1})^2 + (\frac{n_{IRE}}{n_1})^2 sin^2\theta\right]}{2\pi(1 - (\frac{n_{IRE}}{n_1})^2)\left[\left((\frac{n_{IRE}}{n_1})^2\right) sin^2\theta\right]\left(sin^2\theta - (\frac{n_{IRE}}{n_1})^2\right)^{0.5}} \quad 1.17$$

Where d_e= effective thickness, λ=wavelength of light, n_1=refractive index of sample, n_{IRE}=refractive index of IRE and θ=angle of incidence

1.2.5 Amide Bands

The mid-IR wavenumber range (400cm^{-1} - 4000cm^{-1}) is ideal for analysing protein samples. Not only does the mid-IR region give way to fundamental vibrations of molecules but also allows for determination of protein secondary structure. As proteins are made up of chains of amino acid residues there are a large number of amide functional groups present in any sample, resulting in prominent spectral peaks in the amide I and II regions on a given spectrum. The exact position of peaks and shoulders within the amide bands are dependent on the protein secondary structure present [90], thus the amide bands can provide important structural information on a protein sample, as well as how that structure changes under specific conditions, e.g. upon heating [84, 91-94].

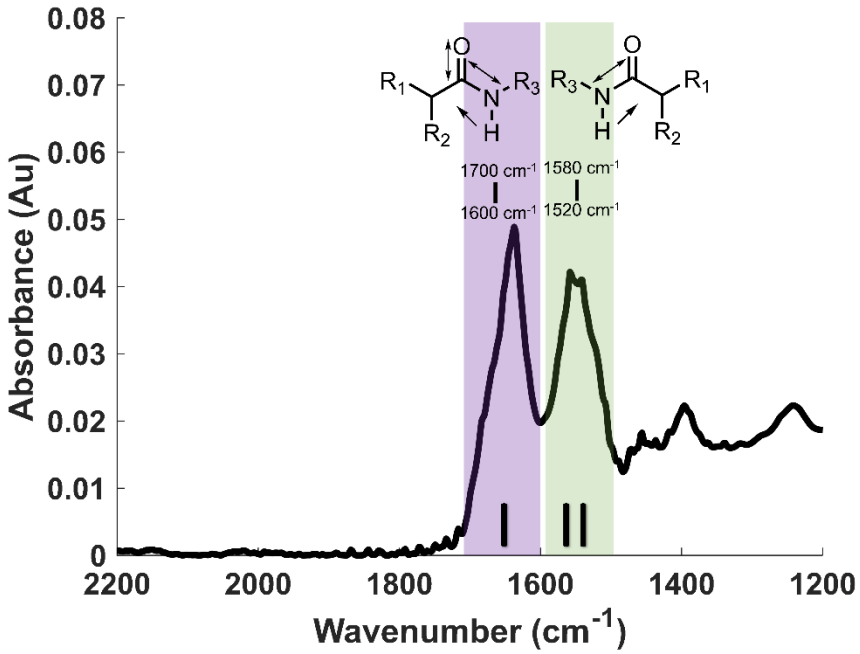

Figure 1.12 Visual representation of the amide I & II vibrational modes present in an absorption spectrum of a protein. Purple highlighted area is the amide I band and green is the amide II band.

The amide I vibrational mode can be found at 1600-1700 cm^{-1} and is made up of primarily C=O stretch coupled to C-N stretch and N-H in-plane bending [77, 90] (Figure 1.12). The exact spectral position at which the amide I peaks resides is dependent on the hydrogen bonding pattern of individual secondary structures; α-helices, β structures, turns, and random coils. The hydrogen bonding pattern comes from the N-H and C=O interacting with surrounding H_2O. If hydrogen bonding is decreased, for example by an increase in temperature, the C=O vibration is enhanced and thus the amide I peak exhibits higher absorption [95]. Within the amide I band on a spectrum, there will be many overlapping peaks, the position of the main peak represents the predominant secondary structure, with shoulders representing other more minor secondary structures in the protein sample [90].To study the secondary structures

represented in the peaks and shoulders of the amide I spectral band derivative analysis, deconvolution and band fitting can be used [77].

The amide II vibrational mode is made up of C-N stretching and N-H bending [77] and resides between 1520 cm^{-1} and 1590 cm^{-1}. Like the amide I band, the amide II band is a complex mixture of peaks representing secondary structure. The amide II vibrational mode is not as strong in absorption as it lacks contributions from the strongly IR absorbing C=O vibrations. C=O can be found in every peptide bond linking individual amino acid residues that make up a given protein. When there is large β secondary structure present with little amounts of other structures, a split in the amide II region of a spectrum can be observed as the result of two peaks [90]. Due to the amide II being predominantly made up of N-H vibrations, this peak provides information on protein backbone and solvent interactions and exhibits greater peak shifts compared to amide I when hydrogen bonding is altered by either temperature [95] or solvent change [96]. When hydrogen bonding is decreased the amide II band shows a decrease in absorbance [96].

Although the amide bands are informative there still exist issues of key spectral features such as amide I vibrations (1600-1800 cm^{-1}) overlapping with H_2O bending vibrations (≈1650cm^{-1}) masking spectral features [77]. In order to mitigate spectral masking water can be subtracted from the absorption spectrum of proteins by ensuring a H_2O specific combination (bend + libration) band at ≈2150 cm^{-1} is completely removed [97].This thesis utilises ATR-FTIR spectroscopy for the analysis of proteins when applying IR spectroscopic techniques.

1.2.6 ATR-FTIR spectroscopy applied to bioprocessing

ATR-FTIR spectroscopy has in recent years been applied to bioprocessing of proteins. The versatility and chemical information provided by this technique is increasingly being utilised in Process analytical technologies (PAT).

One such example of PAT development is work by Großhans et al where ATR-FTIR spectroscopy was successfully implemented to quantify mAbs in-line during CEX chromatography [98]. Different proteins (mAbs and lysosomes) could be differentiated and quantified under flow with the utilisation of partial least squares (PLS) regression. The root mean square error (RMSE) is useful for determining PLS predictive ability compared to a known value in this case concentration and can be calculated by Equation 1.18 .

$$RMSE = \sqrt{\frac{\sum_{i=1}^{n}(y_i - \hat{y}_i)^2}{n}} \quad 1.18$$

Where RMSE= Root mean square error, n=number of observations, y_i= ith iteration of actual observation , $\hat{y}_i$= ith iteration of predicted observation

The Großhans et al. study gave RMSE values of 2.42 mg ml^{-1} and 1.67 mg ml^{-1} for quantification of mAb and lysosome respectively indicating, small variations between ATR-FTIR derived concentrations compared to industry standard UV/Vis derived concentrations. Concentrations reached upwards of 112 mg ml $^{-1}$ for lysosomes in the study [98]. ATR-FTIR spectroscopy was also able to identify PEGylation of the eluted mAbs in the work showing the extra added information obtained using this approach compared to standard methods like UV/Vis.

ATR-FTIR has also been utilised for the study of purification resins. Research by Boulet et al, 2016 showed that ATR-FTIR spectroscopy could assess the amount and state of the SPA ligand of PrAc resins [49]. Changes in the conformation of SPA occurring upon exposure of concentrations of NaOH above 0.1 M could be detected and the stabilising effects of trehalose explored [49]. Further work on the CIP step for PrAc revealed leaching of ligands even in alkaline resistant Protein A resins such as MabSelect SuRe. With each CIP step the Protein A ligand density decreased demonstrated by a reduction in absorbance of the amide I and II bands. mAb bound to the surface layer of resin beads in-column were also successfully quantified [56].

1.3 Raman Spectroscopy

Raman spectroscopy is named after the person to first observe this effect, Sir Chandrasekhara Venkata Raman [99] who won the Nobel prize in physics in 1930. Raman spectroscopy is similar to IR spectroscopy in that it allows for determination of specific vibrational modes in a molecule. The key difference between the two techniques is that Raman spectroscopy utilises scattering and IR spectroscopy utilises absorption. The electromagnetic spectrum and its different forms are described in section 1.2.

1.3.1 Fundamentals of Raman spectroscopy

Electromagnetic radiation can be described as a propagating oscillating dipole as illustrated in Figure 1.13.

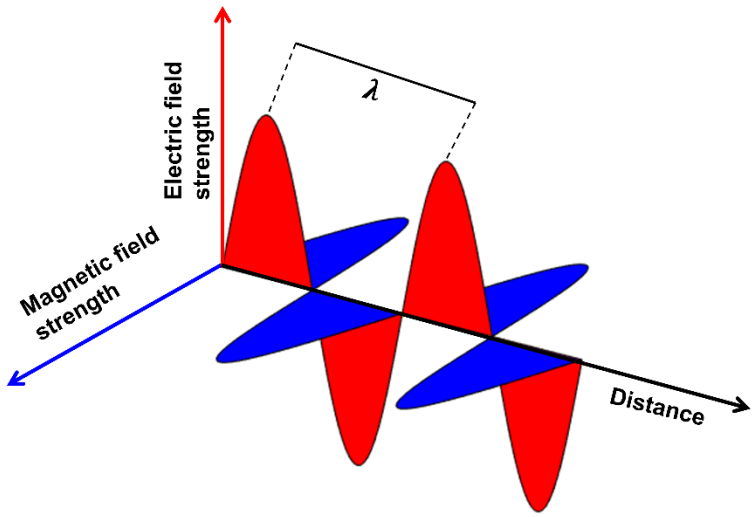

Figure 1.13 Representation of the components in an electromagnetic wave. Electric field shown in Red and magnetic field shown in blue.

If a molecule is exposed to an external electric field such as electromagnetic radiation, distortion or displacement of the electron clouds that make up molecular bonds will occur. If a change in the separation of charge across the bond occurs, the molecule is then considered polarised. The ability of an electron cloud to be displaced by external electric fields is defined as its polarizability (Equation 1.19) [100].

$$\mu' = aE \qquad 1.19$$

Where μ'=induced dipole moment, a=molecular polarizability and E=electric field strength

E is defined by Equation 1.20 and shows how electric field strength varies with time [100].

$$E = E_0 cos 2\pi \nu_0 t \quad 1.20$$

Where E =electric field strength, E_0=vibrational amplitude , ν_0=frequency of wave and t=time

By substituting Equation 1.19 E with Equation 1.20 we get Equation 1.21

$$\mu' = aE_0 cos 2\pi \nu_0 t \quad 1.21$$

Where μ'=induced dipole moment, a=molecular polarizability, E_0=vibrational amplitude , ν_0=frequency of wave and t=time

The electromagnetic radiation's electric field interaction with matter is dependent on the molecular structure, when this interaction occurs a time dependent temporary change in dipole moment is induced. The absorbed energy from incident electromagnetic radiation will cause a change in the energy state of the bond shown in Figure 1.14.

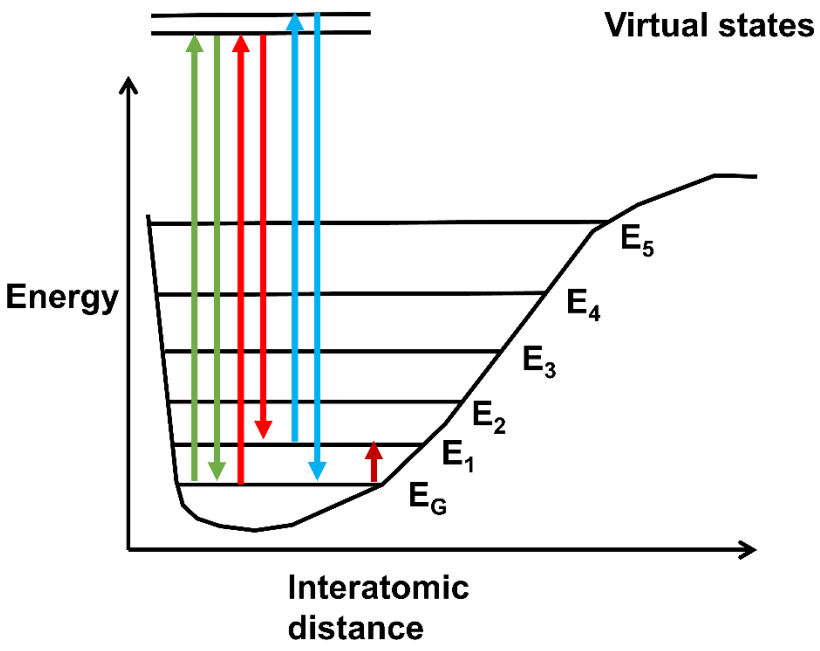

Figure 1.14 The representation of potential energy of a diatomic molecule showing fundamental IR transitions and scattering transitions. Rayleigh scattering (green), Stokes scattering (red), anti-Stokes scattering (blue) and fundamental transition (dark red) are shown.

Hooke's law shown in Equations 1.10 and 1.11 explains the frequencies at which molecular vibrations occur. As described in section 1.2.1 if the electromagnetic radiation has the same wavenumber as the vibrational mode, then absorption will cause a fundamental transition in the vibration of a molecule as shown by the dark red arrow in Figure 1.14. If for instance a monochromatic source is used at visible or near-IR ranges, the frequency of the oscillating

dipole of the incident electromagnetic radiation is much greater than that of the vibrational modes in the molecule. The absorption will cause polarisation and the vibration will go to its highest energy state such as a virtual state before contracting back to ground state and releasing a photon [100]. This absorption and release is known as scattering, as the incident photon will have a different vector compared to the emitted (scattered) photon.

Photons will be scattered in three different ways. The most common way is Rayleigh scattering shown in green in Figure 1.14. The wavenumber of the incident photon will equal that of the scattered photon. There is however a one in a million chance that Stokes or anti-Stokes scattering will occur shown by the red and blue lines respectively in Figure 1.14. Stokes scattering is when the wavenumber of the incident photon is higher than the scattered photon. Anti-stokes is when the wavenumber of the incident photon is lower than the scattering photon. Stokes scattering is more likely to occur than anti stokes since most vibrations are in the ground state.

The Raman scattering effect is explained by looking at the displacement that occurs when electromagnetic radiation is applied to a molecule (1.22) which is similar to Equation 1.20 but components refer to molecule's nuclear displacement rather than the electric field strength of the electromagnetic wave.

$$Q_D = Q_{D0} cos 2\pi \nu_{vib} t \qquad 1.22$$

Where Q_D=nuclear displacement, Q_{D0}=amplitude of vibration, ν_{vib}=frequency of vibration and t=time

Displacements will be small, as the amplitude of vibration will be smaller than the bond length. The polarizability can be expressed as a linear function of nuclear displacement given by a Taylor series 1.23.

$$a = a_0 + \left(\frac{\partial a}{\partial Q_D}\right) Q_D + \ldots, \qquad 1.23$$

Where a=polarizability, a_0=polarizability at equilibrium $\left(\frac{\partial a}{\partial Q_D}\right)$ =rate of change of the polarizability with respect to Q_D and Q_D=nuclear displacement

Since the amplitude of vibration of a molecule is small compared to the oscillating wave, the higher terms in the Taylor expansion can be ignored. Equations 1.21, 1.22 and 1.23 can be combined using the trigonometric Equation $cos\, a\, cos\, b = \frac{1}{2}\big(cos(a-b) + cos(a+b)\big)$ to give Equation 1.24 [100].

$$\mu' = a_0 E_0 cos2\pi\nu_{vib}t + \frac{1}{2}\left(\frac{\partial a}{\partial Q_D}\right) Q_D E_0 (cos\pi(\nu_0 - \nu_{vib})t + cos\pi(\nu_0 + \nu_{vib})t) \quad 1.24$$

Where μ'= induced dipole moment , a=polarizability, a_0=polarizability at equilibrium $\left(\frac{\partial a}{\partial Q_D}\right)$ =rate of change of the polarizability with respect to Q_D ,Q_D=nuclear displacement , E_0=vibrational amplitude , ν_{vib}=frequency of vibration , ν_0=frequency of wave and t=time

The components of scattered photons are shown by Equation 1.24; green shows Rayleigh scattering, red shows Stokes scattering, and blue shows anti-Stokes scattering. The Equation also contains a selection rule for Raman scattering, that for Raman scattering to occur a change in polarizability must be associated with a vibrational mode in order to be considered Raman active as shown in Equation 1.25.

$$\left(\frac{\partial a}{\partial Q_D}\right) \neq 0 \quad 1.25$$

$\left(\frac{\partial a}{\partial Q_D}\right)$ =rate of change of the polarizability

The change in frequency when comparing incident photons to Raman scattered photons is referred to as the Raman shift and is expressed in wavenumber on a resultant spectrum.

1.3.2 Raman spectrometer considerations

A Raman spectrometer can have varying configurations with the experiments described in this thesis using commercially available laboratory spectrometers. The first spectrometer component to consider when using Raman spectroscopy is the excitation laser wavelength. The radiation source on a Raman spectrometer will be monochromatic in nature, as the shift in wavenumber caused by scattered photons is being assessed. A broad band source would complicate calculating the difference in scattered light to multiple wavelengths The wavelength used can vary, with the spectrometer utilising UV visible and IR lasers. The intensity of scattering is inversely proportional to the fourth power of the wavelength of the excitation laser (Equation 1.26) [101] .

$$\sigma \propto \frac{1}{\lambda^4} \quad 1.26$$

Where σ=scattering intensity, λ=wavelength

Based on Equation 1.26 it is more advantageous to use short wavelengths to improve the amount of Raman scattering in a given sample. There are however drawbacks, such as fluorescence produced when a molecule enters an excited energy state as the result of

receiving electrons pushed from other electron clouds. This typically occurs in molecules with conjugated double bonds, where the pi bonds allow for the spread of outer electron orbitals. The difference in energy of the excited state and ground state are low enough for visible light to excite electrons [101].This can be schematically shown with Franck-Condon principles [102, 103] (Figure 1.15) .

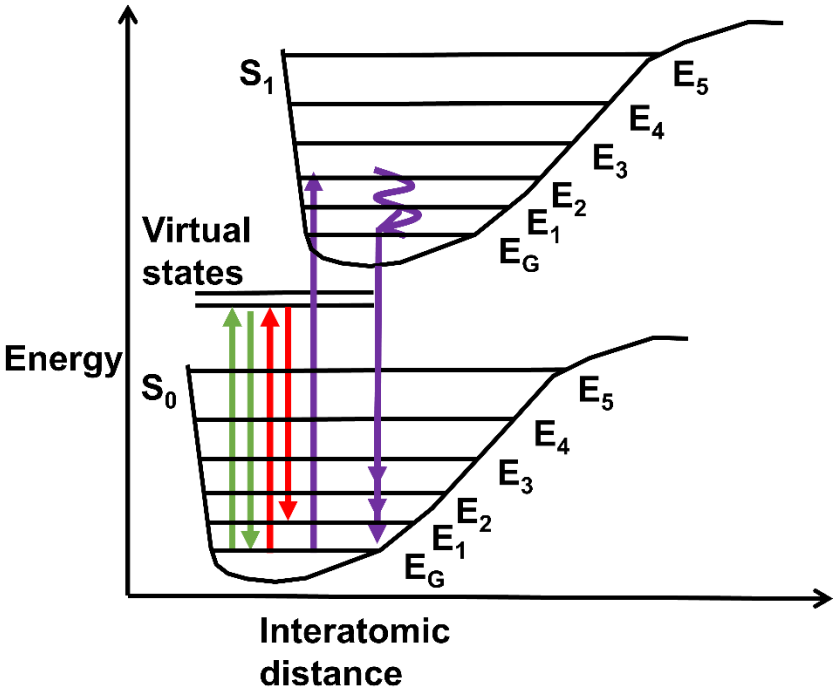

Figure 1.15 Franck-Condon Principal energy diagram for a diatomic molecule showing Raman stokes scattering and fluorescence. Rayleigh scattering (green) stokes shift (red) and fluorescence (purple).

When Stokes shift occurs molecules can reach virtual states as described previously (Raman scattering), however molecules with the capacity can reach excited (S1) states. The S1 state molecule will then undergo vibrational relaxation illustrated by the bending of the purple arrow. Once relaxation has occurred the molecule will revert to the S0 state releasing a photon. The relaxation can return to any energy level (E0-E…) during this process, then undergo vibrational relaxation to return to ground state. This process typically has a 1 in 100 chance to happen and thus is more common than Raman scattering. Due to the range of energy states achieved by fluorescence, this appears as a broad intense peak on a spectrum, masking Raman signals. Proteins containing aromatic residues can self-stabilise when they have excess energy in their vibrations due to their delocalised electrons in π-π bonds and this self-stabilisation results in fluorescence that masks Raman signals. Fluorescence does require more energy than Raman as shown by Figure 1.15. A way to minimise fluorescence is to control laser power to ensure sufficient energy for Raman scattering to occur but not enough for a molecule reach excited states. Another way to decrease fluorescence is to increase laser

wavelength, therefore decreasing all scattering as the energy of each photon is decreased. The fluorescence mechanism occurs over longer than picosecond time scales so this fluorescence can also be reduced by use of a time gated laser with femtosecond range pulses able to only detect Raman scattering [104, 105].

Another key component of a Raman spectrometer is a filter to remove Rayleigh scattered light from the Raman scattered light. This removes the laser wavelength which causes excitation whilst allowing Stokes or anti-Stokes light to pass through the filter (Figure 1.16).

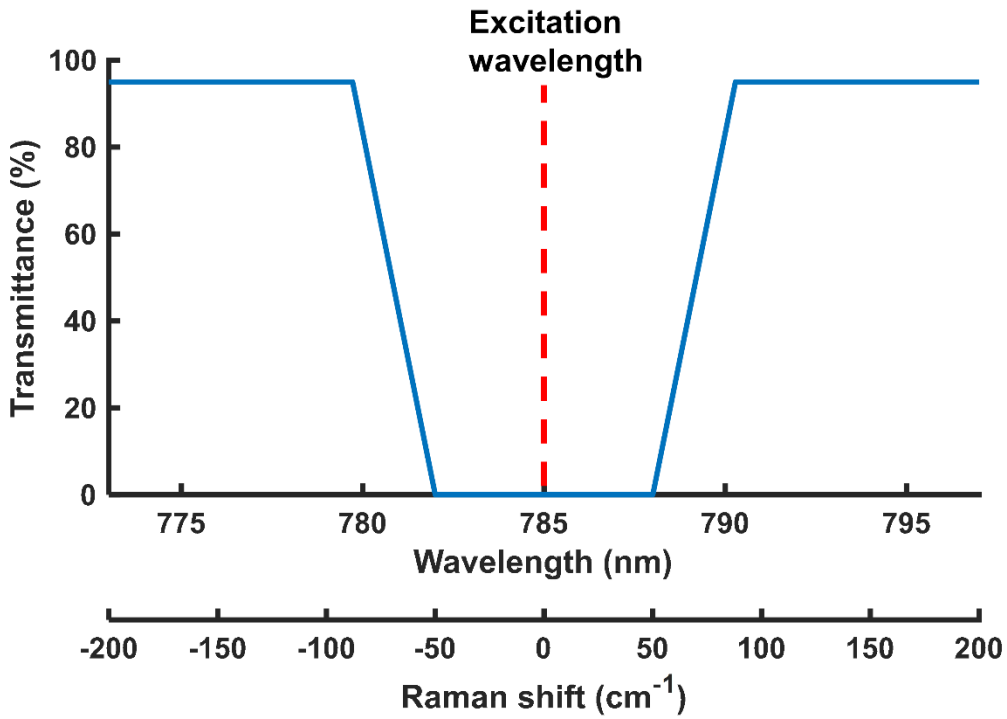

Figure 1.16 Example of transmittance through a holographic notch filter using a 785 nm laser. The excitation wavelength is all light elastically scattered by Rayleigh scattering. The filter results in 0% transmittance within the cut off either side of the excitation wavelength. An equivalent Raman shift in wavenumbers (cm^{-1}) is given to compare to wavelength.

Modern holographic notch filters based on designs by Denisyuk [106] perform a selective rejection action by interference (Figure 1.16). When the interference pattern has one of the original wavelengths applied the second wave front is reconstructed [107]. In reality the filter is likely to have a usable cut-off ~50 cm^{-1} from the excitation wavelength, thus any Raman scattering within this limit will not be displayed on the spectrum [108]. Some spectrometers have been shown to allow for Raman scattered light over ~ 5 cm^{-1} from the Rayleigh line [109]. In order to filter out the Rayleigh scattering, atomic metal vapours can be used. The metal vapour gives a very narrow absorption of light and thus can be selected based on the excitation wavelength used to remove all Rayleigh and Raman scattering within the cut off from the Rayleigh line.

Once scattered light has been filtered in order to remove Rayleigh scattered light the remaining Raman scattered light will be of low intensity. Any Stokes and anti-Stokes light will have a range of shifts in frequency distinct from the Rayleigh scattered light and must be separated to be detected. For separation and detection of Raman scattered light, a diffraction grating and charge coupled detector (CCD) are used respectively.

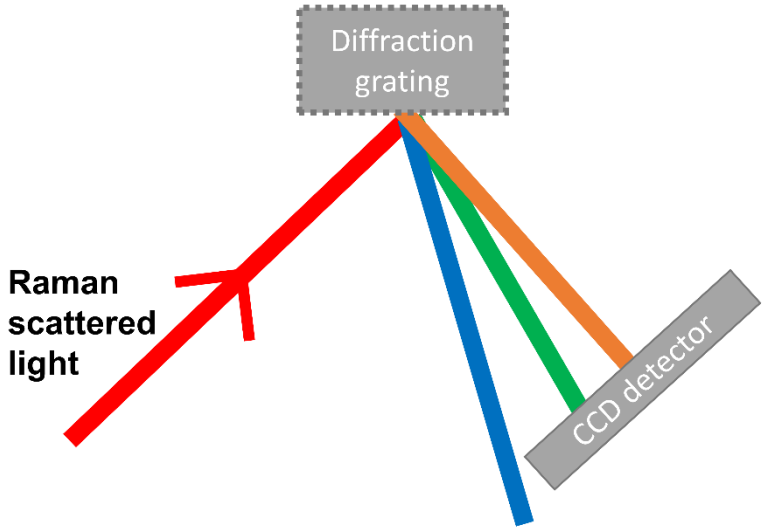

Figure 1.17 Schematic diagram of a difraction grating to spatially separate the multiple discrete frequencies of Raman scattered light into beams of each discrete frequency onto a CCD detector.

The diffraction grating horizontally disperses the Raman scattered light into individual frequencies. The more grooves per mm (grooves mm $^{-1}$) the greater the dispersion of light [110]. This greater dispersion allows for better differentiation between discrete frequencies of Raman scattered light but does mean a smaller region of a given spectrum will be observed as some frequencies will be dispersed away from the detector. To compensate Raman spectrometers have a motorised diffraction grating to allow all frequencies to reach the CCD detector. Multiple diffraction grating positions are used in measurement of a sample in order to obtain the full spectral range of frequencies (50-4000 cm^{-1}). Less light reaching the CCD detector means a reduction in signal strength.

The CCD detector (Figure 1.18) is made up of an array of pixels that convert incident light into electric charge. The amount of scattered light detected is proportional to the charge generated. These spatially different pixels allow for detection of multiple frequencies of light.

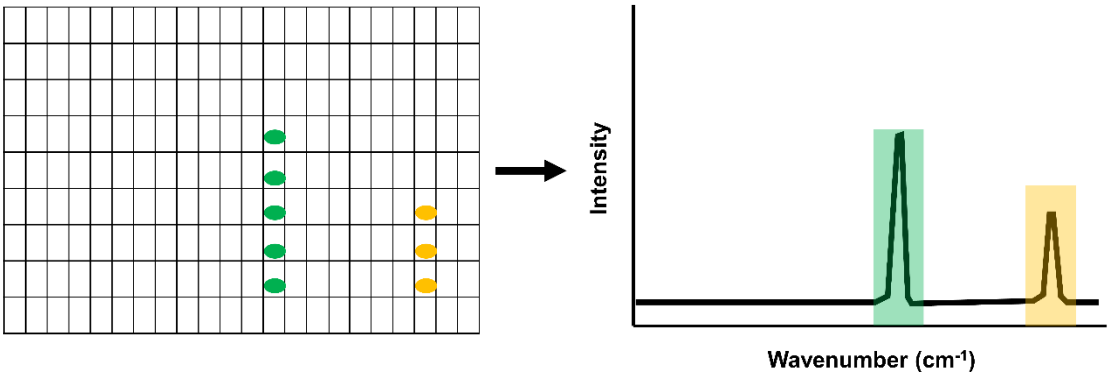

Figure 1.18 Schematic of CCD detector found in a Raman spectrometer and the spectrum produced. Green and yellow represent different frequencies of Raman scattered light and their respective peaks on a Raman intensity spectrum.

The CCD detector utilises the process of pixel binning to sum the horizontally dispersed charge generated by dispersed Raman scattered light from the diffraction grating [111] as shown by Figure 1.18. The size of pixels and the diffraction grating will affect the resultant spectral resolution as the spectrum is reliant on the spatially dispersed frequencies of the Raman scattered light to generate a spectrum [110]. Although sensitive enough for detection of Raman scattering, CCD detectors are also vulnerable to generation of charge from cosmic events [112]. Cosmic events can cause cosmic spikes on a given spectrum and will be represented by one or more very sharp narrow peaks. These events are spontaneous and the chance of occurring is increased with longer measurement times. To compensate for cosmic spikes, methods for removal include nearest neighbour analysis which compares repeat measurements for outlying spectra features [112].

1.3.2 Confocal Raman microscopy

Raman spectrometers are commonly coupled to a microscope allowing for confocal Raman microscopy to be performed. Biological samples often have weak Raman scattering effects and thus require signal enhancement. Utilising a microscope allows electromagnetic radiation from a monochromatic source to be focused on a single area referred to as a spot, thus increasing the amount of Raman scattered light detected. The focused area means a higher energy density is focused on a sample and thus increases the amount of Raman scattered light detected. This allows for lower power lasers to be used preventing unwanted burning or damage to samples. The spot size is typically close to the diffraction limit, defined as the point

where spatially different spots in the X and Y directions are no longer distinguishable from each other (Equation 1.27).

$$r = \frac{1.22\lambda}{2NA} \quad 1.27$$

Where r= distance between two points that are resolved, λ=wavelength of light, NA=Numerical aperture

The numerical aperture (NA) characterises the range of angles that light will pass through an objective lens and is defined by Equation 1.29.

$$NA = n_l sin\theta_l \quad 1.28$$

Where n_l=refractive index of objective θ_l=max half angle of the confocal light

$$sin\theta_l = \frac{D}{f} \quad 1.29$$

Where θ_l= max half angle of the confocal light D= radius of confocal light f=distance to focal point

$sin\theta$ is schematically represented below in Figure 1.19.

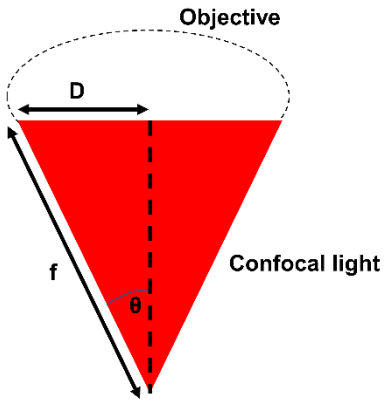

Figure 1.19 Schematic representation of confocal light and the illustration of the physical properties used to calculate NA in equation 1.2.9. Red shows the confocal light.

The NA plays a critical role in the spatial resolution of confocal Raman microscopy, not only in the x and y planes, but also in the z direction when undertaking depth profiling of samples. Research by Everall has explored the role of refraction in depth profiling [113]. When light enters a material with a distinct refractive index, it will undergo refraction and thus the focus point of the light will change. The change in the angle of light by refraction is described in Snell's law discovered in 1621 (Equation 1.30).

$$n_1 sin\theta_1 = n_2 sin\theta_2 \quad 1.30$$

Where n_1 =refractive index of sample n_2=refractive index of second material

The change in focal point for refracted light is expressed as the depth resolution (DR) [113] and is demonstrated by Figure 1.20 and Equation 1.31.

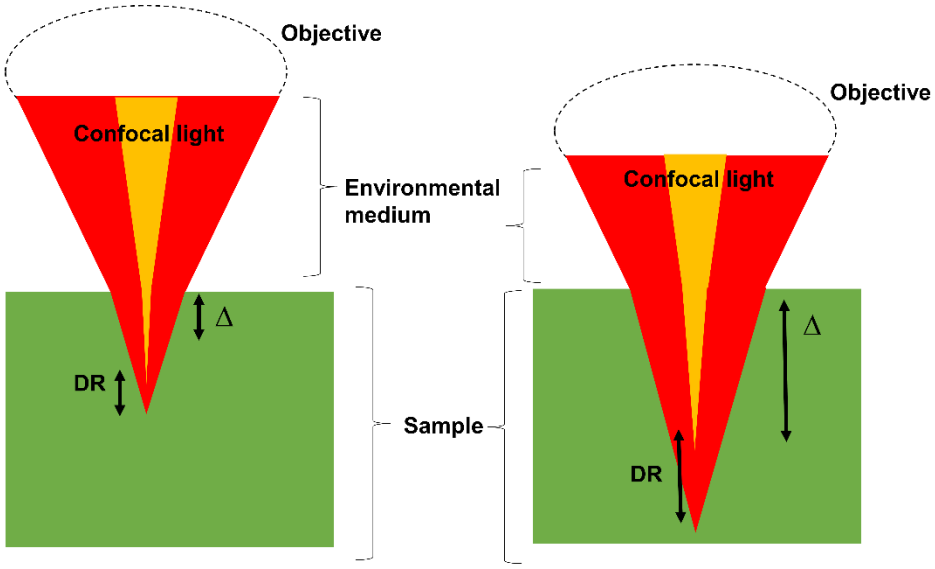

Figure 1.20 Schematic representation of depth resolution during confocal Raman depth profiling at different perceived depths. Marginal rays (red) and paraxial rays (orange) are shown

DR is the distance between the marginal and paraxial focal points of the confocal light shown as the focal points of the red and yellow rays respectively in Figure 1.20.

$$DR = \Delta\left(\left(\frac{NA^2(n_1^2-1)}{(1-NA^2)}+n_1^2\right)^{1/2}-n_1\right) \qquad 1.31$$

Where DR=depth resolution NA=Numerical aperture n_1=refractive index of sample Δ=attempted focus depth

Equation 1.31 shows that as the sample is probed deeper by confocal light the DR increases and thus the illumination volume increases [113]. Thus, depth profiling the sample thickness needs to be accounted for, as the illuminated volume could go beyond the sample and illuminate other samples parts below the desired area. Typically, samples are measured in an environmental medium of air with a refractive index of 1. In this environment DR will increase with increasing depth, although this effect can be mitigated by using immersion oils with the same refractive index as the measured sample thus refraction of light beyond the sample thickness will not occur. The use of immersion oils requires specialist lenses and introduces peaks that can overlap and mask sample specific Raman spectral bands. The addition of extra bands by immersion oils makes this approach unsuitable for analysis of proteins as they exhibit weak Raman scattering.

1.3.3 Application of Raman Spectroscopy to Bioprocessing.

Raman spectroscopy has been applied to bioprocessing of proteins, allowing for utilisation of Amide bands in a similar fashion as described for ATR-FTIR spectroscopy in section 1.2.5. In the application to resins ATR-FTIR spectroscopy is however limited to probing only the surface layer (~ 5 μm) of PrAc resin beads, which can be up to 120 μm in diameter. Confocal Raman spectroscopy is not limited to measuring the surface layer of samples and can be used to explore the distribution of ligands bound at both the surface and within pore regions of agarose beads [114]. Previous studies have applied confocal Raman spectroscopy to the study of mAb binding to a cation resin, Fractogel EMD SO_3, at different ionic strengths [115]. The study demonstrated that it was possible to use this approach to obtain a depth profile for mAb binding to the resin beads and show that mAb binding occurred preferentially at higher ionic strength conditions. A subsequent study using the same approach revealed that mAb desorption from the Fractogel EMD SO_3 occurred at pH 5.0, while at pH 4.0 the mAb adopted a conformation that stayed bound to the resin [116].

Recent studies have utilised the multivariate nature of Raman spectroscopy in the application of characterising multiple mAb characteristics such as purity, pH and formulation compounds [117]. In-line methods have been developed to assess mAb concentration of breakthrough from a Protein A column [118]. The use of Raman spectroscopy utilised PLS regression to quantify mAb and served as a proof of concept for Raman application in the monitoring of mAb concentration during downstream processing.

1.4 AIMS:

The overall aim of the research described in this thesis was to utilise vibrational spectroscopic methods, both ATR-FTIR and Raman spectroscopy, to investigate the causes of degradation of Protein A resin during downstream processing and the monitoring of resin performance during isolation. The specific objectives of were:

- To investigate the Protein A ligand density and conformation on Protein A resins after repeated purification cycle by industry unit operations (Chapter 3).

- To determine if the reduction of binding capacity of Protein A resin after repeated purification cycles is influenced by spatial location within a column (Chapter 3/4).

- To determine the cause of Protein A resin binding capacity decrease after industrial use and examine fouling distribution within the porous matrix of protein A resin at the bead level (Chapter 4).

- To develop and validate confocal Raman spectroscopic methods for both the quantification of biotherapeutics and the monitoring of purification performance in industrial scalable unit operations such as protein A purification (Chapter 5).

Chapter 2- Experimental instrumentation

During the work carried out in this thesis, 4 spectrometers were used to generate spectra, two IR spectrometers and two Confocal Raman spectrometers. Fundamentals of spectroscopy are covered in section 1.2 and 1.3. This section describes the unique set up of each of the four spectrometers.

2.1 ATR-FTIR spectroscopy

2.1.1 Equinox 55 with diamond Golden Gate accessory

The Equinox 55 FTIR spectrometer was used to generate the data presented in Chapter 3. The schematic layout of the Equinox 55 system used can be seen in Figure 2.1.

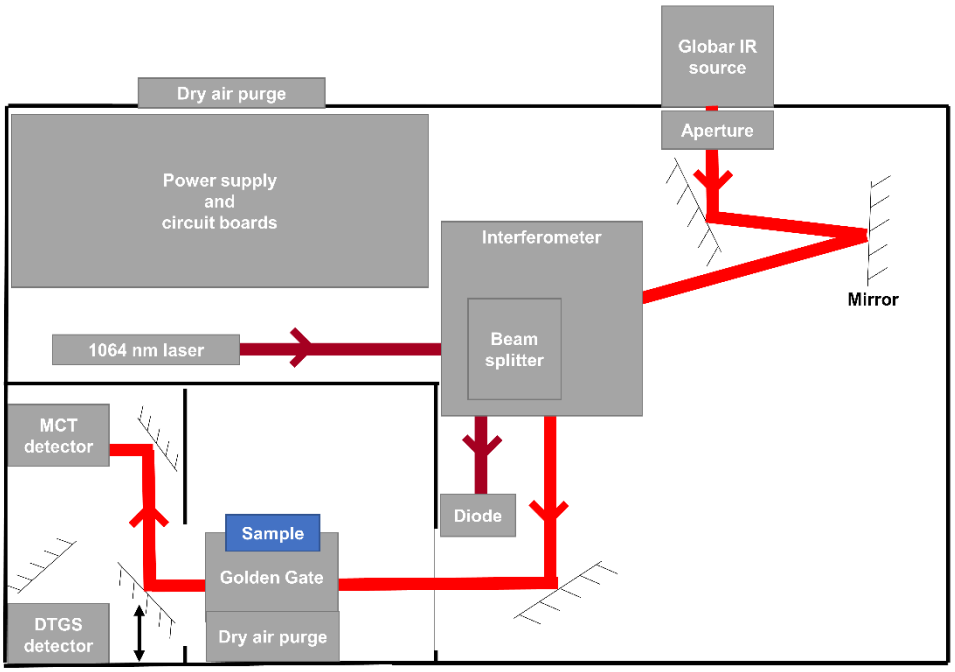

Figure 2.1 Schematic layout of the Equinox 55 FTIR spectrometer with ATR Golden gate accessory. The beam path of the mid IR radiation and 1064 nm radiation are shown respectively by light red and dark red. Spectrometer components are shown by the grey labelled squares.

The Equinox 55 spectrometer utilises a globar (silicon Carbide) IR source, electrically heated to between 1000 K and 1200 K, which emits IR radiation with wavelengths from 2.5-17 μm. The Globar acts like a black body radiation source emitting radiation wavelengths corresponding to the mid-IR region [119] and covers wavenumbers 588-4000 cm^{-1}. Molecular vibrations absorb energy from this mid-IR range as described in section 1.2.1. The system is purged with dry air to minimise radiation being absorbed by strongly absorbing H_2O in the atmosphere. This reduces decay of the signal before it reaches the sample and minimises spectral changes due to CO_2 and humidity levels changing over the course of experiments.

The mid-IR radiation from the polychromatic globar source is then reflected to the interferometer where the radiation is split 50% by a beam splitter, half goes to a fixed mirror and half goes to a moving mirror. The mirrors are positioned perpendicular to each other. The radiation is reflected from the two perpendicular mirrors allowing the two beams to combine (Figure 1.8). A diagram is shown for the Michelson interferometer (section 1.2.2). The combining of the beams causes the generation of an interference pattern in the resultant beam. The modulated beam is then reflected into the sample compartment containing a Golden Gate ATR accessory (Figure 2.2).

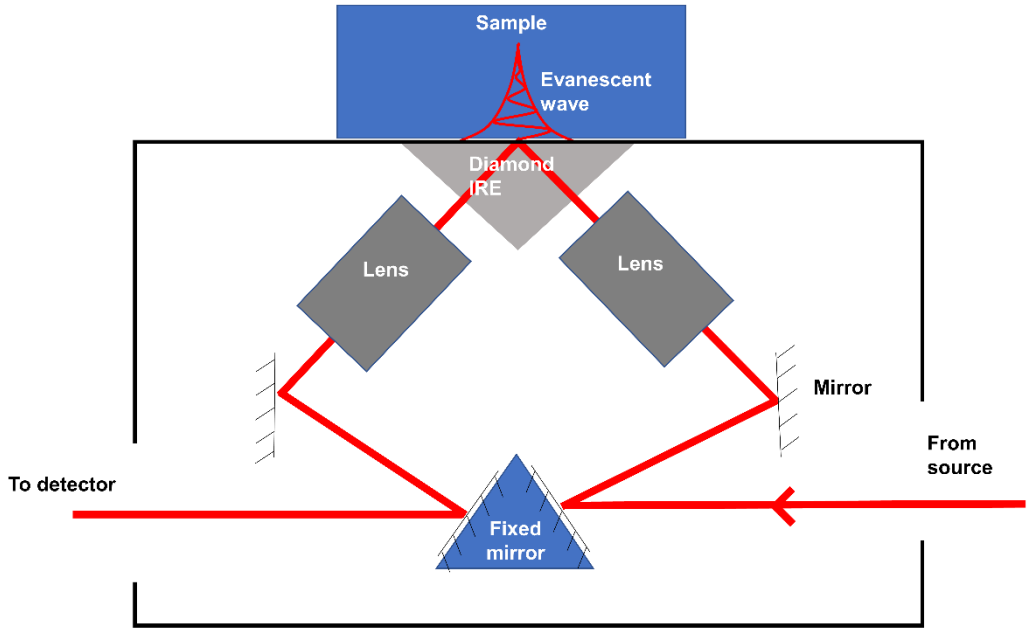

Figure 2.2 Schematic of diamond Golden gate ATR accessory. The beam path of IR radiation is shown by the red line.

The Golden Gate accessory facilitates the use of the ATR mode of IR spectroscopy. IR radiation from the interferometer is reflected into the dry air purged Golden Gate. The IR radiation reaches the fixed mirror, where it is focused through an objective lens on a Diamond IRE with a refractive index of 2.4. The angle of incidence for radiation reaching the prism is fixed at 45 degrees. This is above the critical angle and results in the production of an evanescent wave which probes the sample. According to Harrick's depth Equation (Equation 1.16) [86-88], this means the penetration depth of the evanescent wave across all wavenumbers is fixed and will not change when measuring the same sample.

The Equinox 55 uses a liquid nitrogen cooled mercury cadmium telluride (MCT) detector which detects the full mid-IR range and allows fast interferometer scan speeds and therefore faster measurement of samples. The monochromatic He-Ne 1064 nm laser also emits near IR

radiation into the interferometer. The near IR beam moves coaxial to the globar sources mid-IR radiation in the interferometer. The now modulated near-IR radiation reaches a diode where it is used to calibrate the interferometer mirror positions and wavenumber assignment.

2.1.2 Tensor 27 with Golden Gate accessory for Spectroscopic imaging

In addition to traditional ATR-FTIR spectroscopy ATR-FTIR imaging can be achieved with the addition of a Focal plane array (FPA).This instrument was used to generate chemical images (Figure 3.9) in chapter 3.

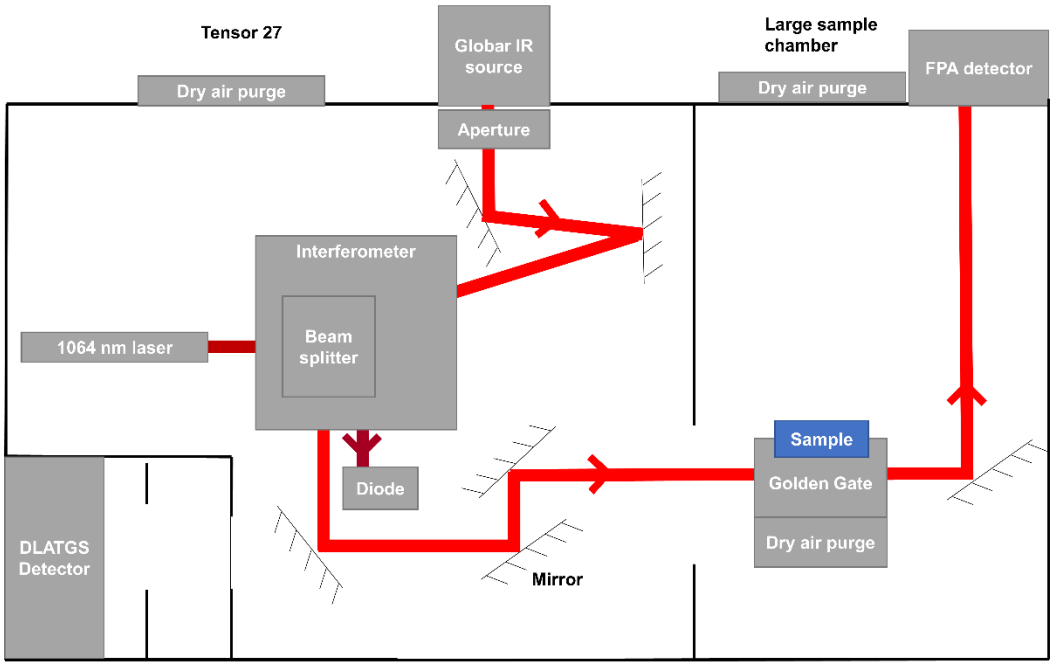

Figure 2.3 Schematic layout of Tensor 27 FTIR spectrometer with large sample chamber, ATR golden gate attachment and FPA. The beam path of the mid IR radiation and 1064 nm radiation are shown respectively by light red and dark red. Spectrometer components are shown by the grey labelled squares.

The Tensor 27 spectrometer, utilised to generate data presented in chapter 3, has a large sample compartment chamber attached to provide a larger sample compartment and space for addition of the FPA. The Globar IR source is heated to a fixed temperature ensuring a consistent emission spectrum. Light passes through an aperture which controls the amount of radiation to reach the interferometer. Once the radiation reaches the interferometer the radiation is split with 50% directed to both the moving and stationary mirrors. The modulated beam is then reflected to the Golden Gate where the evanescent wave produced is used to probe the sample. The radiation is then reflected to the liquid nitrogen cooled MCT FPA detector. The FPA has a 64*64-pixel array allowing for 4096 spectra to be measured simultaneously with each pixel corresponding to a spatial location on the Diamond IRE of the Golden Gate.

2.2 Confocal Raman microscopy

2.2.1 Bruker Senterra II

Confocal Raman spectroscopy measurements described in chapter 4 were performed using a Bruker Senterra II spectrometer. The device incorporates a white light source and a video camera for optical micrographs to be generated and for optical alignment of samples with the Raman laser.

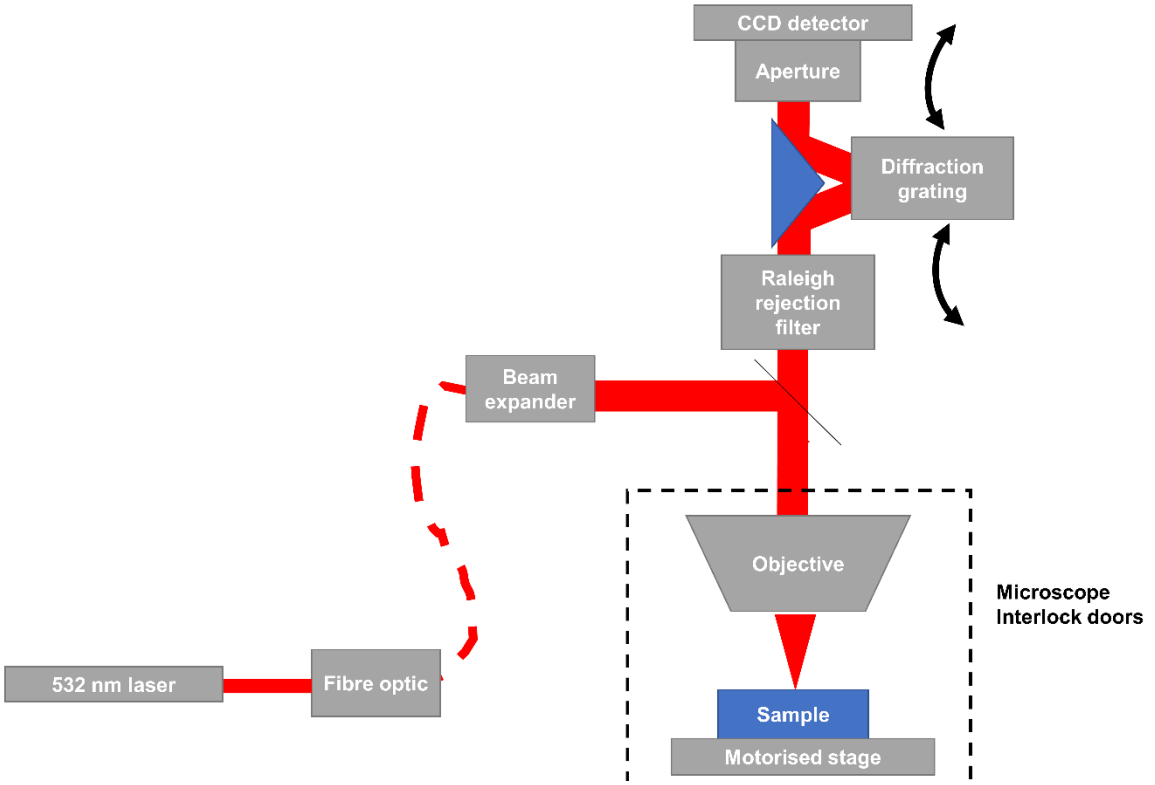

Figure 2.4 Schematic layout of Senterra II Raman spectrometer. The beam path from the laser is shown in red. Spectrometer components are shown as labelled grey squares. The red dotted line represents the path of the fibreoptic cable. Black dotted line represents the microscope interlock doors.

The Interlock doors must be closed for the excitation laser to emit radiation. The excitation laser emits radiation at 532 nm, which is then fed into a fibre optic cable to the main body of the spectrometer (Figure 2.4). Some energy is lost due to the fibre optic [120] .The fibre optic is fed into a beam expander and then directed to the microscope objective. A 50X, 0.65 NA aperture was used to focus the beam onto the sample. Raman and Rayleigh scattered light then comes back through the objective through the variable aperture towards the Rayleigh rejection filter. The aperture can be decreased in size to limit signal reaching the CCD detector and light from out of focus regions will also be filtered out. The Rayleigh rejection filter removes all Rayleigh scattering plus light scattered ~100 cm^{-1} from the Rayleigh rejection filter. The

remaining Rayleigh scattered light is dispersed by diffraction grating. There are two diffraction gratings on the system with 400 and 1200 grooves mm^{-1}. The 1200 grooves mm^{-1} diffraction grating was utilised to displace scattered light onto the electronically cooled CCD in this work. This grating and CCD allows for static scans where the full range from 400-3400 cm^{-1} can be measured simultaneously without the need for multiple grating positions.

2.2.2 Renishaw InVia spectrometer

The Renishaw InVia Spectrometer was utilised in chapter 5 to perform confocal Raman spectroscopic measurements. This system has a white light source for optical alignment on samples that is not shown in the schematic below (Figure 2.5).The source rests above the objective for micrographs to be taken.

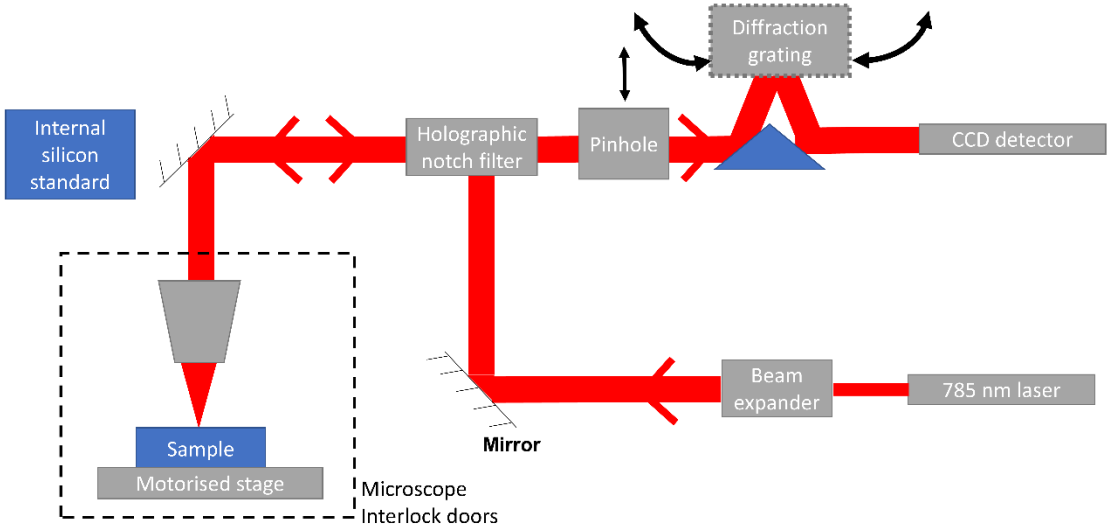

Figure 2.5 Schematic of Renishaw InVia Confocal Raman spectrometer. The beam path from the laser is shown in red. Spectrometer components are shown as labelled grey squares. Black dotted line represents the microscope interlock doors.

Before measurements can begin on the system the interlock doors must be closed, this prevents the laser source from emitting radiation when doors to the stage are open. The system has a choice of two lasers, 532 nm and 785 nm with the 785 nm laser used in this work. The laser is directed to a beam expander which reduces the power density and expands the area covered by the laser. The expanded beam is then reflected to the holographic notch filter then to either the internal silicon standard for calibration or measurement of samples. Calibration of the grating and holographic notch filter is performed based on the peak position of silicon at 520 cm^{-1}. If sample measurement is underway, the beam is directed to the sample via a 10X, 0.25 NA objective lens. The scattered light is then reflected back to the holographic notch filter. The holographic notch filter utilises the excitation wavelength to remove Rayleigh

scattered light. The InVia system incorporates eclipse holographic notch filters which offer improved filtering to allow Raman scattered light >5 cm^{-1} to be separated from Rayleigh scattering [109]. The light is then directed to an optional pinhole in either the in or out position to control the amount light from outside points of focus reaching the detector. The scattered light then reaches the diffraction grating. The system has two gratings available, at 1800 and 1200 grooves mm^{-1}. The light is dispersed onto an electronically cooled CCD detector. Multiple grating positions must be used to achieve the full spectral range with this CCD and grating setup.

Chapter 3- Insight into purification of monoclonal antibodies in industrial columns via studies of Protein A binding capacity by in situ ATR-FTIR spectroscopy

This chapter's contents are reproduced and edited from the manuscript detailed below with permission from the Royal Society of Chemistry:

https://doi.org/10.1039/D1AN00985K

Beattie JW, Rowland-Jones RC, Farys M, Tran R, Kazarian SG, Byrne B. Insight into purification of monoclonal antibodies in industrial columns via studies of Protein A binding capacity by in situ ATR-FTIR spectroscopy. Analyst. 2021(146):5177-85.

3.1 Background

As described in section 1.1.3 the majority of therapeutic mAbs are recombinantly produced in mammalian expression systems. Due to the recombinant source of mAbs, the presence of small amounts of host cell proteins (HCP) and host cell DNA (HCDNA) in the isolated material is possible. Such contaminants have the potential to trigger a harmful immune response [28, 29], an undesirable response referred to as immunogenicity [121].

Various steps are employed in downstream processing of recombinantly produced mAbs in order to reduce HCP and HCDNA to safe levels as well as remove HMWS and culture media components [11, 32]. Although responsible for the removing the majority of contaminating material [29] PrAc is responsible for the majority of downstream processing costs [54] due to high upfront cost and lifetime degradation.

Whilst it is well known that PrAc resins suffer loss of binding capacity over time, one thing that is not well characterized is whether the loss in binding capacity is homogeneous throughout a Protein A column. A better understanding of this has the potential to make resin use more efficient and thus cut costs associated with mAb purification. This chapter describes studies using a combination of SBC analysis and ATR-FTIR spectroscopy to explore the mAb binding performance, ligand density and secondary structure of the SPA ligand/bound mAb in MabSelect SuRe samples obtained from a used Protein A column. FTIR spectroscopy is a non-destructive, label-free method which can detect multiple components in a system simultaneously. For example, in this study agarose, SPA ligand, solvent and IgG are all detected in a measured sample of PrAc resin. The molecular vibrations within a sample absorb mid-IR radiation of specific frequencies resulting in an energy change. This absorption results in spectral bands at specific wavenumbers making up an individual chemical fingerprint. In a measured mid-IR absorption spectrum, prominent spectral features such as the amide I and amide II bands found at 1600 cm^{-1}-1700 cm^{-1} and 1520 cm^{-1}-1600 cm^{-1} respectively are characteristic of proteins as described in section 1.2.5.

PLS regression analysis of the spectroscopic data confirmed the ability of ATR-FTIR spectroscopy to predict performance of affinity resins for mAb capture. The data also shows the additional molecular information which can be obtained from the resin samples by ATR-FTIR analysis compared to traditional OD_{280} nm based SBC assays.

This chapter assesses used Protein A resin (MabSelect SuRe) from different spatial locations within an industrially used 981 ml column. Findings show that the highest losses in binding capacity are experienced at a Protein A resin column inlet and there is a gradual reduction in

binding capacity loss through the length of the column. The loss of binding capacity is not due to a reduction in the amount or conformation of the SPA ligand bound to the resin in the column but is likely due to irreversible binding of mAbs or HCP fouling within the porous matrix of the Protein A resin.

3.2 Materials and methods

3.2.1 IgG4 preparation and isolation

A Glutamine Synthetase Chinese Hamster Ovary (GS-CHO) cell line (Lonza Biologics, Switzerland) was used to express Chimeric mAb B72.3 (IgG4). Cultures were maintained in CD-CHO medium (ThermoFisher, UK) supplemented with L-methionine sulphoximine (Merck, UK) at 8% CO_2 humidified air at a temperature of 36.5 °C. The Chimeric cB72.3 IgG4 was secreted into the CCS. Following protein expression, the CCS was harvested and then frozen at -20 °C prior to further use.

The CCS containing B72.3 IgG4 was allowed to thaw on ice, centrifuged at 4601 *g* for 10 minutes and then passed through a 0.45 µm Supor Acrodisk syringe filter to remove large particulate matter. The filtered media was desalted using a HiPrep 26/10 column (Cytiva, UK) in equilibration buffer (50 mM phosphate/150 mM NaCl, pH 7.4). The desalted media was loaded onto a Protein A MabSelect Sure column (Cytiva, UK) equilibrated with equilibration buffer. The column was washed with equilibration buffer and bound material eluted with 0.1 M sodium citrate, pH 3.3. The purified IgG4 was eluted into neutralization buffer (1 M Tris-HCl, pH 9.0) to raise the pH. The fractions containing the mAb were pooled and the purified cB72.3 IgG4 fractions were buffer exchanged into equilibration buffer and concentrated using 100 kDa molecular weight cut off filters (Merck Millipore, USA). The protein was concentrated to 10 mg ml^{-1}. The amount of cB72.3 IgG4 was quantified by $OD_{280\ nm}$ using a Nano drop lite (Thermo, USA) with an E^{1}% of 13.7. Samples were stored at -80 C° for further use.

3.2.2 Static binding performance of protein A resins

All resin samples analysed in this study were MabSelect Sure. PrAc resin samples from various positions in an AXIChrom 981 ml column previously used for 25 cycles of purification, were provided by GSK Biopharm Process Research. Samples were extracted from different spatial column locations during column unpacking. Precise distances from the column inlet are provided (Table 3.1).

Table 3.1 Location of resin samples relative to the vertical distance from the column's inlet

Sample	Distance from column inlet (cm)
MabSelect SuRe	N/A
Middle, inlet	0 - 5
Middle, center	12-17
Middle, outlet	21 - 26
Side, inlet	0 - 2

An aliquot of 20.8 µl of each resin sample was individually packed, equilibrated and dispensed into a 96 well Supor filter (0.45 µm) plate using a MediaScout® ResiQuot (ATOL, Germany) provided by GSK. Purified B72.3 IgG4 was thawed and diluted to give a range of concentrations.

(1, 2, 3, 4, 5, 6 and 7 mg ml^{-1}) in equilibration buffer. Diluted IgG4 (200 µl) was individually added to the resin samples, and the resin + protein samples were mixed (1000 rpm) for 45 minutes at room temperature. The concentration of unbound IgG4 that flowed through the packed resin was analysed at OD_{280} nm on a Nanodrop lite with an $E^{1\%}$= 13.7. Resin samples were stored at 4ºC. Unused MabSelect Sure was used as a control.

The Langmuir adsorption isotherm was used to determine the mAb binding capacity of the resin samples from different locations within the pilot scale column. The measured amount of protein in the flow-through (C_{eq}) after loading samples of various concentrations of IgG4 (C_0) was used to calculate the binding capacity (Q) of different resin samples using Equation 3.1 [65]:

$$Capacity\ (Q) = \frac{V_{Sample} \times (C_0 - C_{eq})}{V_{resin}} \qquad 3.1$$

Where Q = binding capacity, V_{sample} = volume of mAb, C_0 = initial concentration, C_{eq} = equilibrium concentration and V_{resin} = volume of resin

Once the binding capacities of individual resin samples were calculated, the data was fitted to a Langmuir isotherm (Equation 3.2). This allows for the prediction of maximum binding capacity (Qmax) and dissociation constant (K_d) for each resin sample.

$$Q = \frac{Qmax \times C_{eq}}{K_d + C_{eq}} \qquad 3.2$$

Where Q = binding capacity, Q_{max} = maximum binding capacity, , C_{eq} = equilibrium concentration and K_d = disassociation constant

3.2.3 In situ-ATR-FTIR spectroscopy of Protein A resins

A master chip was designed in SOLIDWORKS 2020 software (Solidworks, USA) and 3d printed using a Form 3 3d printer (Formlabs, USA). The master chip was used to cast Sylgard a 184 PDMS device by soft lithography. The PDMS device had a 1.3 mm micro well designed to cover the IRE of the Diamond Golden Gate™ ATR accessory (Specac, UK). PMMA housing was designed in SOLIDWORKS and then laser cut (Figure 3.1B). The custom PDMS microwell device was affixed to a Diamond Golden Gate™ ATR accessory by custom PMMA housing (Figure 3.1C).

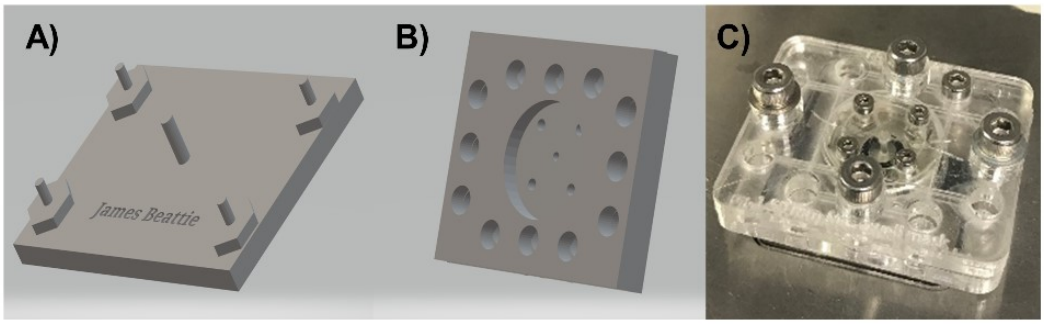

Figure 3.1 The microwell device A) master chip with a 1.3 mm diameter well, B) PMMA housing to secure the PDMS device. C) Final microwell device attached to the Golden Gate accessory.

The ATR accessory was used with an Equinox 55 FTIR spectrometer (Bruker, Germany) equipped with an MCT detector. SBC resin samples (≈10.4 µl in 10 µl of 50 mM PBS, 150 mM NaCl, pH 7.4) were loaded into the microwell. The microwell contents were subjected to a 200 g load through a polyethene filter tip, and custom cut 19-gauge plunger (Figure 3.2). Samples were then measured by co-adding 64 scans between 3800 cm^{-1} - 800 cm^{-1} at a spectral resolution of 1 cm^{-1}.

ATR-FTIR spectra were collected using OPUS 5.5 software (Bruker, Germany). Single channel spectra were ratioed using PBS buffer background spectra and a built-in atmospheric compensation algorithm (utilized simulated vapour spectra). This ensured all background buffer liquid and vapour was removed from the spectra. The removal of spectral bands of water was confirmed by the absence of the libration + OH bending mode [97] at 2125 cm^{-1}. The generated absorption spectra were then imported to Orange [122] with Quasar addon [123]. A rubber band baseline correction was applied to the ATR-FTIR spectra in the range 1800.0 cm^{-1} – 853.6 cm^{-1} using Orange. For PLS quantification, ATR-FTIR spectra were normalized at the glycosidic bending mode of the agarose base matrix at 1067 cm^{-1}. All subsequent data analysis was performed in MATLAB (MathWorks, USA).

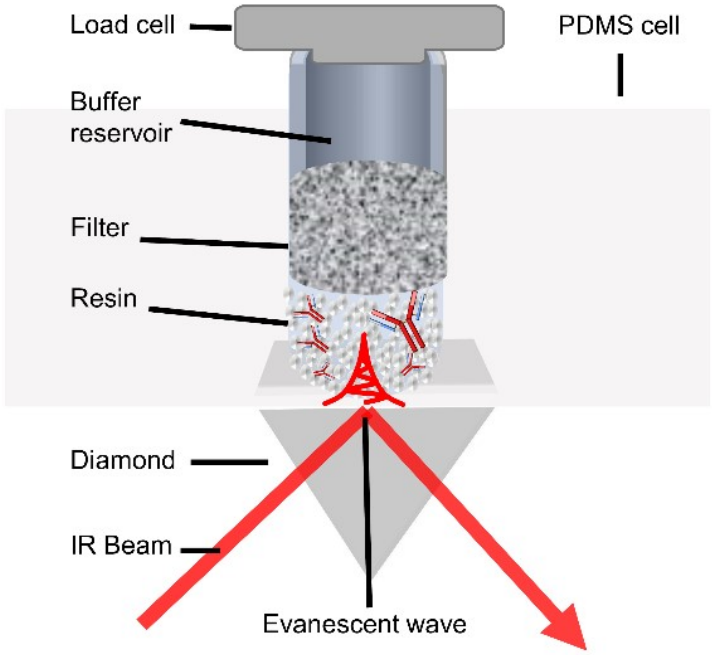

Figure 3.2 Schematic of the in-situ ATR-FTIR spectroscopic setup used for analysis of Protein A resin. The PDMS microwell device was affixed to the ATR accessory by an acrylic top plate. The resin was pressed against the diamond IRE with a controlled load monitored by the load cell. The plunger contained a porous filter and buffer reservoir to ensure small sample volumes did not dry out during measurements. Note that this schematic is not to scale. The evanescent wave is much smaller than the resin in reality

3.2.3 PLS quantification of mAbs bound to Protein A resin

SBC analysis was used to measure the binding capacity of unused MabSelect Sure generating a total of 23 data sets. PLSR of the ATR-FTIR spectral data sets obtained for these unused MabSelect Sure samples using Q as the regression target were utilised to generate a PLS predictive method. The number of PLS components was chosen based on the lowest root-mean-squared error after LOOCV. The model was then applied to the ATR-FTIR spectral data sets of the spent resin (total of 6 spectra for each resin sample) that had been saturated with IgG4 (loaded with 5, 6 and 7 mg ml^{-1}).

3.2.4 Local protein A concentration of Protein A resin

A SPA standard curve was generated using recombinant SPA (Merck, UK) $OD_{280\ nm}$ readings obtained on a Nano drop Lite with $E^{1\%}$=1.65 [124] plotted against ATR-FTIR integrated absorbance of the amide II band (1482-1590 cm^{-1}). A range of SPA concentrations between 0 and 52.95 mg ml^{-1} was used. This standard curve was used to quantify the local SPA concentration of the GSK spent resin samples with no mAbs bound based on the absorbance of the amide II band obtained in each case.

3.3 Results

3.3.1 Static binding capacity optimisation

To ensure accurate adsorption isotherms for mAb binding to Protein A resin according to Equation 3.2, SBC experimental conditions of resin deposition, resin volume, mAb volume and mAb concentration range were optimised. Aliquots of MabSelect SuRe of 50 µl 20% v/v slurry were deposited onto 96 well filters. This volume of slurry equated to depositing 10 µl of resin onto the 96 well plate filter. Each resin sample was loaded with 100 µl mAb across a range of 0.25-5 mg ml^{-1}. The mAb and resin mixture was then allowed to incubate for 30 minutes before collecting flowthrough into a 96 well plate by centrifugation. The collected samples (C_{eq}) were analysed by 280 nm on a Spectramax M2 (Molecular Devices, Germany) well plate reader with E^{1}% of 13.7.

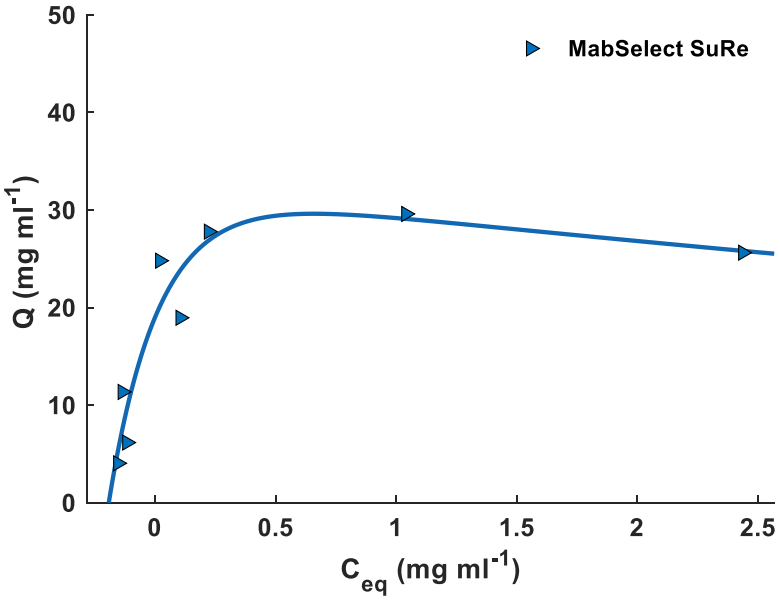

Figure 3.3 Initial adsorption binding isotherm results. Conditions used: C_0 range= 5, 4, 3, 2.5, 2, 1, 0.5, 0.25 mg ml^{-1}, V_{sample} = 100 µl, V_{resin} = 10 µl, incubation time = 30 minutes. The resin samples were dispensed by pipette and C_{eq} was measured at 280 nm on a Spectramax M2 plate reader.

This initial protocol yielded unexpected results. First, Negative values for C_{eq} are observed and are likely due to a sample preparation error as deposition methods were not yet optimised. Second, the Qmax of MabSelect SuRe at 29.53 mg ml^{-1} was below half of both the manufacturer stated value of 65.70 mg ml^{-1} [125] and literature stated value of 59.61 mg ml^{-1} [126] (Figure 3.3). Third, the adsorption isotherm did not exhibit the expected plateau indicating equilibrium of binding was reached [65, 126]. These findings can be explained by the resin not being saturated by the conditions used. Since 10 µl of MabSelect SuRe can hold 0.60-0.67 mg of mAb, the maximum experimental mAb load concentration of only 0.5 mg was

not saturating the incubation time and resin volume were then assessed by loading MabSelect SuRe with 100 µl of mAb at 3 mg ml^{-1}.

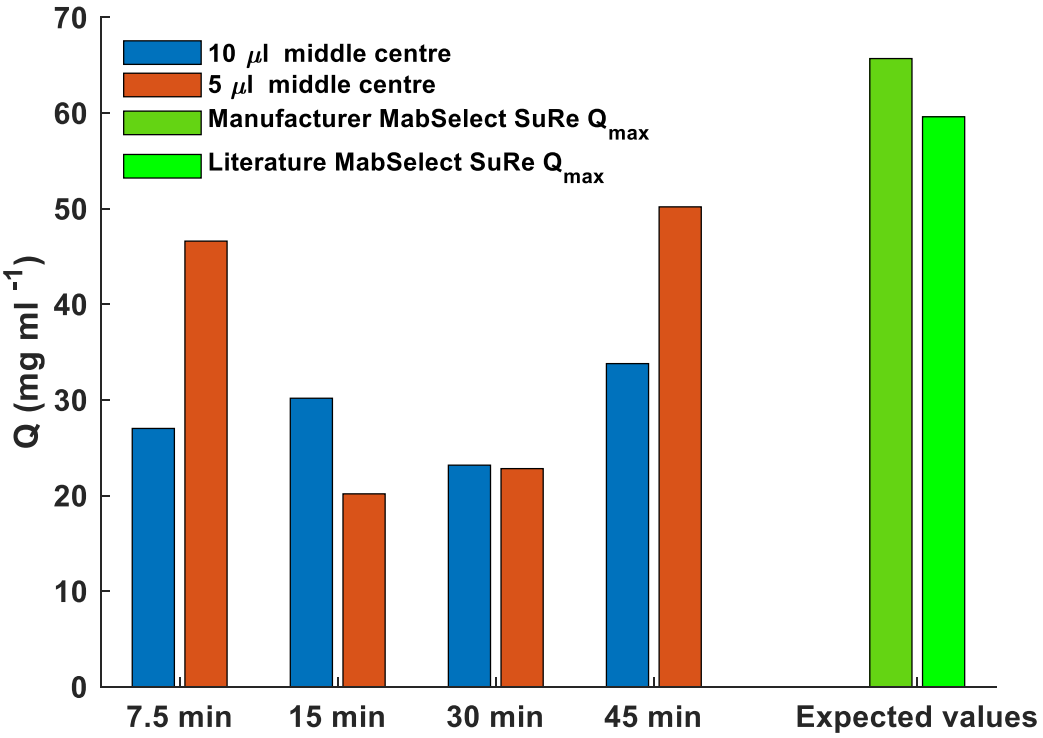

Figure 3.4 Comparison of different binding capacities when incubation time is changed (7.5, 15, 30, 45 minutes) for 10ul and 5 µl of GSK spent resin obtained from the center of the column. Expected values of MabSelect sure from GE Healthcare (dark green) [125] and literature (light green) [126]. C_0=3 mg ml^{-1}, V_{resin}= 5 µl (red) and 10 µl (blue), V_{sample} = 100 µl, dispensed by pipette.

The results indicate that the optimal amount of resin was 5 µl for a 100 µl load of protein at a concentration of 3 mg ml $^{-1}$, as this gave the highest Q value (50.19 mg ml $^{-1}$) after 45 minutes incubation time (Figure 3.4). In contrast, the 10 µl resin sample was underloaded under these conditions (Figure 3.4). The 100 µl of 3 mg ml^{-1} mAb load is equivalent to 0.3 mg protein. According to the literature 5 µl MabSelect SuRe resin can hold 0.30-0.35 mg of mAb. From these results an incubation time of 45 minutes was chosen for all subsequent experiments. This protocol was then applied to unused MabSelect SuRe and used MabSelect SuRe GSK supplied resins (middle inlet and middle outlet).

Table 3.2 Langmuir Isotherm predictions of samples with 45 minute incubation time. C_o=1, 2, 3, 4 and 5 mg ml-1, V_{resin}= 5 µl, V_{sample} =100 µl and dispensed by pipette. N=2.

Sample	Qmax (mg ml^{-1})	Kd (mg ml^{-1})
MabSelect Sure	55.31	0.1
Middle outlet	53.25	0.2
Middle inlet	40.40	0.2

The Langmuir isotherm predictions from resin samples in the column show a significant reduction in maximum binding capacity for resin located at both the inlet middle of the column when compared to the middle outlet of the column with a greater than 10% loss in binding capacity.

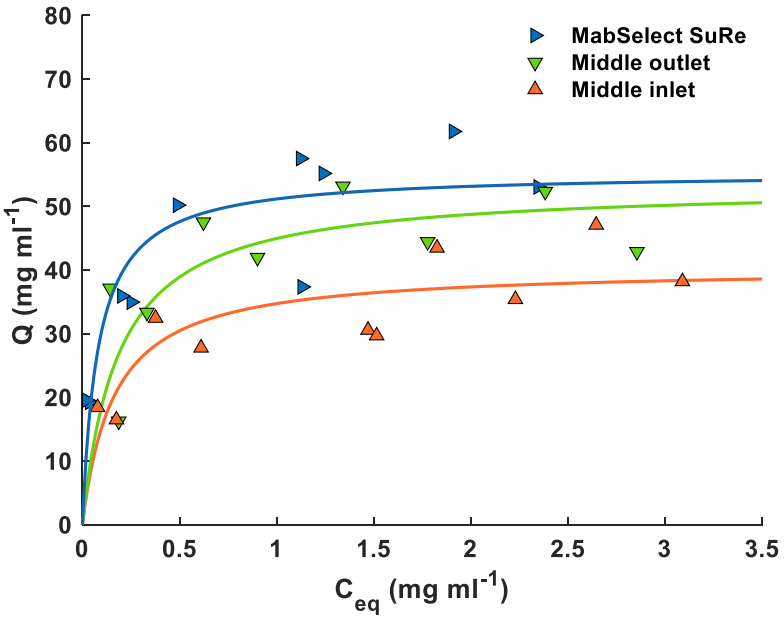

Figure 3.5 Comparison of adsorption isotherms of resin samples obtained from different locations in a pilot-scale column and unused MabSelect SuRe on the Spectramax M2 plate reader. Overall, there is a reduction in Q when compared to unused resin. for N=2.

The data in Figure 3.5 shows that there is a substantial reduction in binding capacity in the middle inlet resin sample compared to the middle outlet of the column and unused MabSelect SuRe. However, the C_{eq} and Q value for each loading concentration is highly variable. It was hypothesised that the amount of resin being dispensed was not consistent, since even very small differences in the volume of resin used for each test condition could introduce marked variability at this scale. A different method to dispense resin was then trialled using a positive displacement pipette.

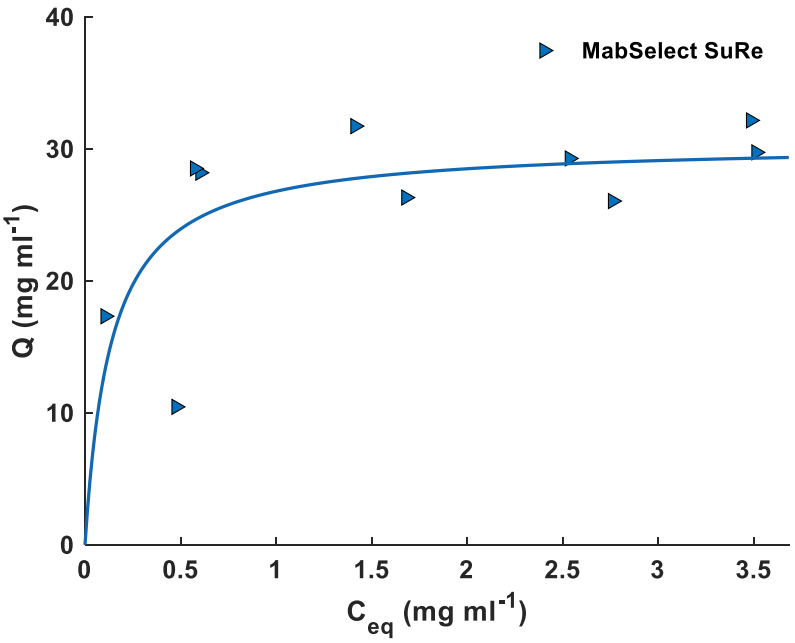

Figure 3.6 Adsorption isotherm obtained for MabSelect SuRe using a positive displacement pipette to dispense sedimented MabSelect Sure. C_0=1, 2, 3, 4 and 5 mg ml^{-1}, V_{resin}= 5 µl, V_{sample} =100 µl, resin and protein incubated for 45 minutes, n=2.

The results from using a positive displacement to deposit sedimented resin in the 96-well plate were more reproducible than the depositing of a suspension by air displacement pipette (Figure 3.6). The average standard deviation for positive displacement was 2.58 mg ml^{-1} compared to 3.56 mg ml^{-1} for pipetting slurry. However, the Q_{max} was around half the values reported in the literature for MabSelect Sure. In addition, there was particularly high variation in the data points generated for lower loading concentrations, for instance 1 mg ml^{-1} loading concentration (C_0) binding capacity of 10.44 and 17.31 mg ml^{-1} were observed . This method of dispensing resin was not reproducible enough for small scale adsorption isotherm assays. A vacuum manifold device (MediaScout® ResiQuot) was sourced from GSK and used for accurate dispensing of 20.8 µl of resin into each well to improve the reproducibility of results. The increased volume of resin required a larger volume and concentration of mAb to be used, since 20.8 µl of MabSelect SuRe could hold 1.24-1.37 mg according to the literature and manufacturers. Thus, 200 µl aliquots of mAb a concentration between 0 and 7 mg ml^{-1} were used, equivalent to a load of a maximum of 1.4 mg of mAb.

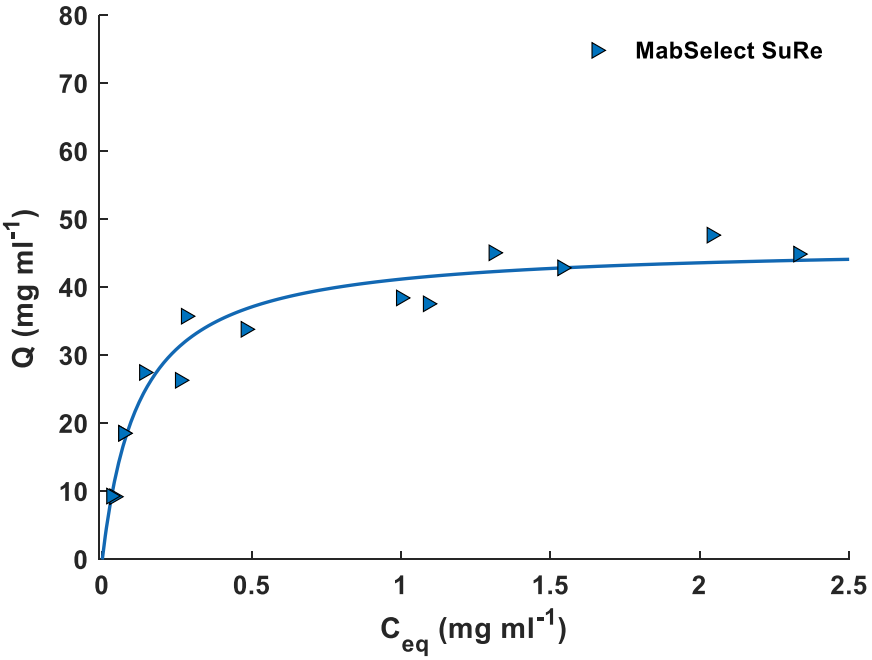

Figure 3.7 Adsorption isotherm results of MabSelect SuRe using a ResiQuot to dispense sedimented MabSelect Sure. C_0= 0, 1 , 2, 3, 4, 5, 6 and 7 mg ml^{-1}, V_{resin}= 20.8 µl, V_{sample} = 200 µl, incubated for 45 minutes, n=2.

Using the ResiQuot and an extended range of loading concentrations for mAb resulted in more reproducible measurements (Figure 3.7). The average standard deviation for MabSelect SuRe at 0.81 mg ml^{-1}, was 4 times lower than obtained for the pipetting slurry and 3 times lower than obtained using positive pipette dispensation. The ResiQuot and loading concertation range of 0-7 mg ml^{-1} were used in subsequent measurements according to section 3.2.2.

3.3.2 Used MabSelect SuRe performance at different spatial locations

With the optimised SBC protocol as described above (section 3.2.2), the performance of the PrAc resins could be assessed. The adsorption isotherm plots generated provide the Qmax and K_d of each resin sample from the column (Figure 3.8).

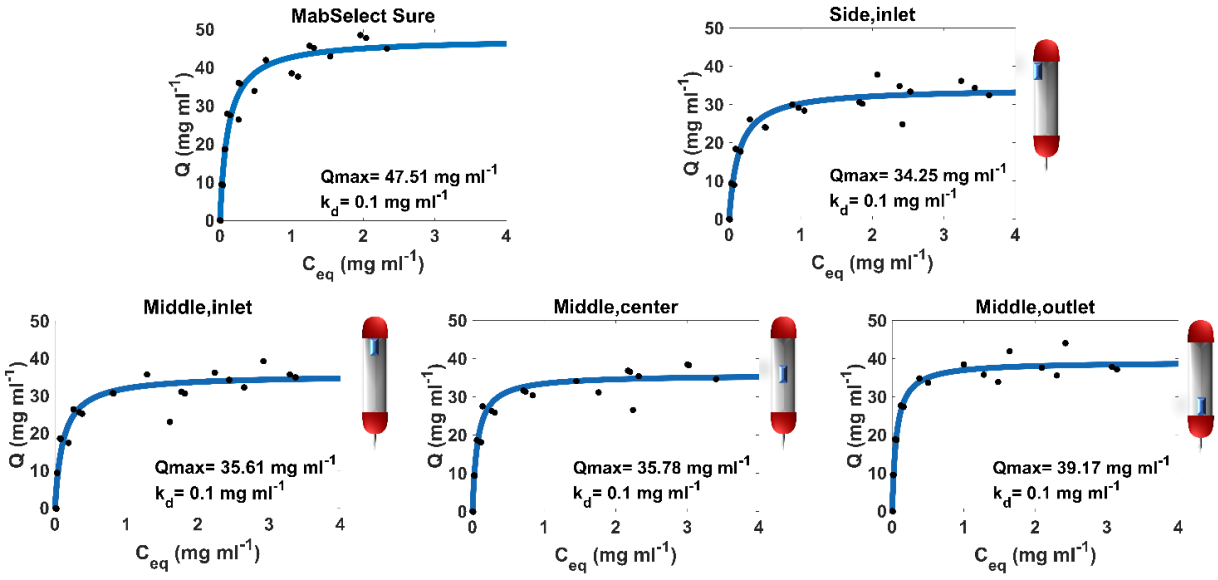

Figure 3.8 Static binding capacity of unused MabSelect Sure and resin samples from different defined locations within a used MabSelect Sure column. Three spent samples were assessed from the middle (inlet, center and outlet) and one spent sample from the side (inlet) of the column. The approximate locations of the resin samples in the original column are indicated by the schematics next to the individual plots. Spent resin has undergone 25 purification cycles. Each OD_{280} nm measurement was carried out in duplicate.

As expected, the unused MabSelect Sure exhibited the highest Qmax value at 47.51 mg ml^{-1} (Figure 3.8). All the used resin samples exhibited a decrease in Qmax compared to the unused resin. The greatest loss in SBC compared to the unused resin is seen in the resin samples at the inlet of the column, where the CCS would be loaded for purification. Resin harvested from the middle outlet of the column retained a higher Qmax of 39.17 mg ml^{-1}. The sample from the center of the column had a slightly higher but overall, very similar Qmax to the inlet sample. On average, the used column exhibited a Qmax decrease from 47.51 mg ml^{-1} to 36.20 mg ml^{-1} compared to unused resin, taking into account measurements from all the different locations of the used column (Figure 3.8,Table 3.3**).**

Table 3.3 Langmuir Isotherm predictions from optimised static binding capacity assays.

Sample	Qmax * (mg ml^{-1})
MabSelect SuRe	47.51 ± 2.07
Middle, inlet	35.61 ± 4.47
Middle, center	35.78 ± 1.48
Middle outlet	39.17 ± 2.60
Side, inlet	34.25 ± 2.37
Overall used column	36.20 ± 2.73

*Qmax values obtained from static capacity binding measurements. C_0=1, 2, 3, 4, 5, 6 and 7 mg ml^{-1}, V_{resin}= 20.8 µl, V_{sample} = 200 µl, incubated for 45 minutes, n=3.

SBC data clearly show that the effects of repeated use on resin differs according to the location of the resin within the column, with resin at the column inlet exhibiting lower binding capacity than that at the outlet. These findings are in agreement with another study on ion exchange columns [66]. Whilst SBC analysis reports on the reduction in the ability of the column to bind antibody it doesn't provide information on the changes within the column that account for this reduction.

The K_d of mAb binding to the SPA ligand was the same (0.1 mg ml^{-1}) for each of the test samples as well as the MabSelect Sure control, indicating that resin use and resin location within the column do not affect binding affinity. This lack of change in binding affinity indicates that despite 25 purification cycles of use the SPA is not structurally altered. To confirm no change in SPA had occurred ATR-FTIR spectroscopy was used.

3.3.3 Optimisation of resin contact with internal reflection element

The absorbance of vibrational modes can vary depending on the contact with the IRE. This is particularly important when measuring convex agarose microspheres up to 150 µm in diameter such as MabSelect SuRe beads[49]. Roughly 10.4 µl MabSelect SuRe was loaded into a micro well device attached to a diamond GoldenGate equipped Tensor 27 with FPA detector. Loads of 100g-400g were applied to the resin sample (Figure 3.9). To select the ideal load to apply, the sugar vibrational mode of the agarose base matrix (1000 cm^{-1} -1200 cm^{-1}) was chosen for integration.

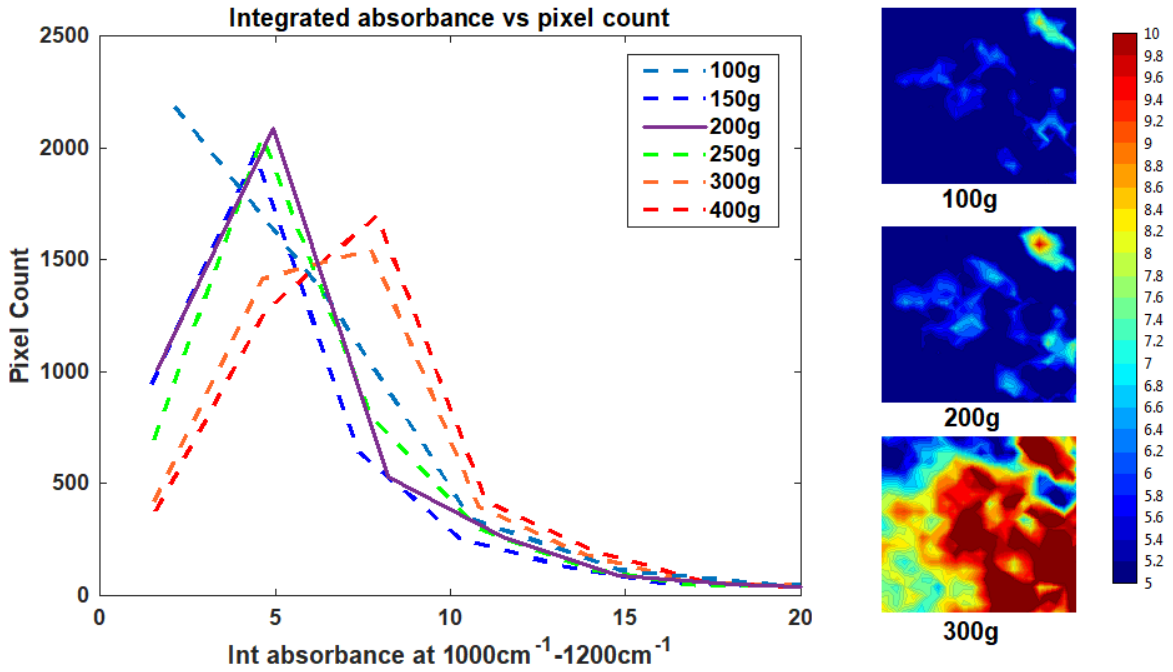

Figure 3.9 ATR-FTIR imaging of MabSelect SuRe under a range of applied loads (100 g,150 g,200 g,150 g, 300 g, 400g). Histogram of pixel count as a function of integrated absorbance of C-O bending, C-O-H stetch and polysaccharide skeletal modes (left). ATR-FTIR spectroscopic images of the resin beads under 100g, 200g or 300g applied load to MabSelect Sure (right).

As can be seen in Figure 3.9, the chemical image shows that the higher the load applied to the resin, the better the contact with the IRE. At higher loads, wide absorbance distributions occur as a result of over-compression of the resin, changing the characteristics of the material. Absorbance distributions can be observed in the histogram in Figure 3.9, which denotes optimal absorbance with a narrow absorbance distribution between 150 g and 250 g. A load of 200 g was chosen as the mass to apply to resin beads for measurements.

3.3.4 ATR-FTIR spectroscopic analysis of the protein A ligand

With ideal load conditions determined for analysis of PrAc resins by ATR-FTIR spectroscopy, the SPA ligand of the different resin samples could be explored.

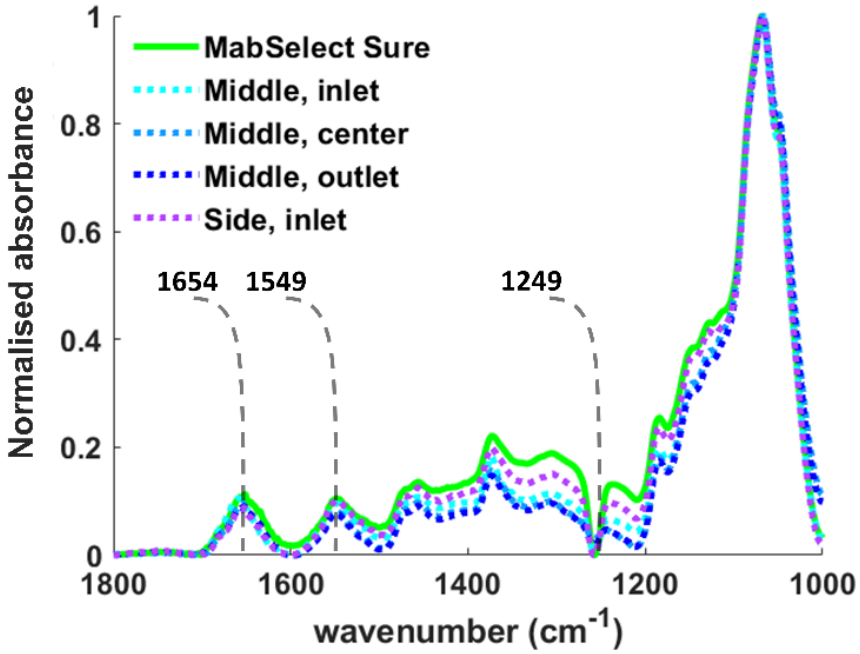

Figure 3.10 ATR-FTIR spectra of unused MabSelect SuRe and used MabSelect SuRe from different column locations. Spectra in the range between 1800 cm^{-1} - 1000 cm^{-1} comparing samples with labelled amide I, II & III bands at 1654 cm^{-1}, 1549 cm^{-1} and 1249 cm^{-1} respectively. There are no significant changes in amide I and II bands of the resin samples measured.

ATR-FTIR spectroscopy of all resin samples show the amide I band at 1654 cm^{-1} (Figure 3.10), indicative of a primarily alpha helical protein [92], in agreement with the known crystal structure of SPA [127]. ATR-FTIR spectroscopy agreed with previous finding in section 3.3.2 that ligand had not changed.

Previous research from Boulet-Audet et al [49] and Pathak et al [128, 129] has indicated loss of SPA ligand as a reason for reduction in SBC. Thus, using in situ ATR-FTIR spectroscopy local SPA concentration was quantified on each resin sample by generating a calibration curve. The amide II band was chosen for quantification as it does not overlap with the water bending mode band at ≈1640 cm^{-1}, unlike the amide I band at ≈1654 cm^{-1}. As described in section 3.2.4 absorbance was plotted against concentration (Figure 3.11).

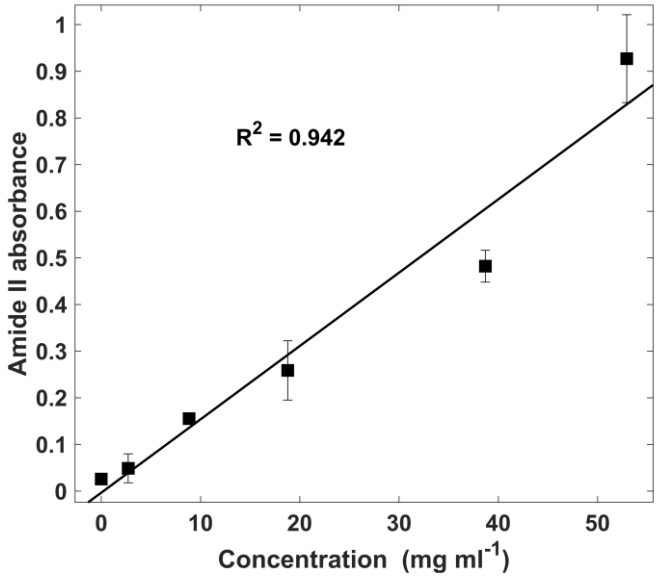

Figure 3.11 Protein A calibration curve. Amide II absorbance integrated between 1590 - 1482 cm^{-1} was plotted against known protein A concentrations calculated using the Beer-Lambert law (OD= 280 nm, E1%=1.65). The data shown is an average of n=2 independent ATR-FTIR spectroscopy experiments and error bars representing standard deviation.

Linear regression was used to predict the concentration of SPA ligand on each PrAc resin sample (Table 3.4).

Table 3.4 Quantified adsorbed mAb and local Protein A ligand concentrations on each resin sample

Sample	Qmax * (mg ml^{-1})	Local Protein A concentration **(mg ml^{-1})
MabSelect SuRe	47.51 ±2.07	31.30 ±9.9
Middle, inlet	35.61 ±4.47	32.73 ±12.1
Middle, center	35.78 ±1.48	27.63 ±0.6
Middle outlet	39.17 ±2.6	20.37 ±7.4
Side, inlet	34.25 ±2.37	29.04 ±1.7
Overall column	36.20 ±2.73	29.77 ±5.45

*Qmax values obtained from static capacity binding measurements. **Local protein A concentration values obtained from ATR-FTIR spectroscopy measurements of resin samples. Amide II band was integrated.

The local SPA concentration obtained for MabSelect SuRe of 31.30 mg ml^{-1} is higher than the resin average of 5.6 mg ml^{-1} stated by manufacturers [130]. This high local concentration compared to the resin average is likely caused by the shallow probing depth [131, 132] of the evanescent wave (effective thickness, <4 µm at 1600 cm^{-1}) utilized in ATR-FTIR spectroscopy

[49]. In this case, the local SPA concentration is calculated from ATR-FTIR spectra representative of the layer of SPA molecules adjacent to the IRE, and thus the local concentration is not the total amount of SPA present in the sample, as previously described [49]. However, it is the density of SPA in surface layer of PrAc resin in this work from the different spatial regions of a pilot-scale industrial PrAc column were studied.

The local SPA concentration of the used resin samples did not significantly vary from each other or the unused MabSelect SuRe (Table 3.4), indicating that the loss in binding capacity is not due to SPA leaching. There was no correlation between local SPA concentration and maximum SBC (Qmax) measurements of the different resin samples. This finding, together with the fact that the spectroscopic analysis revealed no detectable changes in secondary structure of the SPA ligand (no shift or alteration in shape of the Amide I, II and III bands, Figure 3.10**)** in the used resin samples compared to control, indicated that SPA ligand loss and denaturation are not causes of the reduction in binding capacity observed for the used resin samples. It is possible that the reduction in SBC is caused by fouling of the resin by either host cell proteins/DNA or the build-up of irreversibly bound mAb [59]. This is supported by another study which indicated that lower binding capacity at the inlet of an ion exchange column, as seen here for a Protein A column, was the result of greater fouling due to the load material contact time being the highest here [66].

3.3.5 PLS analysis of ATR-FTIR spectroscopic measurements of used Protein A resin in order to predict spatial location performance

ATR-FTIR spectroscopy is sensitive to both chemical functional groups and protein secondary structure of measured samples. This sensitivity can be observed when comparing the spectra obtained for MabSelect Sure control resin with resin bound to different concentrations of mAb (9.23 mg ml^{-1} and 44.90 mg ml^{-1}). Peaks between 1200 cm^{-1} and 1500 cm^{-1} are masked by peaks representative of the base agarose matrix (Figure 3.12).

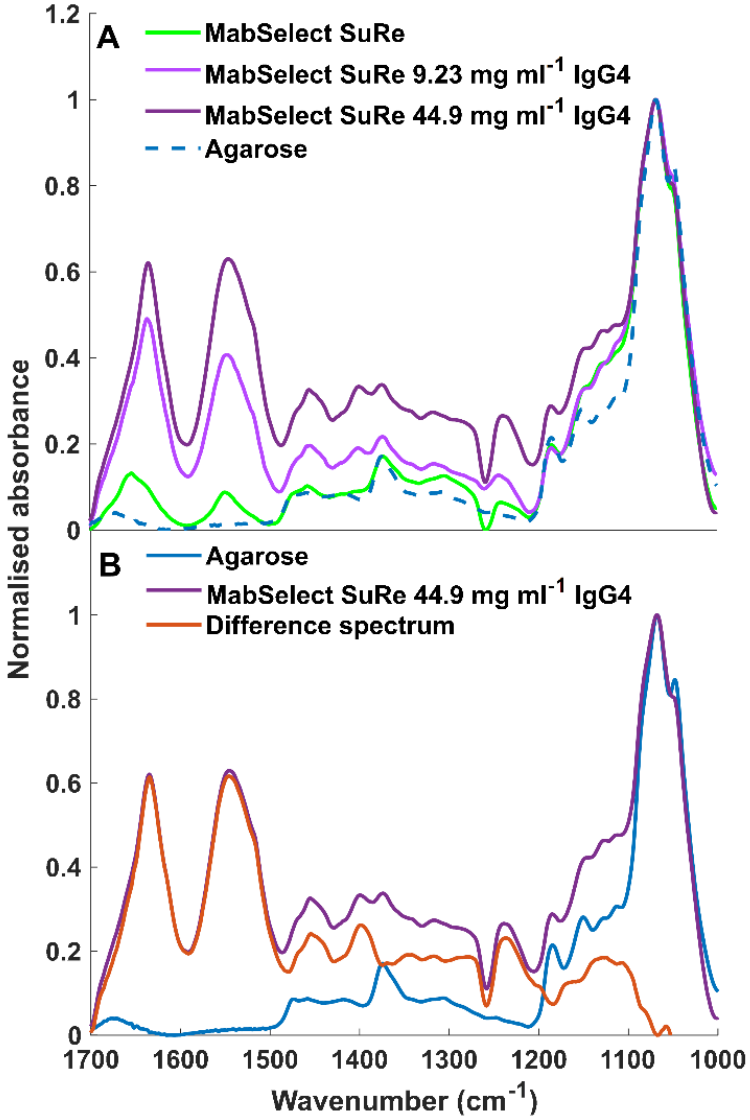

Figure 3.12 ATR-FTIR spectra of resin samples with and without mAb loaded. A) ATR-FTIR spectra of unused MabSelect SuRe in the absence of bound mAbs (green) and mAbs bound at 9.23 mg ml^{-1} (light purple) and 44.90 mg ml^{-1} (dark purple) as well as non-functionalised agarose (dashed blue). B) ATR-FTIR spectra of Agarose and MabSelect Sure with difference spectrum. MabSelect SuRe with 44.90 mg ml^{-1} IgG4 adsorbed (dark purple), non-functionalised agarose (blue), difference spectrum of MabSelect SuRe with 44.9 mg ml^{-1} IgG4 and agarose (orange).

The data reveals protein specific bands for both ligand and mAb by subtraction of the agarose base matrix spectrum allowing for band assignment in this region. As shown in Table 3.5 and Figure 3.12, a wide range of bands present in the measured spectra are representative of the bound mAb and thus can be used for quantification.

Table 3.5 Band assignment of MabSelect SuRe resin with adsorbed mAbs in the fingerprint spectral region 1700 cm-1 - 1000 cm-1.

Wavenumber (cm^{-1})	**Band assignment**
1688 (shoulder)	Amide I β sheets- protein A
1654 (shoulder)	Amide I α helix- protein A [92]
1634 (main peak)	Amide I β sheets- IgG4 [91, 133]
1545 (main peak)	Amide II unordered -IgG4 [92]
1540 (shoulder)	Amide II unordered -IgG4 [92]
1519 (shoulder)	Amide II- IgG4 [133]
1455	CH_3 δ_{as} - IgG4 [91, 133]
1398	CH_3 δ_s – Valine and Alanine- IgG4[93]
1375	Glycosidic linkage - polysaccharide[134]
1238	Amide III β sheets-IgG4 [91, 133]
1185	Glycosidic linkage – polysaccharide [134]
1150	Glycosidic linkage – polysaccharide [134]
1067	Glycosidic linkage *v* – polysaccharide [134]

v is stretching, δ is bending

Partial least squared (PLS) analysis allows utilization of all bands that the algorithm detects as being related to the Y value, in this case the capacity, Q (Equation 2) of mAbs bound to the resin sample. This data contains arrays of thousands of observations representing the absorbance at different wavenumber (1800.0 cm^{-1} – 853.6 cm^{-1}) for each resin sample with known concentrations of mAb bound. The data is broken down into components with each component representing a % of variance in the y value. The training data set utilized here was the in-situ ATR-FTIR spectra of unused MabSelect Sure Resin samples obtained from the OD_{280} nm SBC experiments (Figure 3.8). In total 24 spectra were used, with 1 spectrum excluded due to poor IRE contact (Appendix Figure 8.1). The test data consisted of spectra obtained from ATR-FTIR spectroscopic measurements of 36 spent resin samples saturated with mAbs, with 5 spectra excluded due to poor IRE contact (Appendix Figure 8.1). LOOCV was used to test the model. The optimum number of PLS components used was chosen based on the lowest root mean squared error (RMSE) of the cross-validation set (Figure 3.13).

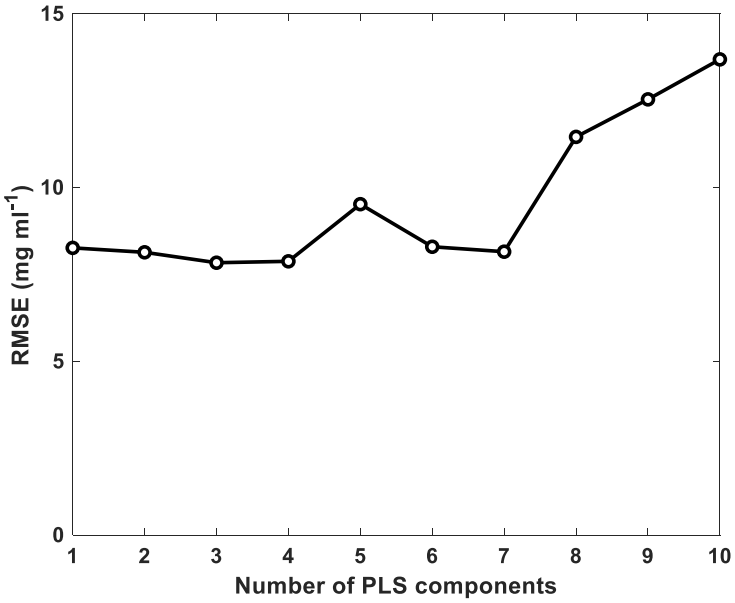

Figure 3.13 Root mean squared error of the PLS model with an increasing number of PLS components. RMSE was calculated by plotting fitted vs observed model for each component using LOOCV (Leave one out cross validation). A total of three PLS components was shown to be optimal for this model.

With each added component the RMSE decreases until the 4th component when a slight increase in RMSE occurs. Increasing RMSE is an indication of overfitting and thus a 3-component model was chosen. When applying the model to the prediction of used resin the RMSE was 6.14 mg ml^{-1} (Table 3.6).

Table 3.6 Statistical analysis of the PLS model with 3 components. Observed vs fitted concentrations of mAbs bound to PrAc resin samples (Appendix Figure 8.2) were used to assess the PLS model. Observed data is the Q value calculated from SBC assays and fitted is the prediction from the PLS model.

Data set	Statistic	Value
Training	R^2	0.84
	RMSE	6.08 mg ml^{-1}
LOOCV	Q^2	0.75
	RMSE	7.84 mg ml^{-1}
Test	Q^2	0.12
	RMSE	6.14 mg ml^{-1}

Utilising 3 components explained 84.09 % of Y variance in the training data. The loading plot spectra generated by the training data set of unused MabSelect SuRe (Figure 3.14) shows the weighting of spectral peaks for each component used to quantify the amount of absorbed mAb.

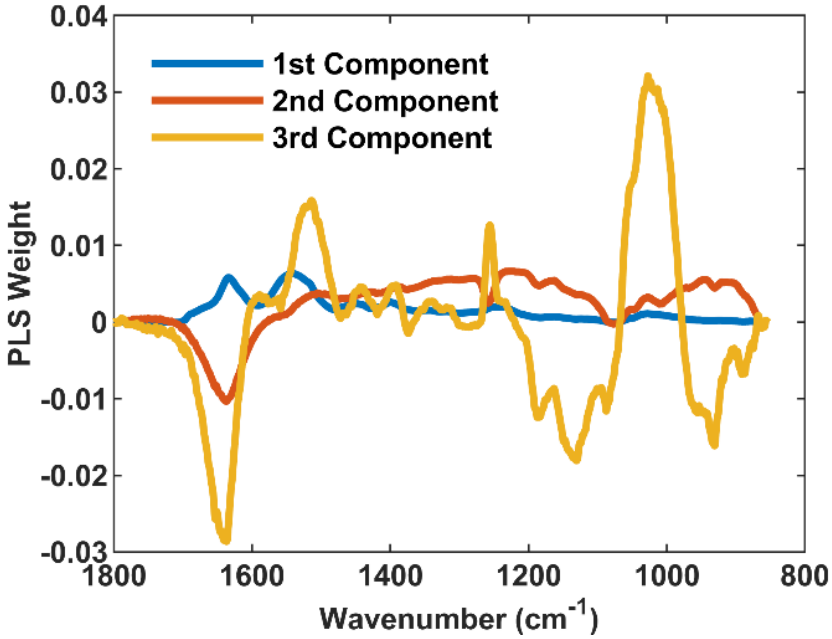

Figure 3.14 PLSR loading plot. The loading plot indicates the spectral bands representative of each component used with the 1st, 2nd and 3rd components shown in blue, red and yellow respectively. The 1st component is representative of most variance in the training spectra, followed by the 2nd and 3rd respectively. A strong PLS weight means a band represents more of the PLS component. Amide I and II bands vary most with varying mAb concentration.

Component 1 was predominantly made up of the amide I and II bands at 1634 cm^{-1} and 1540 cm^{-1} respectively, with these peaks accounting for 72.77% variance in mAb concentration (Figure 3.14). Adding a 2nd component predominantly made up of the amide II band shoulder at 1519 cm^{-1} and amide III band at 1234 cm^{-1} accounted for a total of 80.87% of the variance in mAb concentration. The third component, representative of the amide II band as well as β sheet CH_3 bending and alanine/Valine bending at 1452 cm^{-1} and 1400 cm^{-1} respectively, contributed just an extra 3.22% of variance. This component also selected two peaks represented by non mAb components: PDMS Si-CH_3 at 1256 cm^{-1} and the C-OH Agarose peak at 1008 cm^{-1}. The model was successfully able to predict binding capacity as detailed in Table 3.7.

Table 3.7 Quantified adsorbed mAb on Protein A resins by SBC and ATR-FTIR spectroscopy.

Sample	Qmax * (mg ml^{-1})	Average binding capacity¬ (mg ml^{-1})	Average binding capacity prediction¬¬ (mg ml^{-1})
MabSelect SuRe	47.51 ±2.07	43.38	N/A
Middle, inlet	35.61 ±4.47	34.41	25.80
Middle, center	35.78 ±1.48	33.78	36.10
Middle outlet	39.17 ±2.6	38.01	32.72
Side, inlet	34.25 ±2.37	32.71	28.28
Overall column	36.20 ±2.73	34.63	30.08

*Qmax values obtained from static capacity binding measurements. ¬Average binding capacity is the average binding capacity (Q) of resin when saturated with antibodies by loading with C0 of 5,6 and 7 mg ml-1 IgG4. ¬¬Average binding capacity prediction is the predicted binding capacity of saturated samples obtained from partial least squares regression analysis.

The average binding capacity of saturated spent PrAc resins obtained from the PLS analysis shows the same trend in Qmax values with the resin obtained from the inlet of the used column having the lowest capacity and the resin obtained from the outlet retaining the highest capacity.

3.4 Discussion

Using a combination of in situ ATR-FTIR spectroscopy and SBC assays, the reduction in PrAc SBC is shown to be heterogeneous throughout a used pilot scale chromatography column with the greatest loss of binding capacity occurring at the column inlet. To compare the ATR-FTIR spectroscopy PLS model against the traditional approach for measuring SBC, the coefficient of variation (%CV) of the RMSE of the ATR-FTIR PLS model was calculated as 18%.

$$\%CV(RMSE) = \frac{RMSE}{\bar{y}} X100 \quad 3.3$$

%CV is the coefficient of variation, $\bar{y}$ =the average actual measurement and RMSE=Root mean square error

This was then compared to the %CV calculated for the SBC assay for the overall column average binding capacity; 11%.

$$\%CV(SD) = \frac{SD}{\bar{y}} X100 \quad 3.4$$

%CV = the coefficient of variation, $\bar{y}$ =the average actual measurement and SD=standard deviation

The PLS model produces a good predication of the binding capacity of Protein A resin, meeting industry standards (<20%) compared to the SBC assay and providing additional molecular information such as the secondary structure of the Protein A ligands (Table 3.5)compared to the SBC assay. This could allow further use of the PrAc resin at a column's outlet helping to reduce the cost of mAb purification. Currently, column performance is assessed by overall column binding capacity and not by a detailed analysis of different regions of a column.

PLS regression analysis of ATR-FTIR spectroscopic data allowed for the use of multiple spectral bands representing mAbs bound to used PrAc resins, ensuring an accurate prediction of the binding capacity. As expected, the PLS component explaining the most variance in mAb concentration was made up of the Amide I and Amide II bands, as these are the most informative bands for determining secondary structure from the absorption spectra of proteins.

This data clearly demonstrates that in situ ATR-FTIR spectroscopy can be used to accurately assess the overall performance of a used column. With PLS regression analysis, the model predicted the overall binding capacity of the used column, when saturated with mAbs, to be

30.08 mg ml^{-1}. This prediction is just 4.55 mg ml^{-1} below the SBC calculated binding capacity of 34.63 mg ml^{-1}. Intriguingly, the side inlet exhibited the greatest reduction in binding capacity both from the SBC measurements and the ATR-FTIR spectroscopic analysis, with a slightly lower Qmax than the middle inlet. The resin at the side of the column is subjected to a phenomenon known as the wall effect, which results in resin being less packed at this location, forming a preferential route of flow in the column. A potential consequence of this is that resin at the side of the column is exposed to more contaminants/larger build-up of irreversibly bound mAb than in the center of the column [135].

This work reveals that loss of SBC is not due to SPA ligand leaching or denaturation. The data rather suggests that the reduction in binding capacity is due to irreversible fouling. The chemical nature of these contaminants remains to be revealed. The contaminants are not directly observable in this study, likely due, in part, to these being under the limit of detection after just 25 cycles of purification. Lintern et al reported significant contaminant builds up as detected by MS/MS after 80 purifications [59]. In addition, another study reported that fouling tends to occur in the center of PrAc resin beads [66]. The penetration depth of the evanescent wave used for ATR-FTIR only probes ~5 um of the beads, which can be up to 120 um in diameter indicating that this technique is unlikely to detect contaminants bound to these resin samples. Since ATR-FTIR spectroscopy is more sensitive to surface layer proteins and less able to probe the interior of the MabSelect Sure beads, further analysis using confocal Raman microscopy, which can probe further into the beads should provide additional insights into the causes of binding capacity loss.

This work demonstrates the power inherent in situ ATR-FTIR spectroscopy, as the molecular information gained from this approach allows quantification of mAb binding, assessment of SPA ligand concentration and SPA ligand conformation. Thus, the use of in situ ATR-FTIR spectroscopy in this research represents a substantial advance over SBC analysis alone, providing an in-depth assessment of why resin samples exhibit reduced binding capacity. Therefore, this approach may have a significant potential in industrial mAb processing settings.

Chapter 4- Causes of industrial protein A column degradation, explored using Raman spectroscopy

This chapter's contents are reproduced and edited from the manuscript detailed below with permission from the American Chemical Society:

https://doi.org/10.1021/acs.analchem.2c03063

Beattie JW, Istrate A, Lu A, Marshall C, Rowland-Jones RC, Farys M, et al. Causes of Industrial Protein A Column Degradation, Explored Using Raman Spectroscopy. Analytical Chemistry. 2022;94(45):15703-10

4.1 Background

As described in section 1.1, mAbs are the fastest growing class of BT's. Approximately 80% of the cost of therapeutic mAbs is attributable to downstream processing [55], essential to ensure the final product meets strict regulatory purity requirements [28, 30]. A key component of that cost is Protein A resin [54, 55]. The high costs are exacerbated by lifetime degradation of protein A resins, discernible as a loss in mAb binding capacity over time [55, 59].

Typically mAbs are produced recombinantly in CHO cells [20], and secreted into the growth media. The resultant cell culture fluid contains high levels of mAb as well as host cell proteins [136], media components, cellular DNA and viruses [28, 30] which can cause highly undesirable immune responses in patients if they are present at even low levels in the final formulation [121]. Effective purification of mAbs from cell culture fluid involves a number of different steps, with the key step exploiting PrAc to remove the vast bulk (98%) of contaminants [29].

The data presented in chapter 3 showed that PrAc resin degrades heterogeneously with the inlet of the column exhibiting a lower binding capacity compared to the outlet of the column. ATR-FTIR spectroscopy was successfully used to demonstrate that although binding capacity had decreased more in the inlet compared to the outlet samples, that SPA ligand density did not change, suggesting the build-up of irreversible contaminants rather than ligand loss as the cause of binding capacity reduction. ATR-FTIR spectroscopy was however limited to only observing proteins in the surface layer of resin beads.

Confocal Raman spectroscopy represents a powerful alternative, as it is able to probe much deeper into samples [113], whilst, like ATR-FTIR spectroscopy, providing detailed chemical information and giving insights into protein secondary structure [68, 69]. Additional features are also detectable in Raman spectra, such as amino acid side chains, and particularly aromatic amino acid side chains [70]. Here, the application of confocal Raman to depth profiling of mAb binding to used and unused MabSelect SuRe is described. Results show that mAbs irreversibly foul MabSelect SuRe reducing the pore size of the beads and thus disrupt pore diffusion, the primary driving force of mAb adsorption. PLS regression in combination with Raman spectroscopy shows that the spatial location of resin within a column influences the extent of reduction in binding capacity. The results show that the binding capacity decreases to a greater extent in inlet resin samples and this is reflected in more marked changes in adsorption profiles compared to outlet and unused resin samples.

4.2 Materials and methods

4.2.1 Static binding performance

IgG4 (cB72.3) was prepared, isolated and concentrated to 10 mg ml^{-1} as described previously [49, 56, 137]. MabSelect SuRe resin (Cytiva, UK) was analysed in this study. Used MabSelect SuRe samples in this chapter are from the middle of an AXIChrom 981 ml column as described in section 3.2.2. The protocol was carried out as described by section 3.2.2 with an extended C_0 range of 1, 2, 3, 4, 5, 6, 7 and 9 mg ml^{-1}. The amount of excess unbound IgG4 which flowed through at each loaded concentration was determined on a nanodrop lite at OD_{280} nm with $E^{1\%}$=13.7. The concentration of unbound mAb in the flow through was used to determine mAb binding capacity (Q) of the resin using the mass transfer Equation [65] (Equation 1.2).

4.2.2 Confocal Raman microscopy

Individual protein A resin samples (~10.4 µl), both used and unused, from the SBC experiments were carefully applied to a glass slide using a polypropylene spreader. The beads were visually inspected at 50 X magnification (Figure 4.1), to ensure the beads were not damaged during this step. The glass slide containing the sample was placed onto the sample stage of a SENTERRA II (Bruker, Germany) Raman spectrometer in reflectance mode.

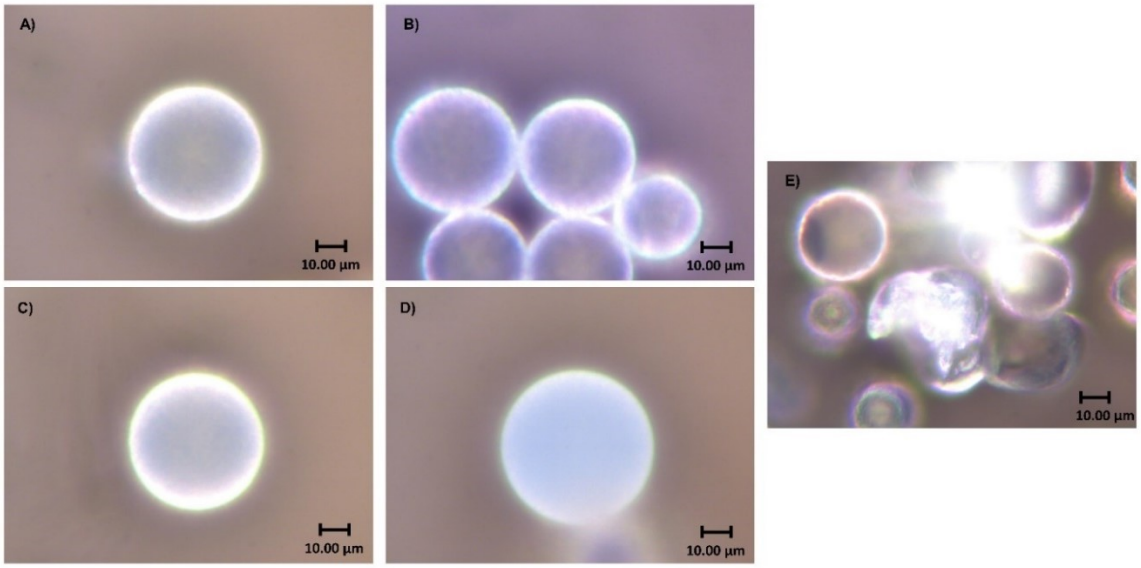

Figure 4.1 Light micrographs of the resin beads following transfer to glass slides for confocal Raman analysis using a polypropylene spreader. The images show the beads are intact after transfer using this approach and illustrate the variation in bead size. The manufacturers state bead size can be up to 120 µm in diameter. In this analysis most beads were found to be between 40 µm and 70 µm. A) MabSelect SuRe bead of 43.7 µm diameter B) MabSelect SuRe beads saturated with mAbs (65.3 mg ml^{-1}). The bead that was analysed was 40.4 µm in diameter. C) Used outlet bead of 46.9 µm diameter. D) Used inlet sample, the analysed bead had a diameter of 44.6 µm. E) Broken MabSelect SuRe beads obtained when transferring without the use of a polypropylene spreader.

Individual protein A beads were measured using a laser at 532 nm with a power 12.5 mW and 50X objective with NA of 0.65. The spectral resolution was 4 cm^{-1}. Samples were measured with 24 co-added scans and an integration time of 3 seconds. A schematic of the experimental setup can be seen in Figure 4.2.

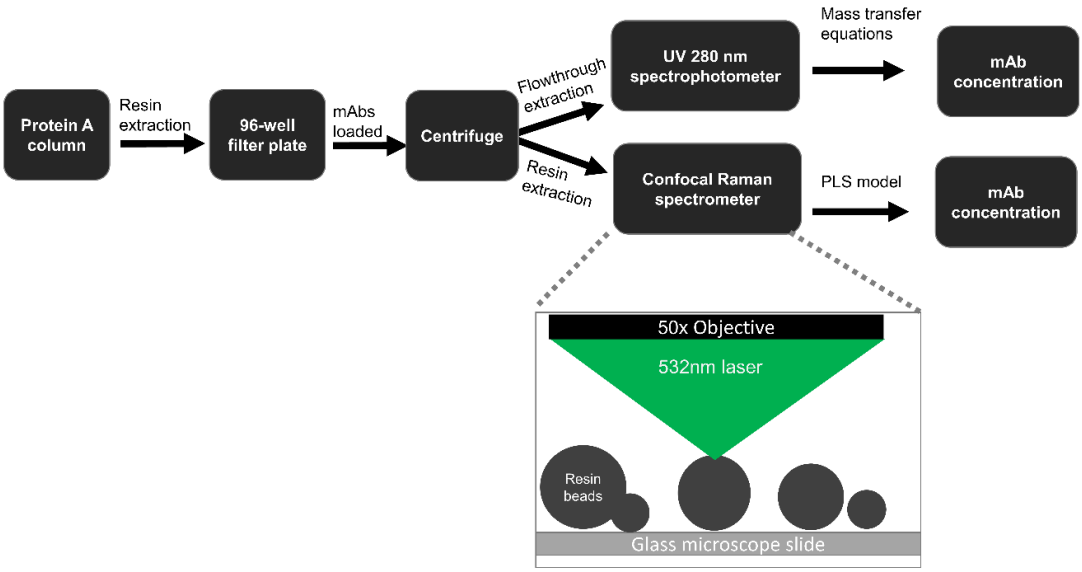

.

Figure 4.2 Schematic of the experimental setup for mAb quantification. Workflow is shown for experiments with measurement setup for Raman spectroscopy measurements shown.

The generated Raman spectra were imported into the software package Orange [122] equipped with the Quasar addon [123]. As an additional control we also carried out a single point measurement on non-functionalised agarose beards (Pierce) to generate a reference spectrum.

For confocal Raman measurements of depth profiling of beads, protein A resin samples with no mAbs added were measured in 10 µm steps along the z-axis. The same experiments were carried out for resin samples with mAbs added (saturated and partially saturated) with the exception that measurements were taken in 5 µm steps along the z-axis. Raman spectra were rubber band baseline corrected between 600 cm^{-1} and 1800 cm^{-1} followed by integration between 600 cm^{-1} and 1800 cm^{-1}. The z spatial location in respect to the bead surface was determined by observing the maximal intensity when plotting integration as a function of stage position (Figure 4.3). The spectra were then vector normalised to compare protein content between measured scattering volumes and different depths of the bead.

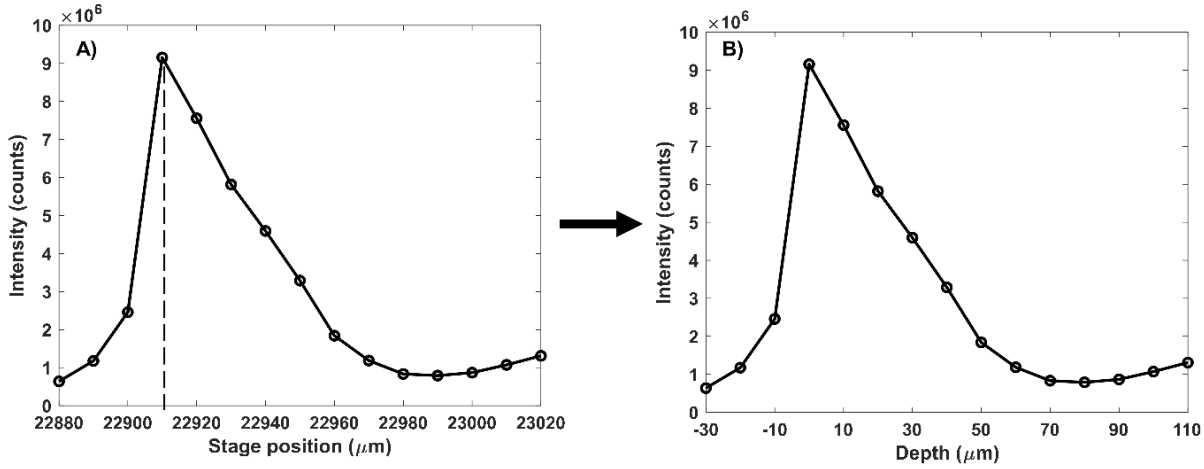

Figure 4.3 Determination of the surface of an individual protein A resin bead using confocal Raman spectroscopy. A) Intensity vs Stage position (distance lens position moved) plot obtained for a used outlet sample bead. The dotted line represents maximum spectral intensity and thus indicates the surface of the sample. B) Intensity vs depth plot for a used outlet resin bead once the stage position has been converted to depth in relation to the surface; 0 µm represents the surface of the resin bead. The resin bead was optically measured to be 53.45 µm in diameter. The Raman spectra were rubber band baseline corrected between 600 cm^{-1} and 1800 cm^{-1} followed by integration between 600 cm^{-1} and 1800 cm^{-1}.

For quantification two individual protein A beads from each of the resin samples generated for SBC analysis were measured. Identification of the spectra with maximal intensity, and thus corresponding to the bead surface layer was determined by two co-added scans and the video-assisted measurement mode in OPUS. Raman spectra were rubber band baseline corrected between 600 cm^{-1} and 1800 cm^{-1} and vector normalised. Spectra was imported into MATLAB (MathWorks, Natick, USA) for PLS regression with the plsregress function which uses the SIMPLS algorithm [138]. Where appropriate 1-way ANOVA was carried out on the spectra.

4.2.3 Generation of in house 75 cycle MabSelect SuRe resin.

As described in section 3.2.1 desalted media was generated [137] . MabSelect SuRe was packed into a tricorn 5/150 column with a final bed volume of 0.343 ml on an AKTA Pure Fast protein liquid chromatography (FPLC) system. Flow rate was set to 0.3 ml min^{-1}. Each purification cycle consisted of equilibrating the column with phosphate buffer (50 mM phosphate/150 mM NaCl, pH 7.4) for 15 CV's followed by loading the column with 15 CV of desalted media. Once loaded the column was washed with phosphate buffer for 10 CV. Bound material was eluted with 0.1 M sodium citrate, pH 3.3 for 15 CV. With each third purification cycle an extra CIP step was performed utilising 0.5 M NaOH for 5 CV. The column underwent a total of 75 cycles of purification and 25 CIP steps before being subjected to LC=Ms/Ms analysis. No changes in the chromatogram were seen during cycling.

4.2.4 Resin preparation for LC-Ms/Ms

The unused MabSelect SuRe, 75 cycle MabSelect SuRe and the GSK used inlet and outlet (100 µl, 50% v/v) resin samples were vortexed at 2500 rpm for 10 minutes. A solution (50 µl) of urea (8 M) and ammonium carbonate (100 mM) was added to the resin slurry followed by addition of dithiothreitol (2 µl, 450 mM) and the sample mixed at 1000 rpm at room temp for one hour. Iodoacetamide (20 µl,100 mM) was then added and the samples incubated for 15 minutes at room temp with mixing at 1000rpm. Trypsin (128 µl, 39.06 µg/L) was added and the resultant slurry mixed at 1000 rpm, 37 °C for 1 hour as described previously [59]. A nano-LC Orbitrap mass spectrometer was used to analyse the samples. The data obtained using a Protein Metrics BYOS® platform. A MS/MS score of 200, MS1 score of 0.95 and FDR of 1% was used to filter out false positives and contaminants. Peptides were identified by searching the UniProt database.

4.3 Results

4.3.1 Quantification of bound mAb by Static binding capacity

The SBC protocol described here allows for both controlled loading of mAbs onto resin samples and assessment of the overall performance of used and unused MabSelect SuRe samples. In this study we evaluated mAb binding to MabSelect SuRe resin samples obtained from the inlet and outlet of a pilot scale column from GSK that had undergone 25 purification cycles and compared these samples with a control of unused MabSelect SuRe resin. The SBC measurements, as described in chapter 3, were repeated in order to generate fresh resin samples for Raman analysis.

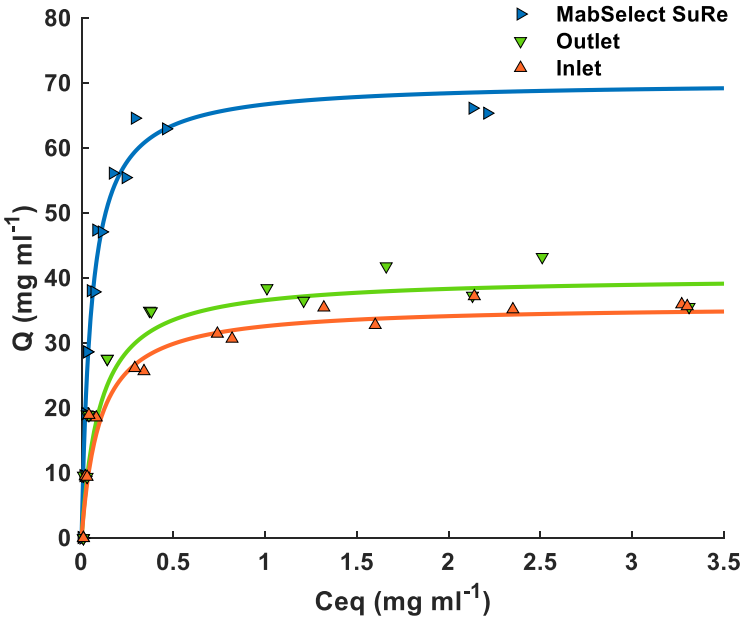

Figure 4.4 Static binding capacity measurements of resin samples fitted to a Langmuir adsorption isotherm. Unused MabSelect SuRe (blue) and used MabSelect SuRe samples obtained from the inlet (orange) and outlet (green) of an AXIChrom 981 ml pilot scale column which had been subject to 25 purification cycles were analysed (See). Each measurement was performed in duplicate.

The unused MabSelect SuRe gave a maximum binding capacity (Qmax) of 70.35 mg ml^{-1}. This value is higher than reported elsewhere in the literature (64 mg ml^{-1}) [48, 65, 126], including in earlier studies [49, 137] and chapter 3. It is not clear why binding capacity is so high in this case, but it might be a function of different batches of resin. In contrast, used samples from the inlet and outlet of a used pilot scale column exhibit markedly reduced maximum binding capacity values of 35.76 mg ml^{-1} and 40.17 mg ml^{-1} respectively (Figure 4.4), consistent with values reported previously [137] (chapter 3). The dissociation constant (Kd) of mAb for the protein A resin samples was 0.1 mg ml^{-1} for all samples.

4.3.2 Confocal Raman spectroscopic quantification of mAbs bound to protein A resin

The individual samples prepared for SBC analysis as described in section 4.3.1 were subsequently used for confocal Raman spectroscopic measurements. The secondary structure of the SPA on both used and unused resin ligands was inspected by confocal Raman spectroscopy (Figure 4.5).

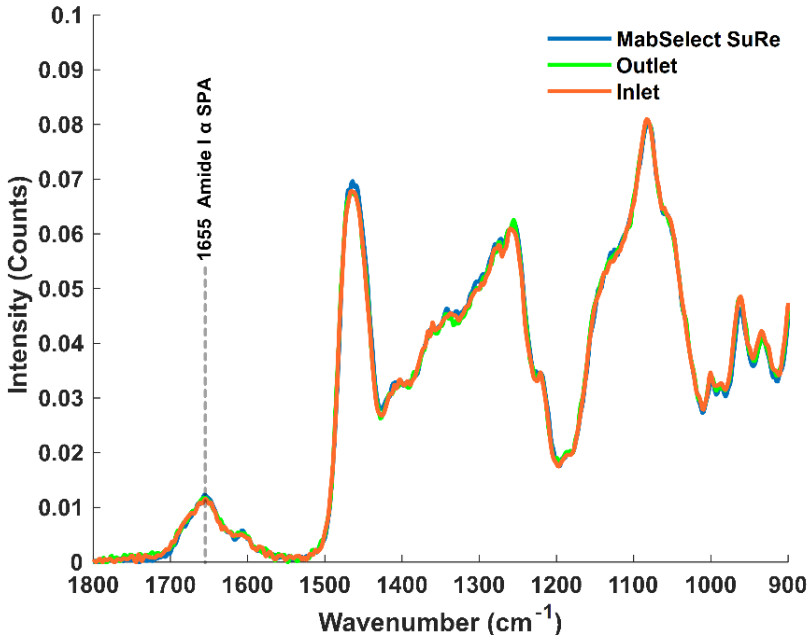

Figure 4.5 Confocal Raman intensity spectra of unused MabSelect SuRe and used MabSelect SuRe from the inlet and outlet of a used 981 ml column. The region 1800 cm^{-1}-900 cm^{-1} of the spectra are shown. There are no significant changes in the amide I bands between samples. Spectra is representative of N=2

SPA specific peaks were the same in both the unused and used resin samples (Figure 4.5). The amide I band at 1655 cm^{-1} in the confocal Raman spectra is indicative of the primarily α-helical structure of SPA. This agrees with earlier ATR-FTIR spectroscopic analysis, which revealed that changes in secondary structure of SPA are not responsible for the drop in SBC observed for the used resin samples [137] (chapter 3) .

In order to accurately perform band assignment of the measured spectra a combination of literature values [69, 115] and spectral comparison was used (Figure 4.6). MabSelect SuRe resin with/without mAbs bound and the non-functionalised Pierce agarose were used to identify and differentiate between protein bands in the measured spectra.

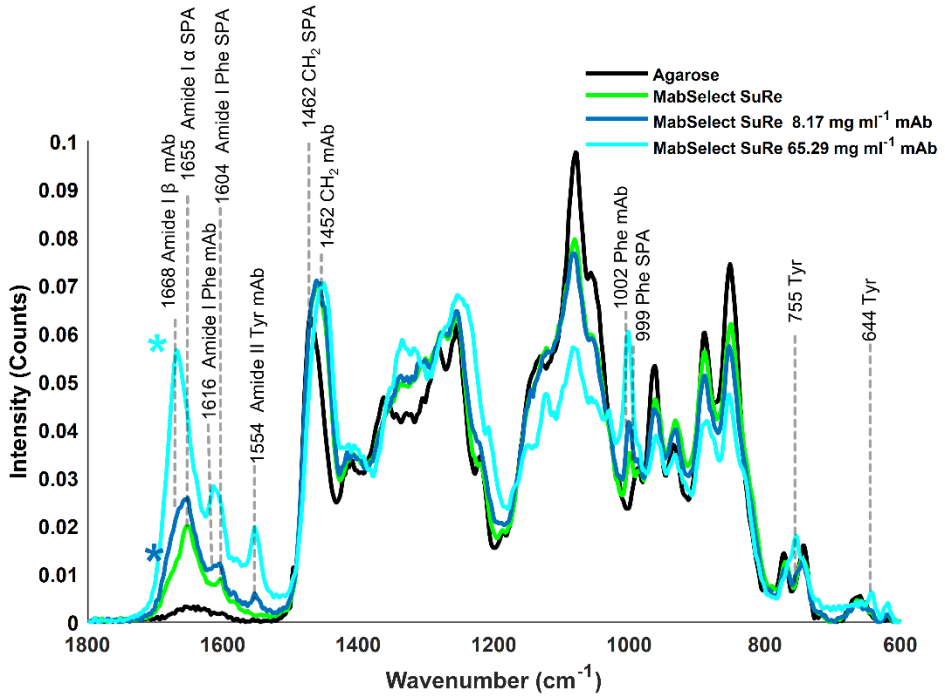

*Figure 4.6 Raman spectra of resin samples. Raman spectra of Pierce nonfunctionalized agarose resin (black), MabSelect SuRe with no mAbs loaded (green), MabSelect SuRe with a non-saturating concentration (8.17 mg ml–1) of mAbs loaded (dark blue), and MabSelect SuRe with a saturating concentration (65.29 mg ml–1) of mAbs loaded (light blue). Assigned spectral bands of protein A and bound mAb are labelled. * = a significant difference in spectral intensity, $p < 0.05$, relative to the control of MabSelect SuRe. Example spectra are representative of n = 2 beads from each individual resin sample.*

SPA has a distinct secondary structure detectable as the amide I band at 1655 cm^{-1} (Figure 4.6, green spectrum), not present in the unfunctionalized agarose (Figure 4.6, black spectrum). The change in conformation of SPA upon mAb binding is detectable in the Raman spectra as a shift in the amide I band from 1655 cm^{-1} to 1668 cm^{-1} (Figure 4.6 light and dark blue spectra). Further structural differences in SPA upon mAb binding, are apparent from the shift in the Phenylalanine (Phe) bands from 999 cm^{-1} and 1604 cm^{-1} to 1002 cm^{-1} and 1616 cm^{-1}, respectively (Figure 4.6, light and dark blue spectra). Tyrosine bands at 1554 cm^{-1}, 755 cm^{-1} and 644 cm^{-1} are also characteristic spectral features of mAb binding to SPA (Figure 4.6, light and dark blue spectra). The Phe and Tyr bands become both more prominent and more defined with increasing mAb concentration (Figure 4.6, dark blue spectrum). There is a significant increase in overall spectral intensity upon addition of both sub-saturating and saturating concentrations of mAb (Figure 4.6, light and dark blue spectra respectively).

PLS regression was used to quantify the bound mAb and to identify those spectral bands that correlate to a change in the binding capacity of resin (Q, the y variable for the PLS analysis). The analysis utilised the confocal Raman secondary structural features, such as the amide I

band, as well as tertiary structural bands representing amino acid side chains, such as Phe, in order to quantify mAbs bound as shown in PLS loading plots (Figure 4.7 A). Raman spectra of unused MabSelect SuRe resin samples with known concentrations of bound mAb were used as the training dataset for PLS regression. LOOCV was applied to test the model's predictive ability through analysis of root mean square error cross validation (RMSECV), R2, Q2 and loading plots (Figure 4.7).

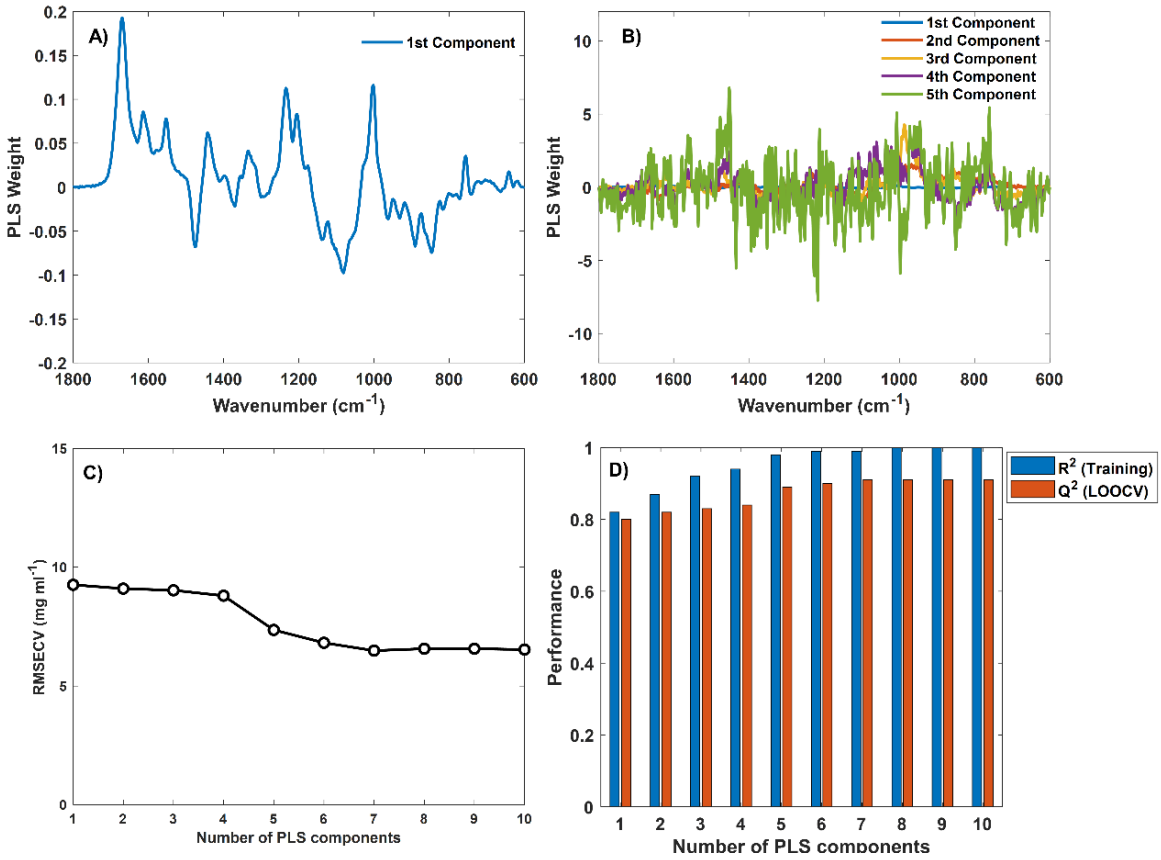

Figure 4.7 Statistical analysis of PLS models A) PLS loading plot of the 1st component. B) PLS loading plot of components 1-5. C) Root mean squared error (RMSE) of the PLS model with increasing number of PLS components. The RMSE cross validation (RMSECV) was calculated by plotting the fitted vs observed model for each component using LOOCV (Leave one out cross validation). D) The R^2 Vs Q^2 plot. R^2 was calculated from the training data set and Q^2 was calculated from LOOCV.

RMSE was shown to be lowest at 7 PLS components, however beyond 5 components the goodness of prediction (Q^2) only marginally increased indicating overfitting of the model (Figure 4.7 C&D). Therefore 5 latent variables were chosen for the model. The first latent variable of the model, which accounted for 82% variance, utilised multiple peaks in the Raman spectrum, most notably both amide I peaks at 1668 cm^{-1} and 1616 cm^{-1}, as well as the Phe band at 1002 cm^{-1}. The next 4 latent variables accounted for ~4 % variance (Figure 4.7) each. Five latent variables resulted in a total variance coverage of 98% (R^2) with a decrease in

coverage after cross validation to 89% (Q^2) (Table.1). To compare with the SBC approach of quantification, the coefficient of variation (%CV) was calculated according to 4.1. The %CV for the model compared to the training data was 9%, %CV increased to 20% once LOOCV was applied (Equation 4.2).

$$\%\boldsymbol{CV}(\boldsymbol{RMSE}) = \frac{\boldsymbol{RMSE}}{\bar{y}} * \mathbf{100} \qquad 4.1$$

%CV =coefficient of variation, $\bar{y}$ =the average actual measurement and RMSE=Root mean square error

The model was applied to the test data set consisting of 64 spectra in total; 32 spectra each for the GSK used inlet and outlet samples. Each of the 32 measurements included 2 individual beads from each SBC condition (8 mAb concentrations for each of n=2 SBC experiments). Test resin samples were loaded with mAbs up to saturation (41.73 mg ml^{-1}). Application of the model to the test data set yielded RMSE and variance values of 7.18 mg ml^{-1} and 0.90 respectively, a performance similar to that of LOOCV (Table 4.1 and appendix Figure 8.3).

Table 4.1 Statistics of the 5 component PLS model. Observed (SBC Q value) vs fitted (PLS prediction) mAb concentrations were used to assess the model.

Data set	Statistic	Value
Training	R^2	0.98
	RMSEC	3.19 mg ml^{-1}
LOOCV	Q^2	0.89
	RMSECV	7.36 mg ml^{-1}
Test	Q^2	0.90
	RMSEP	7.18 mg ml^{-1}

4.3.3 Depth profiling of protein A affinity resin beads

Depth profiling has been used previously to explore mAb adsorption profiles during chromatography polishing steps, normally used after PrAc [115, 116]. Here we depth profiled protein A resin loaded with known concentrations of mAbs. When depth profiling non-uniform sized resin beads it was important to consider that DR decreases as deeper areas of sample are probed as defined by Everall [113] ((4.2) .

$$DR = \Delta\left(\left(\frac{NA^2(n^2-1)}{(1-NA^2)} + n^2\right)^{1/2} - n\right) \qquad (4.2)$$

With confocal Raman, samples appear to have an apparent depth less than the true depth. For example, if a bead of 50 µm in diameter is measured at 40 µm depth with this setup the focal point would be illuminating an extra 11.2 µm and thus beyond the bead into the glass slide below. This meant when fewer points in the z direction could be used, observed in Figure 4.8 B where the MabSelect SuRe and inlet samples cut off.

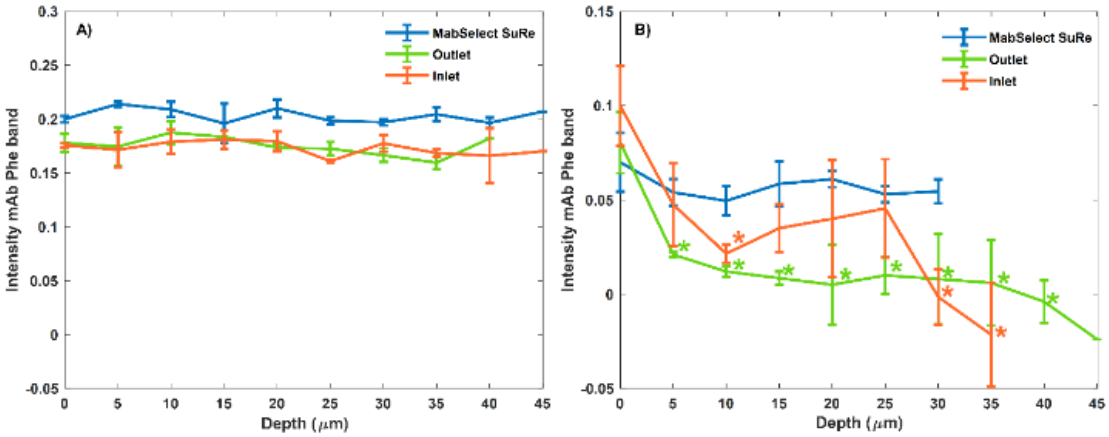

Figure 4.8 Depth profiles of Protein A resins with mAb bound A) Protein A resin depth profiles of adsorbed mAb at saturating concentrations (mean SBC calculated concentration (Q) of resin samples; MabSelect SuRe = 65.68 mg ml^{-1}, Inlet = 37.57 mg ml^{-1}, Outlet =38.80 mg ml^{-1}). B) Protein A resin depth profiles of adsorbed mAb at below saturating concentrations (mean SBC calculated concentration of resin samples: MabSelect SuRe = 19.04 mg ml^{-1}, Inlet = 18.46 mg ml^{-1}, Outlet = 18.85 mg ml^{-1}). The Phe band at 1002 cm^{-1} was integrated (993 cm^{-1} - 1010 cm^{-1}) as a means of observing mAbs bound to the resin samples. Blue = MabSelect SuRe, Green = GSK Used outlet, Orange = GSK used inlet. Data shown is the average of n = 2 measurements ± standard deviation (SD). One way ANOVA was performed on each resin sample. Saturated samples (A) showed no significant difference in intensity at different probed depths. Used resin (inlet/outlet) showed significant differences (=p<0.05) in mAb binding at different probed depths compared to the surface of bead, when mAb was loaded at below saturating concentrations (B). Spectra as a function of depth for the above depth profile of Saturated MabSelect SuRe, partial Saturated MabSelect SuRe, and outlet samples are shown in Appendix Figure 8.4 A–C.*

Depth profiling shows that when unused MabSelect SuRe is loaded with mAbs at or below saturation concentration, binding occurs homogeneously throughout the resin (Figure 4.8 A and B). However, at below saturation concentrations of mAb (~20 mg ml^{-1}), the used resin samples give a heterogeneous adsorption profile, with significantly reduced binding activity occurring in the core of the bead (Figure 4.8 B).

Interestingly, once a saturating concentration of mAb is loaded, a fairly homogeneous depth profile is observed in the used resin samples. One way analysis of variance (ANOVA) showed that for each sample the Phe band intensity did not significantly change at each probed depth for each resin sample (Figure 4.8 A). The Phe band is less intense for both the used inlet and outlet samples at both test concentrations, indicating less mAb binding.

4.3.4 Identification of protein A foulants

Based on previous ATR-FTIR spectroscopic analysis [137], indicating that the drop in binding capacity is not due to either leaching or denaturation of the SPA ligand, and other published reports [59], it can be hypothesized that the reduction in protein A resin binding capacity is due to fouling of the column. However, the precise nature of these foulants was unclear.

Careful analysis of the Raman spectra in the presence of no mAb indicates a slight but noticeable increase in the Phe band for the used resin samples compared to the unused MabSelect SuRe (Figure 4.9 A), indicating the presence of low concentrations of Phe containing proteins within the used resin.

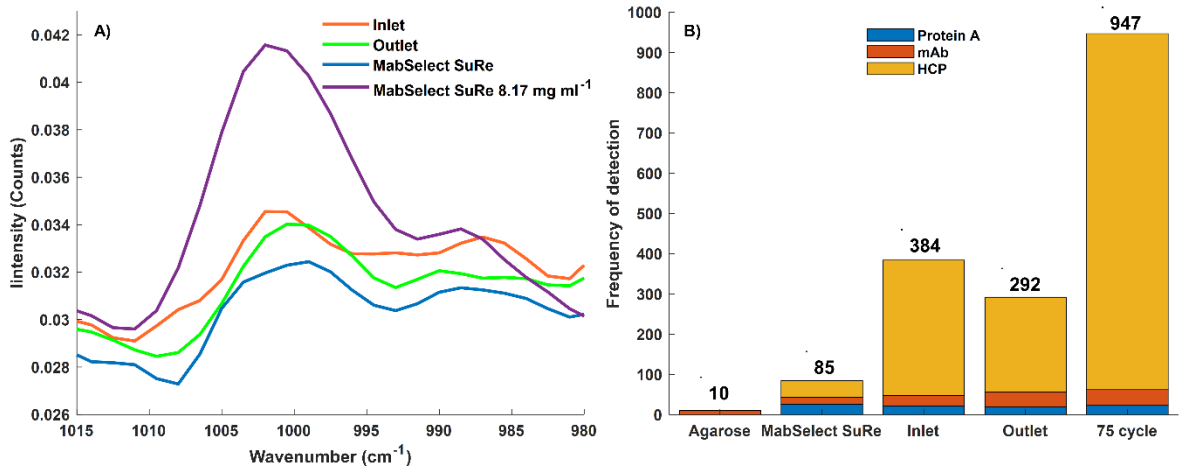

Figure 4.9 Comparison of Raman spectra and LC-MS/MS analysis of Protein A resins with no mAbs loaded A) Confocal Raman spectra obtained from different protein A resin with no mAbs loaded. The Phe band region from spectra obtained from MabSelect SuRe (blue), GSK used outlet (green), GSK used inlet (orange) and MabSelect SuRe with 8.17 mg ml^{-1} mAb bound (purple). The Phe band at 1002 cm^{-1} obtained from the Raman spectra was integrated (993 cm^{-1}- 1010 cm^{-1}) as a means of detecting mAbs bound to resin samples. B) LC-MS/MS analysis showing the frequency of detection of peptides in different protein A resin with no mAbs loaded. Peptides detected for each sample are grouped into categories Protein A (blue), mAb (red), HCP (yellow). HCP in this figure refers to all identified peptides that are not protein A or IgG based. Non-specific mAb peptide fragments are also detected at low frequency in the control samples of agarose and unused MabSelect SuRe and these are likely to be due to contamination during the MS procedure. Spectra as a function of depth for inlet resin beads with no mAbs loaded are shown in Appendix Figure 8.4

Increased Phe band intensity is only detectable at specific depths within the beads. For example, in the case of the inlet resin sample, this increase is only observed at a measurement depth of 30 µm into the beads (up to 38.4 µm considering DR), with a ~55 µm diameter. This depth is close to the surface of the bead where contamination is more likely, since a greater number of adsorption events will occur on and close to the surface, than in the core of the

beads (Figure 4.9B) [115]. A similar result is seen for the outlet resin, where the highest Phe band intensity is observed at 40 μm, on the bead surface.

Comparison of the Phe band peak shape for each used resin sample reveals that the inlet Phe band location at 1002 cm^{-1} matches that of MabSelect Sure + mAbs (Figure 4.9A) indicating the presence of irreversibly bound mAb. The SPA ligand of MabSelect SuRe has a Phe band which resides at 999 cm^{-1}. The less degraded outlet resin has a Phe peak location between that of the SPA and mAb Phe peaks, likely due to a smaller amount of fouling material being present, with both 999 and 1002 cm^{-1} Phe peaks contributing to the resulting peak. Further nano LC-MS/MS analysis confirmed the presence of irreversible bound mAbs as well as a range of other HCPs (Figure 4.9B and appendix Table 8.1) in both used resin samples, with the inlet having 92 more peptide detections than the outlet sample. Peroxidases, known HCPs [139], were present in high peptide frequency.

Generation of a 75-cycle resin sample according to section 4.2.3 showed that following this level of use the amounts of HCPs continue to accumulate but the amount of irreversibly bound mAb stayed more or less the same. A total of 947 peptides were detected in 75 cycle used resin with 23 being SPA, 39 being IgG and 885 being HCP. There is a large increase in HCP when compared to inlet and outlet resin samples (25 cycles of purification). mAb and SPA showed one more peptide detection than the GSK inlet and outlet samples indicating SPA and mAb presence remained consistent regardless of cycle number.

4.6 Conclusions

Loss of binding capacity significantly reduces the lifespan of industrial protein A columns [55, 59], contributing significantly to the overall cost of therapeutic antibody production, and thus continues to limit availability of these life-changing and life-saving drugs. Here we explored the possible causes of the loss of SBC of used MabSelect SuRe resins using confocal Raman spectroscopy. The results confirm earlier findings [137], that spatial location of resin within a column determines the degree to which the binding capacity degrades with use. Sample from a column inlet exhibits lower binding capacity, than that at the outlet, likely due to a larger number of adsorption events occurring at the inlet.

The Raman PLS model was able to predict a wider range of bound mAb concentrations than the PLS model obtained from previous ATR-FTIR spectroscopic analysis [137]. However, the %CV(RMSE) for the Raman model (20%) was higher than the ATR-FTIR spectroscopic model (18%), indicating that the Raman model is slightly less accurate at predicting mAb concentration. Importantly, industry standards (<20%) for predicting binding capacity were met by ATR-FTIR spectroscopic model with the Raman model on the threshold. The Raman model underpredicted test data when actual bound mAb concentrations were below 20 mg ml^{-1} (Appendix Figure 8.3). Raman spectroscopy has an advantage over ATR-FTIR spectroscopy, [137] as it is able to probe past the surface of resin beads to explore causes of column degradation. Thus, as demonstrated by the current study, Raman spectroscopy provides additional information that is not possible to obtain with ATR-FTIR spectroscopy.

Previous studies show pore blockages occurring in protein A resin after use. CLSM, for example, revealed that fluorescently labelled mAbs bound to the resin but were not completely removed by typical CIP procedures [58, 59]. Given that CLSM requires fluorescently labelled mAb and the presence of the fluorophore alters the binding properties of the mAb, it was not clear from these earlier studies whether the pore blockages observed were representative of what would happen in a normal column or were occurring as a result of the modified protein. Here we were able to analyse non-labelled, native protein and confirm that the drop in SBC of the protein A resin is due to build-up of contaminants in the resin pores that both reduces overall binding and limits where mAb binds under non-saturating concentrations of mAb. Pore diffusion is the main transport mechanism by which mAbs bind to protein A resin [140]. Unused MabSelect Sure exhibited the highest binding capacity and a homogeneous binding profile regardless of mAb concentration loaded, indicating that all SPA binding sites are accessible within unused resin beads. In contrast, the used resins exhibit heterogeneous protein binding when loaded with mAbs at concentrations below saturation (Figure 4.8B). It is probable that as the resin has only been used for 25 cycles the level of contaminants makes some of the

locations of the resin beads less accessible but does not block them entirely. Subsequent loading of sub-saturating concentrations of mAb results in the individual mAb molecules preferentially binding to those SPA sites that are most easily accessible. This is supported by a study by Zhang et al [58], which showed that MabSelect SuRe resin beads exhibit decreased pore size and porosity after use. However, once a higher concentration mAb solution is applied, pore diffusion is able to overcome resistance caused by reduced pore size and therefore a homogeneous profile is observed in all resins once saturated with mAb (Figure 4.8 A). This hypothesis is supported by the homogeneous diffusion model observed in polishing steps at saturation by Xiao et al [115] as well a study by Perez-Almondovar [140] showing that large pore size reduces diffusional hinderance.

The Raman spectra, and in particular the presence of the Phe bands, indicated that irreversibly bound Phe containing proteins are the main foulant in used protein A resins. Mass spectrometry analysis confirmed the presence of irreversibly bound mAbs as well as large amounts of peroxidases (categorised as HCP [139]) in the used resins. Peroxidases have been previously shown to interact more strongly with mAbs when compared to other HCPs and to co-elute with mAbs during protein A purification [139]. It was previously suggested that mAb based contaminants act as a nucleation point for further HCP accumulation and this increases with repeated resin use [59].These findings further support this theory with a variety of HCPs being detectable in substantial abundance after just 25 cycles of purification. Further resin use up to 75 cycles shows no further mAb accumulation but a substantial further increase in HCP detection compared to the 25 cycle industrially fouled samples, suggesting that there is a defined process of contaminant build up with initial irreversible mAb binding leading to HCP accumulation.

The combination of Raman spectroscopy and mass spectrometry provides a unique insight into the identity of irreversibly bound contaminants and how the presence of these molecules on the resin does not just affect overall SBC within a column but also binding of the mAb within individual resin beads. With the current set up it is not possible to use a macroscopic optical path that would allow measurement of a large number of beads simultaneously. Whilst it is theoretically possible to perform such an analysis the increased amount of back scatter obtained from the spherical and non-uniform sized beads would introduce a markedly higher amount of background in resultant spectra.

These findings suggest that new CIP procedures need to be designed to allow effective removal of the mAb foulant. Such procedures have the potential to extend the protein A resin lifetime and make mAb production more economical. Furthermore, this study shows that confocal Raman spectroscopy is a very powerful tool for monitoring and managing changes

in resin binding capacity. These findings have the potential to inform new ways of working for large scale therapeutic antibody production.

Chapter 5- Prediction of protein A dynamic binding capacity by confocal Raman spectroscopy

5.1 Background

The application and number of BT's is steadily increasing as discussed in section 1.1. As new BTs are identified, there is a need for both reliable and fast process development to decrease time and cost to produce BT's for patients whilst maintaining strict regulations for product conformity and product quality attributes (PQA's) [141]. BT is used in this work to collectively refer to antibody-based molecules such as Bispecifics, scFvs and mAbs . As each BT and the cell lines used to produce them are unique, the isolation protocol needs to be optimised in each case. In addition, in order to meet legal requirements there is a need to remove a wide range of contaminants from the feed stream containing the expressed and BTs [30]. Changes in PQAs including glycation, formulation, HCP profile and BT titre have the potential to reduce BT efficacy and in the worst cases cause an undesirable immune response in patents [142, 143]. PQA's can be determined by individual methods that require individual BT calibration, for example titre measurements utilise High performance liquid chromatography (HPLC) and requires calibration curves for each BT in order to accurately quantify titre [144] .

Most PQAs are determined with small scale models which have been shown to scale up to industrial scale [141, 145]. The reason for using scalable unit operations for model generation is due to it being impractical to perform at industrial scale due to unit operations such as chromatography being very costly with a protein A resin costing up to $14000 per litre [55]. The individual BT calibration of each method for determining PQAs increases development time and cost exponentially due to the simultaneous development of multiple BTs . Platform based approaches are however preferred as they allow for single calibration towards particular class of BT thus less time required to characterise multiple BTs for clinical trials and markets [145]. During drug discovery phase of developing BT's, lead and hit molecules will be all characterised towards a single disease target simultaneously. The development of bespoke isolation protocols for each lead and hit version of BTs increases cost and time to development that will. The requirement for expensive affinity resins further contributes substantially to the cost of BTs.

The most commonly used step in BT downstream processing is PrAc. PrAc removes the bulk of contaminants from upstream generated clarified unprocessed bulk (CUB) [29]. In order to reduce operational costs for PrAc the DBC analysis is used. DBC determines how much BT binds to a column when a set percentage of product is lost as breakthrough [65]. Breakthrough refers to the analyte (in this case BT) that flows through the column without binding, this solution will also contain contaminants and media components that do not bind to column. In this study the DBC at 10% breakthrough during loading of BT was measured, 10% breakthrough is commonly assessed in literature [60, 61] and industry [52, 62-64] The main

parameters assessed during these assays are the residence time of BT in the column, which is controlled by the flow rate. Due to the fact that BT binding is driven by mass transport phenomena [65], a longer contact time means a higher chance of the BT binding to the SPA ligand. There is however a trade-off between unit operation time and overall BT binding to column. There typically will be a residence time beyond which only minimal gains in DBC will be achieved.

To ensure legal requirements for PQAs are met new technologies and methodologies are being developed to ensure patient safety as complex unit operations are required to generate BTs. Currently DBC is measured by offline by HPLC [63, 146] and in-line by Fast liquid protein chromatography (FPLC) [59, 66], with both utilising 280nm flow cells. Other BT attributes are assessed by size exclusion chromatography [147, 148], HPLC [32, 149] and liquid chromatography mass spectrometry [150]. In order to make the process of monitoring DBC and other BT attributes as effective and efficient as possible and reduce the cost of the BTs, it is important alternative methods are explored. Raman spectroscopy as described by section 1.3 can be used to detect functional groups by the vibrational modes observed in a spectrum [100]. The vibrational modes provide information on the chemical makeup and protein secondary structure of a given sample. Raman spectroscopy has shown promise in its ability to determine and quantify multiple PQAs of a given BT such as formulation pH, formulation stability and glycosylation [117, 151]. Raman spectroscopy has successfully been used in pilot scale bioreactors for both monitoring glycosylation of the expressed protein and glucose concentration of the media [152, 153]. Recently Raman spectroscopy via a fibre optic ball probe was successfully used to quantify the titre of mAb during loading of a protein A column [118].

This chapter describes the development of two new Raman methodologies for use in downstream processing of BTs. The first is a high throughput offline Raman approach to establishing BT titre and DBC on a Protein A affinity column. This approach achieved BT quantification comparable to industry standard methods such as from FPLC (280 nm UV chromatogram) and Protein A HPLC with the added advantage of multivariate data which could be further developed to quantify multiple PQAs simultaneously. The second method utilised a novel inline breakthrough device to determine DBC of PrAc column and BT titre under flow. The inline breakthrough approach served as proof of concept for utilisation of Raman spectroscopy in inline DBC calculations.

5.2 Materials and methods

5.2.1 Determination of offset volume for HiScreen columns

Line clean/pump wash was performed on an ÄKTA ADVANT 25 FPLC system (Cytivia,UK) by flushing the system (lines and sample/buffer pumps) via the built-in pump wash function of the Unicorn 8 software (Cytivia,UK). Filtered MilliQ water was flushed through the system followed by a NaOH (0.5 M) wash with a 15-minute hold time. The system was then flushed with MilliQ water prior to equilibration.

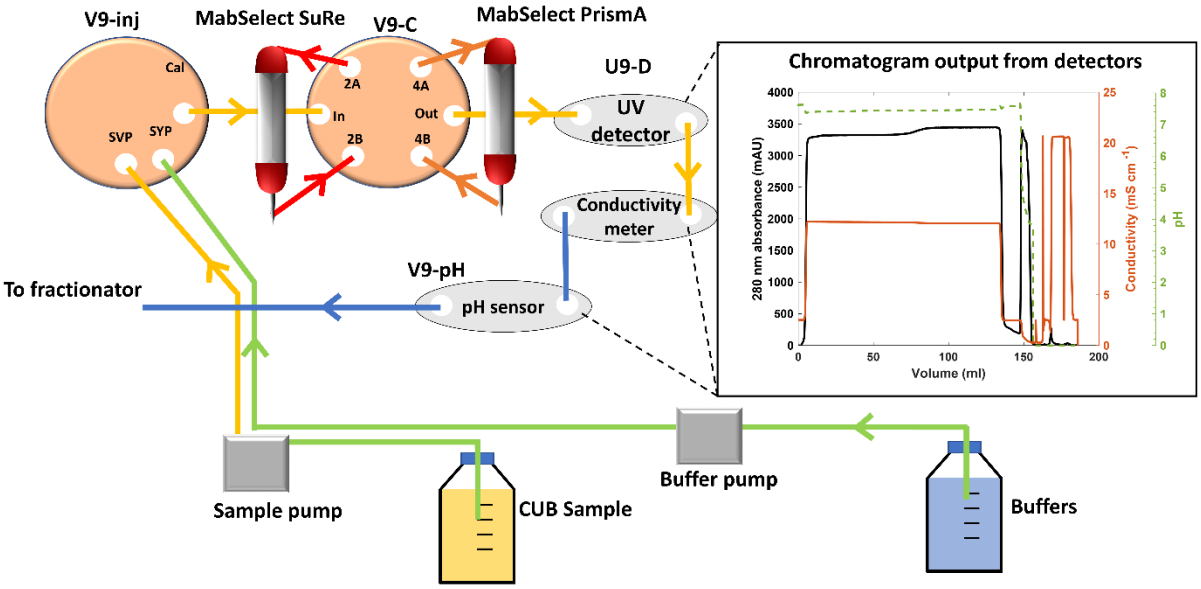

Figure 5.1 Schematic for the ÄKTA ADVANT 25 purification system incorporating HiScreen MabSelect SuRe and HiScreen MabSelect Prism A BT isolation to generate breakthrough curves. The yellow pathway indicates the volume between the sample pump and detector (System hold up volume). The red and dark orange pathways indicate the tubing and void volume of the HiScreen MabSelect SuRe and HiScreen MabSelect Prism A respectively. The void volume is the total volume in the column i.e., between resin beads and within the pores of the resin. The offset volume is the yellow line plus the red/dark orange lines of either column.

HiScreen MabSelect SuRe and HiScreen MabSelect PrismA columns, both with a bed volume of 4.567 ml, were attached to the V9-C valve of the ÄKTA at positions 2 and 4 respectively. Columns were individually washed with MilliQ water followed by 5 CVs of equilibration buffer (55 mM Tris-Base, 45 mM acetic acid, pH 7.5) followed by a 1 ml injection of spike solution (55 mM Tris-Base,45 mM acetic acid,1M NaCl) delivered via the sample pump. The columns were washed with water then loaded with 20% ethanol solution for storage. Chromatograms were exported to Excel using UNICORN 7 (Cytiva) software and processed using MATLAB R2019B (MathWorks). The offset volume between the sample pump and detector for each column (yellow plus the red/orange flow path in Figure 5.1) were calculated from the volume required for the spike solution to reach the ÄKTA conductivity detector.

5.2.2 Biotherapeutic preparation

Unprocessed bulk (UB) solution from pilot scale bioreactors for BT's A, B and C were provided by GSK. Each BT is part of an active medicine development program at GSK and contains an Fc region required for PrAc. Each UB sample was defrosted at room temperature as required then passed through a 0.2 µm bottle top filter (Merck, UK) to remove particulate matter and produce CUB solution. This clarification process was performed in a sterile laminar airflow hood to prevent unwanted microbial growth. CUB samples were aliquoted into a mix of 1 and 5 L containers. The 1 L CUB aliquots were stored at 4 °C for up to 5 days while 5 L CUB aliquots were frozen at -80 °C until further use.

5.2.3 Biotherapeutic isolation to generate breakthrough curves

The ÄKTA was line cleaned between runs as described in section 5.2.1. The HiScreen MabSelect SuRe and HiScreen MabSelect PrismA columns were attached to the valves and tubing as described in section 5.2.1, in order to ensure that the offset delay volume for DBC capacity calculations remained the same through all experiments. Both HiScreen MabSelect columns were equilibrated with 3 CV's of equilibration buffer and then loaded with CUB to at least twice the column DBC stated by the manufacturer (35 mg ml^{-1} for MabSelect SuRe [64] and 65 mg ml^{-1} for MabSelect PrismA [52]). In other words, the column was oversaturated as calculated using Equation 5.1

$$C_S = \frac{V_I * C_0}{V_c} \qquad 6.1$$

Where C_S= oversaturation concentration V_I=injection volume C_0= BT Titre and V_C=Column bed volume

During each protein loading step, 2 ml fractions were collected in a 96 deep well plate maintained at 4 °C. The flow rate was varied between runs, allowing for control of the residence time of BT during each run as shown in Table 5.1.

Table 5.1 Conversion of flow rate to residence time for HiScreen protein A columns used.

Flow rate (ml min^{-1})	Residence time (minutes)
0.466	2
0.776	4
0.931	5
1.164	6
2.328	10

The columns were subsequently washed with 3 CVs of equilibration buffer to remove unbound contaminants and the bound BT eluted with elution buffer (1.8 mM sodium acetate, 28.2 mM acetic acid, pH 3.6). The columns were washed with 3 CVs of MilliQ water followed by 3 CVs CIP buffer (0.1M NaOH) with a 15-minute CIP buffer hold on the column. Once runs were completed the columns were stored in 20% ethanol solution at 4 °C. The volumes for each step described above were expressed as an ÄKTA method file and implemented with scouting runs to change flow rate, V9-C valve position and sample load volume.

5.2.2 Protein A High-pressure liquid chromatography

To calculate the titre of BT in the breakthrough a 1260 infinity II (Agilent) HPLC system fitted with a 20 µm POROS (Thermo Scientific, UK) protein A column was used. A bind elute mode was used. HPLC buffer A (50mM Sodium Phosphate, 0.5 M NaCl, pH 7.0) was used for equilibration and HPLC buffer B (50 mM Sodium Phosphate, 0.5 M NaCl, pH 2.0) was used for elution. A flow rate of 2 ml/min and the column/sample compartments were kept at 5 °C. A detection wavelength of 280 nm was used. The area under the elution peak for each isolated BT was measured and compared to a BT standard curve.

The standard curve was generated by diluting BT standard solutions ~1 mg ml^{-1} (Appendix Table 8.2-Table 8.5). The standard solution concentration for each BT was verified by OD_{280} nm measurements on the Lunatic plate reader (Lunatic, UK) using ε for BT (BT A= 1.440, BT B=1.460 and BT C= 1.515) as shown in Figure 5.7 and Appendix Table 8.2-Table 8.5. The 1 mg ml^{-1} BT standard was placed into the multi-sampler of the 1260 infinity II (Agilent) HPLC system. The POROS column was equilibrated with Mobile phase A then loaded with BT protein standard solution at a range of set volumes (5, 7, 10, 15, 20, 25, 30 µl). Once an individual BT was bound to the column, HPLC buffer B was used to elute the BT from the column. Elution of BT was confirmed by the 280nm detector within the 1260 infinity II HPLC system.

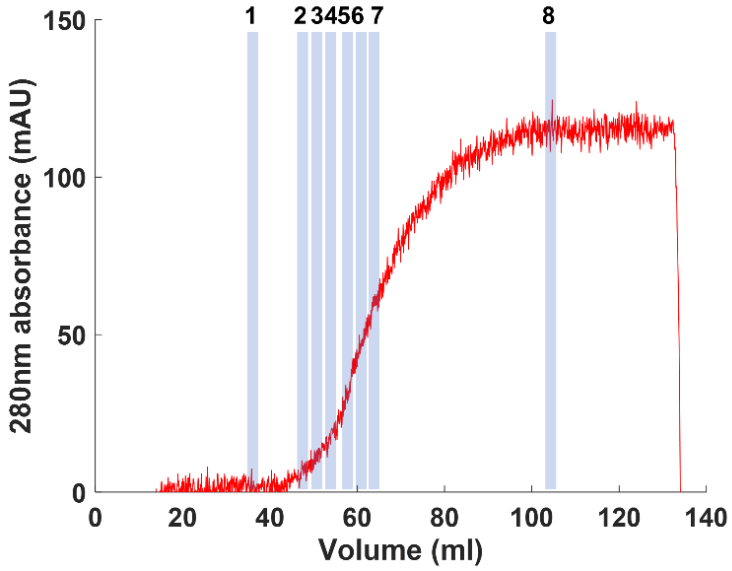

Figure 5.2 Example of DBC sample selection for protein A HPLC analysis. Samples taken from 2 ml fractions collected in 96-deep well plate for Cycle 6 of MabSelect SuRe purification are highlighted in blue with the sample number above. Sample 1 was taken from a 2 ml fraction collected from 36.578 ml prior to any breakthrough occurring. Samples 2, 3, 4, 5 and 7 were collected at 48.578, 52.579, 56.579, 60.580 and 68.580 ml respectively and illustrate various breakthrough amounts. Sample 8 was collected at 104.582 ml and illustrated 100% BT breakthrough.

Breakthrough samples, samples, in aliquots of 100 µl, were collected in a 96 well plate and loaded into the multi-sampler of a 1260 infinity II (Agilent) HPLC system. Eight breakthrough samples were chosen based on the 280 nm readings obtained from the ÄKTA chromatograms. Sample 1 was from before BT breakthrough, samples 2-7 were chosen to cover before and after the 10% breakthrough at 4 ml intervals, sample 8 was chosen as the A_{max} sample, demonstrating 100 % of BT breakthrough. The sample injection volume for each fraction was varied (Table 5.2) to prevent peak area and BT mass on the column exceeding the standard curve values as breakthrough concentrations were much higher (>10x) than standards. Reducing injection volume on HPLC with higher concentration samples allowed for controlled mass loading on the HPLC POROS column.

Table 5.2 Breakthrough fraction injection volume for HPLC.

Fraction	Injection volume (µl)
1	50
2	50
3	30
4	30
5	20
6	20
7	10
8	5

5.2.3 Design of Experiment for Raman instrument parameter optimisation

The Design of Experiment (DOE) feature within the JMP 16 pro software was used to build each experimental design. BT B was used as the model analyte for DOE for both the offline well plate and in-line breakthrough setup. The 785 nm laser was utilised on the Renishaw InVia Raman spectrometer (Renishaw, UK). Resultant spectra were not pre-processed for the DOE experiment responses as the aim was to ensure instrument settings (exposure time , laser power, accumulations) could observe spectral changes when BT titre increases at the expected ranges (0 - 3.60 mg ml^{-1}). Pre-processing would later be used to improve ability of models to Quantify BTs. Spectrometer responses such as Signal to Noise Ratio, Amide I integrated intensity, phenylalanine intensity as well as measurement time were chosen as metrics for DOE performance. The response surface model (RSM) determined specific parameters to be used (offline and inline).

In the offline well plate setup, 200 µl of sample was placed into quartz 96 well plates. Samples were made up of 3.60mg ml^{-1} BT B CUB and 0.26 mg ml^{-1} BT B from breakthrough. were replaced every 4.5 hours of measurements. Laser powers of 500, 250, 50 and 5 mW were tested for the 785 nm laser. Accumulations (range = 2 - 32) and exposure time (range = 2-40 s) parameters were treated as continuous variables by the JMP19 pro software. To check method performance across typical protein concentrations, samples at low (0.26 mg ml^{-1}) and high (3.60 mg ml^{-1}) concentrations were used.

For the breakthrough device, laser power at two discreet values, 250 mW and 500 mW, was used for the in-line setup. Accumulations and exposure time (seconds) were set at a continuous range of 1-10 in JMP pro-16. The lower accumulation and exposure time range were at a reduced range compared to the well plate set up due to the small volume of samples (<1 ml) measured at a flowrate of 0.931 ml min^{-1}. Sample consisted of BT B CUB (3.60 mg ml^{-1}) for inline DOE measurements.

5.2.4 High throughput 96-wellplate Raman microscopy

The InVia confocal Raman system stage was optically focused using a pen mark on the bottom of the transparent quartz 96-well plate. Once the mark was in focus the stage was set 5000 µm from the objective in the z direction. A quartz 96-well plate, containing 200 µl aliquots of individual breakthrough samples as described in Section 5.2.3, was used for Raman microscopy. A plate mapping add-on was used to map the 96-well plate ensuring that all sample wells were analysed. A 10X objective was used with the pinhole in the out position. The 785 nm laser set to 500 mW power, 20 accumulations and an exposure time of 24 seconds was used in combination with the built-in cosmic ray removal setting. Samples were

allowed to be in the well plate for a maximum of 4.5 hours in order to minimise sample evaporation (Figure 5.14). The generated spectra were exported to MATLAB 2019B with PLS toolbox 9 (Eigenvector, USA), for further analysis.

5.2.5 Simulated in-line Raman microscopy of breakthrough curves using custom breakthrough device

A master chip (Figure 5.3 a) was designed in SOLIDWORKS 2020 software (Solidworks, USA) and 3d printed using a Form 3 3d printer (Formlabs, USA). The master chip was used to cast Sylgard a 184 PDMS device by soft lithography. The PDMS channel and the inlet and outlet tubing were 0.5 mm^2 to match ÄKTA tubing dimensions and thus minimise changes in pressure within the device when under flow. A 0.5 mm thick sapphire window was bonded to the channel of the PDMS device. Both the PDMS and sapphire were treated with O_2 plasma in a Harrick plasma cleaner (Harrick, USA) and the two materials pressed together to ensure bonding occurred. The sapphire window was further sealed with a Silicon sealant to prevent and leakage and displacement of the window (Figure 5.3). Sapphire was chosen as a window due to it only having peaks below 700 cm^{-1} and otherwise being transparent where bands from proteins occur on a spectrum.

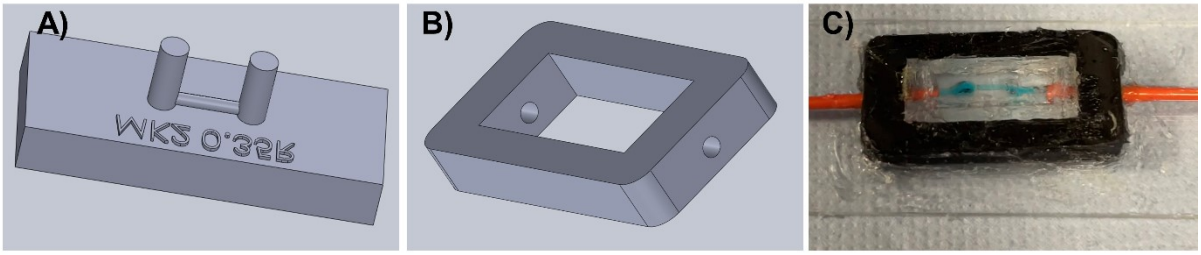

Figure 5.3 Breakthrough device A) Master chip design with 0.5mm^2 surface area channel. B) Breakthrough device external casing. C) Final Breakthrough device sealed with a sapphire window. Blue food colouring was flowed though at 1 ml min^{-1} to visually check for leaks.

A custom breakthrough device with a 0.5 mm^2 channel was placed onto the InVia confocal stage and attached to 0.5 mm^2 ÄKTA PTFE tubing. The inlet was fed through the closed compartment door of the InVia stage compartment. The laser was focused on the breakthrough device channel using a 50X objective and a 1 M urea solution. Breakthrough samples were extracted from the deep well plate (prepared as described in section 5.2.3) and placed into individual syringes. The syringes were then individually attached to the tubing inlet and 100 µl of sample loaded into the inlet tubing using a 11 elite syringe pump (Harvard apparatus, UK) at a flow rate of 0.931 ml min^{-1}. Each sample was then measured under flow through the sapphire window of the breakthrough device at 0.931 ml min^{-1}. The 785 nm laser set to 500 mW power, 1 accumulation and 10 second exposure was used in combination with the built-in cosmic ray removal setting. This process was repeated for each breakthrough

sample. A cleaning step consisting of 400 µl 0.5 M NaOH followed by 400 µl MilliQ water was performed between samples.

5.3 Results

5.3.1 Calculating sample properties for Dynamic binding capacity measurements using industry standard methods.

When calculating the $DBC_{10\%}$ according to Equation 5.2, it was important to know the total delay volume between the sample pump and the detector on the system. The offset volume (V_0) was calculated from the system dead volume and the column void volume (Figure 5.1). This value was used in the $DBC_{10\%}$ calculations (Equation 5.2) for both columns. The offset volumes for both MabSelect SuRe and MabSelect PrismA are shown in in Figure 5.4 a and b/c respectively and were calculated with 0.5 M NaCl equilibration buffer as described in section 5.2.1.

$$DBC_{10\%} = \frac{(V_{10\%} - V_0) * C_0}{V_c} \qquad 5.2$$

Where $DBC_{10\%}$= Dynamic binding capacity at 10% breakthrough $V_{10\%}$= volume at 10% breakthrough V_0=offset volume V_c=column bed volume C_0= BT titre

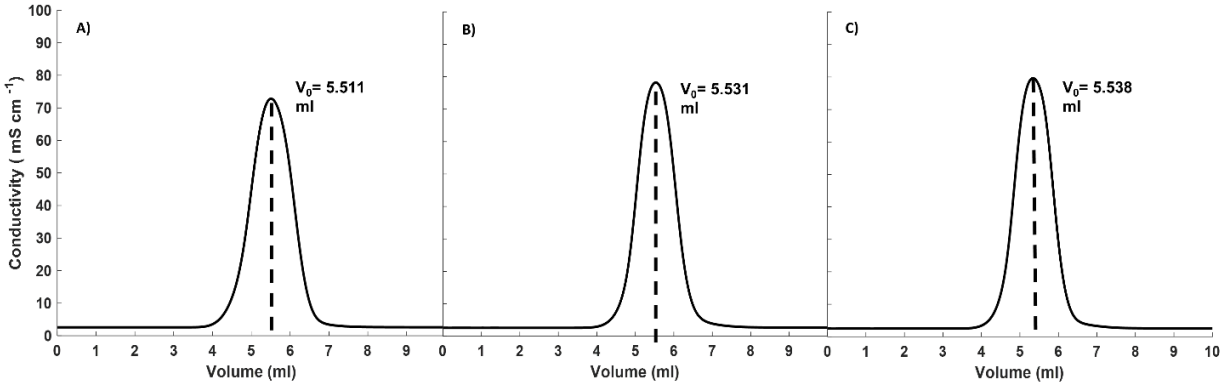

Figure 5.4 Chromatogram of 0.5M NaCl spike test for HiScreen columns A) MabSelect SuRe for 1-29 cycles, B) MabSelect PrismA tubing for cycles 1- 3, C) MabSelect Prism A for cycles 4-29. V_0 is the determined offset volume for the ÄKTA pure 25 system, tubing and column used.

The HiScreen PrismA column experienced a leak in tubing after 3 cycles and thus the tubing to outlet and inlet was changed and a new offset volume for cycles 4-29 was measured as shown in Figure 5.4 C. There was no leaking observed during cycles 1-2 for prism A column. Prism A column cycle 3 conditions (5-minute residence time,0.931 ml min^{-1}) were repeated in cycle 9 (Table 5.3).

A typical Protein A DBC experiment chromatogram for one purification cycle is shown in Figure 5.5 A. To reduce noise in the absorbance, each UV measurement was averaged over 15 (0.077 ml) measurement points, from the detector. During loading (Figure 5.5A; red shading) there are two plateaus in absorbance observed due to 1) flowthrough of HCPs and other

components in the CUB solution which don't bind to the protein A column and 2) breakthrough of BT as the SPA ligand binding sites all become occupied. This second plateau is higher than the first plateau as it contains the breakthrough BT in addition to the HCP and media components. The second peak (peach-shading) is the elution of bound BT using the acidic (pH 3.3) elution buffer and finally the third peak (blue shading) contains bound proteins removed by the CIP step (Figure 5.5 A)

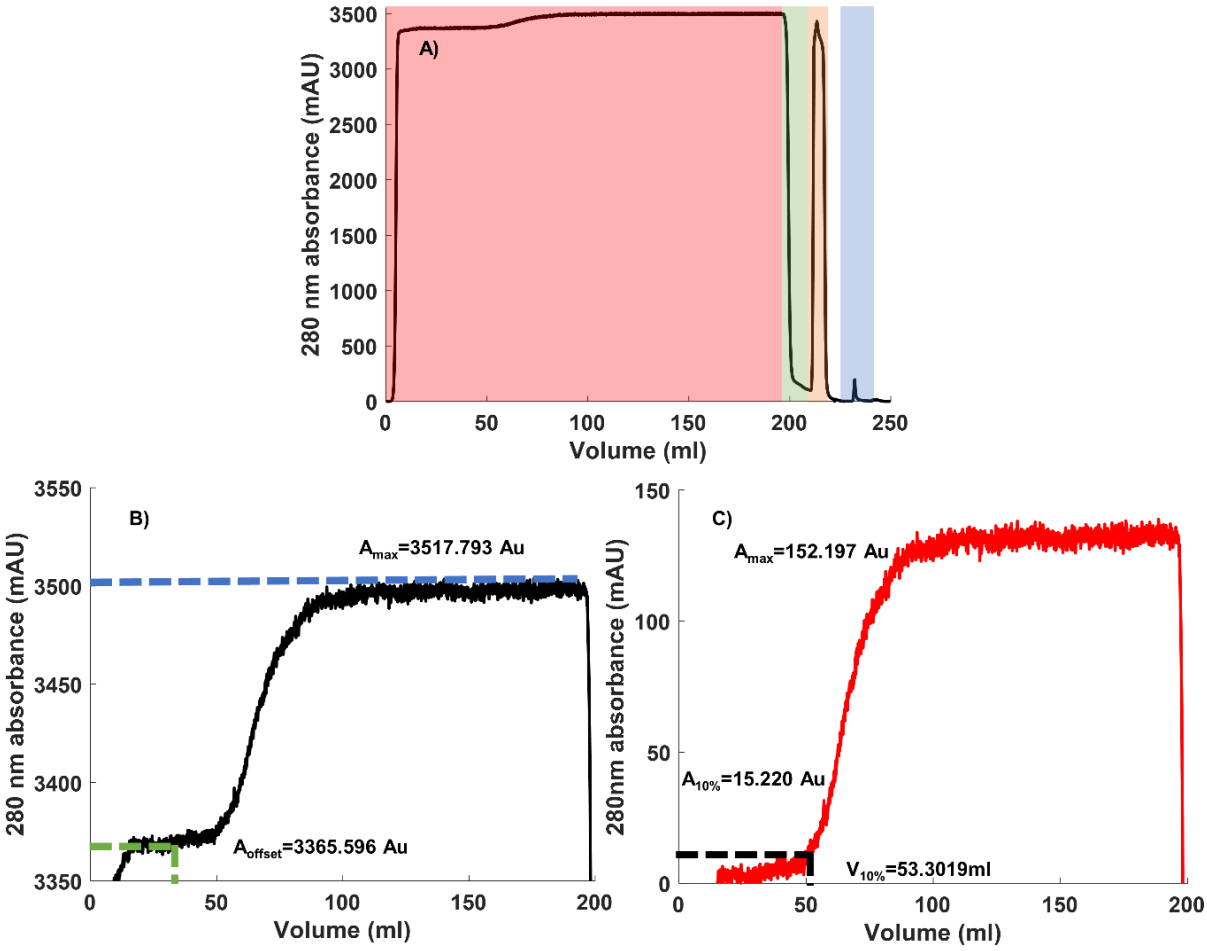

Figure 5.5 Chromatogram obtained for purification cycle 5 of BT B using MabSelect SuRe shown from the loading step. The residence time was 5 minutes. A) Overall chromatogram for the purification cycle. Red, green, peach and blue shading indicate loading, wash, elution, and CIP steps respectively. B) Zoomed in view of the load step showing the two plateaus, the maximal absorbance (A_{max}) obtained for the second plateau, and the absorbance offset (A_{offset}) from HCP and media components. C) The difference in A_{max} obtained for the loading step after subtracting A_{offset} to determine the 10% BT breakthrough volume ($V_{10\%}$).

The 280 nm UV chromatogram (Figure 5.6) was used to obtain the 100% breakthrough absorbance (A_{max}), required for calculation of the DBC. When 100% breakthrough is reached during loading, the breakthrough BT titre is equal to the CUB BT titre as BT can no longer bind to the column so all the BT flows through. In order to obtain 10% of the BT titre or 10% BT breakthrough, 10% of maximum absorbance ($A_{10\%}$) for each BT the chromatogram was offset

by the HCP and media component breakthrough plateau (Figure 5.5 C). The breakthrough volume at $A_{10\%}$ ($V_{10\%}$) was then used in Equation 5.2 to calculate the DBC

The 280 nm UV detector detected an absorbance signal of conjugated double bonds as the CUB is heterogeneous mixture of proteins and unknown media components. This heterogenous mixture means the molar absorptivity of both CUB and column flowthrough is different from pure BT. Since, during loading the HCP/media component of the total flowthrough (contaminants + breakthrough BT) is consistent, the chromatogram UV absorbance obtained by BT B breakthrough can be determined from the difference between A_{max} for contaminant flowthrough and the A_{max} obtained from BT breakthrough (Figure 5.5 C). Furthermore, given that absorbance is proportional to concentration, 10% of the A_{max} signal is equivalent to 10% of the BT from the CUB in the breakthrough. The A_{max} for BT a and BT B was calculated by flowing CUB though the system but bypassing the column in order to ensure no BT is lost to the column (Figure 5.6). BT C was only available in limited amounts so the A_{max} was derived from purification cycle 21 (Table 3) for MabSelect SuRe with a residence time of 10 minutes. The large residence time and lower capacity resin ensured the column is truly saturated and therefore the A_{max} reading was stable across the second plateau as the length of time where the inlet is equal to the outlet concentration was the longest for all BT C experiments.

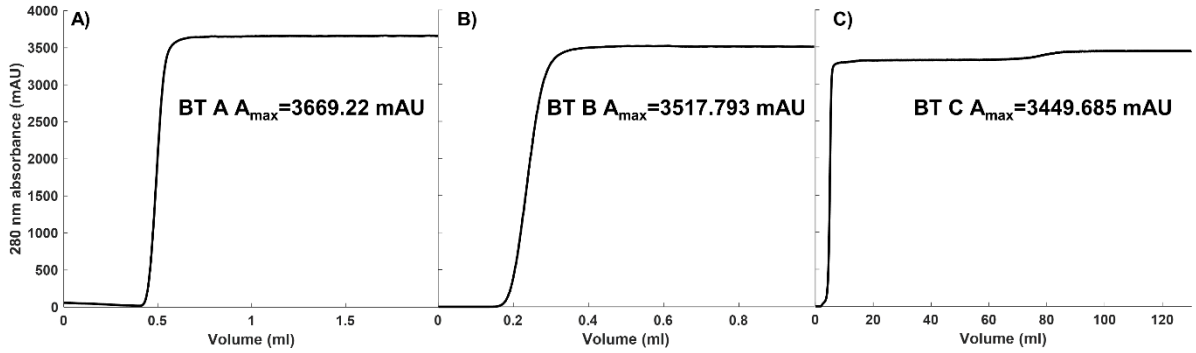

Figure 5.6 280nm A_{max} readings for all BTs. A) BT A A_{max} calculated from flowing BT A CUB bypassing column at 0.931 ml min^{-1}. B) BT B A_{max} calculated from flowing BT B CUB bypassing column at 0.931 ml min^{-1}. C) BT C A_{max} calculated from flowing BT C though HiScreen MabSelect SuRe column at a flow rate of 0.466 ml min^{-1} (10-minute residence time).

Calculating the concentration of each BT in their respective CUB requires pure BT samples obtained by Protein A HPLC. The Beer-Lambert law (Equation 5.3) was used to calculate concentration of BT standards and ensure injection concentration was at ~1 mg ml^{-1} for controlled mass loading on the Protein A HPLC.

$$C = \frac{A}{\varepsilon * l} \quad 5.3$$

Where A=Absorbance, ε=molar absorptivity, C=concentration and l=pathlength

Protein A HPLC isolates very small volumes of BT, the volume loaded on to columns is varied allowing for controlled mass loading on the column. The BT titre of each CUB solution was obtained using standard curves (Figure 5.7), Equation 5.4 and Equation 5.5.

$$C_M = \frac{S_A - b}{m} \quad 5.4$$

Where C_M = mass on column, S_A = peak area, m = standard curve gradient and b = standard curve y intercept

$$C_0 = \frac{C_M}{I_V} = \quad 5.5$$

Where I_V = injection volume, C_0=BT titre of CUB solution

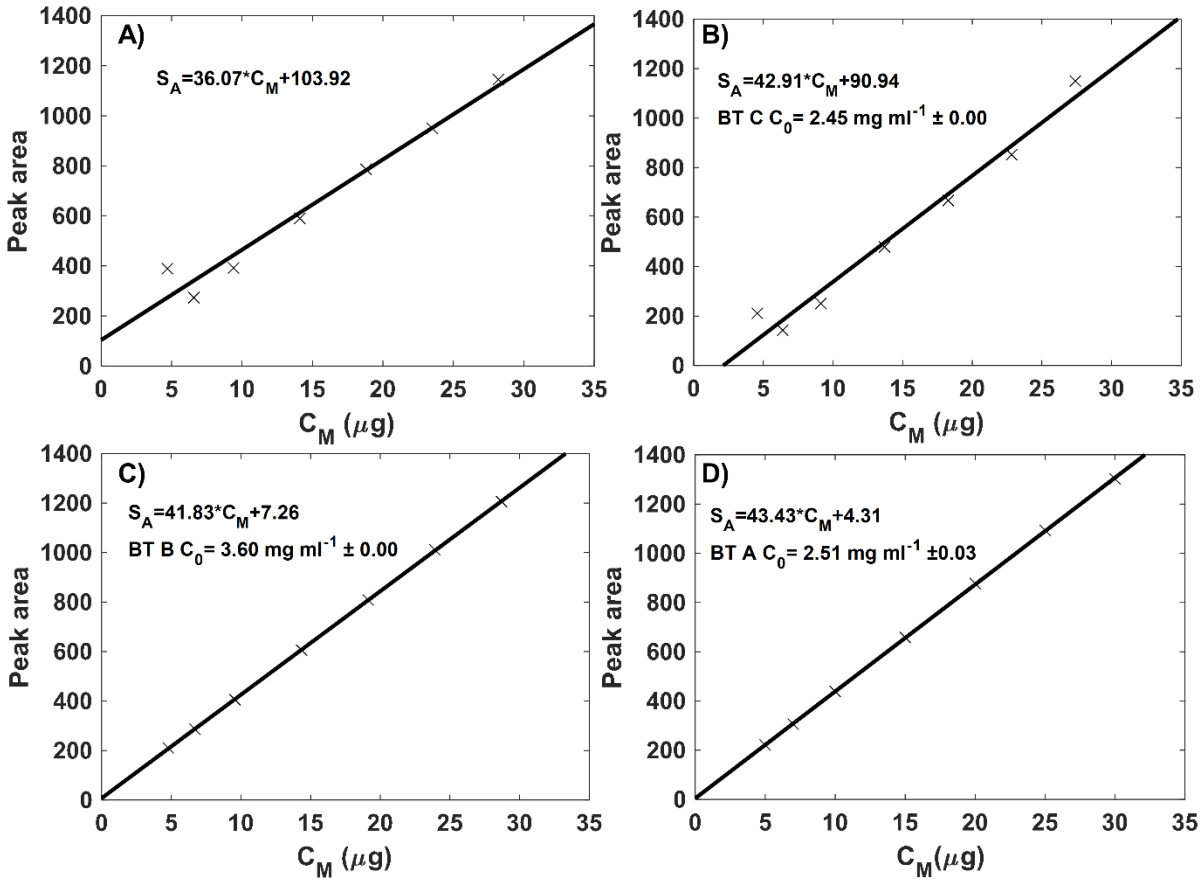

Figure 5.7 Protein A HPLC standard curves for each BT. A) BT B standard curve obtained on HPLC machine 1, used up to cycle 21 for both HiScreen columns, B) BT C standard curve on HPLC machine 1 with CUB BT A Titre shown (n=3) C) BT B standard curve on HPLC machine 2 used for cycles 22 onwards. CUB BT B Titre shown (n=3) D) BT A standard curve on HPLC machine 2. BT A titre shown (n=3).Appendix Table 8.2-Table 8.5 contains peak area and mass. Peak area was measured from Retention time of 2.5 and 2.8 to observe BT monomer.

The individual CUBs had titres of 2.51, 2.45 and 3.60 mg ml^{-1} of BT A, B and C respectively. The C_0 values obtained for the BT using Protein A HPLC in Figure 5.7 was used in the Equation (5.2) to calculate DBC using ÄKTA UV 280nm absorbance readings for HiScreen columns.

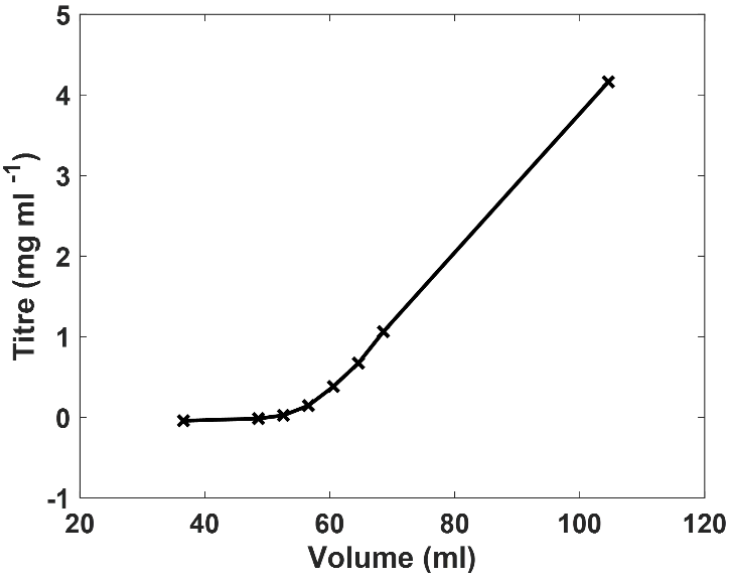

Figure 5.8 Protein A HPLC titre measurements for each selected breakthrough fraction from cycle 6 of MabSelect SuRe. Residence time of 4 minutes with BT B.

Using Protein A HPLC to calculate DBC using Equation 5.2 requires C_0 (Figure 5.7 and Equation 5.5) and the volume of elution for analysed fractions determined by Chromatogram readouts (Figure 5.2). Each collected fraction for HPLC analysis was made up of 2 ml volume, the UV detector sampled a much smaller volume of sample with each measurement point being 0.005 ml thus HPLC fractions were the combination of changing titre over 2ml of breakthrough . The offset volume was also previously calculated as shown in Figure 5.4. In order to calculate the $V_{10\%}$, the titre of each collected fraction was measured (Figure 5.8) and compared to the known C_0 of CUB for relevant BT.

5.3.2 Dynamic binding capacity measurements of relevant industrial Protein A resins by industry standard methods

DBC measurements were carried out using the two different Protein A columns and both BT B and C with 5 different residence times (Table 5.3) in order to compare the effects of residence times and generate training data for the Raman based quantification models. BT A was used with residence times of only 2 and 5 minutes, as typically used by industry. The aim was to test the subsequent Raman model produced from this BT B and C DBC data to predict the DBC performance for BT A, thus demonstrating that the Raman approach could be applied to multiple BT's.

Table 5.3 MabSelect SuRe and MabSelect PrismA DBC parameters and purification cycle number.

HiScreen resin type	Cycle number	Biotherapeutic Molecule	Residence time (minutes)
MabSelect SuRe	1	B	10
MabSelect SuRe	2	B	10
MabSelect SuRe	3	B	10
MabSelect SuRe	4	B	6
MabSelect SuRe	5	B	5
MabSelect SuRe	6	B	4
MabSelect SuRe	7	B	6
MabSelect SuRe	8	B	5
MabSelect SuRe	9	B	4
MabSelect SuRe	10	B	2
MabSelect SuRe	11	B	2
MabSelect SuRe	12	C	2
MabSelect SuRe	13	C	4
MabSelect SuRe	14	C	2
MabSelect SuRe	15	C	4
MabSelect SuRe	16	C	5
MabSelect SuRe	17	C	6
MabSelect SuRe	18	C	10
MabSelect SuRe	19	C	5
MabSelect SuRe	20	C	6
MabSelect SuRe	21	C	10
MabSelect SuRe	22	A	5
MabSelect SuRe	23	A	2
MabSelect SuRe	24	A	5
MabSelect SuRe	25	A	2
MabSelect PrismA	1	B	10
MabSelect PrismA	2	B	6
MabSelect PrismA	3	B	5
MabSelect PrismA	4	B	4
MabSelect PrismA	5	B	2
MabSelect PrismA	6	B	5
MabSelect PrismA	7	B	2
MabSelect PrismA	8	B	4
MabSelect PrismA	9	B	5
MabSelect PrismA	10	B	6
MabSelect PrismA	11	B	10
MabSelect PrismA	12	C	2
MabSelect PrismA	13	C	4
MabSelect PrismA	14	C	2

MabSelect PrismA	15	C	4
MabSelect PrismA	16	C	5
MabSelect PrismA	17	C	6
MabSelect PrismA	18	C	10
MabSelect PrismA	19	C	5
MabSelect PrismA	20	C	6
MabSelect PrismA	21	C	10
MabSelect PrismA	22	A	2
MabSelect PrismA	23	A	5
MabSelect PrismA	24	A	2
MabSelect PrismA	25	A	5

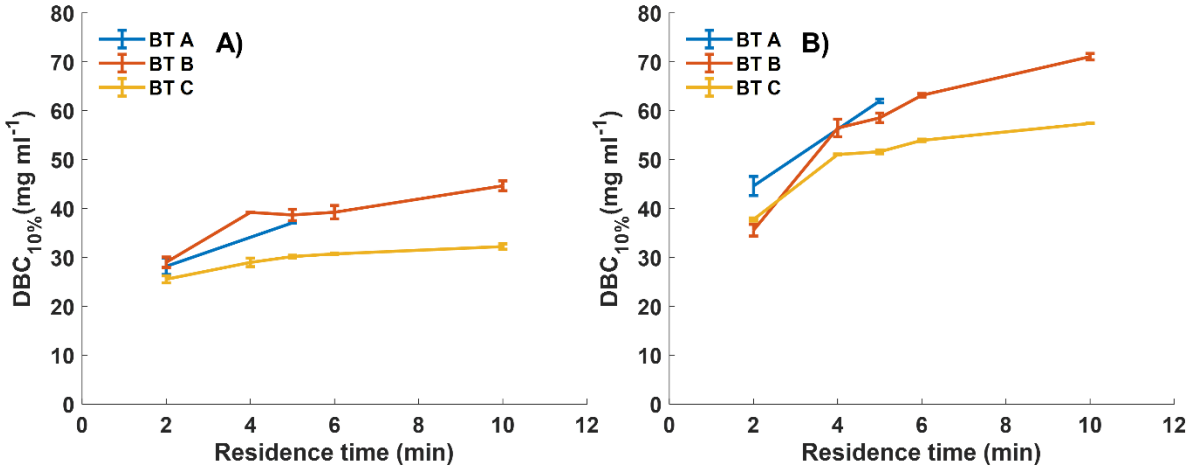

Figure 5.9 DBC of HiScreen columns with BT B and C residence times from 2 – 10 minutes as well as BT A residence times of 2 and 5 minutes calculated form UV 280nm chromatograms. A) DBC results for HiScreen MabSelect SuRe B) DBC results for HiScreen MabSelect PrismA. Blue = BT A Red BT B yellow BT C. Error bars represent standard deviation in calculated DBC during repeated DBC experiments. (N=2).

At 10% breakthrough, a large difference is observed between the HiScreen columns, with MabSelect PrismA exhibiting increased DBC at each residence time for all BTs compared to MabSelect SuRe (Figure 5.9 and Table 5.4). Both columns show an upward trend in DBC as residence time is increased from 2 to 10 minutes, although this was markedly higher in the case of PrismA (Table 5.4). MabSelect SuRe has a relatively narrow DBC range for residence times from 2 to 10 minutes, the DBC increased by 16.18 and 6.67 mg ml^{-1} for BT B and C respectively. Changing residence time from 2 to 10 minutes corresponds to a % increase of DBC by 56% and 26% for BT B and BT C. For PrismA DBC range was observed at 35.48 and 19.64 mg ml^{-1} for BT B and C when increasing Residence time from 2 to 10 minutes. This correlates to a % increase in DBC by 99% and 51% for BT B and BT C, demonstrating that

residence time plays a greater role in BT binding to PrismA resin than SuRe resin for both BTs .

BT A performed similar to BT B with DBC at residence time of 5 minutes with a DBC of 37.09 and 36.70 mg ml^{-1} respectively for on MabSelect PrismA and 61.72 and 63.76 mg ml^{-1} respectively on MabSelect SuRe. Overall higher DBC shows MabSelect Prism A's enhanced performance over MabSelect SuRe even across different BT's.

Both HiScreen columns exhibited lower DBCs for BT C than the other BTs. It is unlikely that this is due to the initial concentration of BT C in the load since the concentrations of BT C and BT A were similar (Figure 5.7). Equilibration buffer is the same pH across all experiments, as each BT is unique there will be slightly different effects to binding. The binding interaction between BT and SPA is known to be facilitated by hydrophobic interactions and salt bridges [45]. As each BT could be of different class or have changes in FC region responsible for binding to SPA, different salt concentrations can enhance or reducing binding affinity by affecting the hydrophobic interactions facilitating the interaction. It is also possible that variations in the structure of BT C affecting their isoelectric point in equilibration buffer. Change in charge of histidine residues at low pH is what allows for BT to become unbound from SPA during elution [47]. As each BT has different overall charge the BT's affinity for SPA will be changed. Exact structural information is unavailable due to BT structure being propriety information. This was one way to calculate DBC, more commonly HPLC is used in industry to measure the DBC of new BTs.

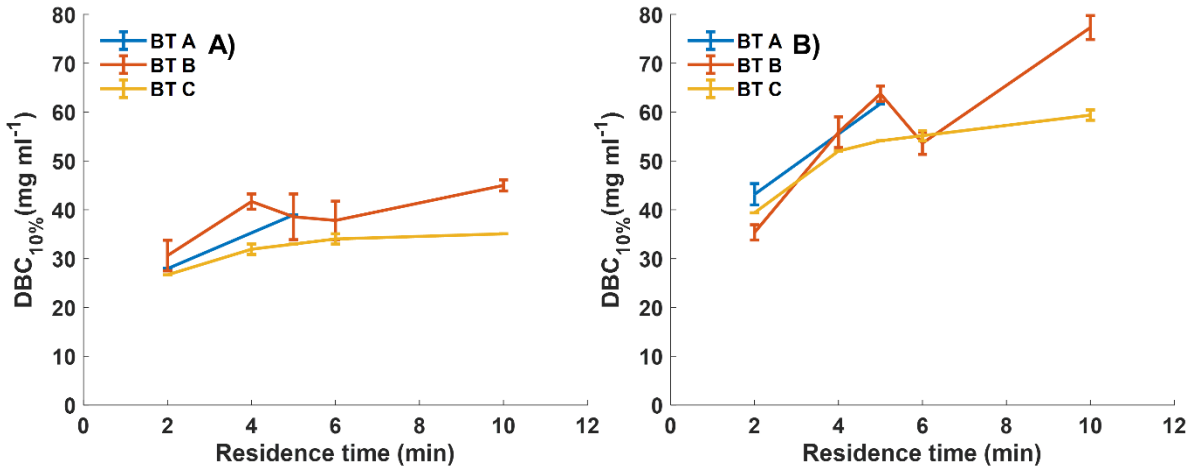

Figure 5.10 HPLC calculated DBC of HiScreen columns with residence times from 2 – 10 minutes. A) DBC results for HiScreen MabSelect SuRe B) DBC results for HiScreen MabSelect PrismA. Blue = BT A Red BT B yellow BT C. Error bars represent standard deviation in calculated DBC during repeated experiments. (N=2).

The HPLC calculated DBC results (Figure 5.10 and Table 5.4) confirm that PrismA has a higher DBC than MabSelect SuRe at all residence times tested for every BT. MabSelect SuRe again has the smallest DBC range when increasing residence time from 2 to 10 minutes, the DBC increased by 14.37 and 8.39 mg ml^{-1} for BT B and C respectively . This corresponded to a % increase in DBC of 47% and 31% for BT B and BT C. As shown for the UV calculated DBCs, MabSelect PrismA has the largest HPLC calculated DBC range, the DBC increased by 41.96 and 19.99 mg ml^{-1} for BT B and C respectively when residence time increased from 2 to 10 mins (Figure 5.10B). This corresponded to an increase of DBC by 118% and 51% for BT B and BT C.

BT A and BT B have residence time 5 minutes giving DBC of 61.71 and 63.75 mg ml^{-1} respectively. Protein A HPLC shows a general trend upwards in DBC as residence time is increased although 6 minutes residence time exhibits a decrease in binding capacity. The same decrease in DBC is shown in the UV predicted DBC (Figure 5.9) although this appears to be increased in HPLC. PrismA shows a decrease in DBC at 6 minutes, this is conflicting with UV results. The decrease appears to be a sampling issue for HPLC with both samples for BT B with 6-minute residence on prism A (Appendix Figure 8.5).

Table 5.4 HPLC and ÄKTA Chromatogram calculated DBC for each HI screen column, BT, and residence time over purification cycles 1-25.

HiScreen resin type	Cycle	BT	Residence time (min)	HPLC DBC (mg ml^{-1})	Chromatogram (mg ml^{-1})
MabSelect SuRe	1	B	10	46.70	46.32
MabSelect SuRe	2	B	10	43.42	43.64
MabSelect SuRe	3	B	10	44.84	45.67
MabSelect SuRe	4	B	6	33.90	37.88
MabSelect SuRe	5	B	5	33.87	37.54
MabSelect SuRe	6	B	4	43.25	39.23
MabSelect SuRe	7	B	6	41.74	40.63
MabSelect SuRe	8	B	5	43.25	39.86
MabSelect SuRe	9	B	4	40.11	39.23
MabSelect SuRe	10	B	2	27.49	30.08
MabSelect SuRe	11	B	2	33.76	27.98
MabSelect SuRe	12	C	2	26.68	26.26
MabSelect SuRe	13	C	4	30.86	28.13
MabSelect SuRe	14	C	2	26.68	24.85
MabSelect SuRe	15	C	4	32.98	29.87
MabSelect SuRe	16	C	5	32.97	30.45
MabSelect SuRe	17	C	6	35.07	30.92
MabSelect SuRe	18	C	10	35.07	31.67
MabSelect SuRe	19	C	5	32.97	29.95
MabSelect SuRe	20	C	6	32.97	30.56
MabSelect SuRe	21	C	10	35.07	32.81

MabSelect SuRe	22	A	5	38.94	37.13
MabSelect SuRe	23	A	2	27.91	29.89
MabSelect SuRe	24	A	5	38.93	37.06
MabSelect SuRe	25	A	2	27.97	26.51
MabSelect PrismA	1	B	10	79.76	71.70
MabSelect PrismA	2	B	6	51.33	62.79
MabSelect PrismA	3	B	5	N/A	N/A
MabSelect PrismA	4	B	4	52.73	54.67
MabSelect PrismA	5	B	2	36.92	34.37
MabSelect PrismA	6	B	5	62.18	58.98
MabSelect PrismA	7	B	2	33.79	36.78
MabSelect PrismA	8	B	4	59.03	58.26
MabSelect PrismA	9	B	5	65.34	57.20
MabSelect PrismA	10	B	6	55.95	63.52
MabSelect PrismA	11	B	10	74.86	70.40
MabSelect PrismA	12	C	2	39.38	38.08
MabSelect PrismA	13	C	4	52.04	50.95
MabSelect PrismA	14	C	2	39.40	37.47
MabSelect PrismA	15	C	4	52.02	51.17
MabSelect PrismA	16	C	5	54.12	51.22
MabSelect PrismA	17	C	6	54.12	54.19
MabSelect PrismA	18	C	10	60.44	57.36
MabSelect PrismA	19	C	5	54.13	52.02
MabSelect PrismA	20	C	6	56.23	53.71
MabSelect PrismA	21	C	10	58.33	57.46
MabSelect PrismA	22	A	2	45.35	46.58
MabSelect PrismA	23	A	5	61.62	62.36
MabSelect PrismA	24	A	2	40.98	42.67
MabSelect PrismA	25	A	5	61.81	61.62

Cycle 3 of Prism A exhibited leak in tubing to column and thus amount of mAb loaded was not accurate; Cycle 3 DBC was not calculated by Chromatogram or by HPLC.

Generating breakthrough samples from DBC experiments took considerable time (2 months) for the number of samples generated. Samples were covered with a foil lid to prevent mixing between wells of a 96 deep well block and frozen at -80 C, to prevent unwanted microbial growth prior to further processing. To ensure samples exhibited no change after 1 freeze thaw cycle Protein A HPLC was performed on the same 8 samples selected for HPLC pre freezing.

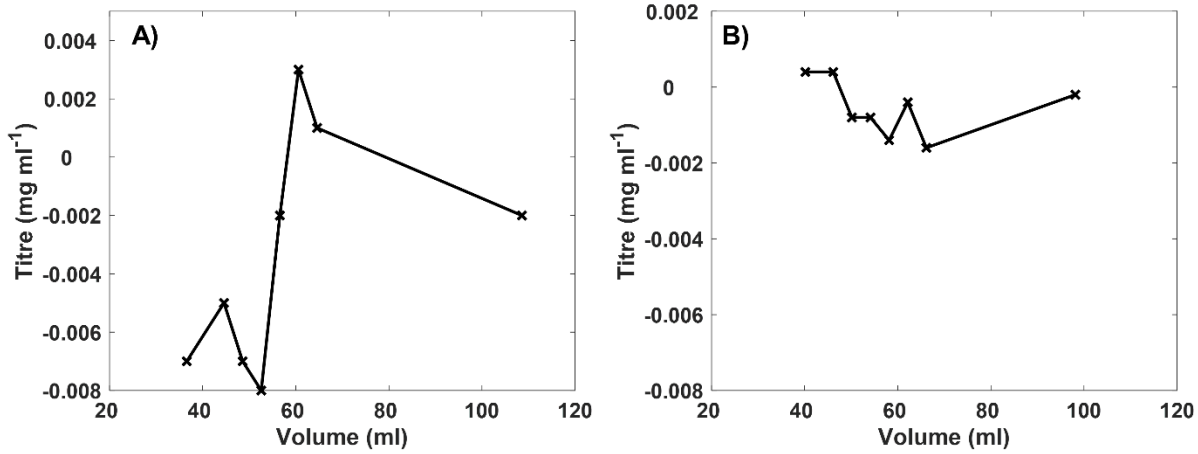

Figure 5.11 HPLC titre measurements of fractions after storing 96-well plates at -80 °C. A) HPLC titre of breakthrough fractions from cycle 6 of MabSelect SuRe after freezing. B) HPLC titre of breakthrough fractions from cycle 7 of MabSelect SuRe after freezing for long term storage.

Due to freezing issues, it was not possible to continue with the DBC generated samples as described above. The result of this section confirms PrismA's superior performance to SuRe resin as well as indicating showing 4 minutes residence time as the point where marginal increases in DBC occur when residence time is increased. For example, with SuRe with both HPLC and chromatogram methods for BT C only increased by ~7% when doubling residence time from 5 to 10 minutes compared to 10% when doubling residence time from 2 to 4 minutes. For the same BT C and residence times on PrismA an increase of 11% is seen when doubling residence time from 5 to 10 minutes compared to 25% when doubling residence time from 2 to 4 minutes. This chapter would have generated a substantial data set for use in training and testing Raman PLS models if issues with storage had not occurred. Data generated for DBC experiments from MabSelect SuRe cycles 5, 8 and PrismA 6 and 9 was subsequently used in section 5.3.3 to compare reproducibility both industry standard methods for DBC analysis.

5.3.3 Reduced Dynamic binding capacity study for generation of BT breakthrough from relevant industrial Protein A resins by industry standard methods

A smaller number of DBC samples compared to section 5.3.2 were generated using BT A and BT B. Samples DBC was calculated using HPLC and chromatogram methods with these samples being subsequently used for Raman analysis as detailed in Table 5.5.

Table 5.5 HPLC and Chromatogram calculated DBC for each HI screen column, BT, and residence time over purification cycles 26-29. Samples were divided into training and test samples for subsequent Raman analysis. BT

HiScreen resin type	Cycle	BT	Residence time (min)	HPLC DBC (mg ml^{-1})	Chromatogram (mg ml^{-1})	Sample designation
MabSelect SuRe	26	A	5	38.94	37.69	BT A Train
MabSelect SuRe	27	A	2	27.64	29.49	BT A Train
MabSelect SuRe	28	A	4	36.97	39.23	BT A Test
MabSelect SuRe	29	B	5	37.45	36.54	BT B Test
MabSelect PrismA	26	A	5	61.27	63.91	BT A Train
MabSelect PrismA	27	A	2	41.37	44.26	BT A Train
MabSelect PrismA	28	A	4	58.63	61.98	BT A Test
MabSelect PrismA	29	B	5	59.21	56.62	BT B Test

Samples were designated as “Train” or “Test” for subsequent PLS analysis (Table 5). Train refers to samples used in the generation of PLS Raman models whereas test samples were used to test the model for predictive ability for the same BT at different residence times or for different BT. Training data samples were generated from BT A at residence times of 2 and 5 minutes. Test data were generated for BT A and BT B at residence times of 4 and 5 minutes, respectively (Table 5.5; Figure 5.12).

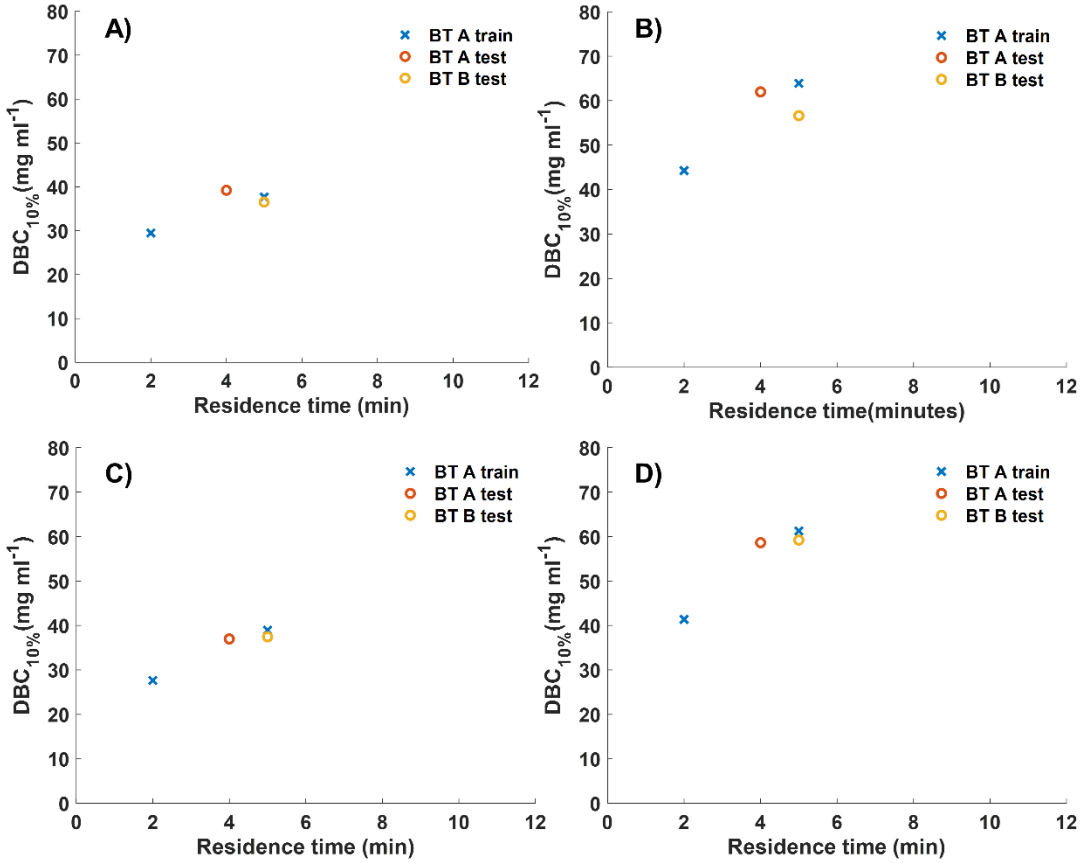

Figure 5.12 HPLC and UV chromatogram calculated DBCs of HiScreen columns over cycles 26-29. DBC results for breakthrough samples used in subsequent Raman analysis. A) UV calculated DBC results for MabSelect SuRe, B) UV calculated DBC for MabSelect PrismA, C) HPLC calculated DBC for MabSelect SuRe and D) HPLC calculated DBC for MabSelect PrismA. Blue X represents BT B at residence times of 2 and 5 min (BT B train). Red circle represents BT B at a residence time of 4 minutes (BT B test). Yellow circle represents BT A at a residence time of 5 minutes

Both the UV chromatogram (Figure 5.12A and B) and HPLC based DBC (Figure 5.12C and D) results show MabSelect PrismA has an increased DBC at every residence time for each BT compared to MabSelect Sure. BT A at 5-minute residence time exhibited a DBC of 38.94 mg ml^{-1} (HPLC) and 37.69 mg ml^{-1} (chromatogram) very similar to BT B which exhibited a DBC of 37.45 mg ml^{-1} (HPLC) and 36.54 mg ml^{-1} (chromatogram). On average there is a DBC decrease of 4% for MabSelect SuRe between BT A and BT B , with MabSelect PrismA decrease in DBC for changing from BT A to BT B is a 8% , therefore the BT's performed similarly with BT A having a slightly higher DBC for the columns. Overall column performance decreased as cycle number increased, due to irreversible binding of HCP contaminants [154]. An example of this column degradation is seen for BT B between cycle 5 (Table 5.4 HPLC and ÄKTA Chromatogram calculated DBC for each HI screen column, BT, and residence time over purification cycles 1-25.Table 5.4) and cycle 29 (Table 5.5) where a ~5 and ~6% decrease in DBC is observed for the UV chromatogram and HPLC methods respectively.

In order to compare both industrial methods the HPLC and UV chromatogram DBC prediction results were compared in terms of coefficient of variation for 5-minute residence time BT B DBC experiments for both HiScreen column types. For MabSelect SuRe DBC predictions from cycles 5,8 and 29 were used. For MabSelect PrismA DBC predictions from cycles 6, 9 and 29 were used. The average %CV between both columns was then calculated for both HPLC and UV chromatogram techniques using Equation 5.6.

$$\%CV(SD)\frac{SD}{\bar{y}} * 100 \qquad 5.6$$

%CV = the coefficient of variation, $\bar{y}$ =the average actual measurement and SD=standard deviation

The UV chromatogram approach achieved a lower %CV of 2.7% compared to HPLC with a %CV of 7.1%. Subsequent DBC values derived from Raman spectroscopic analysis as described below (Section 5.3.5) were compared to UV chromatogram DBC measurements. However, individual BT titres were compared to HPLC since both the Raman spectroscopic analysis and the HPLC analysis were performed on the same 2 ml fractions containing BT breakthrough from DBC experiments (section 5.3.3) such as the example in Figure 5.2.

5.3.4 Raman microscopy optimisation well plate

DOE was used in order to optimise experimental parameters for the Raman spectroscopic analysis. Given the large degrees of freedom for each parameter it is useful if certain parameters that have simple binary choices, such as laser wavelength, pinhole position and laser diffraction grating setting, can be pre-determined prior to DOE. This reduces the overall measurements required for the DOE.

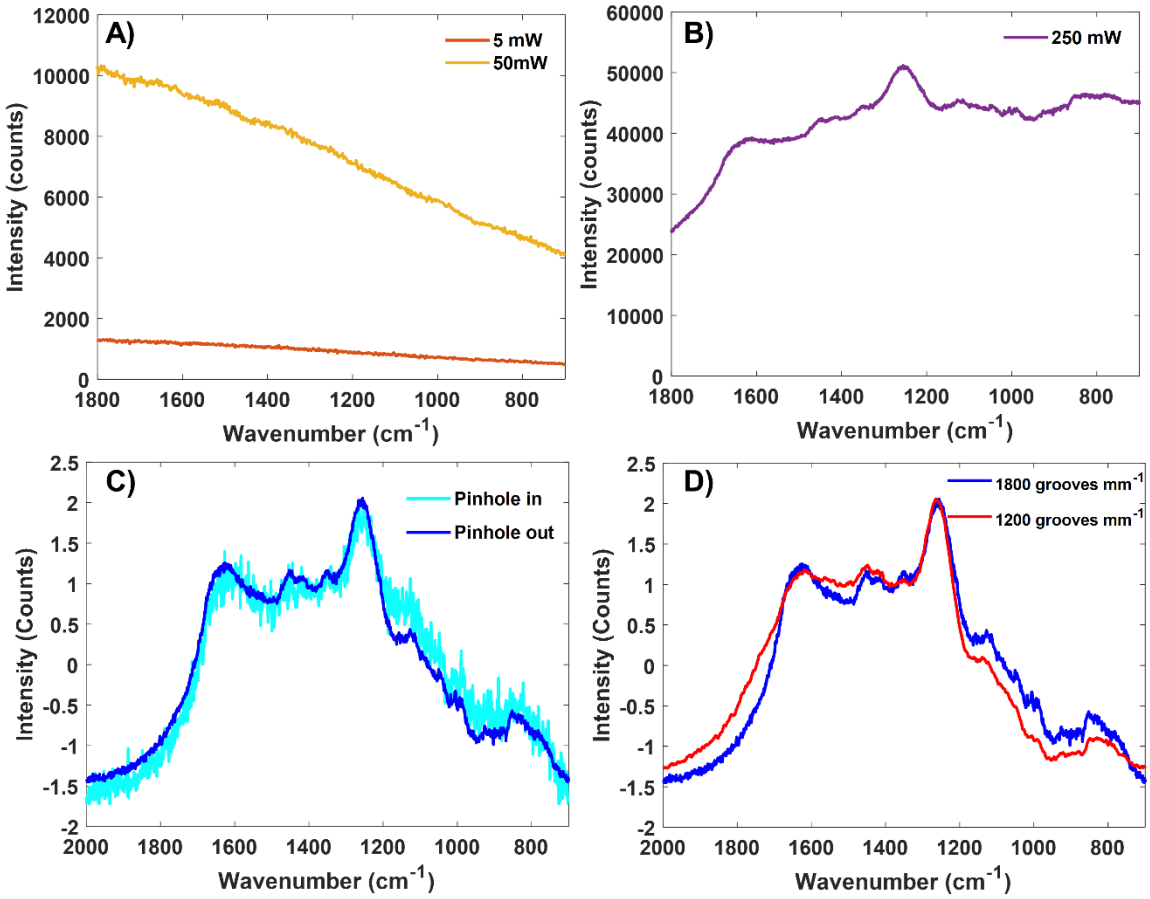

Figure 5.13 Raman spectra of BT B CUB to assess optimal laser, pinhole position and diffraction grating. A) Raman spectra of BT B CUB utilising 532 nm laser. Orange = 5 mW laser power, Yellow =50 mW laser power. B) Raman spectra of BT B CUB utilising the 785 nm laser at a 250 mW laser power setting. Raman instrumentation settings for both laser powers were 4 accumulations,10 s exposure time, pinhole out and 1800 grooves mm $^{-1}$ grating. C) Raman spectra of BT B CUB using the 785 nm laser with different pinhole positions. Spectral acquisition setting were 250 mW, 4 accumulations, 10 s exposure time, 1200 grooves mm $^{-1}$. Light blue = pinhole in, dark blue = pinhole out. D) Raman spectra of BT B CUB using the 785 nm laser with different diffraction gratings. Spectral acquisition settings were 250 mW, 4 accumulations, 10 s exposure time, pinhole out. Dark blue = 1800 grooves mm^{-1} grating and red = 1200 grooves mm $^{-1}$ grating. For C and D spectra was Standard normal variate normalised to make spectra comparable as the pinhole in position reduced overall signal intensity by 11.6 times

The 532 nm laser induced high levels of fluorescence in BT B cub which masked Raman spectral peaks (Figure 5.13 A). The 785nm laser has a lower power density which requires a higher power to ensure sufficient Raman scattering and therefore observable peaks in the spectrum. The 785nm laser yielded observable peaks (Figure 5.13B) and thus was used for all subsequent Raman measurements.

The pinhole can be used to focus the laser to a smaller spot size. A smaller spot size reduces the number of scattered photons that will reach the detector, and therefore the intensity of peaks in a given spectrum. The data was vector normalised to compare spectral noise with or

without the pinhole. In the case of BT B CUB, the pinhole increased spectral noise (Figure 5.13 C, dark blue) and therefore pinhole out position was used for all subsequent Raman measurements.

For laser diffraction grating, there was a choice of 1200 or 1800 grooves mm^{-1} on the Renishaw InVia system. 1200 grooves mm^{-1} grating was chosen as spectral noise was reduced making peaks easier to distinguish from noise, one such peak at 1419 cm^{-1} was only clearly distinguishable from peak at 1451 cm^{-1} with the 1200 grooves mm^{-1} (Figure 5.13 D).

In order to assess how long a 200 µl sample could be left on the microscope stage before evaporation resulted in the laser no longer being focused on the sample was measured using a model aqueous solution of 1 M urea (Figure 5.14).

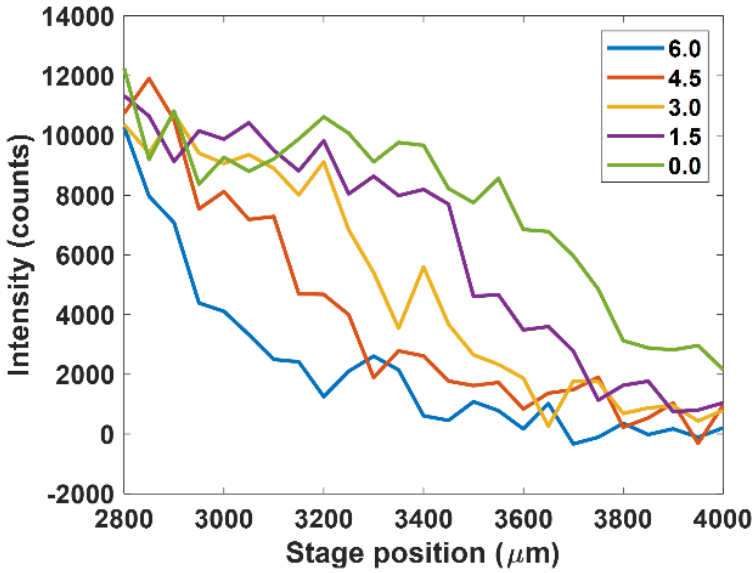

Figure 5.14 Depth profile Raman measurement time course as a function of stage position in the z direction of a 200 µl 1M Urea solution in a 96 well plate. The measurement parameters were the 785nm laser set to the 50 mW setting, 6 s exposure time, 2 accumulations and a grating of 1200 grooves mm^{-1}. All spectra were pre-processed using a Savitzky-Golay filter (window=9 polynomial=1 derivative=0) to reduce noise in the non-optimised spectrometer parameters. CN_{vs} mode of Urea was integrated from the baseline at (932-1075 cm^{-1}). Green= Depth profile at 0 hours. Purple= Depth profile at 1.5 hours. Yellow = depth profile at 3 hours. Red= Depth profile at 4.5 hours. Blue at 6 hours

Over time the water-based urea sample began to evaporate and reduce in volume. Evaporation will cause the sample to increase in concentration, and thus intensity of urea bands would increase. It can be seen that the overall intensity of Urea at 4.5 hours does not go beyond that of the urea signal at 4.5 hours, this indicates the concentration change is not observed by the spectrometer. The effect of no change in maximal intensity can clearly be shown when using less noisy 532nm laser (Appendix Figure 8.6).

The sample surface moved from stage position 3400 µm to 2900 µm over 4.5 hours. Overtime the sample surface moved away from objective, requiring that the stage to be closer to the objective for the laser to remain focused on the sample surface. The surface of the liquid sample is defined as the point of maximal intensity. 4.5 hours leads to a movement of 500 µm in the direction for aqueous samples at room temperature.

The laser was aligned to ensure 785nm laser would always reach the sample and be focused in the z direction. The pre-defined measuring position for the well plate removes the need to align the laser for every single well position measured, saving time spent before measuring samples.

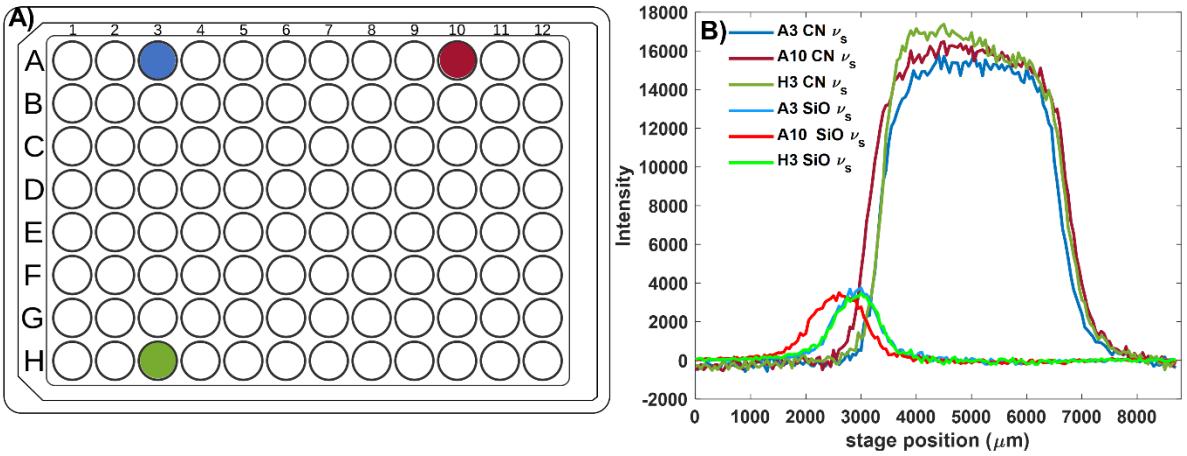

Figure 5.15 Alignment of the 785 nm laser for the quartz well plate in the z direction. A) The wells measured are colour coded to match part B. B) Depth profile of the quartz 96 well plate wells containing 1M urea showing the integration of the CN_{vs} signal (932-1075cm^{-1}) from urea overlayed on the SiO_{VS} signal (475-514cm^{-1}) obtained from the quartz. Dark blue = depth profile of CN_{vs} vibrational mode in well plate location A3, light blue = depth profile of SiO_{vs} vibrational mode in well plate location A3, dark red = depth profile of CN_{vs} vibrational mode in well plate location A10, light red= depth profile of SiO_{vs} vibrational mode in well plate location A10, dark green = depth profile of CN_{vs} vibrational mode in well plate location H3, light green = depth profile of SiO_{vs} vibrational mode in well plate location H3.

The stage position was set to 0 after focusing optically on a permanent pen mark on the far side of well A1 of the 96-well plate. The quartz material that makes up the 96 well plate can be observed between stage positions 1500 - 3500 µm (Figure 5.15 B). The 1 M urea solution in the wells can be observed between positions 3000 - 6750 µm. The observed urea intensity is maximal at 6500-6750 µm (Figure 5.15B). The range of stage positions used is the result of the Stage being not completely level with a ~300 µm movement in z direction when moving across any 7 wells in an x or y direction (Figure 5.15 A and B). As a result, the chosen measurement depth needs to be at least 800 µm below the surface of sample to prevent signal as a result of evaporation over time. A nominal depth of 5000 µm below the surface meets this criterion and has minimal change in intensity across the wells observed (Figure 5.15 B).

With the laser type, grating type, pinhole position and laser aligned the DOE was focused on identifying the optimal laser power, exposure time and accumulation number for sample analysis (Table 5.6). Sample evaporation was taken into consideration ensuring BT B CUB and BT B breakthrough sample at 0.26 mg ml^{-1} titre (cycle 1 MabSelect SuRe, Table 5.3) was replaced every 4.5 hours as described in section 5.2.4. The resultant spectra of BT B CUB (BT titre = 3.60 mg ml^{-1}) and BT B flowthrough (BT titre = 0.26 mg ml^{-1}) using the DOE conditions in Table 5.6 are shown in Figure 5.16.

Table 5.6 Design of experiment parameters for each measurement for well plate Raman samples of BT B CUB (3.60 mg ml^{-1}) and BT B flowthrough (0.26 mg ml^{-1}).

Measurement	Titre (mg ml^{-1})	Accumulations	Exposure (s)	Power (500mw laser)
1	0.26	2	2	1.00%
2	0.26	2	2	100.00%
3	0.26	2	40	10.00%
4	0.26	2	40	100.00%
5	0.26	17	21	50.00%
6	0.26	17	21	50.00%
7	0.26	17	21	50.00%
8	0.26	17	21	50.00%
9	0.26	32	2	10.00%
10	0.26	32	2	100.00%
11	0.26	32	40	10.00%
12	0.26	32	40	100.00%
13	3.60	2	2	50.00%
14	3.60	2	21	10.00%
15	3.60	2	21	100.00%
16	3.60	2	40	50.00%
17	3.60	17	2	10.00%
18	3.60	17	2	100.00%
19	3.60	17	21	50.00%
20	3.60	17	40	1.00%
21	3.60	17	40	100.00%
22	3.60	32	2	50.00%
23	3.60	32	21	1.00%
24	3.60	32	21	100.00%
25	3.60	32	40	50.00%

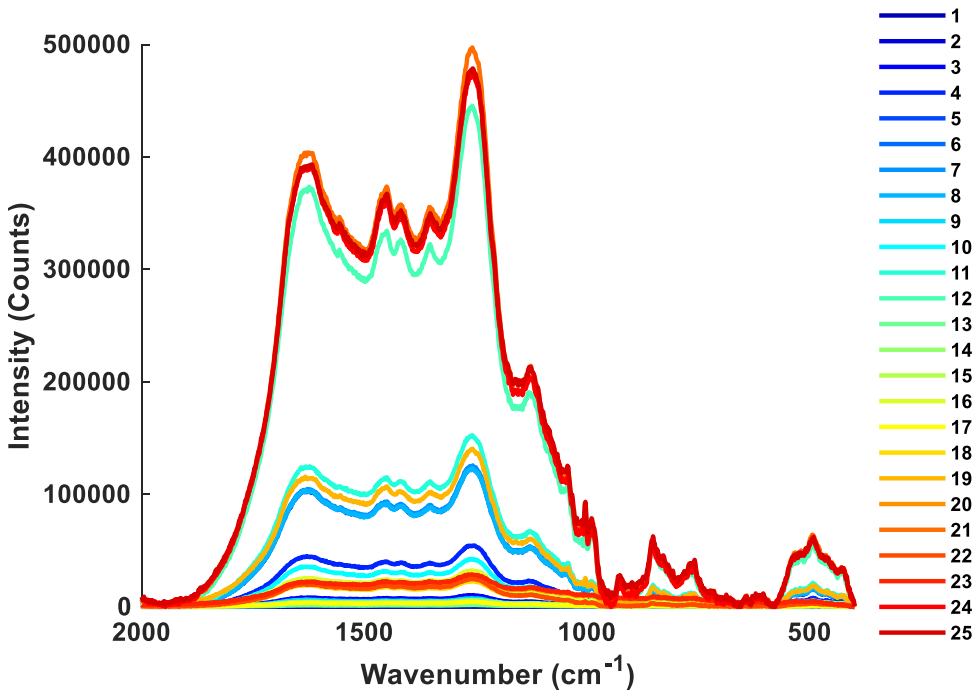

Figure 5.16 Raman spectra using defined parameters in DOE parameter Table 5.6. Spectra was rubber band baseline corrected between 400- 2000 cm^{-1}.

A wide range in spectral intensity is observed due to the wide range of parameters used for the Raman DOE experiments. Another parameter which will affect the overall intensity is the concentration of BT in the CUB measured, due to an increase in detection of protein specific vibrational modes. The log amide I intensity, log of phenylalanine intensity, signal to noise ratio and estimated spectral acquisition time (scans* acquisitions) were chosen as factors for assessing optimal conditions in the DOE Root surface analysis. Using the log of intensity reduced the variability of intensity as the CUB and flowthrough have a large difference in concentration. The difference in BT concentration in the samples used causes changes in instrument intensity responses. However, the aim of this study is to look at instrumental parameter induced changes, creating a log of intensity reduces the effect of concentration induced changes. The range of BT concentration was chosen to confirm two points, i) that saturation of the Raman CCD detector does not occur at high concentration samples and ii) that 10% breakthrough concentrations ~0.26 mg ml^{-1} could be observed using the parameter range in DOE. For the outcome factor desirability maximising intensity and SNR was set. In the case of overall spectral measurement time was set to be minimised in desirability as shorter measurement times would result in higher thoughput of samples with the 4.5 hour window for samples.

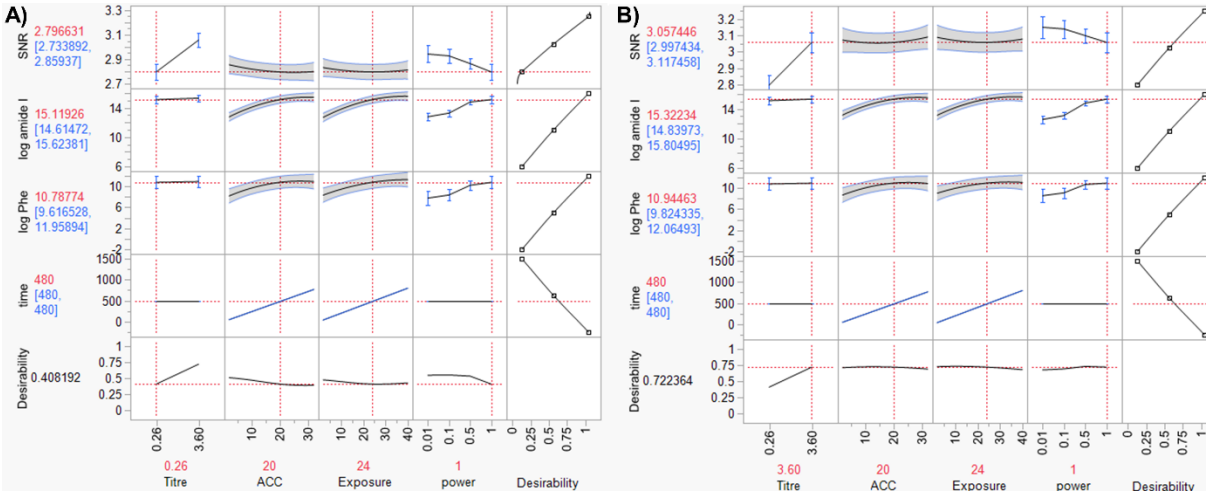

Figure 5.17 Raman DOE prediction profiler for well plate methodology. A) Prediction profiler for low concentration BT B flowthrough sample at 0.26 mg ml^{-1} B) Prediction profiler for high concentration BT B CUB sample at 3.60 mg ml^{-1}. 95% confidence interval can be seen as bars on the individual points. Time is in seconds. ACC us accumulations. Power is in percent of 500 mW. Titre is in mg ml^{-1}

The SNR stayed within 95 % confidence intervals when changing either accumulations or exposure indication little to no effect on SNR by these parameters. Increasing Laser Power did cause SNR to decrease but only by a small amount overall. Even at high power spectral peaks are still distinguishable as shown in Figure 5.16. The log of both amide I and Phe intensity did increase with all instrumental parameters (power, exposure and accumulations). Beyond 20 accumulations and 24 seconds scans the increase in peak intensity stayed within 95% confidence intervals, indicating an increase in either accumulations or exposure would not have any beneficial increase in signal. So, 24 s exposure with 20 accumulations were chosen as instrumental measurement parameters for well based Raman measurements. However, with sample evaporation in mind the overall increase in measurement time would not make the gain in signal intensity worthwhile for a high throughput method of using 96-well plate. There was an increase in signal intensity with increase in laser power from 50 to 100%. Importantly this increase in laser power did not have an effect on total measurement time thus could be increase without decreasing desirability of selected parameters. However, one factor to consider when increasing laser power is sample damage. Laser power was then assessed to see if higher power would cause sample degradation over time.

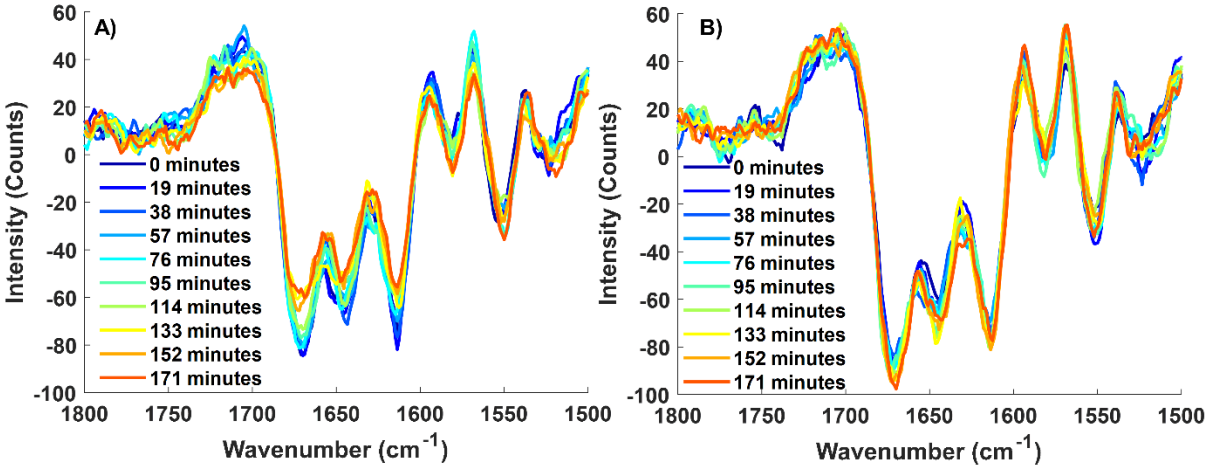

Figure 5.18 Repeated measurements of BT B CUB using DOE derived instrumental parameters of 20 accumulations 24 s exposure and 500mW 785nm laser. A) N1 measurement series of BT B CUB B) N2 measurement Series of BT B CUB. Spectra was rubber band baseline corrected, SNV normalised and Savitzky–Golay filtered (window=33 derivative=2 polynomial=2). Samples were repeat measured 10 times with each measurement taking 19 minutes to acquire.

BT B CUB was subjected to repeated measurements under DOE derived conditions with a 500 mW 785nm laser to assess if BT began to change as a result of the Raman measurements using these parameters. A three-peak analysis of the Amide I band was used to assess changes in protein structure; peak one (1657-1688 cm-1) representing β sheet structures, peak two (1630-1656 cm^{-1}) representing α structures and peak three (1598-1630 cm-1) representing phenylalanine and other aromatic residues in the protein tertiary structure. The ratio of each peak in terms of overall amide I intensity was used for subsequent one-way ANOVA. The β, α and aromatic residues did not significantly change ($p<0.05$) over the 10 repeated measurements with p values of 0.12 ,0.64 and 0.55 respectively. There was no trend in specific amide I intensity repeated measurements indicating the sample was stable under 500mW laser and thus a 500mW (100%) laser power was used for well plate measurements of samples (Figure 5.19).

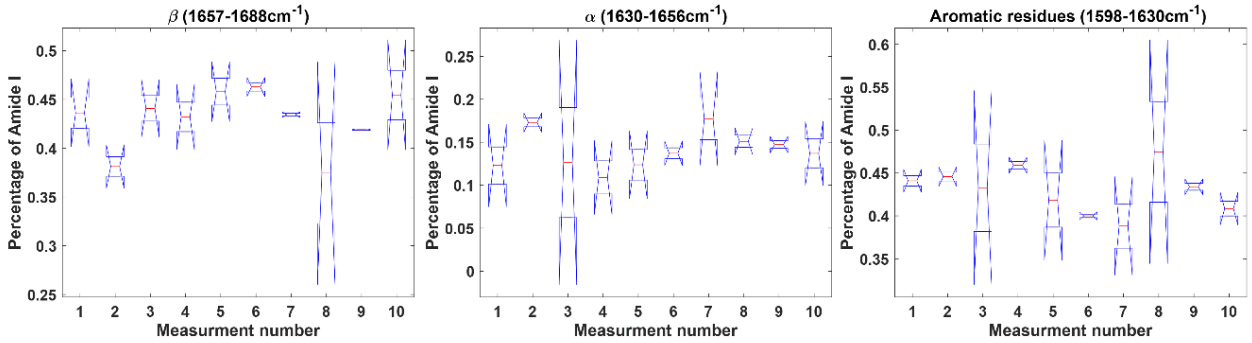

Figure 5.19 ANOVA box plots of Amide I peak percentage from Raman stability measurements of BT B CUB. Three amide I peaks representing β sheet structure (1667-1668 cm^{-1}) α helical (1630-1656cm^{-1}) and aromatic residues (1598-1630cm^{-1}) were analysed. N=2.

5.3.5 Quantification of BT in breakthrough curve using a high throughput well plate Raman microscopy methodology

Once the parameters for well plate-based measurements were established, quantification experiments could begin. Selected 2 ml fractions measured by HPLC analysis in section 5.3.3 to assess DBC of columns were submitted to confocal Raman microscopy using the instrument parameters described in section 5.2.4. The resultant spectra from BT A "Train" flowthrough samples (Table 5.5) were used to train the Simple Partial Least Squares (SIMPLS) algorithm. The ideal number of PLS components was chosen using Root mean squared error (RMSE) values (Equation 5.7).

$$RMSE = \sqrt{\frac{\sum_{i=1}^{n}(y_i - \hat{y}_i)^2}{n}} \qquad 5.7$$

Where RMSE= Root mean square error, n=number of observations, y_i= I^{th} iteration of actual observation , $\hat{y}_i$= i^{th} iteration of predicted observation

The RMSE values for individual models were determined based on actual values obtained from the HPLC derived titre measurements and predicted Raman PLS derived BT titres. This was possible as both HPLC and Raman used the same 2 ml fractions obtained from the DBC experiments.

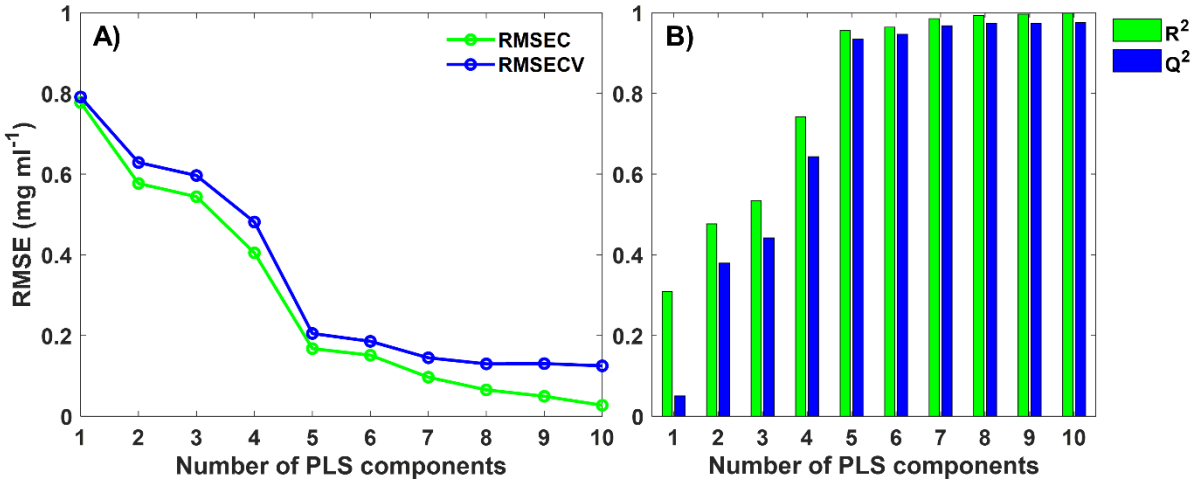

Figure 5.20 Statistical analysis Raman PLS training model and leave one out cross validation of models for well plate measurements of BT A train data sets. Raman data was not pre-processed A) RMSE analysis of PLS models with increasing components. RMSEC is obtained from applying the model against the training model data. RMSECV is obtained from applying the model to leave one out (LOOCV) cross validation of the training data. B) R^2 vs Q^2 plot. R^2 was calculated from the training data set. Q^2 was calculated from LOOCV. Green = Data obtaining from applying model to the training data. Blue = Data obtained from applying model to LOOCV data.

In order to identify the ideal number of PLS components required to prevent over fitting, a model was generated by selecting the number of PLS components where no further gain in RMSE of cross validated data (RMSECV) is observed. When RMSECV increase becomes incremental, the Q^2, known as the goodness of prediction can be used where 1= perfect prediction and 0= no predictive ability. Q^2 was derived from cross validating the data using LOOCV. For the Raman PLS model, 8 components were chosen, as with larger numbers of components, beyond 8 components the RMSCV and Q^2 no longer improved with values of 0.13 mg ml^{-1} and 0.97 respectively (Figure 5.20). The model was applied to the BT A and BT B test datasets.

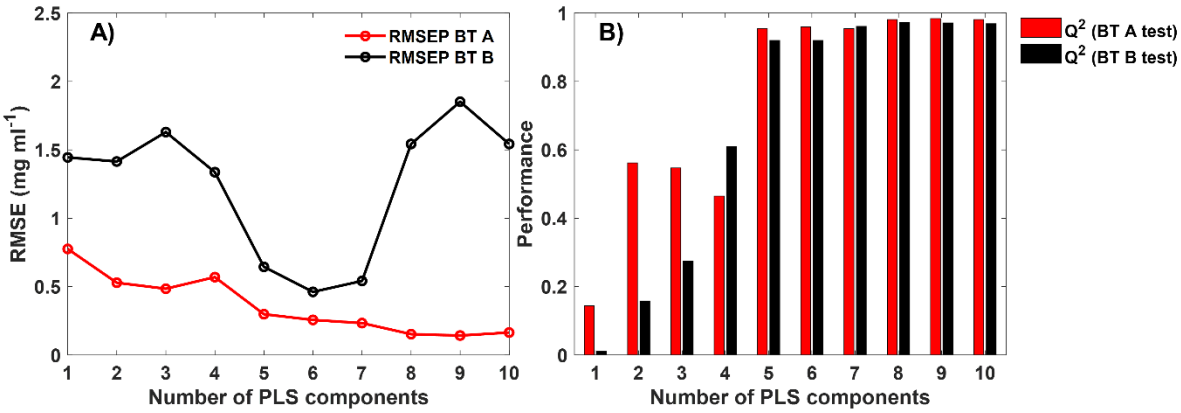

Figure 5.21 Statistical analysis of Raman PLS test models for well plate measurements of BT A and BT B. Raman data was not pre-processed. A) RMSE analysis of PLS model with increasing components. Root mean square error prediction (RMSEP) BT A is the root mean squared error when the model is applied to the BT A and BT B test data. B) Goodness of prediction Q^2 plot was calculated from applying the PLS model to the BT A (red) and BT B (black) test data sets.

When applied to the "Test" data (Table 5.5) the PLS model trained on non pre-processed Raman spectra performed poorly, with the RMSE being up to 11x higher than Cross validation (Figure 5.21). The RMSE was much higher than the expected 10% breakthrough titre concentration range of ~0.20 -0.40 mg ml^{-1}. The model was optimised by pre-processing the spectral data. Three PLS models arose utilising 0^{th} derivative, 1^{st} derivative and 2^{nd} derivative spectra (Figure 5.22). The PLS component number was optimised in the same way as show for the unprocessed spectra.

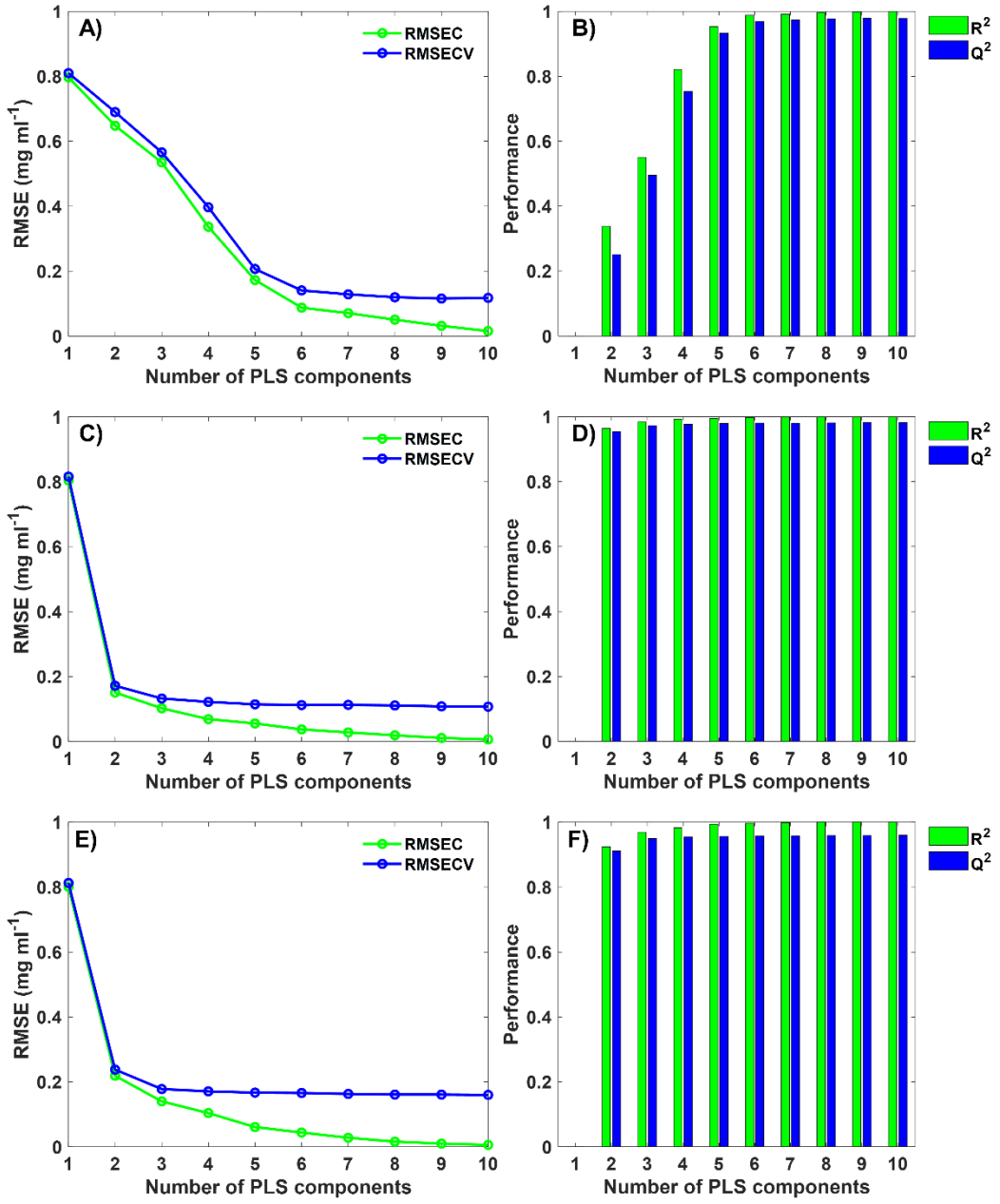

Figure 5.22 Statistical analysis of the Raman PLS model using spectral pre-processing for 0^{th}, 1^{st} 2^{nd} derivative spectra. A) RMSE plot for training data and LOOCV for 0^{th} derivative Raman PLS model. B) Goodness of fit R^2) and goodness of prediction (Q^2) plot for training data and LOOCV for 0^{th} derivative Raman PLS model. C) RMSE plot on Training data and LOOCV for 1^{st} derivative Raman PLS model D) Goodness of fit and Goodness of prediction plot for training data and LOOCV for 1^{st} derivative Raman PLS model E) RMSE plot on Training data and LOOCV for 2^{nd} derivative Raman PLS model F) Goodness of fit and Goodness of prediction plot for training data and LOOCV for 2^{nd} derivative Raman PLS model. and Green=Data from applying model to training data (RMSEC and R^2). Blue= Data from applying model to LOOCV data (RMSE and Q^2). 0^{th} derivative spectra with SNV processing. 1^{st} derivative Raman PLS model with SNV and Savitzky Golay filter (Window= 15 Derivative=1 Polynomial=1) pre-processing. 2^{nd} derivative Raman PLS model with SNV and Savitzky Golay filter (Window= 25 Derivative=2 Polynomial=2) pre-processing

The 0th order model with SNV (standard normal variate) normalisation at 8 components had an RMSE of 0.12 mg ml^{-1} and Q^2 of 0.98 (Figure 5.22 A & B), whereas the 8-component 2nd derivative SNV normalised model had an RMSE of 0.16 mg ml^{-1} and a Q^2 of 0.96. The SNV and Savitzky Golay filter (Window = 25, Derivative = 2, Polynomial = 2) pre-processed model was chosen to be a 8-component model (Figure 5.22 E& F). The SNV and Savitzky Golay filter (Window = 15, Derivative = 1, Polynomial = 1) model performed best in cross validation with an RMSE and Q^2 of 0.11 mg ml^{-1} and 0.98 respectively for a 6-component system (Figure 5.22 C& D) . Of the three optimised Raman PLS models for quantification of BT, the lower RMSE and higher Q^2 showed the 1st derivative model to be best for quantification of BT in flowthrough samples. The model's predictive ability was assessed by Root mean square error of prediction (RMSEP).RMSEP is when the RMSE for the model when applied to "Test" data sets, in this case BTA test and BT B test data defined in Table 5.5.

Table 5.7 Root Mean Squared Error for prediction (RMSEP) for each Raman PLS model when applied to BT A and BT B.

PLS Model	BT A test RMSEP (mg ml^{-1})	BT B test RMSEP (mg ml^{-1})
No pre processing	0.15	1.54
SNV,0th derivative	0.14	1.68
SNV,1st order derivative	0.15	0.15
SNV, 2nd order derivative	0.18	0.63

SNV 1st derivative pre-processing yielded the second lowest RMSEP for BT A based models, however, was the only model to achieve RMSEP below 0.2 mg ml^{-1} when applied to a different BT such as BT B. As DBC at 10% breakthough is being assessed RMSE below 10% titre concentrations (0.2-0.4 mg ml^{-1}) was needed. The 1st derivative pls model is optimal for a platform approach not requiring individual BT calibration when BT changes. The quantification of BT titre in individual BT flowthrough fractions and CUB by Raman spectroscopy meant the DBC for each test DBC experiment could be derived according to Equation 5.2.

Table 5.8 PLS Well plate Raman calculated DBC for each HiScreen column, BT, and residence time over purification cycles 28-29. Samples were BT A and BT B test samples.

HiScreen resin type	Cycle	BT	Residence time (min)	Well plate Raman DBC mg ml $^{-1}$	Sample designation
MabSelect SuRe	28	A	4	38.48 ± 1.09	BT A Test
MabSelect SuRe	29	B	5	37.91 ± 0.00	BT B Test
MabSelect PrismA	28	A	4	60.42 ± 1.09	BT A Test
MabSelect PrismA	29	B	5	59.93 ± 0.00	BT B Test

5.3.6 Raman optimisation of breakthrough device

The DOE approach was also utilised to optimise parameters for Raman spectroscopic analysis using the in-line breakthrough device described in section 5.2.3 (Figure 5.3). Measurements were performed under a flow rate of 0.981 ml min^{-1} and the laser was focused through the sapphire window into the channel of the PDMS device. The DOE was performed with BT B CUB solution and using the instrument parameters described in Table 5.9. A flowthrough sample generated by DBC experiments was not used as was the case in Well plate DOE (section 5.3.4). Each flowthrough sample was only 2 ml in volume and thus not enough as available for DOE experiment measurements, as each measurement would be performed under flow and required >0.6 ml for each measurement.

Table 5.9 Design of experiment parameters for each simulated inline breakthrough Raman measurement of BT B CUB (3.60 mg ml^{-1}).

Parameter/legend reference	Run Order	Accumulations	Exposure (s)
1	1	10	5.0
2	2	1	1.0
3	3	5	10
4	4	5	4.6
5	5	5	10.0
6	6	10	5.1
7	7	5	10.0
8	8	1	7.3
9	9	5	4.6
10	10	7	1.0
11	11	1	1.0
12	12	10	5.1
13	13	5	4.6
14	14	1	10.0
15	15	10	1.0

The resultant spectra from measuring BT B CUB using the parameters described in Table 5.9 are shown in Figure 5.23 .

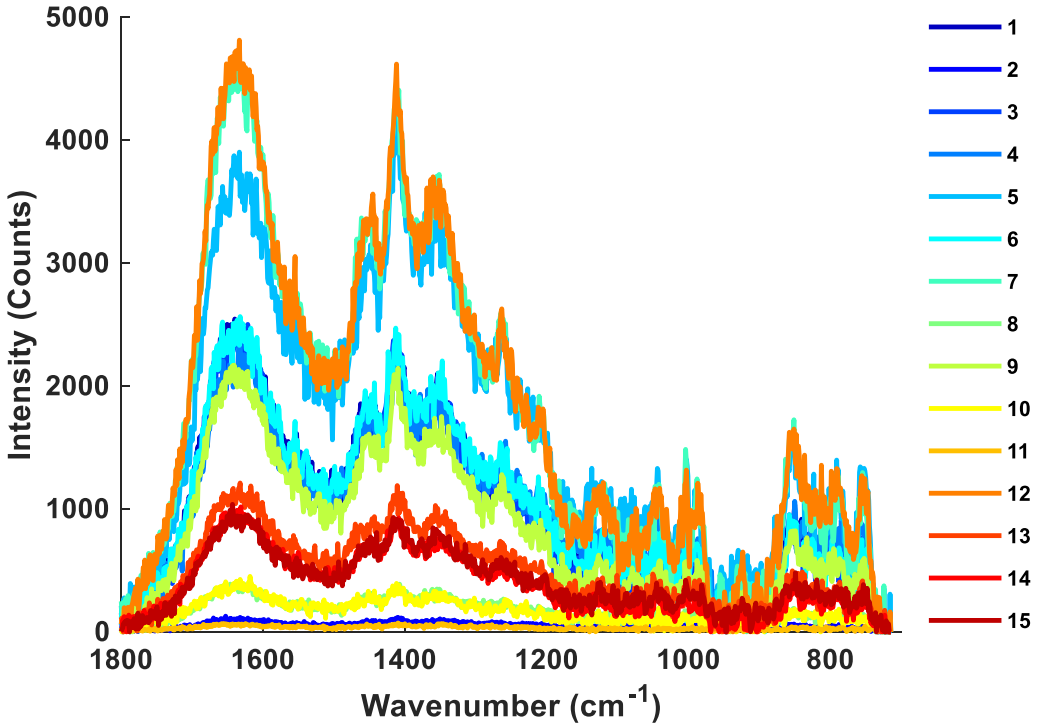

Figure 5.23 Raman spectra using defined parameters in DOE experiments. Table 5.9. Spectra was rubber band baseline corrected between 715-1800 cm^{-1}.

A wide range in spectral intensity is observed even with the reduced parameter ranges used for DOE of the breakthrough device. As the concentration is the same for all experimental measurements in the DOE, the only variables responsible for changes in spectral peak intensities are the instrument parameters. The SNR, Phe intensity and Amide I intensity were chosen as factors for assessing parameter performance. Measurement time was limited due to limited volume, the high flowrate and small volume of the device. As a result of the limited time ranges for sample measurement under flow the cosmic ray filter setting was not used, as this function relies on performing 2 extra scans and averaging out cosmic ray spikes. For the outcome factor of desirability maximising intensity and SNR was set. In the case of overall spectral measurement time was set to be minimised in desirability.

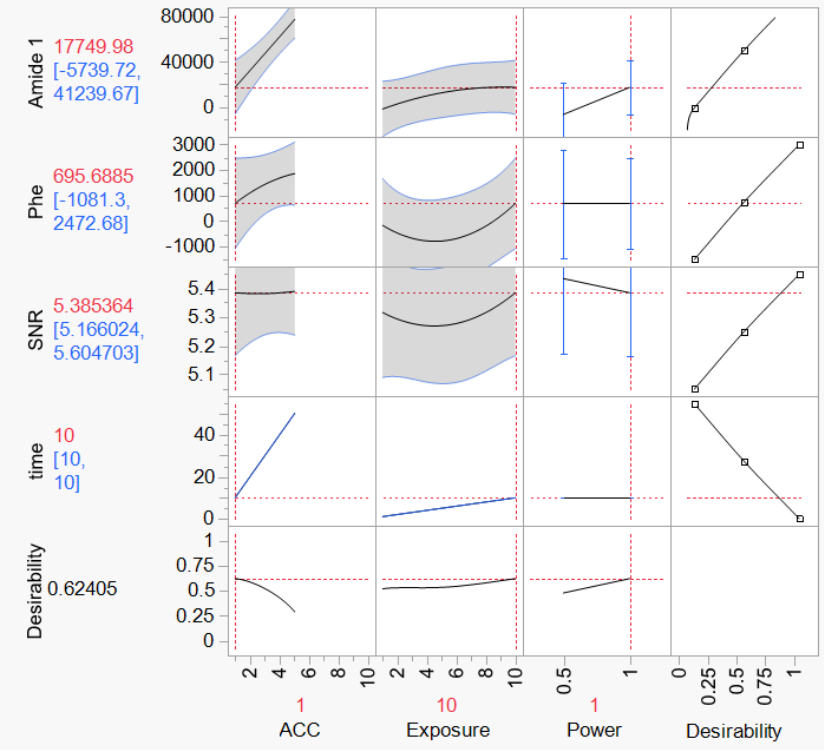

Figure 5.24 Breakthrough device Raman DOE prediction profiler of chosen factors within instrumental measurement ranges. Prediction profiler for BT B CUB titre at 3.60 mg ml^{-1}. 95% confidence interval can be seen as bars on the individual points. Exposure and time are in seconds. ACC is accumulations. Power is in percent of 500 mW.

Exposure had the strongest effect on SNR, although the changes were within the 95% confidence intervals (Figure 5.24). Accumulations had little to no effect on SNR with only an increase of 0.1. However, accumulations did have a greater effect on amide and Phe peak intensity, increasing accumulations produced spectra with increased noise and meant resolving peaks was more difficult. Exposure did increase overall intensity for the amide I and Phe peaks. Increasing laser power to 100% had a detrimental effect on SNR but within confidence intervals and increased spectral intensity. As shown by Figure 5.18, the 500 mW (100%) laser setting did not cause changes in the sample and as this measurement was performed at a lower accumulation and exposure time, 100% laser power was chosen. As the Raman system has to go through different diffraction grating positions to achieve the range of Raman shifts (cm^{-1}) in the spectrum, the true measurement time is greater than just exposure x accumulations and resulted in ≈3x estimated measurement time. An exposure time of 10 seconds, 1 accumulation and 100% laser power were selected.

5.3.7 Quantification of BT in breakthrough curve using Simulated in-line Raman microscopy

Using the parameters determined by DOE fractions selected from the HPLC analysis in section 5.3.3 were measured by Raman spectroscopy in the breakthrough device described in section 5.2.5 under flow simulating in-line measurements at a flow rate of 0.981 ml min^{-1}. The resultant spectra from BT A train flowthrough samples (Table 5.5) were used to train the SIM PLS algorithm. The ideal number of PLS components was chosen using Root mean squared error (RMSE) values in the same manner as described in section 5.3.5. Spectra shown in Appendix Figure 8.7 were removed from data sets as they contained no observable Raman spectrum.

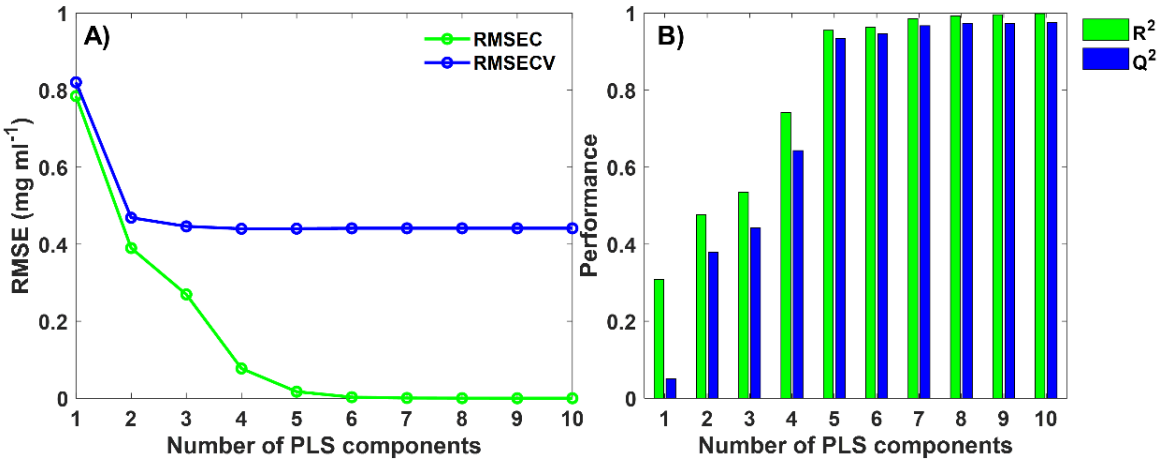

Figure 5.25 Statistical analysis of non-pre-processed Raman PLS training and cross validation of models for breakthrough device measurements of BT A "Train" data sets. A) RMSE analysis of PLS model with increasing components. RMSEC is from applying model against training model. RMSECV is applying model to leave one out (LOOCV) cross validation of training data. B) R^2 vs Q^2 plot. R^2 was calculated from the training data set. Q^2 was calculated from LOOCV. Green=Data from applying model to training data. Blue= Data from applying model to LOOCV data.

The model was optimised by pre-processing spectral data. Three PLS models arose utilising 0^{th} derivative, 1^{st} derivative, 2^{nd} derivative spectra to improve the prediction for both BT A and BT B titres.

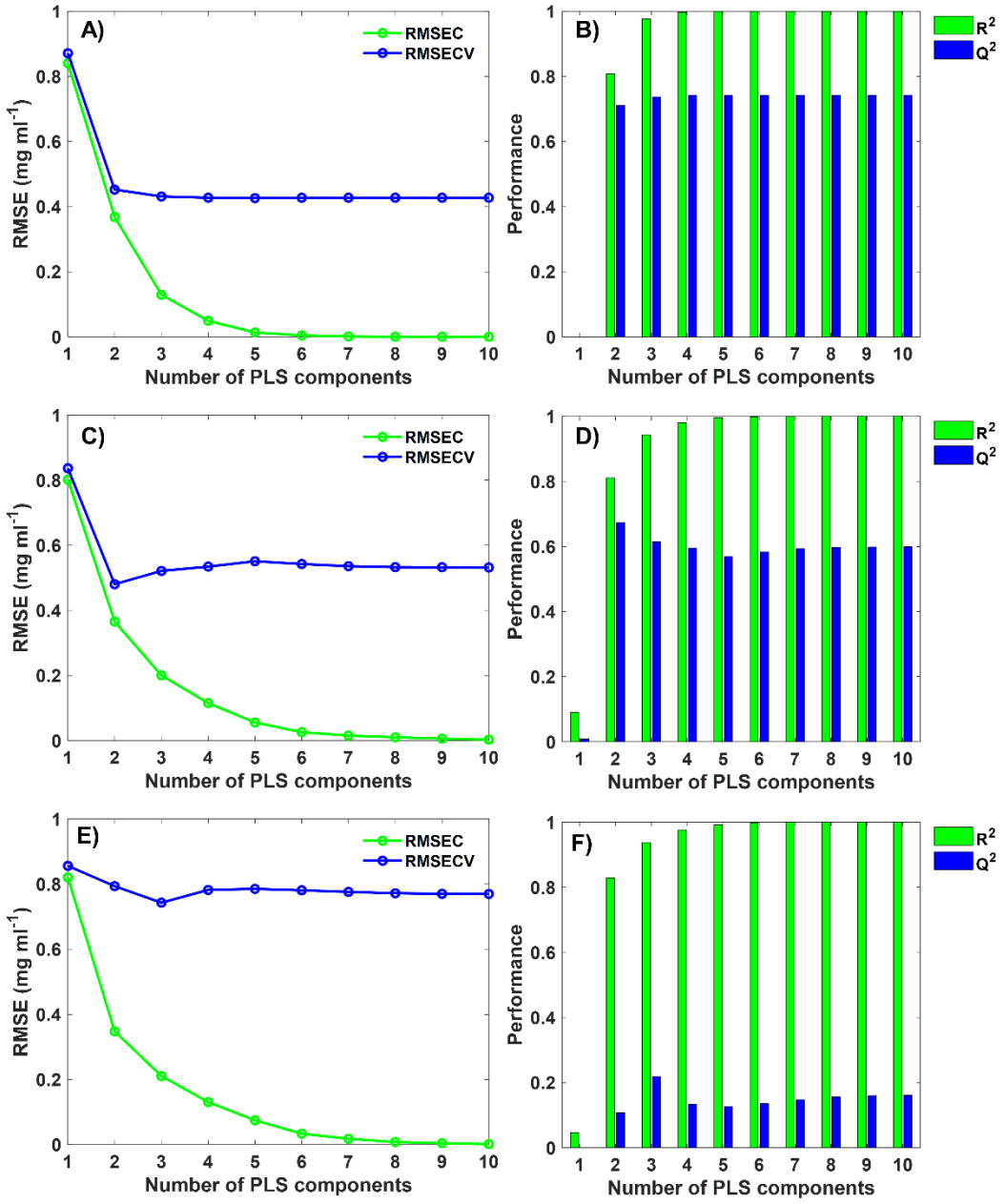

Figure 5.26 Statistical analysis of breakthrough device Raman PLS model using spectral pre-processing for 0^{th}, 1^{st} 2^{nd} derivative spectra. A) RMSE plot on Training data and LOOCV for 0^{th} derivative PLS model B) Goodness of fit (R^2) and Goodness of prediction (Q^2) plot for training data and LOOCV for 0^{th} derivative spectra PLS model C) RMSE plot on Training data and LOOCV for 1^{st} derivative Raman PLS model D) Goodness of fit and Goodness of prediction plot for training data and LOOCV for 1^{st} derivative Raman PLS model E) RMSE plot on Training data and LOOCV for 2^{nd} derivative PLS model F) Goodness of fit and Goodness of prediction plot for training data and LOOCV for 2^{nd} derivative Raman PLS model) pre-processing. Green=Data from applying model to training data. Blue= Data from applying model to LOOCV data. 0^{th} derivative spectra with SNV processing. 1^{st} derivative Raman PLS model with SNV and Savitzky Golay filter (Window= 45, Derivative=1, Polynomial=1) pre-processing. 2^{nd} derivative Raman PLS model with SNV and Savitzky Golay filter (Window= 55, Derivative=2, Polynomial=2) pre-processing

The 0th derivative model with SNV normalisation at 5 components had an RMSE of 0.43 mg ml^{-1} and Q^2 of 0.74 (Figure 5.26 A & B). A 5-component model was used for SNV pre-processed model. The 1st order model using Savitzky Golay filter (Window= 45 Derivative=1 Polynomial=1) with 2 components had a RMSE of 0.11 mg ml^{-1} and Q^2 of 0.98 (Figure 5.26 C& D). 2 components were used for 1st order model. The 2nd order model with 3 components using Savitzky Golay filter (Window = 55, Derivative = 2, Polynomial = 2) pre-processing had an RMSE of 0.74 mg ml^{-1} and Q^2 of 0.22. 2nd order model was chosen to be a 3-component model (Figure 5.26 E& F).

Table 5.10 Breakthrough Raman device root mean squared error of prediction (RMESP) when applying model against test data sets.

PLS Model	BT A test RMSEP (mg ml^{-1})	BT B test RMSEP (mg ml^{-1})
No pre processing	0.51	1.06
SNV,0th derivative	0.45	0.43
1st derivative	0.50	0.69
2nd derivative	0.70	0.83

Of the three optimised Raman PLS models for quantification of BT the lower RMSE and higher Q^2 values indicated that the 0th SNV pre-processed model was best for quantification of BT in flowthrough samples. The models were also compared for the test samples for the quantification of flowthrough samples. In agreement with Cross validation results the SNV pre-processed 0th derivative PLS model performed best at predicting BT titre (Table 5.10). Overall prediction RMSEP was similar across both BTs indicating that the breakthrough device as a means of predicting BT titre could be incorporated into a platform approach to monitor multiple BT's and would not need to be calibrated for each new BT that is purified. From the BT titre the DBC could then be calculated according to Equation 5.2.

Table 5.11 DBC calculated using Raman spectroscopy with inline breakthrough device.

HiScreen resin type	Cycle	BT	Residence time (min)	Breakthrough Raman DBC (mg ml^{-1})	Sample designation
MabSelect SuRe	28	A	4	28.70	BT A Test
MabSelect SuRe	29	B	5	22.36	BT B Test
MabSelect PrismA	28	A	4	57.24	BT A Test
MabSelect PrismA	29	B	5	27.98	BT B Test

5.4 Discussion

Novel Raman spectroscopy methods were successfully used to quantify BTs in CUB solutions with no extra preparative steps. Methods developed consisted of both high-throughput well based methodology and a simulated in-line breakthrough device set up.

Table 5.12 Comparison of DBC predictions for cycles 28 and 29 using HPLC, UV chromatogram, well plate Raman method and simulated inline Raman

HiScreen resin type	Cycle	BT	RT (min)	HPLC DBC (mg ml $^{-1}$)	Chromatogram (mg ml^{-1})	Well plate Raman DBC (mg ml^{-1})	Breakthrough Raman DBC (mg ml^{-1})
MabSelect SuRe	28	A	4	36.97	39.23	38.48	28.71
MabSelect SuRe	29	B	5	37.45	36.54	37.90	22.36
MabSelect PrismA	28	A	4	58.63	61.98	60.42	57.24
MabSelect PrismA	29	B	5	59.21	56.62	59.93	27.98

To compare Raman DBC predictions the methods were compared to chromatogram derived DBC results due to UV chromatograms having a lower %CV(SD) than HPLC. Equation 5.8 was used to compare the HPLC and Raman calculated DBC to UV chromatogram calculated DBC.

$$\%CV(RMSE) = \frac{RMSE}{\bar{y}} * 100 \qquad 5.8$$

%CV =coefficient of variation, $\bar{y}$ =the average actual measurement and RMSE=Root mean square error

The other industrial method of using HPLC had a %CV (RMSE) of only 1.25% showing both methods have been optimised for calculating DBC. Little difference is observed in predicted DBC between these methods. The high throughput well plate and inline breakthrough Raman derived DBC had a %CV of 1.99% and 16.98%. The well plate method observed a slight increase of 0.74% CV% compared to HPLC. This shows the well plate method for Raman performed comparably to the HPLC for predicting DBC. Not only was Raman shown to be just as good as current methods but has added advantages in that Raman was able to be used as a platform approach to quantify BT A and BT B flowthrough after only being trained on BT A data. This indicates Raman is able to quickly quantify multiple BTs without the need of additional calibration, whereas HPLC and UV chromatogram require calibration for each new BT they are used to quantify. This will save time in in the time intensive step of optimising flow

rates for purification of BT's. The trend of Well plate also matches UV with Prism A exhibiting greater DBC than SuRe columns, and BT A at 4 minutes residence time having higher DBC than BT B at 5 minutes residence time.

The Breakthrough device was able to quantify DBC's of BT's but was less accurate than the 96 well plate with approach %CV of 17%. The model served as a proof of concept that Raman can be used inline but would greatly benefit from being actually in-line connected to the ÄKTA system where larger volumes could be analysed i.e. 2 ml sample volumes under flow. The use of a larger volume to measure would mean increased scan and accumulations which would allow for greatly increased signal and spectra with outputs more similar to the 96 well plate methodology. Stronger scattering signals would allow for improved titre differentiation and therefore better DBC quantification. Comparison of DOE sections 5.3.4 and 5.3.6 confirms an increase in scans and accumulations would increase signal dramatically and improve responses. Another way to improve the in-line model would be to use duplicate N=2 measurements for all observed titres allowing for a larger data set similar to the well plates in size to be used in training the PLS model.

Overall, Raman has been shown as a useful tool for calculating BT titre and DBC. These are just one PQA. Access to other meta data for samples such as Glycation and would allow for generation of a model for other quality attributes in collected fractions [151, 152]. Another PQA that could easily be assessed by Raman Is purity of sample if data on high and low molecular weight contaminants was available. The quantification of contaminants has already been shown recent literature [117, 155]. Leaving Raman methodologies with the ability to quantify multiple PQAs in one measurement would reduce the time needed for multiple assays on BT production. Another PQA that could easily be assessed by Raman Is purity of sample if data on high and low molecular weight contaminants was available. The quantification of contaminants has already been shown recent literature [117, 155].

The utilisation on multivariate techniques like Raman would mean quicker and cheaper product characterisation due to time and labour saved costs. Overall improving identified bottlenecks in production will improve availability of new life saving drugs and cheaper production costs will mean BTs will be more accessible to patients.

Chapter 6- Final conclusions and future perspectives

6.1 Final conclusions

BTs are becoming increasingly used to treat a wide range of diseases, due mainly to their very high specificity. However, these life changing and life-saving treatments are extremely expensive and this can limit accessibility to patients. Protein A chromatography (PrAc) is responsible for the majority of downstream processing costs due to the high resin cost, exacerbated by resin degradation, which is detectable as a reduction in binding capacity [54, 55].

In the research described in this thesis, vibrational spectroscopy was successfully used to a) establish static binding capacities of unused and used resin samples, b) demonstrate that binding capacity decay is not homogenous through columns and c) reveal the cause of the decrease in Protein A resin binding capacity. The spectroscopic approaches also d) allowed monitoring of resin performance in small scale unit industrial operations during the downstream processing of BT's.

6.1.1 Both ATR-FTIR and Raman spectroscopy can be used to assess Protein A binding capacity

Protein A resin binding capacity was successfully calculated utilising both ATR-FTIR spectroscopy and Raman spectroscopy meeting industry standards. The used resin samples respective binding capacity could be calculated spatial location was shown by both methods to affect degradation of performance.

The inlet showed marked binding capacity reduction when compared to the outlet of the column therefore column degradation Is heterogeneous in PrAc . With the high cost of columns, this finding shows that the outlet of a column degrades slower than the inlet and thus extended use of outlet region resin could be utilised to reduce waste and cost of Protein A resin. Both spectroscopic methods quantified mAb directly on the resin as opposed to indirectly by observing flowthrough in SBC calculation. Although quantification showed a marked reduction in binding capacity it did not explain why the reduction occurred, both ATR-FTIR and Raman spectroscopy provided chemical information on the conformation of proteins not normally attainable from SBC analysis alone.

6.1.2 Causes of binding capacity decay

In-situ ATR-FTIR spectroscopy allowed SPA ligand density to be quantified and confirmed showed that changes in ligand density did not correlate with the reduction in binding capacity of the used resin form each spatial location. It was hypothesised that the inlet of the column is

exposed to more contaminants than the outlet and thus it seemed plausible that irreversibly bound contaminants were the primary cause of capacity loss in the resin [59, 66].

The chemical information provided by spectroscopy was further utilised to observe the conformation of Protein A ligand on the resin which remained in its native state even after 25 cycles of purification and repeated CIP steps. ATR-FTIR spectroscopy is limited to probing the surface of the resin beads which are up to 120 μm in diameter, thus confocal Raman spectroscopy was used to probe the beads and observe mAb binding within individual beads by depth profiling.

Depth profiling of unused PrAc resin when loaded below saturation with mAb showed homogeneous binding across the beads occurred. Interestingly, in used samples there was heterogeneous binding. When combined with the previous findings that there was no change in the density or state of the Protein A it becomes clear that the ligand is less accessible in the used resins. This is supported by early studies showing a decrease in Protein A resin pore size after repeated use [58].

The effect of the contaminants was clear, however the nature of the contaminates could be explored by assessing the spectral data from each slice a used resin sample with no mAbs loaded. Results indicating the presence of Phenylalanine rich proteins suggested irreversibly bound mAb was contributing to the loss in binding capacity. Mass spec confirmed the presence of mAbs and revealed other HCP protein species bound to the used resins. The HCP species with the highest frequency of detection were species known to co-elute with mAbs during purification. This suggests a mechanism of fouling whereby mAbs become irreversible bound and then act as a nucleation point for HCPs. The gradual build up of the contaminants reduces the pore size in the resin and limits the ability of the mAb to access the Protein A. Confocal Raman and ATR-FTIR spectroscopy were essential for gaining insights into how column usage affects binding capacity both in terms of column location and for revealing the chemical basis of reduced binding capacity.

6.1.3 Raman spectroscopy as an alternative to industry monitoring of changes in dynamic binding capacity.

Monitoring of the dynamic binding capacity of Protein A during operations is essential for approval as column performance metrics is mandated by the FDA. Current industry standard methods, HPLC and UV chromatography are effective but provide no additional informational. Furthermore, these methods require calibration for each new BT, slowing down the development of protocols for each new BT. The high throughput well plate Raman method proved to be at least as effective at analysing DBC and quantifying BT as current industry

methods. However in combination with PLS analysis RAMAN is able to quantify a BT not used in training the PLS model potentially reducing the time and effort required for each new BT. Raman has an extra key advantage, since with further meta information on the BT's, it is theoretically possible to assess other properties of the mAb simultaneously such as glycation and the presence of high molecular weight contaminants. Importantly the added chemical information can provide added insight into batch to batch quality and overall product conformity as mandated by the FDA.

The in-line Raman methodology developed did underperform compared to the well plate and HPLC. The ability to quantify BT and thus the DBC decreased significantly when changing to a BT that was not used in training the PLS model. However, in-line Raman methodology was able to identify BT in cell supernatant which contains thousands of proteins + media components without the need for separation or chemical labels and served as a proof of concept that Raman can be used in-line in the quantification of BTs. Results could be improved by increasing the total measurement time of liquid under flow. Having a spectrometer connected directly to the purification system will remove the limitation of measurement time as larger volumes can be observed and thus the time to observe fractions can increase. Increased measurement time will mean increased signal and decreased noise in spectral results. Overall, this work showcases potential of Raman spectroscopy as an analytical method aiding development of purification protocols and facilitating quality control of BTs.

6.2 Future perspectives

Based on the work presented in this thesis this section makes recommendations for future investigations. Examples of how PrAc would benefit from spectroscopic analysis are detailed.

Since in situ ATR-FTIR spectroscopy can quantify mAbs present on protein A resin, further development of this method to allow on-column ATR-FTIR spectroscopy may be useful. This on column approach would need to ensure contact with the beads is sufficient and ATR-FTIR imaging would aid in this regard. The use of a custom 3d printed column for resin packing would be necessary. As resin are solid spheres, an external plunger to ensure adequate contact with IRE may be needed, it may be possible that packed column pressure is sufficient for contact. The addition of ATR-FTIR spectroscopic information to the continuous OD 280 nm readouts in a chromatogram would be useful and would allow for direct assessment of mAbs bound to Protein A resin; properties such as mAb stability, mAb concentration and ligand stability could all be assessed simultaneously.

Raman spectroscopy could also be implemented on-column through the use of a Raman transparent window made of sapphire. Sapphire would be useful as it can withstand the pressure exerted on it by packed resin and the flow of buffers, typically around 0.3 MPa. Sapphire is a hard material rating 9 on the MOH scale (for reference diamond is 10). Raman spectroscopy could be used to observe single spots of the resin under flow. A step-by-step scan approach to generate chemical images of the resin beads against the sapphire window between purification cycles would allow for assessment of resin surface and binding profile . Another approach for Raman spectroscopy would be the use of a macro imaging alignment allowing for multiple beads to be measured simultaneously. The information gained from this type of analysis will give manufacturers added insight into how BTs are behaving during critical processes such as PrAc. It should be noted that this approach to be applied to any column used in downstream processing.

Vibrational spectroscopy is not limited to just on-column but can also be used in-line to observe all components eluting off the column. Both Raman and ATR-FTIR spectroscopy can provide details on the chemical nature and quantity of eluted components without the need for offline assays. In-line spectroscopy would suit current purification methodologies without the need for custom columns but would require a breakthrough device like the one described in chapter 5. This would allow for quick adaptation to current workflows in downstream processing and help streamline development and production of BTs with added insight into BT behaviour during PrAc.

Chapter 7- References

1. Chenoweth A, Crescioli S. The Antibody Society. Therapeutic monoclonal antibodies approved or in regulatory review. https://www.antibodysociety.org/antibody-therapeutics-product-data/2022 [
2. Kaplon H, Chenoweth A, Crescioli S, Reichert JM. Antibodies to watch in 2022. MAbs. 2022;14(1):2014296.
3. Al Shaer D, Al Musaimi O, Albericio F, de la Torre BG. 2018 FDA Tides Harvest. Pharmaceuticals (Basel, Switzerland). 2019;12(2):52.
4. Sánchez-Trasviña C, Flores-Gatica M, Enriquez-Ochoa D, Rito-Palomares M, Mayolo-Deloisa K. Purification of Modified Therapeutic Proteins Available on the Market: An Analysis of Chromatography-Based Strategies. Frontiers in Bioengineering and Biotechnology. 2021;9.
5. Mullard A. FDA approves 100th monoclonal antibody product. Nature Reviews Drug Discovery. 2021;20:491-5.
6. Kaplon H, Muralidharan M, Schneider Z, Reichert JM. Antibodies to watch in 2020. MAbs. 2020;12(1):1703531.
7. Moorkens E, Meuwissen N, Huys I, Declerck P, Vulto AG, Simoens S. The Market of Biopharmaceutical Medicines: A Snapshot of a Diverse Industrial Landscape. Frontiers in Pharmacology. 2017;8:314.
8. Kaplon H, Reichert JM. Antibodies to watch in 2019. MAbs. 2019;11(2):219-38.
9. Reichert JM. Antibodies to watch in 2010. MAbs. 2010;2(1):84-100.
10. Grilo AL, Mantalaris A. The Increasingly Human and Profitable Monoclonal Antibody Market. Trends in Biotechnology. 2019;37(1):9-16.
11. Kelley B. Downstream Processing of Monoclonal Antibodies: Current Practices and Future Opportunities. Process Scale Purification of Antibodies2017. p. 1-21.
12. Sompayrac La. How the immune system works. Fifth edition. ed. Chichester :2016.
13. Vidarsson G, Dekkers G, Rispens T. IgG subclasses and allotypes: from structure to effector functions. Frontiers in Immunology. 2014;5:520.
14. AlDallal SM. Ofatumumab - a valid treatment option for chronic lymphocytic leukemia patients. Therapeutics and Clinical Risk Management. 2017;13:905-7.
15. Gupta A, Gonzalez-Rojas Y, Juarez E, Crespo Casal M, Moya J, Falci DR, et al. Early Treatment for Covid-19 with SARS-CoV-2 Neutralizing Antibody Sotrovimab. The New England Journal of Medicine. 2021;385(21):1941-50.
16. Kaplon H, Reichert JM. Antibodies to watch in 2018. MAbs. 2018;10(2):183-203.
17. Lampson LA. Monoclonal antibodies in neuro-oncology: Getting past the blood-brain barrier. MAbs. 2011;3(2):153-60.
18. Pardridge WM, Buciak JL, Friden PM. Selective transport of an anti-transferrin receptor antibody through the blood-brain barrier in vivo. Journal of Pharmacology and Experimental Therapeutics. 1991;259(1):66.
19. Wang W. Protein aggregation and its inhibition in biopharmaceutics. International Journal of Pharmaceutics. 2005;289(1-2):1-30.
20. Lonberg N. Human antibodies from transgenic animals. Nature Biotechnology. 2005;23(9):1117-25.
21. Inmaculada Hernandez PP, Samuel W. Bott BS, Anish S. Patel BS, Collin G. Wolf BS, Alexa R. Hospodar BS, Shivani Sampathkumar BS, et al. Pricing of Monoclonal Antibody Therapies: Higher If Used for Cancer? The American Journal of Managed Care. 2018;24(2):109-12.
22. KÖHler G, Milstein C. Continuous cultures of fused cells secreting antibody of predefined specificity. Nature. 1975;256(5517):495-7.
23. Jain E, Kumar A. Upstream processes in antibody production: evaluation of critical parameters. Biotechnology Advances. 2008;26(1):46-72.

24. Morrison SL, Johnson MJ, Herzenberg LA, Oi VT. Chimeric human antibody molecules: mouse antigen-binding domains with human constant region domains. Proceedings of the National Academy of Sciences. 1984;81(21):6851-5.
25. Boulianne GL, Hozumi N, Shulman MJ. Production of functional chimaeric mouse/human antibody. Nature. 1984;312(5995):643-6.
26. Birch JR, Racher AJ. Antibody production. Advanced Drug Delivery Reviews. 2006;58(5):671-85.
27. Matasci M, Hacker DL, Baldi L, Wurm FM. Recombinant therapeutic protein production in cultivated mammalian cells: current status and future prospects. Drug discovery today: Technologies. 2008;5(2-3):e37-42.
28. Grachev V, Magrath D, Griffiths E. WHO requirements for the use of animal cells as in vitro substrates for the production of biologicals (Requirements for biological susbstances no. 50). Biologicals. 1998;26(3):175-93.
29. Tarrant RD, Velez-Suberbie ML, Tait AS, Smales CM, Bracewell DG. Host cell protein adsorption characteristics during protein A chromatography. Biotechnology Progress. 2012;28(4):1037-44.
30. Zoon KC. Points to Consider in the Manufacture and Testing of Monoclonal Antibody Products for Human use Rockville, MD: FDA Center for Biologics Evaluation and Research; 1997 [cited FDA. Available from: https://www.fda.gov/regulatory-information/search-fda-guidance-documents/points-consider-manufacture-and-testing-monoclonal-antibody-products-human-use.
31. Shukla AA, Suda E. Harvest and Recovery of Monoclonal Antibodies: Cell Removal and Clarification. Process Scale Purification of Antibodies2017. p. 55-79.
32. Flatman S, Alam I, Gerard J, Mussa N. Process analytics for purification of monoclonal antibodies. Journal of Chromatography B. 2007;848(1):79-87.
33. Ghose S, Jin M, Liu J, Hickey J, Lee S. Integrated Polishing Steps for Monoclonal Antibody Purification. Process Scale Purification of Antibodies2017. p. 303-23.
34. Wang Y, Chen Q, Xian M, Nian R, Xu F. Application of enhanced electronegative multimodal chromatography as the primary capture step for immunoglobulin G purification. AMB Express. 2018;8(1):93.
35. Liu W, Sun Y, Yu J, Chen Q, Bao Z, Fan X, et al. Advance chromatin extraction improves the performance of electropositive mixed-mode chromatography as a capture step and enables its integration with void-exclusion anion exchange chromatography as a two-column-step purification platform for monoclonal antibody production. Biochemical Engineering Journal. 2019;142:145-52.
36. Curling J. The Development of Antibody Purification Technologies. Process Scale Purification of Antibodies2017. p. 23-54.
37. Arunakumari A, Wang J. Purification of Human Monoclonal Antibodies: Non-Protein a Strategies. Process Scale Purification of Antibodies2017. p. 135-53.
38. Kelley B. Very large scale monoclonal antibody purification: the case for conventional unit operations. Biotechnology Progress. 2007;23(5):995-1008.
39. Walchli R, Fanizzi F, Massant J, Arosio P. Relationship of PEG-induced precipitation with protein-protein interactions and aggregation rates of high concentration mAb formulations at 5 degrees C. European Journal of Pharmaceutics and Biopharmaceutics. 2020;151:53-60.
40. Guiochon G, Beaver LA. Separation science is the key to successful biopharmaceuticals. Journal of Chromatography A. 2011;1218(49):8836-58.
41. Kangwa M, Yelemane V, Ponnurangam A, Fernandez-Lahore M. An engineered Staphylococcal Protein A based ligand: Production, characterization and potential application for the capture of Immunoglobulin and Fc-fusion proteins. Protein Expression and Purification. 2019;155:27-34.
42. Vunnum S, Vedantham G, Hubbard B. Protein a-Based Affinity Chromatography. Process Scale Purification of Antibodies2017. p. 113-33.

43. Hjelm H, Sjodahl J, Sjoquist J. Immunologically active and structurally similar fragments of protein A from Staphylococcus aureus. European journal of biochemistry. 1975;57(2):395-403.
44. Hjelm H, Hjelm K, Sjöquist J. Protein a from Staphylococcus aureus. Its isolation by affinity chromatography and its use as an immunosorbent for isolation of immunoglobulins. FEBS Letters. 1972;28(1):73-6.
45. Deisenhofer J. Crystallographic refinement and atomic models of a human Fc fragment and its complex with fragment B of protein A from Staphylococcus aureus at 2.9- and 2.8-.ANG. resolution. Biochemistry. 1981;20(9):2361-70.
46. Ghose S, Allen M, Hubbard B, Brooks C, Cramer SM. Antibody variable region interactions with Protein A: implications for the development of generic purification processes. Biotechnology and Bioengineering. 2005;92(6):665-73.
47. Nik Jaafar MI, Lowe JA, Ling NR, Jefferis R. Immunogenic and antigenic epitopes of immunoglobulins—VII. The topographical distribution of Fcγ epitopes and the relationship of an iso-allotypic specificity to the presence of histidine 435. Molecular Immunology. 1984;21(2):137-43.
48. Sciences GI. Capacity and performance of MabSelect™ PrismA protein A chromatography resin [Available from: https://cdn.gelifesciences.com/dmm3bwsv3/AssetStream.aspx?mediaformatid=10061&destinationid=10016&assetid=26524.
49. Boulet-Audet M, Byrne B, Kazarian SG. Cleaning-in-place of immunoaffinity resins monitored by in situ ATR-FTIR spectroscopy. Analytical Biochemistry. 2015;407(23):7111-22.
50. Shukla AA, Jiang C, Ma J, Rubacha M, Flansburg L, Lee SS. Demonstration of robust host cell protein clearance in biopharmaceutical downstream processes. Biotechnology Progress. 2008;24(3):615-22.
51. Goey CH, Alhuthali S, Kontoravdi C. Host cell protein removal from biopharmaceutical preparations: Towards the implementation of quality by design. Biotechnology Advances. 2018;36(4):1223-37.
52. MabSelect PrismA affinity chromatography data flie [Internet]. 2020 [cited 20/08/2022]. Available from: https://cdn.cytivalifesciences.com/api/public/content/digi-26546-pdf.
53. Nian R, Zhang W, Tan L, Lee J, Bi X, Yang Y, et al. Advance chromatin extraction improves capture performance of protein A affinity chromatography. Journal of Chromatography A. 2016;1431:1-7.
54. Vermasvuori R, Hurme M. Economic comparison of diagnostic antibody production in perfusion stirred tank and in hollow fiber bioreactor processes. Biotechnology Progress. 2011;27(6):1588-98.
55. Yang O, Qadan M, Ierapetritou M. Economic Analysis of Batch and Continuous Biopharmaceutical Antibody Production: A Review. Journal of Pharmaceutical Innovation. 2019;15(1):182-200.
56. Boulet-Audet M, Kazarian SG, Byrne B. In-column ATR-FTIR spectroscopy to monitor affinity chromatography purification of monoclonal antibodies. Scientific Reports. 2016;6:30526.
57. Close EJ, Salm JR, Iskra T, Sorensen E, Bracewell DG. Fouling of an anion exchange chromatography operation in a monoclonal antibody process: Visualization and kinetic studies. Biotechnology and Bioengineering. 2013;110(9):2425-35.
58. Zhang S, Daniels W, Salm J, Glynn J, Martin J, Gallo C, et al. Nature of foulants and fouling mechanism in the Protein A MabSelect resin cycled in a monoclonal antibody purification process. Biotechnology and Bioengineering. 2016;113(1):141-9.
59. Lintern K, Pathak M, Smales CM, Howland K, Rathore A, Bracewell DG. Residual on column host cell protein analysis during lifetime studies of protein A chromatography. Journal of Chromatography A. 2016;1461:70-7.

60. Freiherr von Roman M, Berensmeier S. Improving the binding capacities of protein A chromatographic materials by means of ligand polymerization. Journal of Chromatography A. 2014;1347:80-6.
61. Gagnon P, Nian R, Lee J, Tan L, Latiff SM, Lim CL, et al. Nonspecific interactions of chromatin with immunoglobulin G and protein A, and their impact on purification performance. Journal of Chromatography A. 2014;1340:68-78.
62. Muller E, Vajda J. Routes to improve binding capacities of affinity resins demonstrated for Protein A chromatography. Journal of Chromatography B. 2016;1021:159-68.
63. Pabst TM, Thai J, Hunter AK. Evaluation of recent Protein A stationary phase innovations for capture of biotherapeutics. Journal of Chromatography A. 2018;1554:45-60.
64. Cytiva. MabSelect SuRe affinity chromatography data flie 2020 [Available from: https://cdn.cytivalifesciences.com/api/public/content/digi-13584-original.
65. Hahn R, Schlegel R, Jungbauer A. Comparison of protein A affinity sorbents. Journal of Chromatography B. 2003;790(1-2):35-51.
66. Jasulaityte G, Johansson HJ, Bracewell DG. Chromatography process development aided by a dye-based assay. Journal of Chemical Technology and Biotechnology. 2019;95(1):132-41.
67. Teske CA, Schroeder M, Simon R, Hubbuch J. Protein-labeling effects in confocal laser scanning microscopy. The Journal of Physical Chemistry B. 2005;109(28):13811-7.
68. Maiti NC, Apetri MM, Zagorski MG, Carey PR, Anderson VE. Raman spectroscopic characterization of secondary structure in natively unfolded proteins: alpha-synuclein. Journal of the American Chemical Society. 2004;126(8):2399-408.
69. Kengne-Momo RP, Daniel P, Lagarde F, Jeyachandran YL, Pilard JF, Durand-Thouand MJ, et al. Protein Interactions Investigated by the Raman Spectroscopy for Biosensor Applications. International Journal of Spectroscopy. 2012;2012:462901.
70. Takeuchi H. Raman structural markers of tryptophan and histidine side chains in proteins. Biopolymers. 2003;72(5):305-17.
71. Puppels G. Laser irradiation and Raman spectroscopy of single living cells and chromosomes: Sample degradation occurs with 514.5 nm but not with 660 nm laser light*1. Experimental Cell Research. 1991;195(2):361-7.
72. Bohr N. LXXIII. On the constitution of atoms and molecules. The London, Edinburgh, and Dublin Philosophical Magazine and Journal of Science. 1913;26(155):857-75.
73. Coblentz WW. Radiometric Investigations of Infra-red Absorption and Reflection Spectra: U.S. Government Printing Office; 1906.
74. Michelson AA, Morley EW. On the relative motion of the Earth and the luminiferous ether. American Journal of Science. 1887;s3-34(203):333.
75. Thompson RQ. Experiments in software data handling. Journal of Chemical Education. 1985;62(10):866.
76. Griffiths PR, de Haseth JA. Fourier Transform Infrared Spectrometry2007.
77. Stuart BH. Infrared Spectroscopy: Fundamentals and Applications: Wiley; 2004.
78. Bassan P, Kohler A, Martens H, Lee J, Jackson E, Lockyer N, et al. RMieS-EMSC correction for infrared spectra of biological cells: Extension using full Mie theory and GPU computing. Journal of Biophotonics. 2010;3(8-9):609-20.
79. Venyaminov S, Prendergast FG. Water (H2O and D2O) molar absorptivity in the 1000-4000 cm-1 range and quantitative infrared spectroscopy of aqueous solutions. Analytical Biochemistry. 1997;248(2):234-45.
80. Edelmann A, Lendl B. Toward the optical tongue: flow-through sensing of tannin-protein interactions based on FTIR spectroscopy. Journal of the American Chemical Society. 2002;124(49):14741-7.
81. Glassford SE, Byrne B, Kazarian SG. Recent applications of ATR FTIR spectroscopy and imaging to proteins. Biochimica et Biophysica Acta (BBA) - Proteins and Proteomics. 2013;1834(12):2849-58.

82. Poonprasartporn A, Chan KLA. Label-free study of intracellular glycogen level in metformin and resveratrol-treated insulin-resistant HepG2 by live-cell FTIR spectroscopy. Biosensors and Bioelectronics. 2022;212:114416.
83. Kazarian SG, Chan KLA. Micro- and macro-attenuated total reflection Fourier transform infrared spectroscopic imaging. Applied Spectroscopy. 2010;64(5):135A-52A.
84. Tiernan H, Byrne B, Kazarian SG. Insight into Heterogeneous Distribution of Protein Aggregates at the Surface Layer Using Attenuated Total Reflection-Fourier Transform Infrared Spectroscopic Imaging. Analytical Chemistry. 2020;92(7):4760-4.
85. Frosch T, Chan KL, Wong HC, Cabral JT, Kazarian SG. Nondestructive three-dimensional analysis of layered polymer structures with chemical imaging. Langmuir. 2010;26(24):19027-32.
86. Ohta K, Iwamoto R. Experimental Proof of the Relation between Thickness of the Probed Surface Layer and Absorbance in FT-IR/ATR Spectroscopy. Applied Spectroscopy. 1985;39(3):418-25.
87. Harrick NJ, Beckmann KH. Internal Reflection Spectroscopy. In: Kane PF, Larrabee GB, editors. Characterization of Solid Surfaces. Boston, MA: Springer US; 1974. p. 215-45.
88. Harrick NJ. Variable Angle Attachment for Internal Reflection Spectroscopy. Analytical Chemistry. 1965;37(11):1445-.
89. Harrick NJ, du Pre FK. Effective thickness of bulk materials and of thin films for internal reflection spectroscopy. Applied Optics. 1966;5(11):1739-43.
90. Kong J, Yu S. Fourier transform infrared spectroscopic analysis of protein secondary structures. Acta Biochim Biophys Sin (Shanghai). 2007;39(8):549-59.
91. Boulet-Audet M, Byrne B, Kazarian SG. High-throughput thermal stability analysis of a monoclonal antibody by attenuated total reflection FT-IR spectroscopic imaging. Analytical Chemistry. 2014;86(19):9786-93.
92. de Jongh HH, Goormaghtigh E, Ruysschaert JM. The different molar absorptivities of the secondary structure types in the amide I region: an attenuated total reflection infrared study on globular proteins. Analytical Biochemistry. 1996;242(1):95-103.
93. Barth A. The infrared absorption of amino acid side chains. Progress in Biophysics and Molecular Biology. 2000;74(3-5):141-73.
94. Byrne B, Beattie JW, Song CL, Kazarian SG. ATR-FTIR spectroscopy and spectroscopic imaging of proteins. In: Ozaki Y, Baranska M, Lednev IK, Wood BR, editors. Vibrational Spectroscopy in Protein Research: Academic Press; 2020. p. 1-22.
95. Demmel F, Doster W, Petry W, Schulte A. Vibrational frequency shifts as a probe of hydrogen bonds: thermal expansion and glass transition of myoglobin in mixed solvents. European Biophysics Journal. 1997;26(4):327-35.
96. Wasacz F, Olinger J, Jakobsen R. Fourier transform infrared studies of proteins using nonaqueous solvents. Effects of methanol and ethylene glycol on albumin and immunoglobulin G. Biochemistry. 1987;26(5):1464-70.
97. Dousseau F, Therrien M, Pézolet M. On the Spectral Subtraction of Water from the FT-IR Spectra of Aqueous Solutions of Proteins. Applied Spectroscopy. 2016;43(3):538-42.
98. Grosshans S, Rudt M, Sanden A, Brestrich N, Morgenstern J, Heissler S, et al. In-line Fourier-transform infrared spectroscopy as a versatile process analytical technology for preparative protein chromatography. Journal of Chromatography A. 2018;1547:37-44.
99. Raman CV, Krishnan KS. A New Type of Secondary Radiation. Nature. 1928;121(3048):501-2.
100. Ferraro JR, Nakamoto K, Brown CW. Basic Theory. In: Ferraro JR, Nakamoto K, Brown CW, editors. Introductory Raman Spectroscopy. San Diego: Academic Press; 2003. p. 1-94.
101. Rayleigh L. XXXIV. On the transmission of light through an atmosphere containing small particles in suspension, and on the origin of the blue of the sky. The London, Edinburgh, and Dublin Philosophical Magazine and Journal of Science. 1899;47(287):375-84.
102. Condon E. A Theory of Intensity Distribution in Band Systems. Physical Review. 1926;28(6):1182-201.

103. Franck J, Dymond EG. Elementary processes of photochemical reactions. Transactions of the Faraday Society. 1926;21(February):536-42.
104. Lipiainen T, Pessi J, Movahedi P, Koivistoinen J, Kurki L, Tenhunen M, et al. Time-Gated Raman Spectroscopy for Quantitative Determination of Solid-State Forms of Fluorescent Pharmaceuticals. Analytical Chemistry. 2018;90(7):4832-9.
105. Kneipp J, Kneipp H, Kneipp K. SERS--a single-molecule and nanoscale tool for bioanalytics. Chemical Society Reviews. 2008;37(5):1052-60.
106. Denisyuk YN. Photographic Reconstruction of the Optical Properties of an Object in Its Own Scattered Radiation Field. Soviet Physics Doklady. 1962;7:543.
107. Gabor D. A New Microscopic Principle. Nature. 1948;161(4098):777-8.
108. Battey DE, Slater JB, Wludyka R, Owen H, Pallister DM, Morris MD. Axial Transmissive f/1.8 Imaging Raman Spectrograph with Volume-Phase Holographic Filter and Grating. Applied Spectroscopy. 1993;47(11):1913-9.
109. Maczka M, Gagor A, Ptak M, Stefanska D, Macalik L, Pikul A, et al. Structural, phonon, magnetic and optical properties of novel perovskite-like frameworks of TriBuMe[M(dca)3] (TriBuMe = tributylmethylammonium; dca = dicyanamide; M = Mn(2+), Fe(2+), Co(2+), Ni(2+)). Dalton Transactions. 2019;48(34):13006-16.
110. Lerner JM. Imaging spectrometer fundamentals for researchers in the biosciences—A tutorial. Cytometry Part A. 2006;69A(8):712-34.
111. Denson SC, Pommier CJS, Denton MB. The Impact of Array Detectors on Raman Spectroscopy. Journal of Chemical Education. 2007;84(1):67.
112. Maury A, Revilla RI. Autocorrelation Analysis Combined with a Wavelet Transform Method to Detect and Remove Cosmic Rays in a Single Raman Spectrum. Applied Spectroscopy. 2015;69(8):984-92.
113. Everall NJ. Confocal Raman microscopy: Why the depth resolution and spatial accuracy can be much worse than you think. Applied Spectroscopy. 2000;54(10):1515-20.
114. Larsson M, Lindgren J, Ljunglof A, Knuuttila KG. Ligand distributions in agarose particles as determined by confocal Raman spectroscopy and confocal scanning laser microscopy. Applied Spectroscopy. 2003;57(3):251-5.
115. Xiao Y, Stone T, Bell D, Gillespie C, Portoles M. Confocal Raman Microscopy of Protein Adsorbed in Chromatographic Particles. Analytical Chemistry. 2012;84(17):7367-73.
116. Xiao Y, Stone T, Moya W, Killian P, Herget T. Confocal Raman Characterization of Different Protein Desorption Behaviors from Chromatographic Particles. Analytical Chemistry. 2014;86(2):1007-15.
117. Wei B, Woon N, Dai L, Fish R, Tai M, Handagama W, et al. Multi-attribute Raman spectroscopy (MARS) for monitoring product quality attributes in formulated monoclonal antibody therapeutics. MAbs. 2022;14(1):2007564.
118. Rolinger L, Rüdt M, Hubbuch J. Comparison of UV- and Raman-based monitoring of the Protein A load phase and evaluation of data fusion by PLS models and CNNs. Biotechnology and Bioengineering. 2021;118(11):4255-68.
119. Stewart JE, Richmond JC. Infrared Emission Spectrum of Silicon Carbide Heating. Journal of Research of the National Bureau of Standards. 1957;59(6):405.
120. Lewis IR, Griffiths PR. Raman Spectrometry with Fiber-Optic Sampling. Applied Spectroscopy. 1996;50(10):12A-30A.
121. Wang W, Roberts CJ. Protein aggregation - Mechanisms, detection, and control. International Journal of Pharmaceutics. 2018;550(1-2):251-68.
122. Demšar J, Curk T, Erjavec A, Gorup Č, Hočevar T, Milutinovič M, et al. Orange: data mining toolbox in Python. the Journal of machine Learning research. 2013;14(1):2349-53, 1532-4435.
123. Toplak. M, Read. S, Boronics. F, Solheim. J, Roudenko. O, Eduardo. J, et al. Quasars/orange-spectroscopy: Release 0.5.0. 2020.
124. Goding JW. Use of staphylococcal protein A as an immunological reagent. Journal of Immunological Methods. 1978;20(Apr):241-53.
125. Capacity and performance of MabSelect PrismA protein A chromatography resin [Internet]. GEHealthcare. 2017 [cited 08/07/2020]. Available from:

https://cdn.gelifesciences.com/dmm3bwsv3/AssetStream.aspx?mediaformatid=10061&destinationid=10016&assetid=26524.
126. Pakiman N, Isa N, Hassan MA, Walter J, Abdullah N. Comparison of binding capacity and affinity of monoclonal antibody towards different affinity resins using high-throughput chromatography method. Journal of Applied Sciences. 2012;12(11):1136-41.
127. Graille M, Stura EA, Corper AL, Sutton BJ, Taussig MJ, Charbonnier JB, et al. Crystal structure of a Staphylococcus aureus protein A domain complexed with the Fab fragment of a human IgM antibody: structural basis for recognition of B-cell receptors and superantigen activity. Proceedings of the National Academy of Sciences of the United States of America. 2000;97(10):5399-404.
128. Pathak M, Rathore AS. Mechanistic understanding of fouling of protein A chromatography resin. Journal of Chromatography A. 2016;1459:78-88.
129. Pathak M, Lintern K, Johnson TF, Nair AM, Mukherji S, Bracewell DG, et al. Analytical tools for monitoring changes in physical and chemical properties of chromatography resin upon reuse. Electrophoresis. 2019;40(23-24):3074-83.
130. Hans J. Johansson AL, Ronnie Palmgren, inventor; GE Healthcare Bio Sciences AB, assignee. Affinity chromatography matrix. EP2010.
131. Chan KLA, Kazarian SG. Attenuated total reflection Fourier transform infrared imaging with variable angles of incidence: a three-dimensional profiling of heterogeneous materials. Applied Spectroscopy. 2007;61(1):48-54.
132. Harrick NJ. Electric Field Strengths at Totally Reflecting Interfaces. Journal of the Optical Society of America. 1965;55(7):851-7.
133. Moore WH, Krimm S. Vibrational analysis of peptides, polypeptides, and proteins. II. beta-poly(L-alanine) and beta-poly(L-anaylglycine). Biopolymers. 1976;15(12NA-NA-770103-770104):2465-83.
134. Sekkal M, Huvenne J-P, Legrand P, Sombret B, Mollet J-C, Mouradi-Givernaud A, et al. Direct structural identification of polysaccharides from red algae by FTIR microspectrometry I: Localization of agar inGracilaria verrucosa sections. Mikrochimica Acta. 1993;112(1-4):1-10.
135. Sinnott RK. Flow of Fluids Through Granular Beds and Packed Columns. In: Chhabra R, Basavaraj MG, editors. Coulson and Richardson's Chemical Engineering: Butterworth-Heinemann; 2019. p. 335-86.
136. Goey CH, Bell D, Kontoravdi C. CHO cell cultures in shake flasks and bioreactors present different host cell protein profiles in the supernatant. Biochemical Engineering Journal. 2019;144:185-92.
137. Beattie JW, Rowland-Jones RC, Farys M, Tran R, Kazarian SG, Byrne B. Insight into purification of monoclonal antibodies in industrial columns via studies of Protein A binding capacity by in situ ATR-FTIR spectroscopy. Analyst. 2021(146):5177-85.
138. de Jong S. SIMPLS: An alternative approach to partial least squares regression. Chemometrics and Intelligent Laboratory Systems. 1993;18(3):251-63.
139. Zhang Q, Goetze AM, Cui H, Wylie J, Tillotson B, Hewig A, et al. Characterization of the co-elution of host cell proteins with monoclonal antibodies during protein A purification. Biotechnology Progress. 2016;32(3):708-17.
140. Perez-Almodovar EX, Carta G. IgG adsorption on a new protein A adsorbent based on macroporous hydrophilic polymers. I. Adsorption equilibrium and kinetics. Journal of Chromatography A. 2009;1216(47):8339-47.
141. Rathore AS, Winkle H. Quality by design for biopharmaceuticals. Nature Biotechnology. 2009;27(1):26-34.
142. Wang W. Instability, stabilization, and formulation of liquid protein pharmaceuticals. International Journal of Pharmaceutics. 1999;185(2):129-88.
143. Le Basle Y, Chennell P, Tokhadze N, Astier A, Sautou V. Physicochemical Stability of Monoclonal Antibodies: A Review. Journal of Pharmaceutical Sciences. 2020;109(1):169-90.

144. Schmidt PM, Abdo M, Butcher RE, Yap M-Y, Scotney PD, Ramunno ML, et al. A robust robotic high-throughput antibody purification platform. Journal of Chromatography A. 2016;1455:9-19.
145. Baumann P, Hubbuch J. Downstream process development strategies for effective bioprocesses: Trends, progress, and combinatorial approaches. Engineering in Life Sciences. 2017;17(11):1142-58.
146. Chen J, Tetrault J, Ley A. Comparison of standard and new generation hydrophobic interaction chromatography resins in the monoclonal antibody purification process. Journal of Chromatography A. 2008;1177(2):272-81.
147. Vetter FL, Zobel-Roos S, Strube J. PAT for Continuous Chromatography Integrated into Continuous Manufacturing of Biologics towards Autonomous Operation. Processes. 2021;9(3).
148. Arosio P, Barolo G, Muller-Spath T, Wu H, Morbidelli M. Aggregation stability of a monoclonal antibody during downstream processing. Pharmaceutical Research. 2011;28(8):1884-94.
149. Goetze AM, Schenauer MR, Flynn GC. Assessing monoclonal antibody product quality attribute criticality through clinical studies. MAbs. 2010;2(5):500-7.
150. Hogwood CEM, Tait AS, Koloteva-Levine N, Bracewell DG, Smales CM. The dynamics of the CHO host cell protein profile during clarification and protein A capture in a platform antibody purification process. Biotechnology and Bioengineering. 2013;110(1):240-51.
151. McAvan BS, France AP, Bellina B, Barran PE, Goodacre R, Doig AJ. Quantification of protein glycation using vibrational spectroscopy. Analyst. 2020;145(10):3686-96.
152. A. Gibbons L, Rafferty C, Robinson K, Abad M, Maslanka F, Le N, et al. Raman based chemometric model development for glycation and glycosylation real time monitoring in a manufacturing scale CHO cell bioreactor process. Biotechnology Progress. 2022;38(2):e3223.
153. Rowland-Jones RC, Graf A, Woodhams A, Diaz-Fernandez P, Warr S, Soeldner R, et al. Spectroscopy integration to miniature bioreactors and large scale production bioreactors–Increasing current capabilities and model transfer. Biotechnology Progress.37(1):e3074.
154. Beattie JW, Istrate A, Lu A, Marshall C, Rowland-Jones RC, Farys M, et al. Causes of Industrial Protein A Column Degradation, Explored Using Raman Spectroscopy. Analytical chemistry. 2022.
155. Lohmann LJ, Strube J. Process Analytical Technology for Precipitation Process Integration into Biologics Manufacturing towards Autonomous Operation-mAb Case Study. Processes. 2021;9(3):488.

Chapter 8- Appendix

8.1 Supplementary material

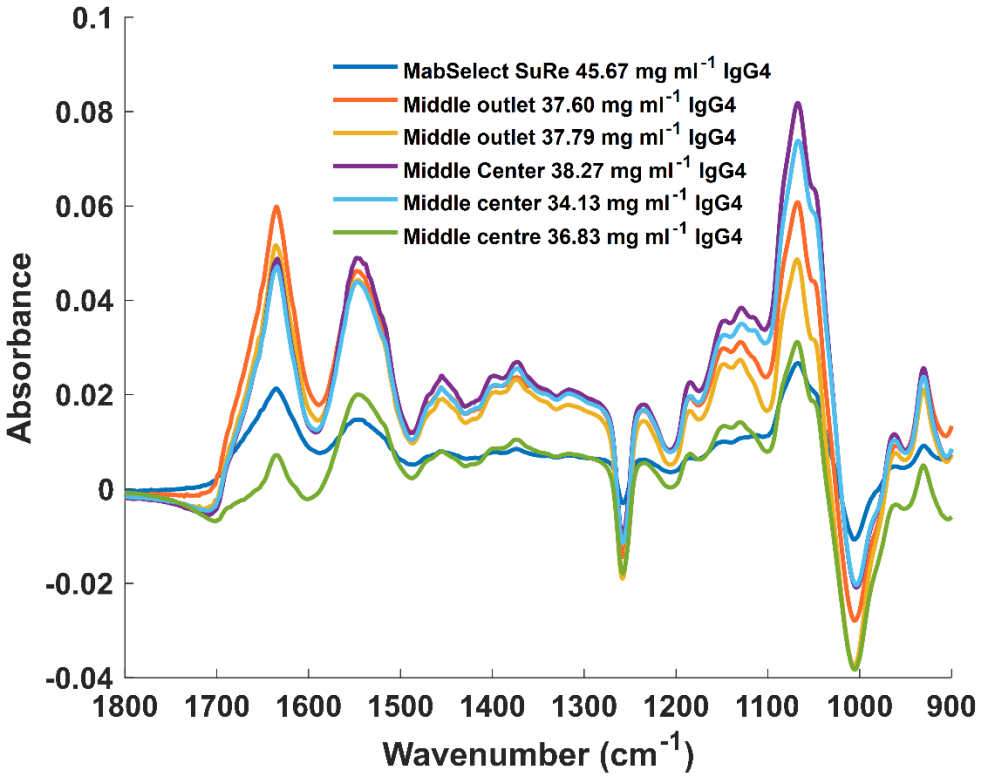

Figure 8.1 ATR-FTIR spectra excluded from the PLS training and test data. Test data was evaluated by comparing prediction to SBC observed binding capacities, if values were over 10 mg ml^{-1} different then raw spectra was assessed. MabSelect SuRe 45.67 mg ml^{-1} IgG4 (dark blue) was removed from the training data due to poor contact as shown by extremely weak glycosidic bending agarose band at 1067 cm^{-1}, upon normalisation this would cause Amide bands to be overrepresented. The middle center 36.83 mg ml^{-1} IgG4 (green) also exhibited weak agarose band. Middle Center 36.83 mg ml^{-1} (green) exhibited overly weak Amide I band. The Amide I should be the same as or higher than the Amide II band due to extra contributions from the C=O stretch. This was due to over subtraction of Water bending mode which results in under predictions of resins samples. Middle outlet 37.60 mg ml^{-1} (orange) IgG4 exhibited strong subtraction of PDMS bands at 1256 cm^{-1}, this is due to PDMS from the microwell device being replaced by the resin beads as more PDMS is present in background spectrum compared to single channel. Middle outlet 37.79 mg ml^{-1} (yellow), Middle center 38.27 mg ml^{-1} (purple) IgG4 and middle center 36.83 mg ml^{-1} (green) IgG4 also exhibited PDMS being displaced by resin. This results in underrepresented bands after normalisation and weakened bands in the 1000-1500 cm^{-1} range.

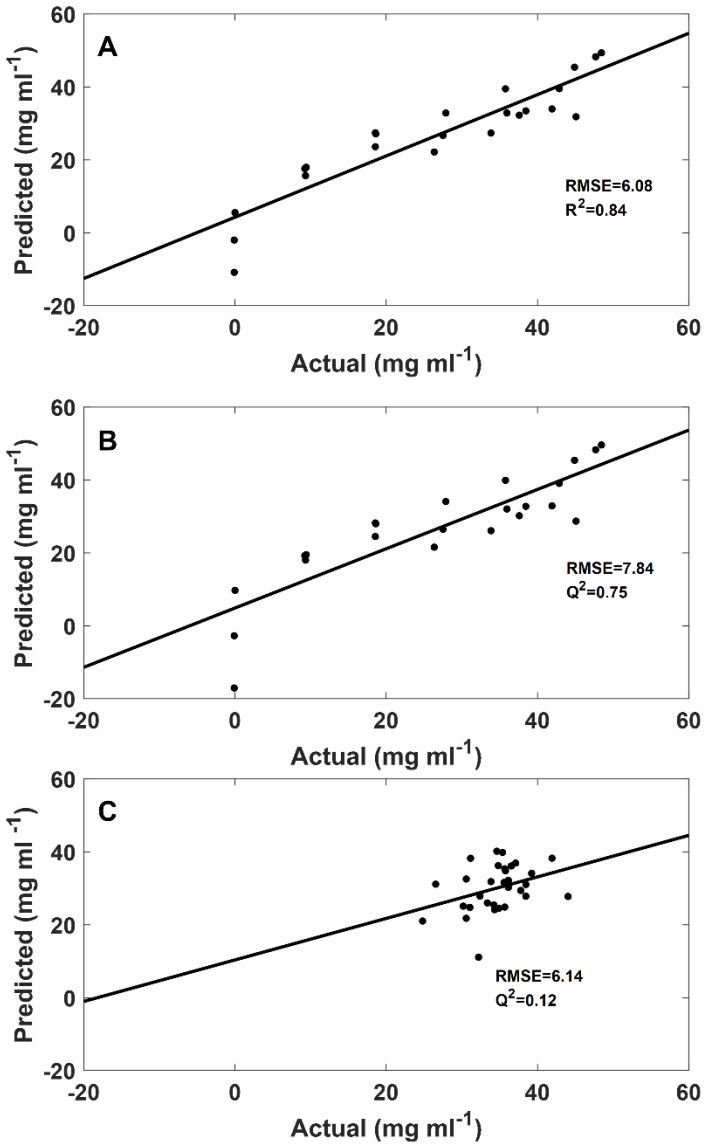

Figure 8.2 Actual vs predicted plot concentrations of mAbs bound to the PrAc resin samples. A) Training data, B) leave one out cross validation and C) test data. Actual data is the Q value calculated from the SBC assays and predicted data was obtained from the PLS model.

8.2 Supplementary material

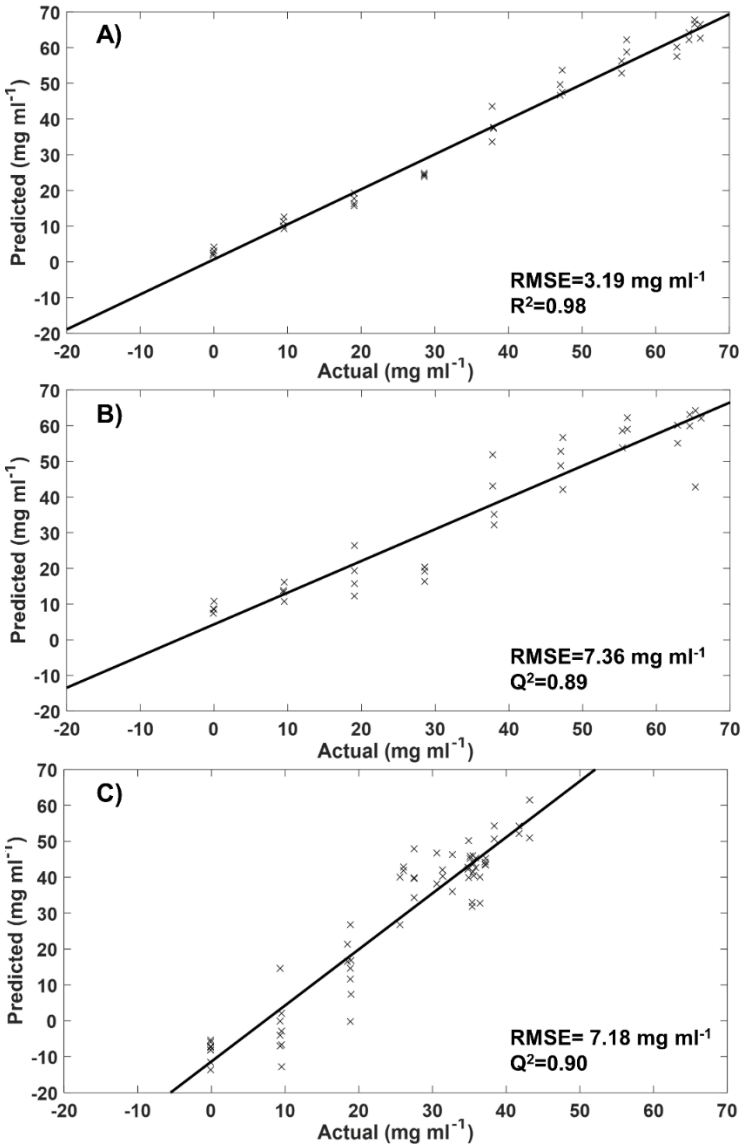

Figure 8.3 Actual vs predicted plot concentrations of mAbs bound to protein A affinity resin samples; A) training data B) leave one out cross validation and C) test data. Actual is the Q value from SBC measurements and predicted was obtained from the Raman PLS regression model.

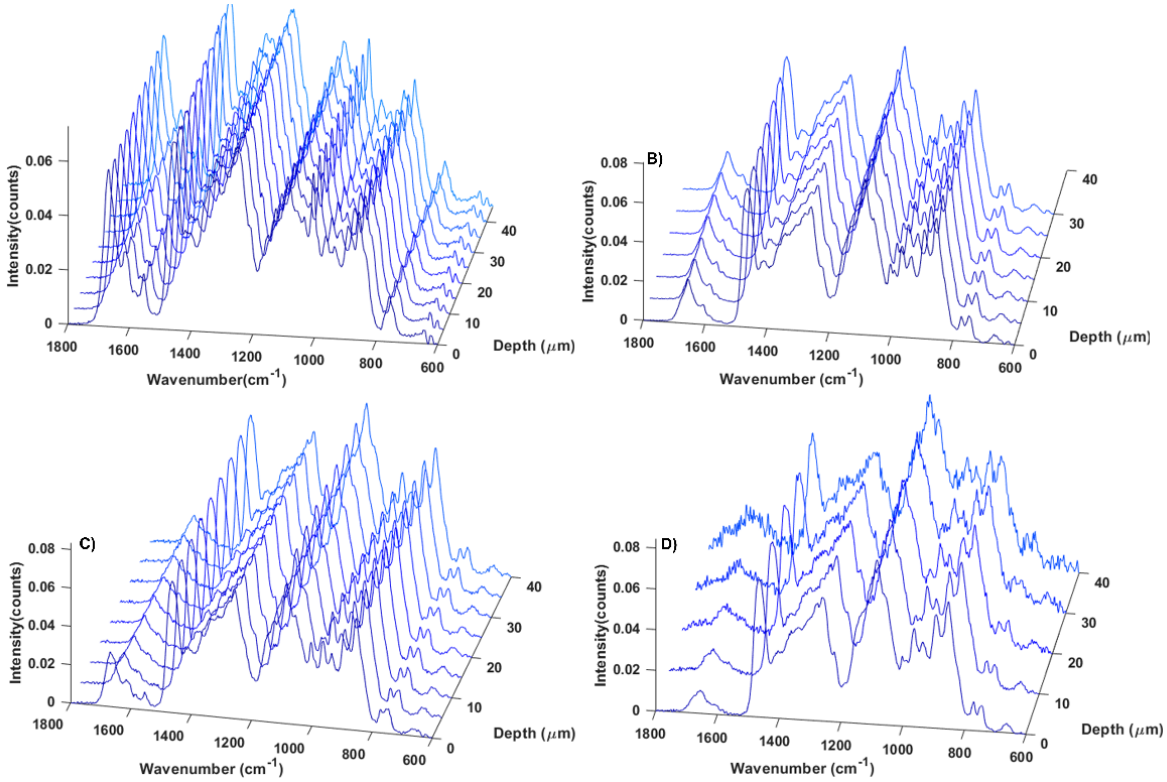

Figure 8.4 Raman spectra of resin samples plotted as a function of depth from the surface. A) MabSelect SuRe saturated with 65.68 mg ml-1 of mAb. B) MabSelect Sure partially saturated with concentration of 19.04 mg ml-1 of mAb. C) Outlet resin bead partially saturated with concentration of 18.85 mg ml-1 of mAb D) inlet resin bead with no mAbs loaded.

Table 8.1 HCPs Detected by LC- MS/MS in inlet outlet and 75 cycle resin sample. X denotes presence of protein in sample

	Inlet (25 cycles)	Outlet (25 cycles)	75 cycle sample
Endoplasmic reticulum chaperone BiP			X
Rab GDP dissociation inhibitor			X
Prolyl-tRNA synthetase (Fragment)			X
60S ribosomal protein L13			X
Importin-5			X
Sushi repeat-containing protein SRPX			X
Beta'-coat protein			X
T-complex protein 1 subunit theta			X
T-complex protein 1 subunit theta			X
Trifunctional purine biosynthetic protein adenosine-3			X
60S acidic ribosomal protein P0			X
Transketolase			X
ACTB	X	X	X
Ubiquitin	X		X
Arginine--tRNA ligase, cytoplasmic			X
Solute carrier family 2, facilitated glucose transporter member 9			X
Metavinculin			X
3-hydroxyacyl-[acyl-carrier-protein]f dehydratase	X		X
Aspartate carbamoyltransferase			X
Cullin-associated NEDD8-dissociated protein 1			X
60S ribosomal protein L9			X
RNA helicase			X
Peroxiredoxin-1	X	X	X
40S ribosomal protein S8			X
Staphylococcal nuclease domain-containing protein			X
Phosphoglycerate mutase 1			X
Alpha-mannosidase			X
40S ribosomal protein S18			X
Coiled-coil domain-containing protein 80			X
Ribosomal protein L15			X
Alpha-actinin-1			X
Tubulointerstitial nephritis antigen-like	X	X	X
Histone H3			X
Septin-9			X
Pyruvate kinase	X	X	X
HSPA2	X		X
Importin subunit beta-1			X
Hexokinase			X

Alpha-1,4 glucan phosphorylase			X
Galectin			X
CCT-epsilon	X		X
Coatomer subunit alpha			X
Transforming protein RhoA			X
Phospholipid transfer protein	X		X
ATP-binding cassette sub-family E member 1			X
Cytoplasmic dynein 1 heavy chain 1 (Fragment)			X
Heat shock protein HSP 90-alpha			X
Peptidyl-prolyl cis-trans isomerase			X
Nucleoside diphosphate kinase			X
Peroxidase	X	X	X
Heat shock protein HSP 90-beta	X	X	X
Non-specific serine/threonine protein kinase	X		X
T-complex protein 1 subunit delta			X
Histone H2A		X	X
60S acidic ribosomal protein P0			X
Filamin-B			X
Tyrosine-protein kinase receptor	X		
T-complex protein 1 subunit gamma	X		X
Small nuclear ribonucleoprotein Sm D1			X
L-lactate dehydrogenase A chain			X
CCT-alpha	X		X
Laminin subunit alpha-5		X	
Elongation factor 1-alpha	X	X	X
Collagen alpha-1(XII) chain (Fragment)		X	
Elongation factor 1-alpha 1	X		X
Thrombospondin-1	X		X
Basement membrane-specific heparan sulfate proteoglycan core protein	X	X	X
Peptidyl-prolyl cis-trans isomerase			X
Clathrin heavy chain			X
Alpha-actinin-4 (Fragment)			X
Alpha-actinin-4			X
40S ribosomal protein S16			X
Spectrin beta chain, brain 1			X
Guanine nucleotide-binding protein subunit beta-2-like 1	X	X	X
40S ribosomal protein S3a			X
Junction plakoglobin	X		
ATP citrate synthase			X
Synaptic vesicle membrane protein VAT-1-like			X
Glyceraldehyde-3-phosphate dehydrogenase	X	X	X
60S ribosomal protein L7			X
60S ribosomal protein L11			X
GPI ethanolamine phosphate transferase 3			X
Clusterin	X	X	X
Phosphoglycerate kinase			X
Phosphoglycerate kinase			X

Isoleucyl-tRNA synthetase			X
D-3-phosphoglycerate dehydrogenase			X
GTP-binding nuclear protein Ran			X
Histone H4		X	X
Protein-synthesizing GTPase			X
Endoplasmin			X
Tubulin beta chain	X		X
40S ribosomal protein SA	X		X
Lipase	X		
Protein arginine N-methyltransferase 5			X
Matrix metalloproteinase-19			X
Elongation factor 2	X	X	X
Cytoplasmic FMR1-interacting protein			X
Lysosomal alpha-glucosidase	X		
F-actin-capping protein subunit beta			X
Adenylosuccinate lyase		X	X
Phosphoglycerate kinase	X		X
T-complex protein 1 subunit eta	X		X
CCT-beta	X		X
Tenascin-X		X	
Tenascin-X		X	
Ribosomal protein			X
40S ribosomal protein S4			X
60S ribosomal protein L13a			X
40S ribosomal protein S11			X
Elongation factor 1-gamma	X		X
Glyceraldehyde-3-phosphate dehydrogenase		X	X
Fibronectin			X
40S ribosomal protein S20			X
T-complex protein 1 subunit zeta			X
GST class-pi	X	X	X
Fructose-bisphosphate aldolase			X
60S ribosomal protein L7a			X
Tubulin alpha chain	X		X
Phospholipase B-like			X
Importin-7			X
Keratin, type I cytoskeletal 19	X		X
Keratin, type I cytoskeletal 14	X	X	X
Keratin, type I cytoskeletal 17	X		X
Keratin, type I cytoskeletal 42	X		
Triosephosphate isomerase			X
L-lactate dehydrogenase			X
26S proteasome non-ATPase regulatory subunit 2			X
40S ribosomal protein S9			X
Procollagen C-endopeptidase enhancer 1			X
AP-2 complex subunit alpha			X
2-phospho-D-glycerate hydro-lyase	X	X	X
Glutaminyl-tRNA synthetase			X

Filamin-A			X
Keratin, type II cytoskeletal 6A	X	X	X
Keratin, type II cytoskeletal 71	X	X	X
Aldose reductase-related protein 2	X		
Elongation factor 1-gamma			X
Ras GTPase-activating-like protein IQGAP1			X
Heat shock cognate 71 kDa protein			X
60S ribosomal protein L34			X
GTP-binding nuclear protein Ran			X
6-phosphogluconate dehydrogenase, decarboxylating	X		X
Keratin, type II cytoskeletal 5	X		
Glutathione transferase		X	X
40S ribosomal protein S15a			X
Pigment epithelium-derived factor			X
Glutathione S-transferase	X	X	
Uncharacterized protein			X
UDP-glucose 6-dehydrogenase	X	X	X

8.3 Supplementary material

Table 8.2 Calibration curve for BT B on HPLC machine 1. Iv is injection volume. Concentration of diluted BT standard used was verified on lunatic n=3.

BT B C_M (µg)	Peak Area	I_V (µL)	Concentration of standard (mg ml^{-1})
4.70	389	5	0.94 ±0.01
6.58	273	7	0.94 ±0.01
9.40	392	10	0.94 ±0.01
14.10	590	15	0.94 ±0.01
18.80	786	20	0.94 ±0.01
23.50	950	25	0.94 ±0.01
28.20	1145	30	0.94 ±0.01

Table 8.3 Calibration curve for BT c on HPLC machine 1. Iv is injection volume. Concentration of diluted BT standard used was verified on lunatic n=3.

BT C C_M (µg)	Peak Area	I_V (µL)	Concentration of standard (mg ml^{-1})
4.57	211	5	0.91 ± 0.01
6.39	143	7	0.91 ± 0.01
9.13	251	10	0.91± 0.01
13.70	479	15	0.91± 0.01
18.27	667	20	0.91± 0.01
22.83	852	25	0.91± 0.01
27.40	1150	30	0.91± 0.01

Table 8.4 Calibration curve for BT C on HPLC machine 2. Iv is injection volume. Concentration of diluted BT standard used was verified on lunatic n=3.

BT B C_M (µg)	Peak Area	I_V (µL)	Concentration of standard (mg ml $^{-1}$)
4.78	211	5	0.96 ± 0.01
6.70	286	7	0.96 ± 0.01
9.57	405	10	0.96 ± 0.01
14.35	606	15	0.96 ± 0.01
19.13	808	20	0.96 ± 0.01
23.92	1011	25	0.96 ± 0.01
28.70	1206	30	0.96 ± 0.01

Table 8.5 Calibration curve for BT A on HPLC machine 2. Iv is injection volume. Concentration of diluted BT standard used was verified on lunatic n=3.

BT A C_M (µg)	Peak Area	I_V (µL)	Concentration of standard (mg ml $^{-1}$)
5.00	221	5	1.00 ± 0.02
7.00	306	7	1.00 ± 0.02
10.00	438	10	1.00 ± 0.02
15.00	658	15	1.00 ± 0.02
20.00	877	20	1.00 ± 0.02
25.00	1093	25	1.00 ± 0.02
30.00	1302	30	1.00 ± 0.02

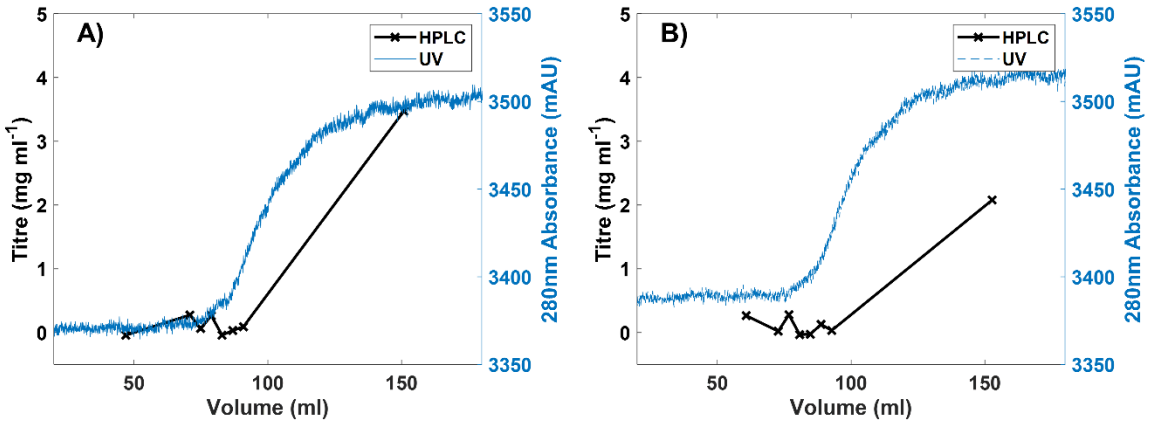

Figure 8.5 Comparison of HPLC titre from selected fractions and 280 nm absorbance from chromatogram for BT B flowthrough on flowthrough at 6 minute residence time. A) purification cycle 2 B)purification cycle 10e Blue line is UV absorbance from chromatogram. Black marked points are HPLC measured BT B titre of fractions. In both samples the titre does not follow trend of absorbance at start of increase in UV curve. This is due to human sampling error.

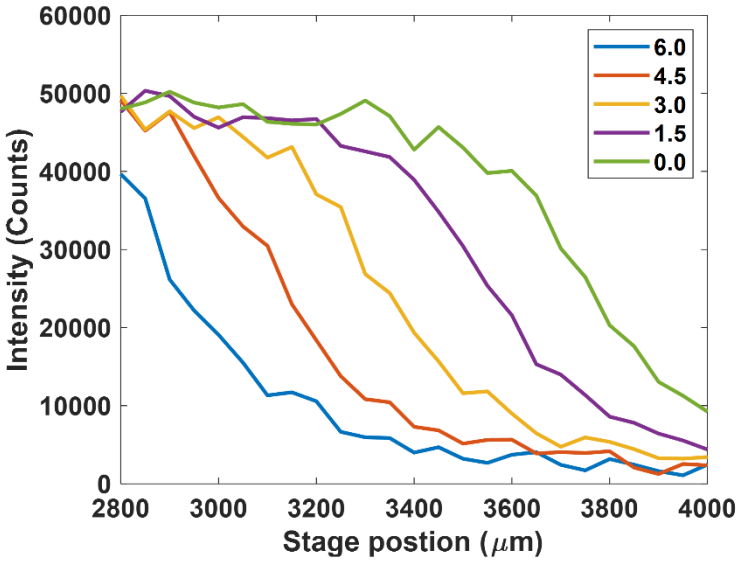

Figure 8.6 Depth profile Raman measurement time course as a function of stage position in the z direction of a 200 µl 1M Urea solution in a 96 well plate. The measurement parameters were the 532nm laser set to the 5 mW setting, 2 s exposure time, 2 accumulations and a grating of 1800 grooves mm^{-1}. All spectra were pre-processed using a Savitzky-Golay filter (window=9 polynomial=1 derivative=0) to reduce noise in the non-optimised spectrometer parameters. CN_{vs} mode of Urea was integrated from the baseline at (932-1075 cm^{-1}). Green= Depth profile at 0

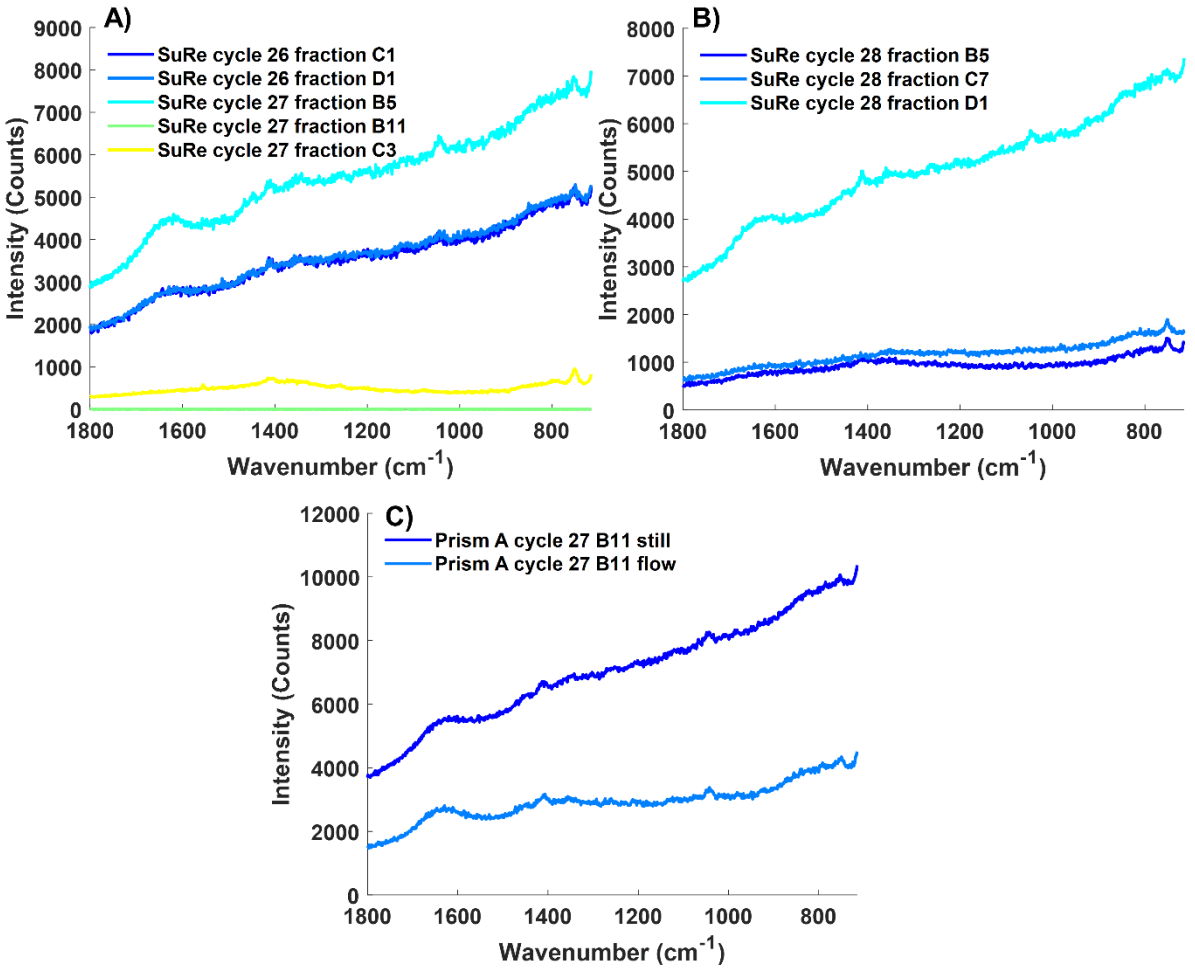

Figure 8.7Raman spectra removed from inline breakthrough pls model training and test data sets. A) Training data removed from training model. Cycle 26 fraction C1, D1 and Cycle 2 fraction B5 had flow interrupted during measurement 6 .Cycle 27 fraction B11 and C3 observed no CUB signal due to misalignment B) Test data removed from predictions. SuRe cycle 28 fraction B5 and C7 observed no signal due to mis alignment with channel. Fraction D1 had flow interrupted during measurement so could not be used. C) Example of effect of flow on Raman spectrum. Flow caused changes in spectral intensity so any spectrum where flow was interrupted should not be used as would skew predictions.